NEW FRONTIERS IN STRAIN-TUNING: APPARATUS DEVELOPMENT, AND TUNING OF THE NEMACITY OF FESE ACROSS A WIDE STRAIN RANGE

Jack Michael Bartlett

A Thesis Submitted for the Degree of PhD
at the
University of St Andrews

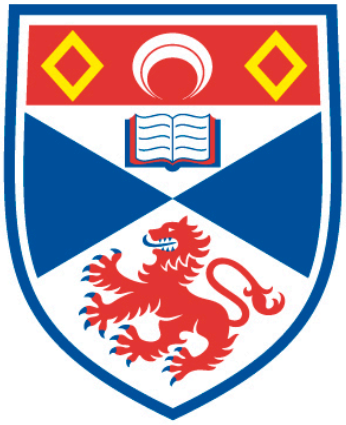

2019

New Frontiers in Strain-Tuning: Apparatus Development, and Tuning of the Nematicity of FeSe Across a Wide Strain Range

Jack Michael Bartlett

University of
St Andrews

This thesis is submitted in partial fulfilment for the degree of

Doctor of Philosophy (PhD)

at the University of St Andrews

November 2018

Candidate's declaration

I, Jack Michael Bartlett, do hereby certify that this thesis, submitted for the degree of PhD, which is approximately 52,000 words in length, has been written by me, and that it is the record of work carried out by me, or principally by myself in collaboration with others as acknowledged, and that it has not been submitted in any previous application for any degree.

I was admitted as a research student at the University of St Andrews in August 2014.

I received funding from an organisation or institution and have acknowledged the funder(s) in the full text of my thesis.

Date Signature of candidate

Supervisor's declaration

I hereby certify that the candidate has fulfilled the conditions of the Resolution and Regulations appropriate for the degree of PhD in the University of St Andrews and that the candidate is qualified to submit this thesis in application for that degree.

Date Signature of supervisor

Permission for publication

In submitting this thesis to the University of St Andrews we understand that we are giving permission for it to be made available for use in accordance with the regulations of the University Library for the time being in force, subject to any copyright vested in the work not being affected thereby. We also understand, unless exempt by an award of an embargo as requested below, that the title and the abstract will be published, and that a copy of the work may be made and supplied to any bona fide library or research worker, that this thesis will be electronically accessible for personal or research use and that the library has the right to migrate this thesis into new electronic forms as required to ensure continued access to the thesis.

I, Jack Michael Bartlett, have obtained, or am in the process of obtaining, third-party copyright permissions that are required or have requested the appropriate embargo below.

The following is an agreed request by candidate and supervisor regarding the publication of this thesis:

Printed copy

Embargo on all of print copy for a period of 2 years on the following ground(s):

- Publication would preclude future publication

Supporting statement for printed embargo request

My thesis includes research that is yet to be published.

Electronic copy

Embargo on all of electronic copy for a period of 2 years on the following ground(s):

- Publication would preclude future publication

Supporting statement for electronic embargo request

My thesis includes research that is yet to be published.

Title and Abstract

- I agree to the title and abstract being published.

Date Signature of candidate

Date Signature of supervisor

Underpinning Research Data or Digital Outputs

Candidate's declaration

I, Jack Michael Bartlett, understand that by declaring that I have original research data or digital outputs, I should make every effort in meeting the University's and research funders' requirements on the deposit and sharing of research data or research digital outputs.

Date Signature of candidate

Permission for publication of underpinning research data or digital outputs

We understand that for any original research data or digital outputs which are deposited, we are giving permission for them to be made available for use in accordance with the requirements of the University and research funders, for the time being in force.

We also understand that the title and the description will be published, and that the underpinning research data or digital outputs will be electronically accessible for use in accordance with the license specified at the point of deposit, unless exempt by award of an embargo as requested below.

The following is an agreed request by candidate and supervisor regarding the publication of underpinning research data or digital outputs:

Embargo on all of electronic files for a period of 2 years on the following ground(s):

- Publication would preclude future publication

Supporting statement for embargo request

My thesis includes data/digital outputs that are yet to be published.

Date Signature of candidate

Date Signature of supervisor

New Frontiers in Strain-Tuning: Apparatus Development, and Tuning of the Nematicity of FeSe Across a Wide Strain Range

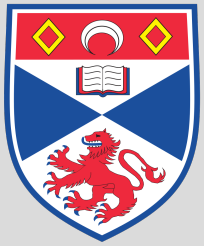

Jack Bartlett

UNIVERSITY OF ST ANDREWS

"*Nature is our kindest friend and best critic in experimental science if we only allow her intimations to fall unbiased on our minds.*"

Michael Faraday

ABSTRACT

Over the last decade, an 'iron age' of superconductivity has challenged the paradigm of unconventional pairing established by copper-oxide-based materials. Fascinatingly, in these iron-based compounds superconductivity emerges from a state in which electrons choose to distinguish between two equivalent directions of the underlying crystalline axes. The origin of this 'nematic' state is highly debated.

This thesis concentrates on FeSe, a material appealing because its nematicity does not occur in proximity to long-range magnetic order. Although uniaxial strain couples to nematic order, experiments to date have focused on applying only a small symmetry-breaking strain. The mechanical properties of FeSe make utilising established piezoelectric-based apparatus, designed for continuous tuning of large uniaxial strains, challenging. In this thesis we develop a platform to which samples can be adhered, and apply large anisotropic strain to FeSe. When of the same symmetry as the nematicity, and larger than the structural distortion, this applied strain fully constrains the lattice. We provide a precise set of resistivity measurements across a wide temperature and strain range, revealing vital new phenomenologies.

We establish the relationship between electrical transport and nematicity across a large strain range at the structural transition and, by isolating the influence of domain walls, characterise the elastoresistivity for temperatures below this transition. By tracking the onset of domain formation, we determine the temperature dependence of the spontaneous structural distortion, and use this to extract the intrinsic resistivity anisotropy within a single nematic domain. Interestingly, we discover a crossover at $\sim 50\,\mathrm{K}$ between distinct high- and low-temperature behaviours.

This thesis is also concerned with the development of apparatus for tuning strain. We conceptualise a new type of stress-controlled cell, which can apply large (up to 8 GPa in compression) uniaxial stresses to microstructured samples – pushing them to their ultimate mechanical limit.

ACKNOWLEDGEMENTS

Embarking on a PhD is a challenging journey that one cannot hope to complete without the help of others. I am thankful for the fantastic support of those around me, from friends, family, and colleagues, that made my PhD not only possible but thoroughly enjoyable. This thesis is a cumulation of four years of work, starting out at the University of St Andrews, before moving to the Max Planck Institute for Chemical Physics of Solids (CPfS) in Dresden where I spent the majority of my PhD and completed experimental work. As a member of the Scottish Doctoral Training Centre in Condensed Matter Physics (CM-CDT) throughout this time, I have benefited greatly from the additional skills training and community of fellow students.

I would first like express considerable thanks Andy Mackenzie, not only for giving me this opportunity, but also welcoming me into the group, and always providing his time and advice. Being a part of the Physics of Quantum Materials Group has been an immensely stimulating experience, fostered by a positive, social and open atmosphere.

Experimental work was conducted under the supervision of Clifford Hicks, to whom I owe a great deal of gratitude for his guidance and teaching. The opportunity to conduct world-leading experimental physics, whilst being able to take part in cutting-edge apparatus development under Cliff, is one that I have greatly relished. Without Cliff's ingenuity many aspects of the work presented in this thesis would not have been possible. I would also like to thank him for involving me in collaborative work with colleagues in Japan, and consequently for my short visit to the Institute for Solid State Physics at the University of Tokyo – this was a incredible experience.

I would like to extend warm appreciation and acknowledgement to Alexander Steppke. As the occupant of the desk opposite mine, Alexander provided endless assistance throughout my time in Dresden, from science to the German language, and everything in between. In the latter part of my PhD, a closer collaboration was formed through joint work on the FeSe project. Not only was Alexander vital to the success of this project, but from him I also learnt an immense amount. He patiently taught

me Python and cryogenics, as well as epitomising the scientific process and imparting a positive influence on the way I conduct research. We shared many late-night head-scratching discussions, and Alexander's formidable problem solving skills were critical in progressing such a challenging project.

I would like to acknowledge Po-Ya Yang, whose involvement in the apparatus development project propelled forward construction; a compliment to his skill and dedication. I would also like to thank Suguru Hosoi. He introduced FeSe into our group, forming the core of this thesis, and we formed a close collaboration and friendship. Several additional, but important, names deserve acknowledgement for their assistance in my project. Mark Barber was a continual and faultless provider of knowledge in all areas. The expertise of Markus König and Sebastian Seifert was essential for technical developments. Thomas Lühmann's LabView wizardry was vital to the smooth running of our experiment, and meant that he was always able to respond quickly to ambitious requests. The later technical aspects of solid platform development were greatly assisted by the contributions of Hilary Noad. I also learnt a great deal in working closely with Dan Sun on $PdCrO_2$. There are too many names to list for all the people who have offered help, advice and useful discussions along the way. To name a few I would like to thank Burkhard Schmidt, Manuel Brando, Chris Hooley, Kent Shirer and Toni Helm.

I would like to thank the tireless work of the CDT administrators, Julie Massey, Christine Edwards, and more recently Wendy Clark and Debra Thompson. They provided endless support, as the beating heart of the Centre. Equally, I wish to thank all the administrative and technical staff working behind the scenes at CPfS. In particular, I would like to thank Claudia Strohbach of the guest administration for her support.

Fellow PhD students bore the brunt of many of my struggles. I would firstly like to thank those with whom I shared (the legendary times in) Office 120: Philip Ireland, Elliott Levi, Scott Taylor, Ian van Beek, Lewis Bawden and Maximilian Schulz. My PhD would not be the experience it has been without the close bonds formed with 'original gang' Max Planck students: Maja Bachmann, Veronika Sunko, Nabhanila Nandi, You-Sheng Li and Fabian Jerzembeck. It has additionally been a pleasure spending time and discussing with new students Philippa McGuinness, Po-Ya Yang and Bélen Zúñiga. The company of such talented individuals has been amazing.

In the duration of my studies towards this thesis I have been fortunate to have twice been able to live with good friends also undertaking a physics PhD. Scott, words cannot describe the fondness with which I look back on our year in St Andrews. Max, you are an inspirational chap who enhanced my life in so many ways. It was a great

joy to shared my time in Dresden living with David Siebrasse, and Hella van Lengerich – and I am grateful for the people outside the institute to whom you introduced me.

I am extremely thankful for my family. My parents and siblings have put up with much dinner-table physics over the years! Without your support and encouragement I would not be where I am today. Additionally, I would like to thank my grandparents who stimulated my intellectual curiosity from a young age.

Kirsten, words fail me in expressing how eternally grateful I am for the support, joy, and sanity you have provided throughout this whole journey. Thank you for being my best friend. With your endless love and patience, I owe everything to you.

This work was supported by the EPSRC Research Council via the Scottish Doctoral Training Centre in Condensed Matter Physics (under grant number EP/L015110/1), as well as the Max Planck Gesellschaft.

Research data underpinning this thesis are available at https://doi.org/10.17630/2c041fd5-37cb-4225-bb4e-0b75d4231d21.

Contents

List of Figures

List of Tables

1 Introduction

Broadly speaking, the most significant open question in the field of modern condensed matter is that of unconventional superconductivity. How can we understand a wide range of materials in which evidence points to the superconducting state being formed by pairing not explained by the 'conventional' exact many-body solution formulated by Bardeen, Cooper and Schrieffer? The key to answering this question is likely sensitive to different underlying mechanisms specific to certain materials, or classes of materials, and resolution is thus not expected to be as simple as a single 'Eureka!' discovery. Recognising features common to different materials displaying such unconventional pairing is the most basic place to start, and this can be powerful.

To the non-physicist, 'superconductivity' is likely recognisable due to the longstanding, and slightly outlandish, promise that it holds the solution to our energy crisis. Such a realisation requires the superconducting state – in which current can flow without dissipation, and thus electricity to be transmitted without loss – to be achieved at, or close to, room temperature. In the 1980's a surge of optimism grew from a discovery of 'high-temperature' superconductivity in copper-oxide based compound $La_{2-x}Ba_xCuO_4$, with $T_c \sim 40\,\mathrm{K}$ (this is around 140 °C colder than the coldest place on Earth) for which Bednorz and Müller were later awarded the Nobel prize. The superconductivity in this material is unconventional, and decades of subsequent research has revealed similar high-T_c superconductors, the highest with $T_c \sim 135\,\mathrm{K}$ at ambient pressure, all with a common thread: planes of copper ions coordinated with oxygen.

The high transition temperatures under ambient conditions in these copper-based compounds were long shared by no other materials, establishing the viewpoint that it was a unique feature of their specific phase diagram, in which superconductivity emerges from antiferromagnetism. Research over the last decade has forced this viewpoint to be discarded. This emanated from the observation of high-T_c superconductivity (26 K) in fluorine-doped LaOFeAs – a material built upon *iron* rather than copper. In the many subsequently discovered iron-based superconductors (the maximum T_c of which

is 56 K at ambient pressure) an important type of physics has emerged: electrons break the underlying rotational symmetry of the lattice. The physical origin of this so-called 'nematic' state is highly debated, but its importance is undoubted as upon cooling superconductivity emerges from this state.

Study of nematicity is challenged by the dilemma that once a symmetry is broken the effects will be seen in all observables of the system, regardless of the exact mechanism or degrees of freedom which drive it. Although most iron-based superconductors undergo a tetragonal-to-orthorhombic structural phase transition, it is electronic rather than lattice degrees of freedom which are thought to drive the transition. Furthermore, iron-based superconductors are multi-band metals with orbital and spin degrees of freedom, and thought to be in an intermediate-strength correlation regime. The big-picture questions regarding nematicity in these materials involve determining the relative contributions of orbital-selective coherence, spin fluctuations and orbital fluctuations. Shedding light on this problem from a theoretical perspective, and in an unbiased way, is challenging, especially considering the extent of inputs which must be constrained. Any physical situation which simplifies the picture is clearly highly valuable. FeSe is attractive in this sense as it exhibits no long-range magnetic order at ambient pressure, and furthermore it is structurally simple. This in no way implies that spin fluctuations can be ignored however. Additional simplification can be achieved by removal of the structural degree of freedom. Experimentally, this corresponds to fully constraining the lattice through application of an orthorhombicity larger than that of the spontaneous structural distortion. Fixing the lattice in this way naturally poses the question of whether a signature of the nematic transition would still be observable.

Deep insight into the properties of a broken-symmetry state can, in general, be gained by studying the phase transition from which it emerges, as well as its response to a conjugated field. Uniaxial strain with the same symmetry as the orthorhombic distortion is conjugate to the nematicity. Highly precise application of a tuneable, uniaxial deformation across a large strain and temperature range is extremely technically challenging, and use of such a technique for investigating iron-based superconductors – which is clearly powerful for probing nematicity – has consequently not yet been fully achieved. Furthermore, such experimental information would prove indispensable for constraining theoretical studies. These models would not only have to fit to the unstressed material, but also to any additional orthorhombic distortions applied.

The main focus of this thesis concerns realisation of the technique proposed above. Technological breakthroughs in the last few years have established the field of 'strain-tuning', using piezoelectric-based apparatus to apply large uniaxial pressures in a highly

precise and tuneable manner at cryogenic temperatures. In extending this technique to accommodate the challenging mechanical properties of FeSe – it is soft and flakey – we can contribute a set of precise and reliable electrical transport measurements in which we both tune and fix the orthorhombicity of the lattice, and couple to the underlying nematic order. By isolating the effect of twin boundaries, we can characterise the elastoresistivity over the large range of temperatures below the structural transition temperature; another achievement obtained by no other previous work. Reiterating the initial motivation already posed: we can investigate whether there exists any signature of the nematic transition, even when the lattice is held fixed. In pursing this, we unveil a wealth of interesting phenomenological observations.

Experimental physics concerns the precise acquisition of measurable quantities under controlled conditions. Methods for increasing this precision are driven forward by technological advances, which are thus crucial for obtaining deeper insights into nature. In a tale of two halves, this thesis is also concerned with development of a new type of uniaxial pressure cell. This apparatus is stress controlled and can apply extremely large deformations, allowing materials to be pushed to their ultimate mechanical limit. Realisation of such a device expands the phase diagram of any material further than before, making it a powerful tool for investigating physics in a new limit.

A brief overview of the organisation of this thesis is as follows. In Chapter 2, we outline important background physics relevant to understanding the properties of FeSe. This starts with basic phenomenology of broken symmetry, enabling the concept of electronic nematicity to be introduced. With a focus on the nematic state, we review literature and current understanding of iron-based superconductors, before progressing on to the properties of FeSe. Following this, a detailed description of experimental methods will be given in Chapter 3. Starting with the fundamentals of describing deformations in solids, we then describe strain-tuning and established piezoelectric-based apparatus. Extension of this technique, via a considerable developmental effort, to enable application of in-plane strain to FeSe, is the focus of the latter half of this chapter. Next, in Chapter 4 we present measurements of electrical transport on FeSe under continuously tuned in-plane strain, constituting the core scientific results of this thesis. Lastly in Chapter 5, we shift gears, focusing on an engineering-based development conceiving novel apparatus to apply controlled tuneable stress to microstructured samples. This commences with an overview of the principles of stress-apparatus development, before describing the considerations, tests and simulations required to establish the final apparatus design.

2 | Background Physics

The constituents of matter – atoms composed of electrons surrounding a nuclear core of protons and neutrons – have been known for over a century. In the matter we interact with on a daily basis, i.e. solids and liquids, these atoms are closely separated or 'condensed' with interatomic spacings of $\sim 0.1\,\text{nm}$, such that the energy scale from electromagnetic forces dominates their interactions. To gain the simplest understanding regarding the origin of the properties of solids and liquids, one should consider a large (10^{23}) system of interacting particles. The quantum-mechanical equation which describes the energy of such a system, and therefore in principle (nearly) all matter, is simple to write down: it consists of the kinetic energy of each constituent, plus its Coloumb interaction with every other particle. One might naively claim that the job is done; we have identified all constituents and the equation which governs their behaviour. This is a hollow victory, as even with the most powerful computers this equation cannot be solved for more than a few particles. Even if such a solution could be obtained, it would probably not be a useful way to understand nor predict physical phenomena. It would seem then that we are doomed from the outset, however with simplifications, approximations (and ingenuity of course) we can accurately describe and understand the underlying physics that gives rise to most electrical, mechanical, magnetic and optical properties of crystalline solids.

In throwing away all interactions, the basic properties of simple metals can be obtained. As postulated by Pauli, the fundamental fermionic nature of electrons means they cannot occupy the same states with the same quantum numbers, and so form an inert gas up to a boundary in momentum space between occupied and unoccupied states. This boundary defines the so-called Fermi surface, and only electrons occupying states within a window of thermal energy $k_B T$ of this surface can participate in electrical and thermal transport. By introducing a periodic potential emanating from the underlying lattice, it is revealed that some electron energies are forbidden, and available states are arranged into 'bands'. This band picture explains why some solids

are metals, and others insulators or semiconductors. However the amount of success provided by this picture should be surprising since we are still neglecting electron-electron interactions, and a quick comparison of kinetic and Coloumb interaction energies gives a ratio $E_C/E_K \sim r_s/a_0$, i.e. electron separation in units of the Bohr radius. In most metals this ratio is greater than one and thus interactions cannot be ignored, giving a picture more closely analogous to a liquid rather than a gas. Resolution of this dilemma was provided by Landau: when adiabatically turning on electronic interactions, the relevant excitations are quasiparticles which can be mapped on to single-particle excitations [1]. Near the Fermi surface these excitations are long lived and act as if non-interacting (but with renormalised parameters), even in the case of strong interactions. This theory of the Fermi liquid is one of the cornerstones of conventional condensed matter physics.

It is clear then that acquiring a full understanding of even simple materials is quite a complex task. Modern condensed matter physics research is concerned with an even richer palette of phenomena than just simple solids and liquids. One encounters phases which can only be understood by many-body collective phenomena such as superconductivity and superfluidity, as well as phases which can only be understood by introducing the concept of topology. Our understanding is then challenged by materials which exhibit a breakdown of Fermi-liquid behaviour, or unconventional superconductivity, and these phases coexist and compete with ordering due to spin and orbital degrees of freedom. From this vantage point, the failures of the reductionist approach that we opened with – in which we sought the simplest description of the most fundamental constituents of the system – is made firmly apparent.

An important aspect of investigating these complicated systems is looking for generic features, and thus underlying mechanisms, which help understand a larger class of materials. For example: does understanding the origin of unconventional superconductivity in $YBa_2Cu_3O_{7-\delta}$ help understand its origin in other superconductors with copper-oxide layers? And then what about other unconventional superconductors in general? This issue is particularly relevant in experimental condensed matter physics, in which understanding must be gained through measurement of one specific material at a time, and measurable properties can differ even if they have the same origin. It is therefore important to pinpoint features which depend only on macroscopic properties and not microscopic details; this is the underlying concept of ‘universality’. The second cornerstone of condensed matter physics, again accredited to Landau, is a theory of continuous phase transitions which depends only on symmetry, thus displaying such universality, and makes testable predictions without need for precise

microscopic information. This has profound consequences, bringing remote areas of physics together, and will be our starting point for the discussion of background physics relevant to this experimental research.

In this chapter we will first introduce some general concepts regarding broken symmetry and the Landau formalism of second-order phase transitions as briefly introduced above. This will be applied to structural phase transitions and used to introduce the concept of nematicity from a hard condensed matter point of view. Nematicity and its origin will then be discussed generally in the context of the iron-based superconducting compounds. In the latter half of the chapter we will focus on the binary material FeSe, which forms the focus of this thesis. We place an emphasis on describing nematic order and its possible origin, and present a review of recent experimental and theoretical results.

2.1 Broken symmetry in condensed matter

2.1.1 Introduction

Symmetry is a ubiquitous underlying concept within mathematics and the natural sciences. It has long been recognised by humans due to its physical tangibility – nearly all animals have either bilateral or radial symmetry. More formally, symmetry is defined as the collection of transformations which leave an object unchanged. This is more concretely defined mathematically within group theory, which allows the concepts of symmetry to be applied to more abstract objects like mathematical functions and physical laws. Symmetry has far-reaching consequences for the fundamental laws of physics. The translational invariance of space leads to the conservation of momentum, and of time leads to the conservation of energy. These are examples of Noether's theorem which, loosely speaking, draws the profound conclusion that the continuous symmetries of a system result in conserved quantities.

Every entity can be characterised by its symmetry – or equally importantly its lack thereof – and in fact one usually thinks of an absence of symmetry as being 'more' symmetric. However, an object has higher symmetry if it is invariant to a larger group of transformations compared to the low symmetry state. For example the continuous rotational symmetry of a circle is *reduced* in going to the discrete four-fold symmetry of a square. On the largest scale, the universe has full translational and rotational invariance – it is approximately isotropic in all directions – however on an atomic scale we know that most solids are crystalline and thus of a lower and discrete symmetry.

Many phase transitions in physical systems are defined by a change of symmetry as a thermodynamic variable is varied. In particular, the appearance of a second-order (i.e. a continuous) phase transition implies a change in symmetry. Naively understanding why a change of symmetry occurs from a thermodynamic perspective is straightforward: with temperature as a tuning parameter the system tries to minimise its free energy according to $F = E - TS$, where E is its energy and S its entropy. At high temperatures the TS term dominates and the system wishes to maximise its entropy, giving the disordered (high-symmetry) phase. Conversely at low temperatures the ground-state energy of the system must be minimised, and this can occur by loss of symmetry into an ordered state. The low-temperature phase is characterised by a parameter ϕ which becomes non-zero at the transition temperature T_c in going from the disordered to ordered phase; this is referred to as the order parameter. The change in ϕ at T_c can either be discontinuous as for a first-order transition, or continuous as for a second-order phase transition. Whereas for the latter a change of symmetry always occurs, it is not necessarily a requirement of the former.

The phenomenology of broken symmetry connects distant topics across the breadth of physics: for example both the para-ferromagnetic and normal metal-superconductor transitions are second-order. In the language of quantum mechanics, at high temperature both the system and its Hamiltonian are invariant under the same symmetry operations of some group $\mathcal{G}$, but below T_c the system is only invariant under an subset of $\mathcal{G}$ with the Hamiltonian remaining unchanged under the whole group. This is quite a baffling scenario; the system seems to have 'chosen' to drop certain symmetries even though they are present in the underlying Hamiltonian. This predicament is resolved by understanding that the broken-symmetry ground state is not a true stationary state, but instead a superposition of equal-energy eigenstates. It is therefore only metastable, with a extremely long stability time – especially at at low-temperatures and with large particle numbers.

Continuous phase transitions are defined by a broken symmetry, and with some further consideration we can identify other expected properties of the system across this phase transition. First, as the transition is approached the response of the system to a small applied field (that matches the symmetry change) will diverge. Secondly, a rigidity of the order parameter against spatial variations is expected via a term $\rho(\nabla\phi)^2$ in the free energy. This term accounts for the mechanical rigidity of solids: the order parameter specifies the degree of localisation of the atoms into a periodic array, and the gradient term specifies the resistance of the system to spatial variations in the atomic locations. Thirdly, the symmetry change may not occur macroscopically in

the same way, splitting the material up into domains with different degenerate values of the order parameter. Such regions are separated by domain walls, and at these interfaces there can be large local variations in the order parameter. Domains can be thermodynamically stable if the energy cost of creating domain walls is less than the energy gain from allowing a non-uniform order parameter. If, for example, the ordered phase implies a structural deformation but the sample is held rigidly, then permitting a non-uniform order parameter – i.e. domain walls – will reduce the elastic energy of the system. Finally, when the broken symmetry is continuous*, the energy spectrum for excitations is gapless, meaning that excitations can occur with a long wavelength at any nonzero temperature. These excitations increase the entropy of the system, and for dimensions $d \leq 2$, destroy long-range order at any nonzero temperature. This is the Mermin-Wagner theorem.†

2.1.2 Landau theory

Although the most commonly encountered phase transition from liquid to solid involves a change of symmetry, the order parameter change is discontinuous. We seek a description of symmetry-changing transitions across which the order parameter varies continuously. As already prefaced in the introduction to this Chapter, Landau's general theory of continuous phase transitions gives a description of the macroscopic properties of a system without concern for microscopic details [2]. We have also established that the ground-state equilibrium configuration of a system is obtained by minimising its free energy F, and that a phase transition is characterised by the appearance of an order parameter ϕ. Bringing these together: a system's behaviour through a phase transition is given by minimising F with respect to ϕ, and from this its thermodynamic properties can be determined. F is in principle a complicated function of ϕ, but with the simple and powerful knowledge that the order parameter is zero above T_c and, for a second-order transition, small below T_c, comes Landau's theory. The free energy can be constructed as a Taylor expansion of the small parameter ϕ, and imposed to have the same symmetry as the system in the disordered phase,

$$F(T,\phi) = F_0 + \alpha_0(T) + \alpha_1(T)\phi + \alpha_2(T)\phi^2 + \cdots = F_0 + \sum_i \alpha_i(T)\phi^i, \tag{2.1}$$

where F_0 is the order-parameter-independent free energy of the system.

*And global, but this is more subtle.

†The excitement and surprise behind physical realisation of graphene stems from this: it displays stable long-range order in two-dimensions!

A brief aside: Landau's construction is a mean field theory, and so assumes that every constituent feels only the averaged effects of all others. As such we have only a single averaged order parameter $\phi \equiv \langle\phi\rangle$. It therefore means that long range correlations and fluctuations are ignored. At the transition these effects become significant, explaining why some theoretical predictions differ from experimental observations.

We start with the instructive and relevant example of a system with Ising (Z_2) symmetry. Such a system (under no external field) is invariant to a sign change of the order parameter: $F(T,\phi) = F(T,-\phi)$. This describes a spin that is only allowed to point up or down, a structural distortion from C_4 to C_2 symmetry, or – as we will see – nematicity in a tetragonal system. Furthermore, by considering Z_2 variables we may take ϕ to be real. For F to have Ising symmetry we must neglect the odd powers in Equation 2.1, and we also restrict ourselves to just the lowest two terms. Relabelling the coefficients for convenience to $\alpha_2(T) \equiv \frac{1}{2}a(T)$, and $\alpha_4(T) \equiv \frac{1}{4}b(T)$, making the b coefficient positive to ensure that the order parameter remains bounded and neglecting its temperature dependence, the free energy becomes

$$F(T,\phi) = F_0 + \frac{1}{2}a(T)\phi^2 + \frac{1}{4}b\phi^4. \tag{2.2}$$

Minimising the free energy $\partial F/\partial\phi = a(T)\phi + b\phi^3 = 0$ gives a trivial solution $\phi = 0$, i.e. no order at all, and two non-trivial solutions $\phi = \sqrt{\frac{-a(T)}{b}}$ and $\phi = -\sqrt{\frac{-a(T)}{b}}$. When $a(T)$ is negative the non-trivial solution becomes real, and as we expect the non-zero order parameter to occur in the disordered state for $T < T_c$, we make $a(T) = a_0(T - T_c)$, giving

$$\phi = 0, \quad \text{for } T > T_c \tag{2.3}$$

$$\phi = 0, \quad \text{and} \quad \phi = \pm\sqrt{\frac{a_0(T_c - T)}{b}}, \quad \text{for } T < T_c. \tag{2.4}$$

The form of the $F(T,\phi)$ and temperature evolution of ϕ are shown in Figure 2.1(a) and (b). For $T < T_c$, $a(T)$ changes sign and we clearly see two degenerate minima at nonzero order parameter.

We now look into the influence of an external field h. This couples linearly to the order parameter, and breaks the symmetry in the high-temperature phase, reducing

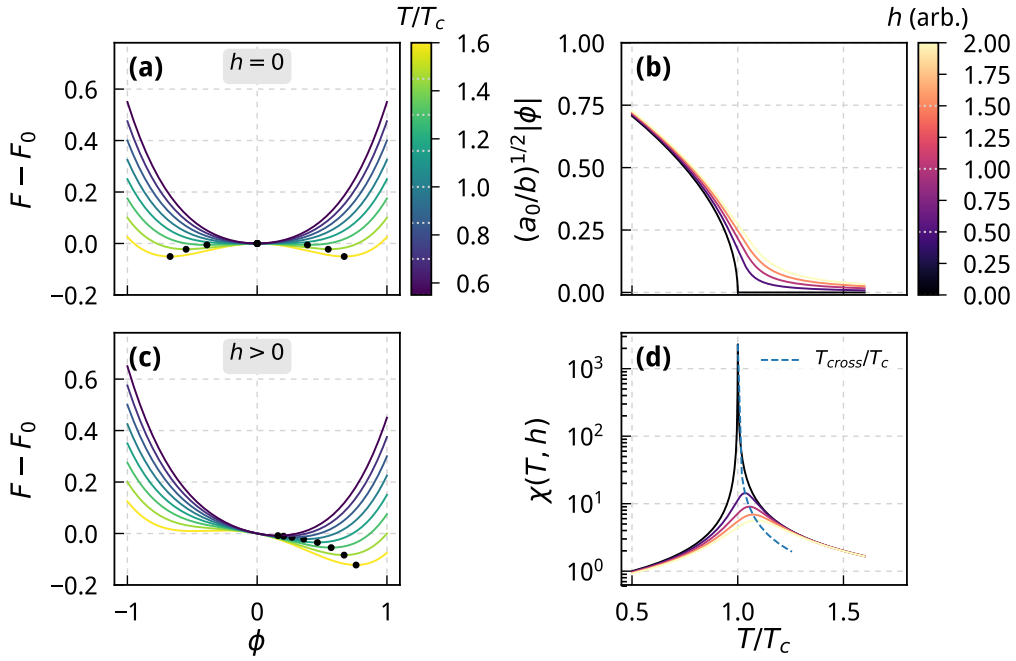

Figure 2.1 | (a) Free energy difference $F - F_0$ in the vicinity of a second order phase transition which occurs at $T = T_c$. Below this temperature two non-zero minima appear with equal energy but opposite order parameter sign – as shown by black markers. **(b)** Evolution of the order parameter ϕ with temperature and external field. **(c)** Free-energy contours as in panel (a), but under an external field h. Now a non-zero minimum occurs at all temperatures and the transition becomes a crossover. **(d)** Susceptibility χ as a function of temperature and field. The peak in χ (which can be taken as a proxy for the crossover temperature) is shown by the dashed line.

the second order transition to a crossover. Now the free energy takes the form

$$F(T,\phi,h) = F_0 + \frac{1}{2}a(T)\phi^2 + \frac{1}{4}b\phi^4 - h\phi, \tag{2.5}$$

and as shown in Figure 2.1(c) for $h > 0$, $F(T,\phi,h)$ is minimal at a non-zero order parameter for all temperatures. The general dependence of this minimum is now a complicated function of a, b and h, however calculating it numerically gives the temperature dependence of ϕ shown in panel (b), and we see that the crossover temperature and width both increase with field.

An important measurable quantity for characterising second-order phase transitions

is the amount the order parameter changes with field $\chi = \partial\phi/\partial h\big|_{h\to 0}$; this is the susceptibility. A general expression is found by differentiating Equation 2.5, $\partial F/\partial\phi = \partial F_{h=0}/\partial\phi - h = 0$, giving

$$\chi = \frac{\partial\phi}{\partial h} = \left(\frac{\partial^2 F_{h=0}}{\partial\phi^2}\right)^{-1}. \tag{2.6}$$

To first order and at zero field, $\chi = 1/a(T) \propto |T - T_c|^{-1}$ – i.e. it diverges at $T = T_c$ when approaching from both above and below the transition temperature. This is the well-known Curie-Weiss law, and highlights an important and interesting feature of second-order phase transitions: there is a measurable precursor which indicates that a transition will occur. This phenomenon further distinguishes first- and second-order transitions. Although the mean-field picture here is qualitatively correct, fluctuations mean that the exact details of the divergence will depend on corrections from terms beyond mean field. Taking the physical example of a paramagnetic system which becomes ferromagnetic at T_C: the magnetism M is the order parameter, and the diverging susceptibility can be observed by measuring M under a small magnetic field H. The numerically calculated susceptibility for increasing fields is shown in Figure 2.1(d), and we can extract the crossover temperature via its peak. This is indicated by the dashed line which increases according to $(T - T_c) \propto h^{2/3}$. A more subtle effect of the external field is seen by inspecting the higher-in-energy minima of $F(T, \phi, h)$. Whereas for zero field, there are always two minima below T_c, for finite h there is some temperature range within which this second minimum does not exist, and the temperature at which it appears decreases according to $(T - T_c) \propto -h^{2/3}$. This is the point at which metastable domains may form.

2.1.3 Structural phase transitions

An important example of a transition into an ordered state with Ising-like symmetry is that of a crystal reducing its discrete rotational symmetry from four-fold (C_4) to two-fold (C_2). This is the case for a tetragonal-to-orthorhombic (T-O) structural transition. Such a transition is referred to as being ferroic, and materials for which the ferroic state exhibits domains which, outside of domain walls, vary only in strain are referred to as ferroelastic – this is a well-developed field [3, 4]. It is also relevant for many interesting copper-oxide and iron-based superconductors which undergo such a transition as part of a more complex phase diagram. Casting aside for now the physical mechanism which might drive such a transition, we take the phenomenological approach of Landau introduced in the previous section.

Structural phase transitions are characterised by a spontaneous distortion of the lattice, and the resulting 'structural' strain is a convenient order parameter, not least because it is a thermodynamic variable (ignoring the effect of domains for now; these result in strain not uniquely specifying the system's state). Tetragonal symmetry can be broken either by antisymmetric normal strains along the tetragonal axes ($\varepsilon_{xx} - \varepsilon_{yy}$) or by a shear strain ($\varepsilon_{xy}$) as explained in detail in Section 3.1.3, and these are equivalent under rotations of 45°. This decreases one lattice parameter and increases the other, and assuming the unit cell preserves its volume* then $a_O = a_T(1+\delta)$, $b_O = a_T(1-\delta)$ and $c_O = c_T$, where O and T denote the orthorhombic and tetragonal lattice constants respectively†. The order parameter can then conveniently be defined as $\delta(T) = \varepsilon = (a_O - b_O)/(a_O + b_O)$ and we always define $b_O < a_O$. The material of focus in this thesis, FeSe, undergoes a shear-type T-O transition which, using the notation we will introduce in Chapter 3, we label $\varepsilon_6 \equiv \delta$.

For the case in which spontaneous strain is the primary order parameter and is driven by the elastic part of the free energy, the ferroelastic phase transition is 'true and proper' [4, 5] and the Landau treatment is the same as in the previous section. In this case, $\phi \equiv \varepsilon_6$, $T_c \equiv T_S^0$ (the meaning of the subscript will soon become obvious) and the external field is the thermodynamically conjugate variable to strain i.e. stress $h \equiv \sigma$.

For many materials however, the structural distortion is not the primary order parameter and the phase transition is driven by a degree of freedom that is not the lattice. Based on evidence which we will later discuss (see Section 2.3.1), this is the case for iron-based superconductors, and thus to describe the structural phase transition in FeSe we must extend the Landau free energy to include a coupling between the spontaneous strain ε_6 and the true (primary) order parameter ϕ – again without concern yet to what this might physically be.

To first order the strain energy is given by $\frac{1}{2}\sum_{ik} C_{ik}\varepsilon_i\varepsilon_k$,‡ where C_{ik} are elastic constants (as explained in Section 3.1.2). Shear spontaneous strain has only a single tensor element ε_6 and so this simply becomes $\frac{1}{2}C_{66}\varepsilon_6^2$. How the order parameter couples with the structural strain is a complicated matter [3] which depends on symmetry arguments, however if ϕ and ε have the same symmetry, then all combinations $\phi^m\varepsilon^n$ are allowed provided ϕ^p is part of the free energy (where $p = m+n$). If this is true, the simplest, and lowest order coupling allowed by symmetry is bilinear, i.e of the form

*This is a highly accurate assumption for the Fe-based superconductors.

†For simplicity we drop the subscript, using just a and b for the two in-plane orthorhombic unit cell lengths.

‡This is a nice callback to our discussion of generalised elasticity in Section 2.1.1.

$\phi\varepsilon$, and we can now form our new free energy

$$F(T,\phi,\varepsilon_6,\sigma) = F_0 + \frac{1}{2}a(T)\phi^2 + \frac{1}{4}b\phi^4 + \frac{1}{2}C_{66}^0\varepsilon_6^2 + \zeta\phi\varepsilon_6 - \sigma\varepsilon_6, \tag{2.7}$$

where $a(T) = a_0(T - T_S^0)$, and ζ is the coupling constant between ϕ and ε. For a given temperature Equation 2.7 is a surface, meaning it can be minimised with respect to both ϕ and ε_6, and as with T_S^0 we add a superscipt to the elastic modulus. Computing this numerically under various stresses, as shown in Figure 2.2(a), we arrive at a result which at first inspection looks qualitatively the same as for single-order-parameter example: ϕ is zero at high T and, at zero field, abruptly grows below some transition temperature. Furthermore, the structural strain undergoes a transition at the same temperature, allowing ϕ to conveniently be tracked via measurement of ε_6. Looking closely however, we make a striking observation: the transition does not occur at $T = T_S^0$ but at a higher temperature, even when $\sigma = 0$. This phenomenon originates from the coupling between the order parameter and the structural strain, essentially giving a feedback mechanism which enhances the transition temperature. The lattice is a polarisable medium which enhances the the order parameter, and if we make the lattice stiffer as shown in Figure 2.2(b), we inhibit this feedback, and the transition temperature comes back down. An equivalent effect is achieved by decoupling ε_6 and ϕ by decreasing ζ.

We can derive this quantitatively too. Dropping the the ϕ^4 term for simplicity and considering the case for zero field $\sigma = 0$, then

$$\frac{\partial F}{\partial \phi} = a(T)\phi + \zeta\varepsilon_6 = 0, \tag{2.8}$$

$$\frac{\partial F}{\partial \varepsilon_6} = C_{66}^0\varepsilon_6 + \zeta\phi = 0. \tag{2.9}$$

Rearranging Equation 2.9 for ϕ and substituting it into Equation 2.8, and vice versa for ϕ, gives:

$$\left(a(T) - \frac{\zeta^2}{C_{66}^0}\right)\phi = 0, \quad \text{and} \quad \left(C_{66}^0 - \frac{\zeta^2}{a(T)}\right)\varepsilon_6 = 0. \tag{2.10}$$

There are two ways to view these equations. Both $a(T)$ and C_{66} are renormalised by the coupling ζ between the lattice and the order parameter. To first order $a(T) = \chi^{-1}$, as we saw in Section 2.1.2, and so this can be viewed as a renormalisation of the susceptibility. With $a(T) = a_0(T - T_S^0)$, we can absorb this renormalisation into the transition temperature, and so the 'observed' transition occurs at T_S which is larger

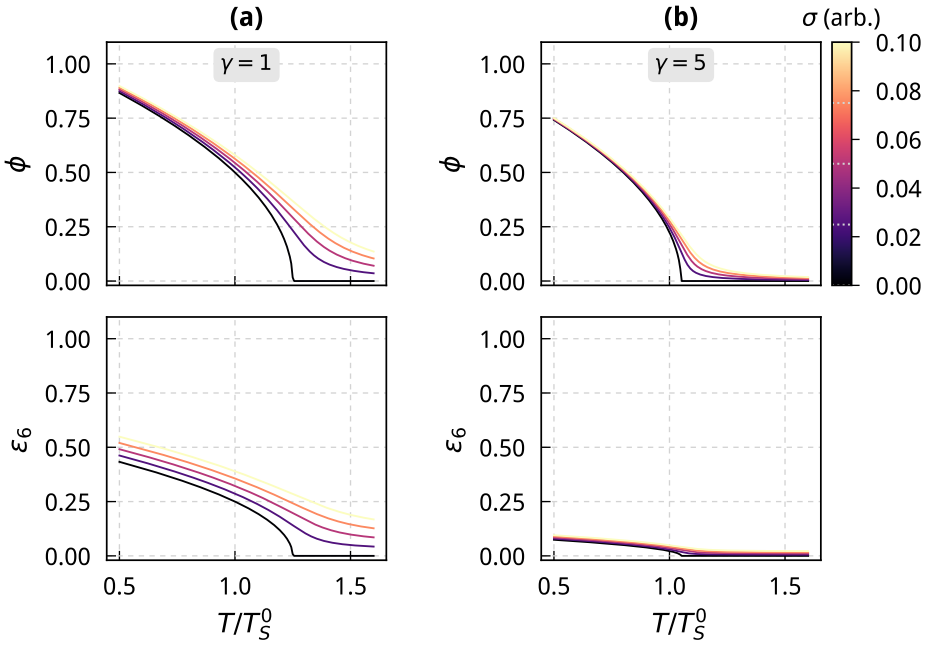

Figure 2.2 | Temperature and stress dependence of bilinearly coupled order parameters. **(a)** Primary order parameter ϕ (top) and spontaneous strain ε_6 (bottom) as a function of temperature and stress for a 'low stiffness' lattice. **(b)** As in panel (a) but for a stiffer lattice. In these plots we actually tune the dimensionless parameter $\gamma = bC_{66}^0/(a_0 T_S^0)^2$.

than the 'bare' value T_S^0

$$T_S = T_S^0 + \frac{\zeta^2}{C_{66}^0 a_0}. \tag{2.11}$$

Equation 2.10 can equally can be viewed as originating from a complete softening of the C_{66} elastic mode

$$C_{66} = C_{66}^0 - \frac{\zeta^2}{a_0(T - T_S)}. \tag{2.12}$$

Our inclusion of the sign change in a inadvertently chooses ϕ as the primary order parameter, however we see that the renormalised elastic modulus still ends up temperature dependent. Including it in C_{66} instead does not alter the outcome. This equivalence between the temperature dependence of the two order parameters, regardless of which is primary, preludes an important theme in the iron-based superconductors which we return to in the next section.

Of course in reality, the symmetry is often not broken equally across an entire macroscopic sample, and domains of orthorhombic distortion at 90° to each other

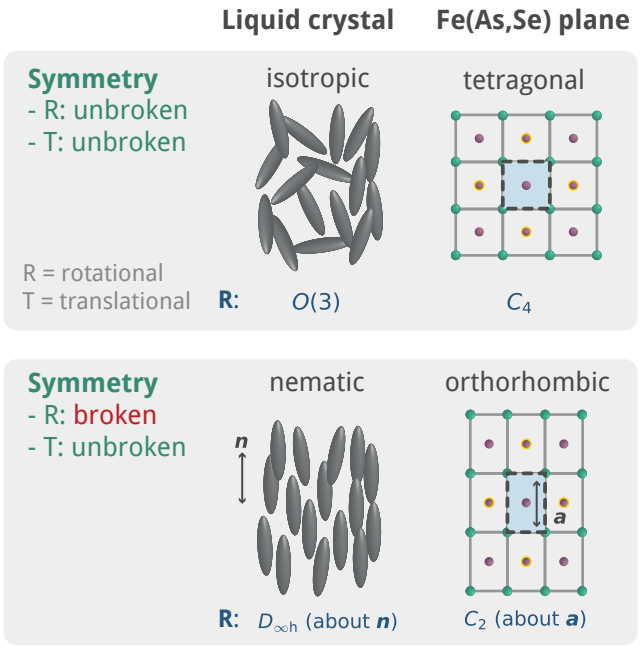

Figure 2.3 | Schematic explaining the analogy between liquid crystal and structural nematic phases, using the tetragonal to orthorhombic transition in the iron-based superconductors as an example. In the low-temperature ordered phase of both (bottom) the rotational symmetry is broken, whilst the translational symmetry remains. This defines an axis but has no sense of direction.

complicate matters. In a ferroelastic material, this gives rise to elastic hysteresis when sweeping the stress – a defining characteristic of such a material – and such domains mean that for an unstressed sample in equilibrium, sample-averaged quantities do not display any in-plane anisotropy. In general, the number of different domain types is given by a ratio of the number of symmetry elements in the high-temperature phase with the number in the low symmetry phase – in our case two. These are separated by twin boundaries (the sample is said to be 'twinned') which can be viewed as internal surfaces between two crystals. They therefore carry a surface energy and their equilibrium configuration is given by the competition of this energy cost with the gain of forming a uniformly broken-symmetry state. To measure sample-averaged properties which reflect the symmetry of the ordered phase, the sample must be detwinned with an external stress. The symmetry is subsequently broken in the high-temperature phase too, forcing the transition to become a crossover.

2.1.4 Nematicity

Electronic analogues exist for all three basic states of matter: the alkali metals can be well described as a non-interacting 'gas' of electrons, Landau extended this to describe an interacting electron 'liquid', and electrons can form a crystalline 'solid' as predicted by Wigner. Liquid crystals are a state of matter with liquid-like short-range

correlations in some directions, and solid-like long-range correlations in others. In the simplest liquid-crystal phase, rod-like constituents break their rotational symmetry whilst remaining translationally invariant. This scenario is shown in Figure 2.3 and is known as a 'nematic' liquid crystal. Within the last decade increasing evidence points towards the existence of an analogous nematic state for electrons. In the context of quantum liquids, a nematic phase is defined more generally as one breaking an underlying symmetry which under the interchange of two axes leaves the system unchanged, and does not affect other symmetries [6]. For example, a C_2 symmetric state emerging from broken rotational but not translational symmetry, or rotational but not time-reversal symmetry, would be nematic.

Under this definition, the C_4 tetragonal to C_2 orthorhombic ferroelastic transition considered in the previous section is classed as 'nematic', even when true-proper, and driven by regular lattice fluctuations. Such physics is well understood in the context of phonons and therefore 'lattice nematicity' does not attract our attention*. In many strongly correlated materials, including iron-based superconductors, the nematic transition may be driven by electronic degrees of freedom, and as such 'electronic nematicity' has become an exciting topic in these materials. The key difference here is that an electronic-driven nematic transition would still occur even if the lattice was held fixed, whereas a structural-driven one would not. It is hoped that determining the origin of nematicity holds the key to understanding physics in other parts of the phase diagram, most notably the superconductivity.

Figure 2.3 shows the liquid-crystal analogy schematically, and we now highlight its limitations. The structural transition breaks a discrete rather than continuous rotational symmetry, and into C_2 rather than $D_{\infty h}$ symmetry. There are two possible orientations of the in-plane orthorhombic axes, and so the nematicity is Ising-like, whereas in the liquid crystal any direction can be chosen, so long as all rods align along their length. 'Nematic' can therefore just be translated to 'in-plane anisotropy' in the context of structural phase transitions.

Although 'nematicity' is spoken of almost as if it were a distinct physical degree of freedom of the electrons, it should be stressed that it is not. We refer just to the primary order parameter ϕ having a certain symmetry, and keep in mind that it must be driven by an actual physical degree of freedom, such as from spin or orbital degeneracy. We now have some context for the undefined order parameter defined in the previous section, and thus can already describe the phenomenology of a nematic transition:

*Although it should be noted that phonons originate from bonding between atoms, which is also due to electronic interactions.

the nematic order parameter ϕ will rise continuously at a renormalised transition temperature T_S^0, and will be tracked by a structural distortion. Inspecting Figure 2.2, we see that a dilemma emerges, how do we distinguish which is the primary order parameter and which just follows? After all Equations 2.8 and 2.9 are completely symmetric and a reduction in symmetry of ϕ will present itself as a symmetry breaking in ε_6, giving a 'chicken-and-egg' scenario. Furthermore, if we can pin down the nematicity as being electronically driven, how do we determine which of the electronic degrees of freedom drive the transition? This is again a challenging question as both will exhibit an anisotropy in the broken symmetry phase. We later return to these questions after first reviewing some basic properties of iron-based superconductors.

2.2 Iron-based compounds

Interest in iron-based compounds (FeBCs) originally stems from the study of superconductivity rather than nematicity. The field of unconventional superconductivity – that is, the study of materials with pairing not mediated by phonons but by some other mechanism – embodies a large wealth of research stretching over the last four decades. To give a brief overview: unconventional pairing was first used to explain superfluid ^{3}He [7], and then for superconductivity in heavy-fermion material $CeCu_2Si_2$ [8]. Extension into the field of 'high-temperature' superconductivity occurred with discovery of copper-oxide material $La_{2-x}Ba_xCuO_4$ measured at ambient pressure with a transition temperature of $T_c \sim 40\,\mathrm{K}$ [9] almost thirty years ago. This spawned an era of research on 'cuprate' materials, and since then much effort has been dedicated to discovering other classes of materials which have even higher transition temperatures. An overview of different families of superconducting materials is presented schematically in Figure 2.4.

High-temperature superconductivity was long thought to be exclusive to the cuprates, but the discovery of superconducting materials with iron rather than copper as a building block challenged this idea. The first FeBC exhibiting superconductivity, discovered in 2006, was LaOFeP with $T_c \sim 4\,\mathrm{K}$ [10], with the field gaining traction in 2008 due to discovery of a high T_c in fluorine doped LaOFeAs at $\sim 26\,\mathrm{K}$ [11]. Both of these are layered materials, sharing a common structural motif consisting of planar iron atoms tetrahedrally coordinated with pnictogen atoms (As, P) (and thus referred to as pnictides) which sit above and below the plane, as shown in Figure 2.4. T_c of fluorine doped LaOFeAs was found to be dramatically enhanced with hydrostatic pressure, reaching $\sim 43\,\mathrm{K}$ under approximately $4\,\mathrm{GPa}$ [12]. A flurry of new discoveries

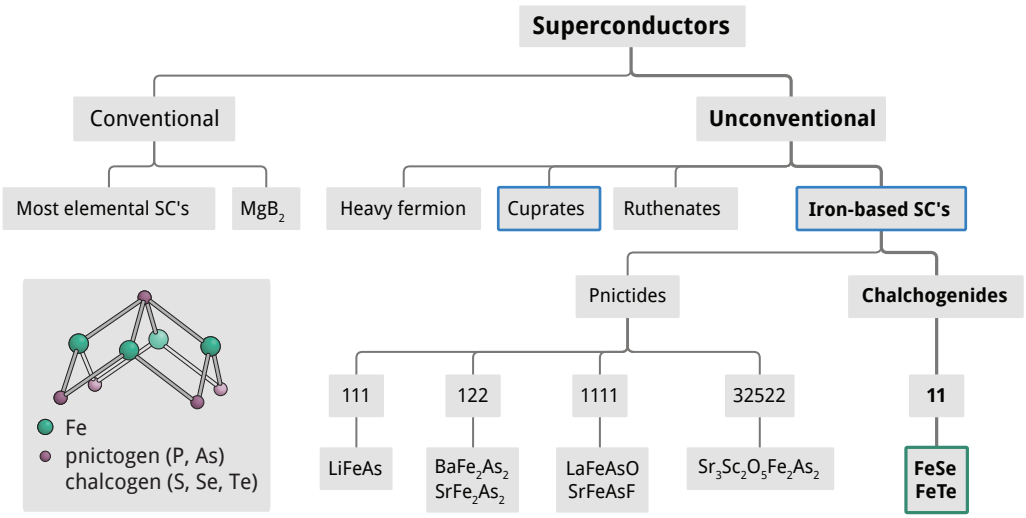

Figure 2.4 | Different families of superconductors. FeSe's placement in this family tree is highlighted in bold, and 'high-temperature' superconducting families are outlined in blue. Inset: common structural motif of iron-based superconductors which, in the tetragonal phase, features a square lattice of Fe atoms tetrahedrally coordinated to pnictide or chalcogenide atoms above and below.

followed within 2008, including FeSe [13] (showing Fe can be coordinated with chalcogen atoms too), LiFeAs [14], $(Ba_{1-x}K_x)Fe_2As_2$ [15], and with T_c topping out at 56 K for $Gd_{1-x}Th_xFeAsO$ [16]. These families are commonly referred to by the stoichiometry of the parent compound, i.e. '11' for FeSe, '111' for LiFeAs, and so on. Without any intermediate 'blocking' layers, FeSe is the simplest iron-based compound (FeBC) exhibiting superconductivity, and is the material of focus of this thesis. Significantly more complicated materials have also found to be superconducting, such as 32522 [17] and 21311 [18] compounds. The large chemical variety throughout which Fe-based superconductivity exists is astonishing, but also presents itself as a challenge, with the chemical phase space growing rapidly with introduction of doping. What is clear however, is that the iron layers must be important for the occurrence of superconductivity, just as the copper layers are in the cuprates. In general, the existence of a class of materials distinct from the cuprates but exhibiting high transition temperatures presents hope for identifying common elements important for high-temperature superconductivity.

Unconventional superconductivity is the common thread driving excitement in all these materials and, although not a main theme of this thesis, it is important to give

some background to this topic and its recent developments for FeBCs – especially as these are intimately connected to the physics already discussed. Conventional superconductivity is explained by the mean field theory of Bardeen, Cooper and Schreiffer (BCS) [19] on the basis that low-energy fermions can pair under an arbitrarily small attractive potential. This potential originates from electron-ion interactions, whereby Coulomb repulsion is overcome by an electron-generated polarisation of the ionic lattice, which can then attract a second electron due to the ionic relaxation being slow on the timescale of electrons. In BCS theory, electronic interactions are wave-vector-independent, implying that the coordinate part of the pairing wavefunction is symmetric with $l = 0$; pairing is therefore referred to as being 's-wave' [20]. Other types of pairing interactions can result in states with non-zero angular momentum, giving d- and p-wave pairing (and so on for higher values of l). Unconventional superconductivity can be more precisely defined then as a superconducting state with a pairing wavefunction not of the isotropic s-wave form, with an origin not from electron-phonon interactions.

Soon after discovery, the pairing in iron-based superconductors was proposed to be unconventional, initially suspected due to the size of T_c. For most FeBCs, superconductivity emerges in close proximity to a magnetic instability, and in $LaFeAsO_{1-x}F_x$ specifically, the destructive effects of spin fluctuations (SFs) were argued to dominate over the calculated size of electron-phonon coupling [21]. Furthermore, in the same material an early specific heat study found the γ coefficient to vary with magnetic field as $\sqrt{H}$ [22, 23] – the predicted behaviour for SF-mediated superconductivity. Since then, the ability to directly probe the superconducting gap with angle resolved photoemission spectroscopy (ARPES) and quasiparticle interference (QPI) has provided evidence for sign-changing, anisotropic and nodal features – all unexplained by conventional phonon-mediated pairing [24–27].

To determine the origin of superconductivity, it is important to first resolve the structure and symmetry of the gap function $\Delta(\mathbf{k})$. For cuprates, the majority of evidence supports d-wave pairing mediated by the exchange of spin fluctuations [28]. For such pairing, the gap function changes sign between $\mathbf{k}$ and $\mathbf{k}' = \mathbf{k} + \mathbf{Q}$, where $\mathbf{Q} = (\pi, \pi)$ is the momentum at which the pairing interaction is peaked. It is this change in sign which enables the repulsive interaction from SFs to facilitate pairing. Evidence from inelastic neutron scattering and QPI also points towards SFs as the mechanism for pairing in pnictides [24, 29–31], despite their vastly different electronic structure which is complicated by multiple orbitals crossing the Fermi level. In this case, $\mathbf{Q}$ connects hole and electron sheets giving an $s_\pm$ state – i.e. isotropic but opposite in sign on

electron and hole Fermi surfaces.

The $s_{\pm}$ proposal for pnictides is of course debated. Such a pairing symmetry is expected to be sensitive to impurities due to interband scattering, but several pnictide families are found to be surprisingly robust to impurities [32]. Furthermore, the resonance-like peak in neutron scattering can also be interpreted by considering strong-correlations via quasiparticle dampening, thus not requiring a change in sign of the superconducting gap [33], therefore giving conventional s_{++} pairing. This leads back to the question of whether phonons are important, however first-principles calculations for $LaFeAsO_{1-x}$ give an electron-phonon coupling strength corresponding to T_c being 5-6 times smaller than observed [34].

Another debate for 122 compounds concerns the existence of nodes (i.e. points at which the gap function becomes zero), which generally give clearer signatures in thermodynamic probes than changes in gap sign do. Penetration depth and thermal conductivity measurements find evidence for nodes in $BaFe_2(As_{1-x}P_x)_2$ [35], and although nodal $s_{\pm}$ superconductivity can still originate from spin-fluctuation pairing, T_c is predicted to be low [36]. Contention is a common theme in FeBCs, with the pairing symmetry and origin of superconductivity being no exception. A more or less agreed upon property, however, is that pairing in FeBCs is singlet (for which the spin susceptibility is expected to shrink below T_c), and this has been confirmed from NMR and Knight shift experiments on 1111, 122 and 11 compounds [25, 37]. Several important questions still remain such as: what is the relationship between superconductivity and nematic and magnetic phases? And does this help enhance T_c?

The apparent success of spin fluctuations to explain pairing in FeBCs is challenged by the existence of superconductivity in bulk FeSe – a material absent of magnetism, but also exhibiting superconductivity, at ambient pressure. Furthermore, FeSe is more strongly correlated than 122 compounds and has smaller Fermi surfaces. As established, nematicity and orbital selective coherence are important topics for this material, and we will return to discuss superconductivity and its relation to these topics in Section 2.4.1.

Returning now to discuss other differences between the phase diagrams of cuprates and iron-based compounds. Cuprates play host to a plethora of additional phases other than superconductivity [38]. At high temperatures and ambient pressures, the parent phase is a paramagnetic Mott insulator with a single band crossing the Fermi level, becoming antiferromagnetic (AFM) below the Néel temperature T_N. AFM and superconducting phases compete, such that under application of pressure, or through doping, T_N is suppressed and superconductivity emerges. The superconducting phase is dome-like, with T_c peaking at some optimal doping or pressure. The cuprates

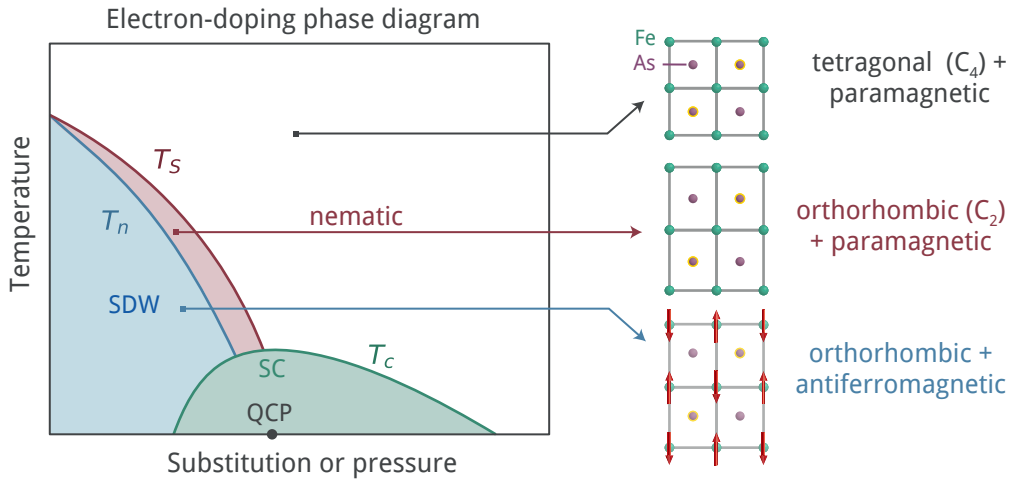

Figure 2.5 | Phase diagram of electron-doped $BaFe_2As_2$, based on the thermodynamic and transport measurements of Ref. [42], and neutron scattering study of Ref. [43]. At ambient pressure, and high temperatures the system is tetragonal and paramagnetic, and upon cooling becomes orthorhombic and antiferromagnetic (AFM). The antiferromagnetic phase is suppressed with pressure or doping, and superconductivity then emerges.

have a rich, multifaceted phase diagram which additionally includes pseudogap (in which the Fermi surface is partially gapped), strange-metal (with resistivity linear in T) and Fermi-liquid phases. Furthermore many cuprates, such as $(La_{1-x}Sr_x)_2CuO_4$ and $YBa_2Cu_3O_{7-\delta}$* exhibit a tetragonal-to-orthorhombic structural distortion [40], and for states close to the pseudogap energy there is experimental evidence for electronic nematicity [41].

Quite remarkably, many similarities are shared by the generic phase diagram of the pnictides: at ambient pressure, there is an AFM transition, and a dome of superconductivity emerges upon doping or application of pressure. Conversely, several crucial differences must be highlighted. Whereas the copper-oxide layer is two-dimensional (not always completely however – slight buckling can occur), the pnictogen/chalcogen atoms are located above and below the iron-atom plane, as shown in the inset of Figure 2.4. Most significantly, the parent FeBCs are multiband metals (the Fe^{2+} ions form a $3d^6$ configuration and so six electrons occupy five orbitals) not single-band Mott insulators, and additionally the antiferromagnetism is stripe-like. Whether the same mechanisms drive the phase diagram of the cuprates and FeBCs, and even if

*Albeit at $\sim 700\,^{\circ}C$ [39], far from the interesting aspects of the phase diagram.

different FeBCs have the same underlying physics is a highly debated question.

Although the phase diagram of each compound is unique and has its own subtleties, most features are captured by the 122 (pnictide) compounds which, because of the relative ease with which high-quality samples can be grown, are viewed as a paradigm of iron-based superconductivity, thus dominating early research efforts. The phase diagram of electron-doped Ba-based 122 compound $Ba(Fe_{1-x}Co_x)_2As_2$ is shown in Figure 2.5. Not only does magnetic order form at low temperatures, but at zero doping and pressure it is concurrent with a T-O structural phase transition. As pressure is applied or the material doped, a splitting opens up between the T-O and magnetic transitions. These compounds are therefore candidate electronic nematic materials, with the orthorhombicity between the T-O and magnetic transitions almost certainly associated with interactions that drive the magnetic order. That nematicity might be linked to high-temperature superconductivity is also a core question that has motivated a wealth of research regarding its role and origin; and we now explore the topic of nematicity in more depth.

2.3 Nematicity in iron-based compounds

In this section we will explore how different degrees of freedom can be disentangled, and highlight numerous scenarios which can give rise to electronic nematicity. Such discussion is contextualised by experimental and theoretical work on iron-based compounds.

2.3.1 Electronic versus structural nematicity

We return to the question of how one can distinguish which order parameter is primary and thus drives the structural transition. As seen in Section 2.1.3, this is complicated by the fact that any measurable quantity will exhibit an anisotropy in the low-symmetry phase, and a coupling between the order parameter and structural strain will give a transition in both. We take ϕ to be associated with some electronic degree of freedom, and address how to quantitatively identify the structural transition as being driven by ϕ and thus electronic-nematic.

A first hint is given by observation of the structural distortion being small with respect to the resistivity anisotropy [44], but more concrete resolution was first provided by the Fisher group at Stanford University [45] through consideration of various susceptibilities of the system. Stress σ, with the same symmetry as the spontaneous strain, is the conjugate field to the transition, and so two 'conventional' susceptibilities

can be defined from the derivative of ϕ and ε^* with respect to σ. Starting with the free energy Equation 2.7, and taking the derivative, first with strain $\partial F/\partial\varepsilon = C^0\varepsilon+\zeta\phi-\sigma = 0$, followed by stress, then

$$\zeta\frac{\mathrm{d}\phi}{\mathrm{d}\sigma} + C^0\frac{\mathrm{d}\varepsilon}{\mathrm{d}\sigma} = 1. \tag{2.13}$$

Using the relation $\frac{\mathrm{d}\phi}{\mathrm{d}\sigma} = \frac{\mathrm{d}\phi}{\mathrm{d}\varepsilon}\frac{\mathrm{d}\varepsilon}{\mathrm{d}\sigma}$ then the 'structural' susceptibility is $\chi_\varepsilon = \partial\varepsilon/\partial\sigma = 1/\left(C^0 + \zeta\frac{\mathrm{d}\phi}{\mathrm{d}\varepsilon}\right)$. Reciprocally, the 'electronic' susceptibility is $\chi_\phi = \partial\phi/\partial\sigma = 1/\left(\zeta + C^0\frac{\mathrm{d}\varepsilon}{\mathrm{d}\phi}\right)$.

Because both stress *and* strain are experimentally tuneable fields, another feasibly measurable susceptibility can be defined: the change in electronic order parameter with ***strain***, i.e. $\chi_n = \partial\phi/\partial\varepsilon$, referred to in literature as the 'nematic' susceptibility. Following a similar procedure to that above, but starting with $\partial F/\partial\phi = a\phi + \zeta\varepsilon = 0$, and again taking a derivative with respect to field yields $a\frac{\mathrm{d}\phi}{\mathrm{d}\sigma} + \zeta\frac{\mathrm{d}\varepsilon}{\mathrm{d}\sigma} = 0$. This now gives $\chi_n = -\zeta/a$[†]. This can then be substituted into χ_ε and χ_ϕ. Summarising these quantities:

$$\chi_\varepsilon = \frac{\partial\varepsilon}{\partial\sigma} = \frac{a}{C^0a - \zeta^2}, \quad \chi_\phi = \frac{\partial\phi}{\partial\sigma} = \frac{\zeta}{\zeta^2 - C^0a}, \quad \chi_n = \frac{\partial\phi}{\partial\varepsilon} = \frac{-\zeta}{a}. \tag{2.14}$$

In the above, we have not specified which of a or C goes through zero, leaving open the possibility of whether it is the strain or the electronic order parameter which is the primary one. As expected from Figure 2.2 and our previous discussion, χ_ε and χ_ϕ both diverge regardless of whether a or C passes through zero - i.e. regardless of which is the primary order parameter. However this apparent symmetry is broken by $\frac{\partial\phi}{\partial\varepsilon}$ as strain couples directly to the electronic order parameter. Most importantly we see that χ_n will diverge only if a passes through zero, i.e. if ϕ is the primary order parameter. This tells us we must measure ϕ under conditions of controlled strain across an infinitesimal range, and if ϕ is primary then χ_n will diverge, following a Curie-Weiss form above the transition. Also neat is that this susceptibility diverges due to the bare a coefficient, and therefore at T_S^0 rather than T_S. The conclusions drawn from this analysis highlight the power of Landau theory – with some simple algebra a measurable prediction with fundamental consequences can be made.

The question of how to directly measure ϕ requires consideration. Provided it is electronic in origin, then it should arise from either spin or orbital degrees of freedom. The spin state can be directly probed by neutron scattering experiments, and the

*We'll drop the subscripts for sake of generality.

[†]$\chi_n = 1/a$ is often used in literature, giving $C_{66} = C_{66}^0 - \zeta^2\chi_n$, but the meaning is the same. Our change in sign is due to the elastic energy being positive in Equation 2.7, as per the convention in Ref. [3].

relative orbital population somewhat directly through ARPES. However combining either of these measurement techniques with the application of tuneable strain is very challenging technically. Both spin and orbital order will however influence the electrical transport properties, with the former expected to give rise to an anisotropy in the scattering either due to local magnetic order originating from defects [46, 47] or spin fluctuations [48, 49], and the latter to give an anisotropy in the electronic structure via the Drude weight [50, 51]. Measurement of resistivity whilst applying a tuneable strain is much more technologically plausible.

An obvious anisotropic transport quantity, and thus suitable nematic order parameter, is the resistivity anisotropy:

$$\phi = \frac{\rho_a - \rho_b}{\rho_a + \rho_b}. \tag{2.15}$$

To determine χ_n, ϕ must be measured whilst varying the strain by an infinitesimal amount about zero. In measuring both transverse and longitudinal resistivity (easiest via two separate samples) then to first order $\phi \sim 2[(\Delta R/R)_{xx} - (\Delta R/R)_{yy}]$ and if the strain is applied with the same principal axes as the spontaneous distortion* then this quantity has additional physical significance with $\phi/2 \propto 2m_{66}$ where m_{66} is the in-plane shear component of the elastoresistivity. In the original work pioneering this technique [45, 52] strain was applied via a piezoelectric stack to which the sample was directly mounted; this is now the standard method.

This technique was originally demonstrated via investigation of $Ba(Fe_{1-x}Co_x)_2As_2$ (i.e. the electron-doped compound with a phase diagram as in Figure 2.5) [45]. In sweeping across a small range of strain about the neutral point for different temperatures, and plotting the average value of its derivative, a clear divergence is observed. As explained, this is cut off by the transition at $T_S = 138\,\mathrm{K}$, but Curie-Weiss fitting gives the bare transition temperature of $T_S^0 = 116\,\mathrm{K}$, i.e. 22 K lower. Similar studies have proven the diverging nematic susceptibility to be ubiquitous, being observed in the also-electron-doped $Ba(Fe_{1-x}Ni_x)_2As_2$, hole-doped $Ba_{1-x}K_xFe_2As_2$, isovalently-substituted $BaFe_2(As_{1-x}P_x)_2$ as well $FeTe_{1-x}Se_x$ [53], as shown in Figure 2.6. In these materials superconductivity therefore emerges from a state characterised by strong nematic fluctuations. This raises the question of whether a nematic quantum critical point lies beneath the superconducting dome, and if so how this affects T_c [54]. A natural extension of this work is to investigate the resistivity anisotropy for $T < T_S$. This requires the sample to be detwinned, which can be achieved mechanically [44] or with a magnetic field [55]. The results we will present in Chapter 4 suggest that these

*This turns out to be at 45° degrees to the tetragonal unit cell – see Section 3.1.3.

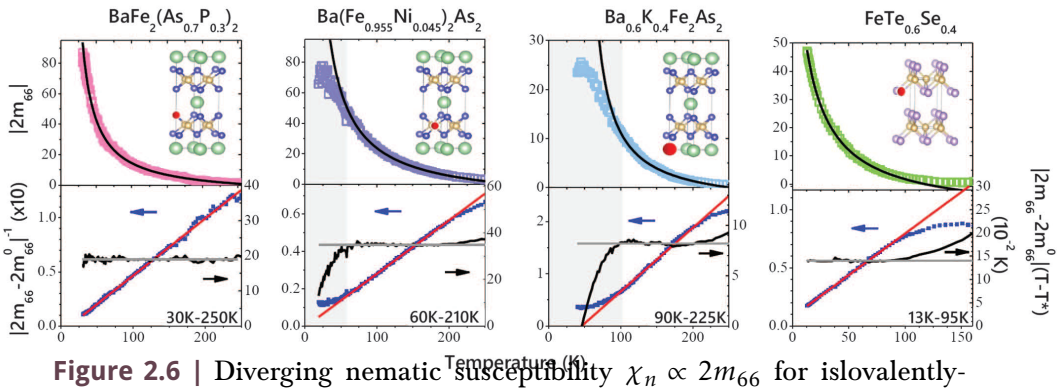

Figure 2.6 | Diverging nematic susceptibility $\chi_n \propto 2m_{66}$ for islovalently-substituted $BaFe_2(As_{1-x}P_x)_2$ (far left), electron-doped $Ba(Fe_{1-x}Ni_x)_2As_2$ (centre-left), hole-doped $Ba_{1-x}K_xFe_2As_2$ (centre-right) and $FeTe_{1-x}Se_x$ (right). All four compounds are fitted well by a Curie-Weiss dependence above the transition. Reproduced from Ref. [53] with permission from AAAS.

studies did not achieve complete detwinning, motivating the need for large tuneable pressures, a unique capability that we have, and a method for positive verification that the sample is in fact fully detwinned. Furthermore, elastoresistivity studies to date fail to extract information below T_S, as the effect of twin boundaries – i.e. their direct contribution to resistance, and effects of their pinning – cannot be separated. We address this issue. Leading on from this, direct investigation of the behaviour of domain walls is a relatively untouched upon topic, and another which we can uniquely shed light on.

It is important to note that this Curie-Weiss analysis assumes that $\mathrm{d}(\rho_a - \rho_b)/\mathrm{d}\varepsilon \propto \mathrm{d}\phi/\mathrm{d}\varepsilon$. For $T \to T_S^0$ the nematic susceptibility $\chi_n = \mathrm{d}\phi/\mathrm{d}\varepsilon$ diverges, and so the strain variation of ϕ must become the dominant contribution to the variation of $\rho_a - \rho_b$. Over a wide temperature range there is no reason to assume that the constant of proportionality *remains* constant however, or that higher order contributions to the elastoresistivity do not become relatively more important. This is important as the divergence occurs at the *bare* transition temperature $T_S^0 < T_S$, which cannot be accessed by the measurement, and Curie-Weiss fitting must be conducted at temperatures higher than T_S^0. That experimental data are so well fitted by a Curie-Weiss dependence indicates that the proportionality is in fact almost certainly highly constant over a wide temperature range. Our argument does not alter the conclusions of this work – the divergence still signifies that the nematic order is electronically driven – it just means the Curie-Weiss fitting may not be quantitatively correct. With our experimental capabilities of tuning strain across a large range, we will later (in Section 4.3) support

this discussion with evidence presented from our measurements.

The simple sample-on-stack technique utilised above applies not only an asymmetric strain with principal axes aligned with the orthorhombic distortion, but also a symmetric component. This component affects the electrical response, and much work has been dedicated to this problem by the Fisher group, who have laid the foundations for decomposing the elastoresistivity tensor into A_{1g}, B_{1g} and B_{2g} symmetry channels [56–58].

2.3.2 Spin and orbital order

In-plane anisotropy is a well-observed phenomenon in FeBCs and, due to the considerations presented in the previous section, the nematic state is most likely electronically driven. Inspecting the phase diagram of the hole-doped and isovalently-substituted 122 compounds, in which antiferromagnetic (AFM) and structural transitions are concurrent, the nematic order would appear to simply be driven by the spin degree of freedom. A small splitting between these two transitions for the hole-doped compound, as shown in Figure 2.5, challenges this viewpoint. Here the structural transition occurs at a higher temperature than the AFM transition, but both track each other closely with doping, indicating that they are intimately connected. We now address how spin and/or orbital electronic degrees of freedom might drive a nematic transition, and examine some elementary background physics to better understand the interplay between them. This is a highly debated aspect of research on FeBCs.

Strong correlations

Landau Fermi-liquid theory explains how the excitations of an interacting-electron system can be mapped onto those of non-interacting system of free electrons, even for materials with strong correlations such as Sr_2RuO_4 [59]. An alternative approach for explaining strong correlations is that of Hubbard, in which one considers a lattice of atomic sites which, for a single orbital per site, is described in two dimensions by the simple (to write at least) and well-known Hamiltonian:

$$H = -\sum_{ij,\varsigma} t_{ij}\left(\hat{c}^{\dagger}_{i\varsigma}\hat{c}_{j\varsigma} + \text{h.c.}\right) + U\sum_{i}\hat{n}_{i\uparrow}\hat{n}_{i\downarrow}, \tag{2.16}$$

where i and j index the site, and ς the spin, which is Ising-like and can either be up $\uparrow$ or down $\downarrow$. The first term is a sum over nearest neighbours, and represents a hopping, at energy gain t, by annihilating an electron from site i and creating it on neighbouring

site j and this dictates the band width. The second term counts the number of electrons on site i with opposite spin; this imposes a cost U for double occupancy of a single site. This term represents a short-range Coloumb repulsion and is particularly applicable for elements with $3d$ valence electrons, such as in the transition metal oxides, due the small spatial extent of the orbitals. In general, this model is used to study the balance between a drive to delocalise (through t), and a drive to localise (through U).

Two parameters can be 'tuned' in Equation 2.16: the interaction strength U/t, and occupation $n = N_{\text{el}}/N_{\text{site}}$. In the case where $U/t \ll 1$ the system is weakly interacting and itinerant, the interaction is treated as a small perturbation, and the Fermi-liquid description holds true. For $U/t \gg 1$ the system becomes strongly interacting and if $n = 1$, i.e. a half-filled band, then where band theory would predict a metal, the electrons are now localised on each site giving an insulator with gap $E_g \sim U - 2zt$, where z is the coordination number. This is the so-called Mott insulating state.

A key example of such physics occurs in the cuprates, in which Cu^{2+} ions give a $3d^9$ electronic configuration which for hole doping can effectively be described by the single-band Hubbard model [60]*, and displays a Mott insulating state. For iron-based superconductors Fe^{2+} ions give a $3d^6$ configuration, for which six electrons occupy five orbitals, and we encounter multiorbital physics. Extending the Hubbard model by inclusion of degenerate orbitals on each atomic site (still at half filling) results in an increase in the critical U at which a Mott-insulating state forms [61]. However, the parent FeBCs are an electron away from half filling, and furthermore are not observed to be Mott insulating suggesting they occupy an intermediate-coupling regime.

The orbital degree of freedom for six electrons among five degenerate orbitals introduces a new energy scale into the problem. Filling is dictated by Hund's rules: firstly the total spin S should be maximised; and given S, the total angular momentum L should be maximised. Such an on-site intraorbital effect originates from minimising the Coloumb repulsion via the Pauli principle and screening. Tetrahedral coordination of the Fe sites in FeBCs causes a crystal-field splitting of the five-fold degeneracy into two sets of orbitals. The e_g orbitals $d_{x^2-y^2}$, and d_{z^2} are lower in energy; and t_{2g} orbitals d_{xy}, d_{yz}, d_{xz} higher in energy. Figure 2.7(a) shows the real-space form of $3d$ orbitals. A small splitting between the d_{xy}, and $d_{yz,xz}$ orbitals can additionally occur due to the crystalline tetragonal symmetry. Filling then depends on competition between Hund's rule coupling J and the crystal-field splitting. Assuming the crystal

*This work actually used the $t-J$ model which is equivalent to the Hubbard model for $U/t \gg 1$. The reason this can be described by single band is more subtle than just one unoccupied state being available; Ref. [60] assumes a binding between a hole from the oxygen ions to a hole on the copper ion, forming a singlet.

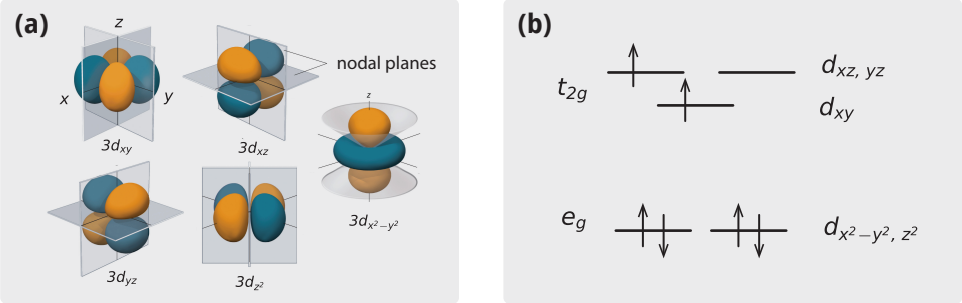

Figure 2.7 | (a) Real-space form of the $3d$ orbitals relevant to the physics of iron-based superconductors. Reproduced from Ref. [62]. CC BY-NC-SA 3.0. **(b)** Filling of six electrons across five orbitals in the case that the tetrahedral crystal-field splitting is larger than Hund's coupling.

field splitting is larger than Hund's coupling, then the e_g levels will be completely filled, giving the $S = 1$ scenario shown in Figure 2.7(b). Extra terms are gained by the Hubbard Hamiltonian for this scenario, making it even harder to solve. Whereas before we only considered the energy cost of two electrons occupying the same orbital on the same atom, we must now additionally consider two electrons occupying different orbitals on the same atom, and with different spins. The Hamiltonian becomes

$$H = H_t + \sum_i H_{\text{int},i} + H_{\text{cf}}. \tag{2.17}$$

Hopping can now occur not only between atoms i and j, but also orbitals α and β, giving $\hat{H}_t = -\sum_{ij}\sum_{\alpha\beta,\varsigma} t_{ij}^{(\alpha\beta)}\left(\hat{c}^\dagger_{i\alpha,\varsigma}\hat{c}_{j\beta,\varsigma} + \text{h.c.}\right)$. The interaction component concerns the energies on a single atomic site i, given by

$$H_{\text{int},i} = U\sum_\alpha \hat{n}_{\alpha\uparrow}\hat{n}_{\alpha\downarrow} + U'\sum_{\alpha\neq\beta}\hat{n}_{\alpha\uparrow}\hat{n}_{\beta\downarrow} + \left(U' - \frac{J}{2}\right)\sum_{\alpha<\beta,\varsigma}\hat{n}_{\alpha\varsigma}\hat{n}_{\beta\varsigma} - J\sum_{\alpha\neq\beta} 2\mathbf{S}_\alpha\cdot\mathbf{S}_\beta + \sum_{\alpha\neq\beta}\left(\hat{c}^\dagger_{\alpha\uparrow}\hat{c}^\dagger_{\alpha\downarrow}\hat{c}_{\beta\uparrow}\hat{c}_{\beta\downarrow} + \text{h.c.}\right). \tag{2.18}$$

The first three terms regard the energy cost (i) U of opposite spins on the same orbital; (ii) U' of opposite spins on different orbitals; (iii) $(U' - \frac{J}{2})$ same spins on different orbitals, where J is the Hund's coupling which favours this arrangement*, and in the

*Caution: 'intraorbital' and 'interorbital' are sometimes used in a single atom sense, to mean 'within the same orbital' or 'between different orbitals' of the *same* atom; or in a multi-atom sense to mean 'within orbitals of the same atom', and 'within orbitals of different atoms'. In the former definition U and U' would be intra- and inter-orbital energies. However we stick to the latter convention.

case of rotational symmetry $U' = U - 2J$. There is additionally a Hund's coupling term favouring parallel spins, and a term accounting for pair hopping [63]. Lastly we add in the crystal field splitting $H_{\text{cf}} = \sum_{i\alpha\varsigma} \epsilon_\alpha \hat{n}_{i\alpha\sigma}$. As will become increasingly apparent, Hund's coupling plays a vital role in the physics of FeBCs determined, in a localised description, by this effective Hubbard model.

Much evidence points towards FeBCs being strongly correlated, such as a reduction of the Drude peak in optical conductivity [64, 65], as well as mass renormalisations of 3–4 in ARPES for $BaFe_2As_2$ [66], which can be even larger for chalcogenides [67]. This is supported by theoretical work starting from a strong-correlations picture [68]. If the Hund's coupling energy scale plays a role then this might explain why the FeBCs exhibit strong electron correlations whilst not being close to a Mott insulating state and without evidence of a Hubbard band [69]. In other words, strong correlations might originate from $J > t$ rather than the original Hubbard-Mott paradigm of $U > t$, especially seeing as it is generally accepted from both theory and experiment that U is smaller than the band width in the iron-pnictides [51, 69]. From this, the idea of a 'Hund metal' emerges, with properties dictated by J as well as U. Such physics was first suggested theoretically in Ref. [70] and shown to be important for iron-pnictides in the pioneering work of Ref. [71] in which Hund's coupling was found to reduce the coherence of low-energy quasiparticles, demonstrating that J really is relevant and can given rise to strong correlations. This is summarised by a calculation of the low-temperature Fermi liquid specific heat coefficient γ, as demonstrated in Figure 2.8(a). Calculations for a five-orbital Hubbard model with $n = 6$, as per Equation 2.17 [72] show that the interplay between Hund's coupling and crystal-field splitting strongly affects the critical U for a Mott-insulator transition, as shown in Figure 2.8(b). This will becomes important later when discussing orbital-selective Mott physics. Although at half filling Hund's coupling decreases the critical U, for all other occupancies (apart from for a single electron or hole) Hund's coupling can actually increase the critical U – as shown in panel (b) – whilst suppressing quasiparticle coherence*. We now address the question of how this relates to spin and orbital ordering.

Orbital ordering

An orbital degree of freedom can give not only electronic correlations, as explained in the previous section, but also lead to ordering. Because these orbitals have real-space directionality, as seen in Figure 2.7(a), an orbital degeneracy is unstable – this is the

*The so-called two-faced 'Janus' nature of Hund's coupling.

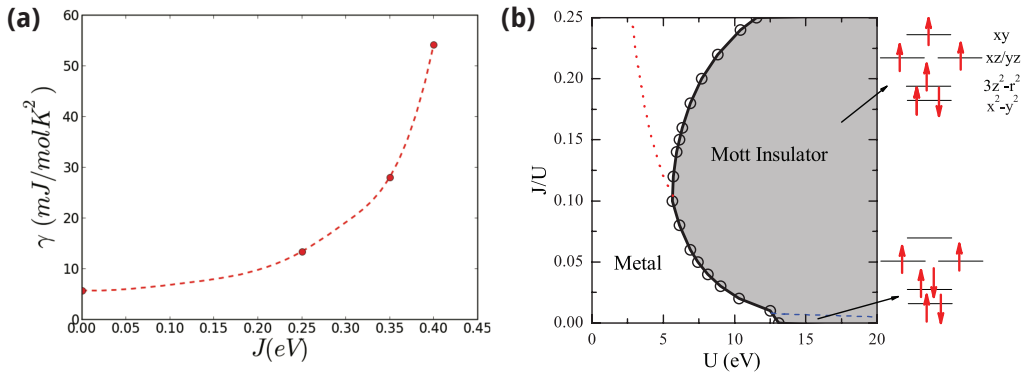

Figure 2.8 | (a) Low-temperature Fermi-liquid specific heat coefficient γ as a function of Hund's coupling J, demonstrating the increase in correlations with J. Reproduced from Ref. [71]. © Deutsche Physikalische Gesellschaft. Reproduced by permission of IOP Publishing. CC BY-NC-SA. **(b)** Theoretical calculation based on Equation 2.17, for five crystal-field split orbitals and six electrons, showing the ground state phase diagram with Hund's coupling J and Hubbard U. The dotted line shows a crossover from a weakly to strongly correlated metal. Reproduced with permission from Ref. [72]. Copyright 2019 by the American Physical Society.

well-known Jahn-Teller effect. We consider the effect of a distortion δ. When the occupancy of the orbitals can change in response to this distortion, there is an energy gain linear in δ. However, the elastic energy is quadratic in δ, guaranteeing an energy minimum at nonzero δ. The real-space form of the orbitals then dictates in which way the energy can be minimised. For degenerate t_{2g} orbitals, a distortion pushing the lobes of either d_{xy} or d_{yz} orbitals further apart will reduce the energy, giving a structural instability from tetragonal to orthorhombic. Such orbital order is driven by an electron-lattice interaction and is the simplest picture in which an electronic degree of freedom, i.e. the orbital occupancy, can drive a structural phase transition with an Ising-like degeneracy. The broken degeneracy between d_{xz} and d_{yz} causes an orbital-occupation imbalance and a nematic state below some critical temperature. Fitting this into our Landau phenomenology for a nematic transition, the orbital occupation or resulting quadrupolar moment is a suitable order parameter, ζ is the orbital-lattice coupling, and the Jahn-Teller energy is therefore characterised by $E_{JT} = T_S - T_S^0$ [73, 74]. Quadrupolar effects can be probed through ultrasound measurements of the elastic constants, and in Ref. [73] a Curie-Weiss fit of C_{66} in $Ba(Fe_{1-x}Co_x)_2As_2$ – the only elastic constant which softens – an energy of $E_{JT} = 20\,K$ was found, which is in good

agreement with resistivity anisotropy measurements [45].

A description of orbital order does not necessarily imply orbital-*driven* nematicity. Spin fluctuations can in fact drive orbital order if the orbital order increases the phase space for spin fluctuations – a general concept known as 'order-by-disorder' in which a system can transition into a non-energy-minimum state if it allows more fluctuations and thus higher entropy [75]. Furthermore Fernandes et al. [76] showed that nematic fluctuations above T_S can explain the change in elastic properties seen in ultrasound data, claiming it to support magnetic fluctuations driving the structural transition – a first taste of the dichotomy between spin- and orbital-driven physics.

Other mechanisms can drive orbital ordering beyond this 'classical' scenario. Considering the case of two degenerate orbitals and one electron per site, then a second index is introduced in the Hubbard model, corresponding to which orbital is occupied. Viewing this orbital degree of freedom as a 'pseudospin' (e.g. $\tau = +\frac{1}{2}$ and $\tau = -\frac{1}{2}$ for occupation of orbital $\alpha = 1$ and $\alpha = 2$ respectively) we can consider an exchange effect analogous to the exchange interaction for spins (whereby virtual hopping gives a $2t^2/U$ energy gain for oppositely aligned spins on different sites giving antiferromagnetism in the basic Hubbard model). This is known as Kugel-Khomskii superexchange [77]. With both spin and pseudospin it becomes favourable (with a $2t^2/(U-J)$ energy gain) for spins to be aligned but on different orbitals, thus giving ferromagnetic spin ordering and 'antiferro' orbital ordering [78]*. Of course this is entangled with the conventional Jahn-Teller mechanism thus causing a structural instability, and distinguishing the two effects is difficult. The above simple picture occurs in case of quarter filled d_{yz} and d_{xz} bands, but it was also shown that orbital order can occur in the pnictides at half-filling due to Hund's energy [51], giving rise to orbital-driven nematicity and magnetism. For two electrons in three orbitals several orbital-ferro and orbital-stripe orders are possible [79], although little insight is gained into which drives nematic order. A renormalisation of exchange constants in this model causes the magnetic transition to occur at lower temperature.

Having established that experimental work supports an intermediate-correlation picture, the above fully-localised models cannot provide whole picture. Orbital order can also originate from an itinerant model, as shown theoretically by Ref. [50], in which a splitting between d_{xz} and d_{yz} can occur due to a nesting Pomeranchuk-like instability between electron and hole pockets, producing band dispersions which agree with ARPES [80]. In this scenario a resistivity anisotropy originates from the anisotropic

*For this we use a simplified version of Equation 2.17 assuming no hopping exists between orbitals on the same atom, or between atoms – see Ref. [78] p254.

Drude weight of d_{xz} and d_{yz} bands, and this mechanism additionally gives rise to antiferromagnetic order, making it a suitable candidate to explain the phase diagram of pnictides.

Although there is much theoretical work which supports orbital-driven nematicity in the pnictides (Ref.s [50, 51, 81] in addition to the above) most of these do not give orbital order in the absence of magnetic order as per the splitting between T_S and T_N. Experimental support is mostly based on the observed splitting between d_{xz} and d_{yz} orbitals in angled-resolved photoemission spectroscopy (ARPES) [80]. We now briefly discuss the opposing school of thought in which nematicity is driven by magnetic order.

Magnetic ordering

For pnictides, long-range magnetic order closely tracks the structural phase transition. This is stripe-like antiferromagnetism whereby spins are ferromagnetically aligned along one Fe-Fe direction and antiferromagnetically along the other [82].

This system can be described by two sublattices, where the magnetic interaction is stronger within rather than between each sublattice. Each sublattice is antiferromagnetically ordered with Néel vectors $\mathbf{m}_1$ and $\mathbf{m}_2$. Their relative orientation gives an Ising-like order parameter $\phi = \mathbf{m}_1 \cdot \mathbf{m}_2$, and reversing the sign of ϕ corresponds to rotating the stripes between vertical and horizontal. Based on this alone, two different symmetries are available, the breaking of which need not be simultaneous, and this can provide an explanation for the splitting between T_S and T_N. The Ising-like Z_2 symmetry of the sublattices can be broken first at T_S, and then the continuous rotational $O(3)$ symmetry at T_N giving long range magnetic order. Essentially the system can choose a stripe direction before the spins have formed long range order. As for the origin of this: Ref. [76] demonstrated that spin fluctuations at the onset of magnetic order can drive the Z_2 symmetry breaking, thus explaining why $T_N < T_S$ in electron-doped $BaFe_2As_2$. In general, for both $Ba(Fe_{1-x}Co_x)_2As_2$ and other pnictides, the nematic order is considered to be a melted form of the lower-T magnetic order, sometimes referred to as a vestigial order to the magnetic order. Whereas an anisotropic Drude weight should give a resistivity anisotropy which persists to $T \to 0$, anisotropic scattering from spin fluctuations should give a resistivity anisotropy that peaks at higher T. Due to the technical challenge of achieving full detwinning whilst not applying too great a orthorhombic distortion, no current work reliably extracts the resistivity anisotropy below T_S – we have such a capability and present this in Chapter 4.

The above consideration is reconcilable with both localised (the context in which

we formed the discussion) and itinerant pictures. First-principles calculations suggest that magnetism in the pnictides is closer to being itinerant than localised [83], due to nearly-nested sections of the Fermi surface. Similar to the itinerant orbital scenario, in this picture a resistivity anisotropy can arise from anisotropic electronic structure, as suggested by ARPES measurements [84] or by scattering from anisotropic magnetic fluctuations [48].

What we take away from this section is that magnetic and orbital orders are intimately connected, and that both can originate from localised and itinerant scenarios, either as a driving force of the nematic transition or a consequence. Answering the question of which drives the nematicity is thus not as simple as just 'spin' or 'orbital' ordering, and this fuels debates. In reality, nematicity likely originates from a complicated combination of spin and orbital fluctuations, whose relative effects are mixed in with that of orbital-selective coherence (a topic we will address in Section 2.4.3). This further motivates experiments under different applied orthorhombicities of the lattice, which can add vital constraints to theoretical models. Furthermore, for theoretical calculations it is easy to conceive of a model which ignores the effects of one type of order, to try and investigate the other. Experimental realisations of such a process would clearly be highly valuable, and provide hope in disentangling the complicated interplay between structural, orbital and spin degrees of freedom.

2.4 FeSe

Based on the previous section, motivations for studying an iron-based superconductor without long-range magnetic order should be clear. The chalcogenide compound FeSe displays no such magnetic order at ambient conditions [85], whilst also being structurally simple, composed solely of the basic building block of FeBCs. Although first synthesised in 2008 [13], lack of pure, high-quality single crystals allowed pnictide studies to dominate early research. Synthesis breakthroughs, most notably in 2013 [86] and continuously since then [87], have lifted FeSe to similar heights of interest, excitement, and contention.

At ambient conditions bulk FeSe is metallic, undergoing a high-temperature structural phase transition from tetragonal to orthorhombic and becoming superconducting at low temperatures. For pure crystals these transitions occur at $T_S \sim 90\,\mathrm{K}$ and $T_c \sim 9\,\mathrm{K}$ respectively [87]. We first review basic experimental observations of bulk FeSe, focusing first on ambient conditions.

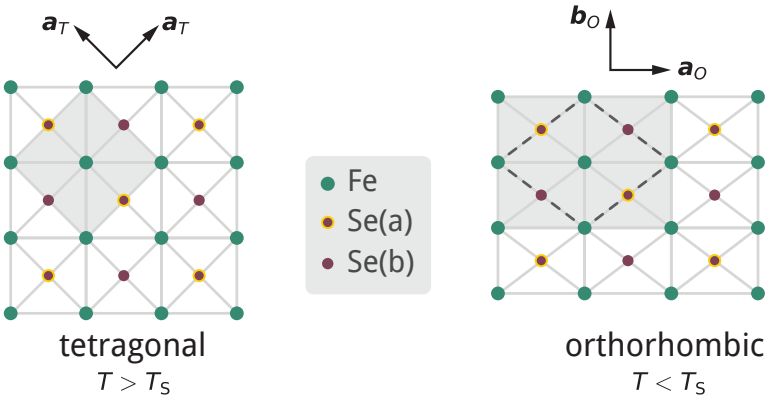

Figure 2.9 | In-plane crystallographic structure of FeSe. For $T > T_S$ the crystal is tetragonal, becoming orthorhombic via a shear distortion (emphasised by the dashed line) below T_S due to a structural instability. The Fe-Fe bond length increases and decreases by an approximately equivalent amount, along the $\mathbf{a}_O$ and $\mathbf{b}_O$ directions respectively. Selenium ions, which sit above and below the iron plane, are denoted by Se(a) and Se(b).

2.4.1 Basic aspects

Structural phase transition

Through the structural transition, the crystallographic symmetry of FeSe changes from tetragonal with space group $P4/nmm$ (which belongs to the $4/mmm$ point group*), with lattice constants $a_T = b_T = 5.32\,\text{Å}$, $c = 5.49\,\text{Å}$, to $Cmma$ orthorhombic [85, 88]. The unit-cell volume is preserved to high accuracy across this transition (although it will not remain perfectly constant), and we take the convention $a_O > b_O$†, such that $a_O = a_T(1+\delta)$, $b_O = a_T(1-\delta)$, as shown in Figure 2.9. A spontaneous orthorhombic distortion δ characterises the transition, which is equivalently labelled as the 'structural strain' ε_S. Furthermore, the distortion is shear type: the principal axes of the distortion are rotated by 45° with respect to the unit cell axes – as seen in Figure 2.9. As such, $\varepsilon_S = \varepsilon_{xy} \equiv \varepsilon_6 \equiv \delta$ (where x and y reference the tetragonal unit cell). One Fe-Fe bond length increases while the transverse length decreases. Although not reflected in the two-dimensional projection of Figure 2.9, selenium ions alternate between being above and below the iron plane, and the Fe-Se bond length is thought to remain essentially constant through the transition, causing a subtle change in the Fe-Se bond angle [85].

*D_{4h} in Schoenflies notation.

†This convention is consistent with FeSe literature, but opposite to the standard crystallographic definition of $a < b < c$.

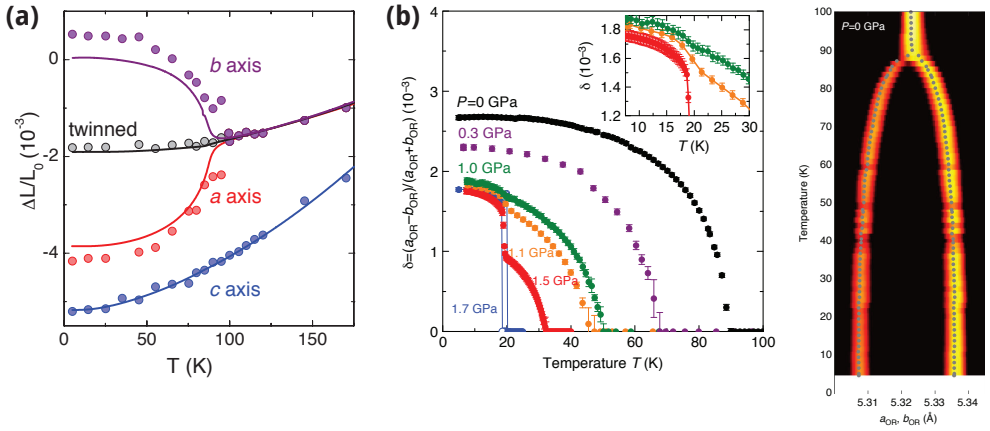

Figure 2.10 | (a) Relative changes in lattice constants (with respect to room temperature) for both in- and out-of-plane directions measured by thermal expansion. The b-axis variation is inferred by comparison between twinned and detwinned values. X-ray data are provided for comparison. Reproduced with permission from Ref. [89]. Copyright 2019 by the American Physical Society. **(b)** Left: Orthorhombic distortion δ determined through measurement of lattice constants using X-ray diffraction on single crystal FeSe. Although measured for various hydrostatic pressures, we focus on $P = 0\,\text{GPa}$. Right: evolution of in-plane lattice parameters with temperature at zero pressure. Reproduced from Ref. [90]. CC BY 4.0.

A consequence of this structural transition is the formation of fine-scale structural twins below T_S which can be visualised using polarised light microscopy [91]. To measure any in-plane anisotropy the sample must be first detwinned and this is most effectively achieved mechanically (as in Ref. [91] using tension) through application of a fixed force. An unavoidable consequence of this procedure is the breaking of tetragonal symmetry *above* the transition – a shortcoming that again we can uniquely address. The behaviour of lattice parameters is observed neatly in directional measurement of thermal expansion [89] – as shown in Figure 2.10(a) – however because this is sensitive to the extent of detwinning it fails to give reliable values for the orthorhombic distortion. A reliable measure of δ is provided by X-ray diffraction on single-crystal samples, as shown in Figure 2.10(b) [90]. This gives a low temperature distortion of $\delta = 0.27\,\%$ which becomes 95 % saturated below $\sim 40\,\text{K}$. As expected for a structural transition regardless of its origin, a decrease in Young's modulus and softening of the C_{66} elastic component have been observed [92], and we discuss elastic properties further in Section 3.1.3.

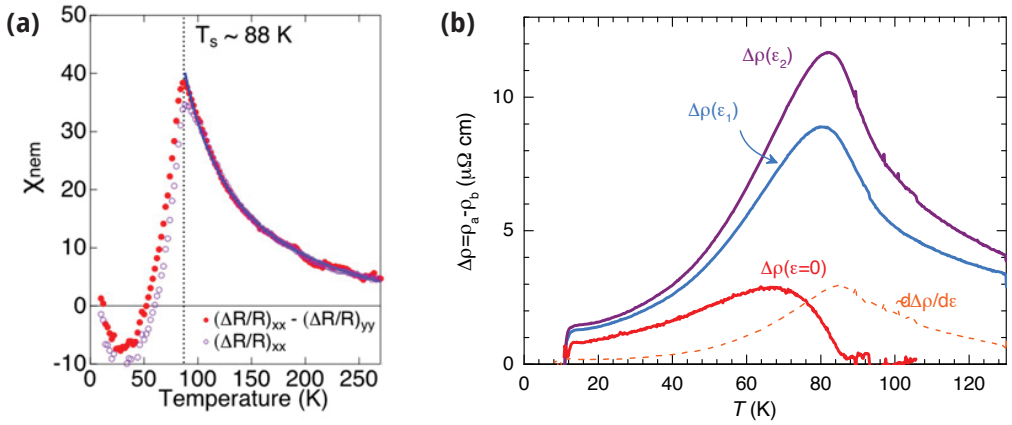

Figure 2.11 | (a) Diverging nematic susceptibility of FeSe determined via the asymmetric component of elastoresistance. Reproduced from Ref. [93]. CC BY-NC-ND. **(b)** Resistivity anisotropy under two uniaxial tensions ε_1 and ε_2, and extrapolated to zero strain (shown in red). Reproduced with permission from Ref. [91]. Copyright 2019 by the American Physical Society.

Nematicity

Observation of a diverging elastoresistivity in FeSe confirms the nematicity to be electronically driven [93], as shown in Figure 2.11(a) for resistivity measured along both x and y to ensure extraction of only the asymmetric response. Comparison of this extraction with just the $(\Delta R/R)_{xx}$ response shows the symmetric elastoresistivity to be weak. In the measurements of Figure 2.11(a) $T_S^0 \sim 34\,\mathrm{K}$, however two similar studies, Ref.s [91] and [94], give $T_S^0 \sim 83\,\mathrm{K}$ and $\sim 66\,\mathrm{K}$ respectively. As explained in Section 2.1.3, these are renormalised from T_S due to coupling between the nematicity and lattice, but the large variation between T_S^0 extraction reflects variability in the data, in addition to the uncertainty introduced by the fitting being constrained to be above T_S.

Above T_S, the resistivity in FeSe increases under tension and decreases under compression, and so $\rho_a - \rho_b > 0$. This is opposite in sign to electron doped $BaFe_2As_2$ [45], but in agreement with our naive expectation that tension decreases bandwidths (giving a smaller orbital overlap) thus resulting in a higher resistivity. Extraction of the resistivity anisotropy below T_S requires the sample to be detwinned, resulting in a non-zero anisotropy above T_S and enhancing it below. To our knowledge, only a single study attempts to determine the resistivity anisotropy as a function of temperature [91]. As shown in Figure 2.11(b), they measure the 'detwinned' resistivity ρ_t under two different uniaxial stresses, then infer the resistivity anisotropy by assuming $\rho_t = (\rho_a + \rho_b)/2$, and

extrapolate to zero strain to extract the 'intrinsic' zero-strain anisotropy. This peaks at 70 K at 4 % of the average in-plane resistivity, and gradually decreases upon cooling. We will later address the validity of this analysis using our data under continuously tuned strain, which contradict the dependence shown in Figure 2.11(b).

Electronic structure

The exact electronic structure of FeSe is complicated, and several aspects are sources of contention. We start by describing more accepted phenomenology. Density functional theory (DFT) predicts a band structure similar to that of other iron-based superconductors, with small quasi two-dimensional hole (electron) Fermi surfaces at the Brillouin zone (BZ) centre (corners) with d_{xy}, d_{xz} and d_{yz} character – as shown in Figure 2.12(a). The electronic structure can be probed via magnetotransport, quantum oscillations, ARPES and STM, and Ref. [95] succinctly reviews recent measurements and understanding regarding the electronic structure of FeSe.

We concentrate on results from ARPES measurements. Whereas DFT predicts three quasi-2D hole pockets at the zone centre (Γ point) occupying a large part of the BZ and with character of all three t_{2g} orbitals, as observed by ARPES these bands are shifted down such that only d_{xz} and d_{yz} cross the Fermi level, as shown in Figure 2.12(c). Significant renormalisation (d_{xy} by a factor of 9) suggests strong correlations. As shown by measurements on detwinned crystals [98], below T_S there is a splitting between the energies of the xz and yz orbitals, this is 10 meV at Γ as $T \to 0$. Conversely d_{xy} is largely unaffected by the structural transition.

The electron pockets at the zone corners are much more poorly resolved by ARPES. Two bands cross the Fermi level, again occupying a much smaller area of the BZ than expected, and d_{yz} is renormalised by a factor of ~ 4. As shown in Figure 2.12(b) ARPES observes a (famously) large splitting of 50 meV between two features, the origin of which is debated. One claim [99] is that this is a splitting between $d_{xz,yz}$ bands, with $E_{xz} < E_{yz}$ (i.e. a −50 meV shift), offering a convenient explanation of the origin of nematicity due to orbital ordering. However, improvements in resolution and measurements on detwinned crystals suggest it may actually be between $d_{xz,yz}$ and d_{xy} [96], especially as it does not appear to increase upon further cooling below T_S. If this is the case, a $d_{xz,yz}$ splitting can still occur in the orthorhombic phase as the bands are no longer protected by fourfold symmetry, but this would not explain nematic order. Furthermore, some measurements observe this splitting, some do not [95]. Measurements on detwinned crystals [97] allow for the true nematic nature of the Fermi surface to be revealed, as summarised schematically in panel (d).

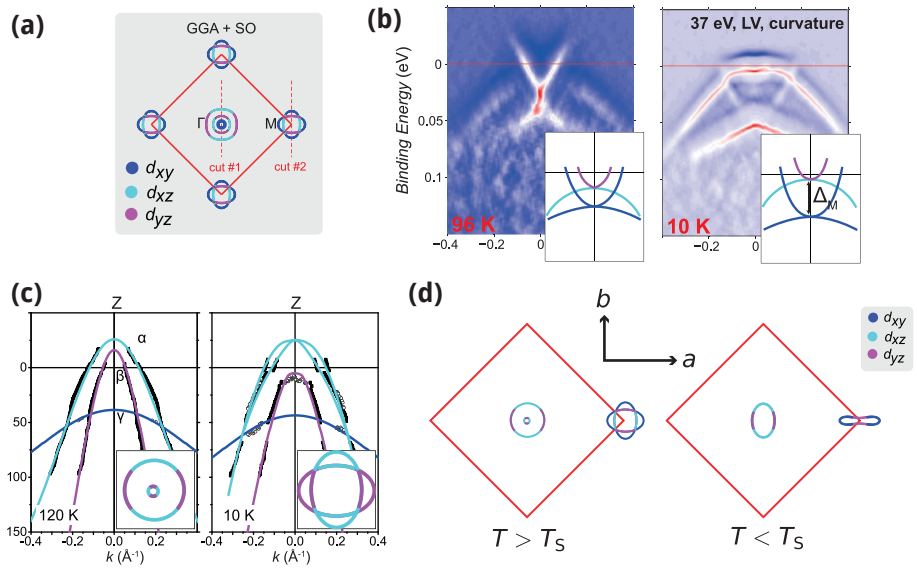

Figure 2.12 | (a) Fermi surfaces of FeSe as predicted by density functional theory. Reproduced with permission from [94]. Copyright 2019 by the American Physical Society. **(b)** Angle resolved photoemission spectroscopy (ARPES) measured for the electron pocket in the zone corner for $T > T_S$ (left) and $T < T_S$ (right). Insets show one interpretation of the band structure in which the splitting is between d_{xy} and $d_{xz,yz}$. Reproduced from [96]. CC BY 3.0. **(c)** ARPES measurements at the zone centre for the hole-like Fermi surfaces. Reproduced with permission from [94]. Copyright 2019 by the American Physical Society. **(d)** Schematic of Fermi surfaces above and below the structural transition temperature T_S, based on results from Ref. [97].

As introduced in Section 2.3.2, strong correlations in FeSe originate not from the Hubbard interaction U, but instead from interactions due Hund's coupling which occur due to an orbital blocking mechanism. This gives rise to the large mass renormalisations observed in the electronic structure of FeSe [80] and additionally results in orbital-selective effects which will be discussed in more detail in Section 2.4.3.

Effect of hydrostatic pressure

Having already emphasised the differences between bulk FeSe and the pnictides, it is unsurprising that such dissimilarities extend to the phase diagram under hydrostatic pressure, as shown in Figure 2.13(a). This phase diagram was obtained through measurement of resistivity [100], and qualitative features have been reproduced by X-ray diffraction and Mössbauer spectroscopy [90]. T_S decreases monotonically under

pressure, with an initial slope of $\mathrm{d}T_S/\mathrm{d}P \sim 31\,\mathrm{K/GPa}$ [101], and there is a large enhancement of the superconducting transition temperature with $\mathrm{d}T_c/\mathrm{d}P \sim 5.8\,\mathrm{K/GPa}$ [101, 102]. The variation of T_c is non-monotonic and the overall increase occurs in a complex three-step process shown clearly in Figure 2.13(a). This increase differs from the behaviour of 122 pnictide compounds in which superconductivity is suppressed in the orthorhombic phase (see Figure 2.5), whereas for FeSe superconductivity persists far into the orthorhombic phase and favours tetragonality.

Application of hydrostatic pressure additionally induces a dome of antiferromagnetic order which appears beyond $\sim 2\,\mathrm{GPa}$ and peaks at $T_N \sim 45\,\mathrm{K}$ at 4 GPa [100]. That the magnetic ordering temperature *increases* whilst the nematic transition temperature decreases is very much in contrast to electron-doped $BaFe_2As_2$, in which they track each other closely [103]. Determining the exact type of magnetic order present in FeSe is difficult as neutron experiments under pressure fail to resolve magnetic signals [104], however considerable Fermi-surface reconstructions indicate that the magnetic order is antiferromagnetic [105], and X-ray diffraction data [90] suggest that this is stripe-like due to broken tetragonal symmetry in the magnetic phase.

Effect of chemical substitution

Another method of tuning iron-based compounds is by chemical substitution. Replacement of selenium by sulphur ($FeSe_{1-x}S_x$) is isovalent and therefore particularly useful, giving rise to a chemical pressure and subsequently a decrease in lattice parameters [106]. The phase diagram of $FeSe_{1-x}S_x$ is shown in Figure 2.13(b). Analogous to hydrostatic pressure, the initial effect of this substitution is to suppress T_S and enhance T_c. Although T_c only increases to a maximum of $\sim 12\,\mathrm{K}$ (i.e. not as high as with pressure), T_S is completely suppressed at approximately 16 % sulphur content. Interestingly, there is no appearance of magnetic order, and as such sulphur doping enables investigation of a pure nematic quantum critical point (NQCP), as well as the relationship between nonmagnetic nematic fluctuations and superconductivity. The inequivalence between pressure and sulphur substitution is thought to originate from the subtle effect each has on the chalcogen height from the iron plane. This quantity decreases monotonically under sulphur substitution but increases under hydrostatic pressure, and is important for the existence of hole-like pockets at the Brillouin zone corners, and consequently for Fermi surface nesting [107].

This nematic quantum critical point has been studied via the nematic susceptibility determined through measurement of elastoresistivity [93] (as described in Section 2.3.1). A Curie-Weiss-like divergence was observed for all compositions, with the bare nematic

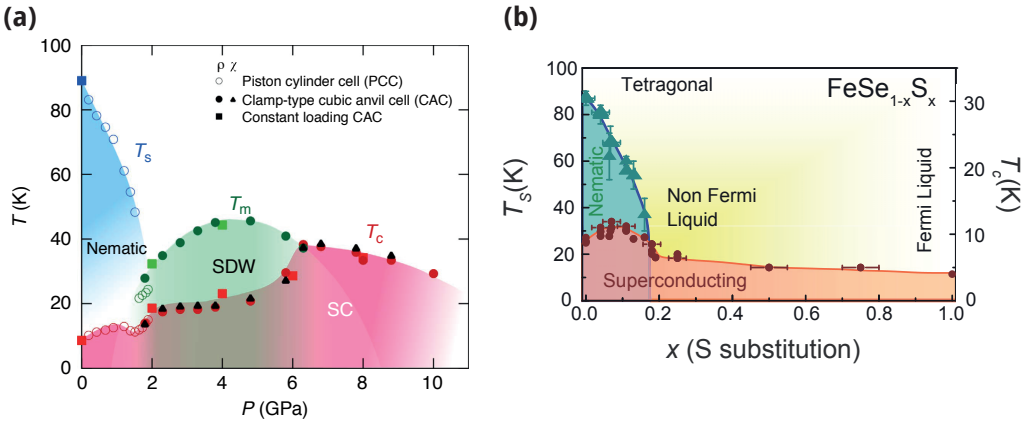

Figure 2.13 | (a) Phase diagram of bulk FeSe as a function temperature and hydrostatic pressure obtained via resistivity measurements. Nematic and superconducting orders respond strongly to pressure, and above $\sim 2\,\text{GPa}$ a dome of magnetic order appears. Reproduced from Ref. [100]. CC BY 4.0. **(b)** In contrast, no magnetic order appears upon substituting selenium for sulphur (S), despite this being isovalent and acting as a chemical pressure (data obtained via transport and thermodynamic measurements). Note that T_S and T_c are on different axes. Reproduced with permission from Ref. [106]. Copyright 2019 by the American Physical Society.

transition temperature changing sign again at 16 % sulphur content. That this sign change indicates a NQCP is supported by a region of non-Fermi-liquid behaviour, as shown in Figure 2.13(b). This is determined from the deviation from two of the exponent n in the resistivity dependence $\rho = \rho_0 + AT^n$. Unlike for various doings of $BaFe_2As_{22}$ (as seen in Figure 2.5), for FeSe T_c is not a maximum at the NQCP – another notable difference between these materials. Both sulphur content *and* pressure were tuned together in Ref. [106], in which the pressure range over which magnetic order occurs was found to reduce with sulphur content. Furthermore, high-temperature superconductivity occurs at either side of the dome-like AFM phase, whilst remaining suppressed near the NCQP and AFM peak, indicating a clear competition between superconductivity and magnetism.

The lack of magnetic order in $FeSe_{1-x}S_x$, even after doping has suppressed the nematic state, is powerful for investigating superconductivity and its relationship to nematicity. Evidence for an anisotropic superconducting gap has been observed by thermal conductivity and specific heat measurements with an abrupt change in the gap structure at the nematic quantum critical point [108]. Another study utilising

spectroscopic-imaging scanning tunnelling microscopy finds two distinct pairing states either side of the nematic end point [109]. We will discuss these in more detail in the next section.

Superconductivity

Leading on from the general discussion of superconductivity in Section 2.2, we will now examine this state in bulk FeSe which emerges below $T_c \sim 9\,\mathrm{K}$. This differs from superconductivity in pnictides as it exists at ambient pressure and does not emerge from long-range magnetic order. That superconductivity is unconventional can be suspected based on the previous discussion for other FeBCs, in addition to the general observation of an extremely large ($\sim 40\,\mathrm{K}$) enhancement of T_c with hydrostatic pressure. This is supported by a wealth of work that we will now highlight.

Despite lacking magnetic order, strong spin fluctuations have been detected in FeSe using inelastic neutron scattering, with a fluctuating moment larger than that of pnictides [110]. Furthermore, inelastic neutron diffraction measurements also observe a spin resonance mode (i.e. a peak in the spin correlation function at the stripe-type wave vector) which suggests pairing is mediated by spin fluctuations (SFs) of the sign-changing type [111]. Observation of a sign change is also supported by Bogoliubov quasiparticle interference (BQPI) measurements [26, 31]. An important feature of such SF-mediated superconductivity is that pairing interactions should be dependent on the orbital character of the Fermi surfaces. Observation of a direct relationship between superconducting gaps and orbital character using ARPES provides strong evidence for SF-mediated pairing, showing that the gap magnitude follows the distribution of d_{yz} orbital weight [27]. Orbital fluctuations can also be invoked to explain pairing, however such a mechanism is proposed to give sign-preserving s_{++} pairing [112]. In the proposal of Ref. [112], pairing is due to orbital fluctuations which are large even if the electron-phonon interaction they are induced by is small, thus allowing a high T_c state to be realised.

As with pnictides, the existence of nodes is a hot topic for FeSe. Early specific heat measurements supported a non-nodal superconducting gap [113], however more recent measurements, using the same technique but on higher-quality samples, suggest evidence for nodal gaps [114]. This is in contrast to the BQPI measurements of Ref. [26] which found the gap to be nodeless. Conversely, an observation of increasing consensus is the highly anisotropic nature of the superconducting gap on both electron and hole Fermi surfaces. BQPI measurements find $\Delta_{\mathrm{max}}/\Delta_{\mathrm{min}} \gtrsim 15$, indicating and intimate connection between nematicity and superconductivity [26]. ARPES measurements are

in agreement with a strong gap anisotropy, but have not yet established the existence of line nodes [115]. This large anisotropy is surprising for a material with such small Fermi surfaces, implying that the pairing interaction varies rapidly across small regions of momentum space.

The BQPI work of Ref. [26] observes a fascinating piece of phenomenology: $\Delta(\mathbf{k})$ is maximal on parts of the Fermi surface with predominantly d_{yz} orbital character, and minimal where d_{xz} and d_{xy} character is dominant. This is supported by ARPES measurements [27, 115], however such an observation cannot be explained by the expected anisotropy due to crystallographic symmetry. An obvious connection emerges here with the topic of orbital selectivity, which will be covered in relation to nematicity in Section 2.4.3. Hund's rule interactions 'decouple' bands such that electrons of different orbital types can have different correlation strengths. Superconducting pairing itself can then become 'orbital-selective', whereby only electrons of a specific orbital character condense into pairs. The treatment of this effect is more subtle than simple Fermi surface shifts, and the inclusion of orbital-selective correlations in spin-fluctuation theory for FeSe yields promising agreement to BQPI and ARPES data [116], making orbital-selective spin fluctuations a promising candidate for the pairing mechanism. This is supported by recent theoretical work showing that orbital-selective spin fluctuations mediate pairing that is not only orbital-selective but also nematic (i.e. inter-pocket pair scattering becomes anisotropic) [117].

That superconductivity emerges from a nematic state in FeSe cannot be ignored. Although theoretical proposals exist describing how nematic fluctuations can cause pairing in FeSe thin films [118], for bulk crystals the recent theory of Ref. [119] establishes that nematicity only weakly affects T_c. This work argues that the gap anisotropy can be explained by a low-energy model for nematic order *without* the need for making $d_{xz,yz}$ orbital quasiparticle weights inequivalent by hand. When discussing the origin of nematicity in Section 2.3 we expressed the difficulty of simplifying the problem to just 'orbital' or 'spin' degrees of freedom, identifying the problem as likely concerning a complicated combinations of both, mixed in with orbital-selective coherence. The same is likely true for the origin of superconductivity too, and in fact many theories branded as being based upon spin fluctuations also contain contributions from orbital fluctuations [25]. The valuable theory work of Ref. [120] takes an unbiased approach which puts magnetism, superconductivity, and orbital order on equal footing. Using renormalisation group analysis, they argue that provided all Fermi surfaces are small (as they are in FeSe) a spontaneous orbital order is first developed, then $s_{\pm}$ superconductivity, and magnetic order not emerging down to $T = 0$.

Several other observations regarding superconductivity must briefly be mentioned.* Despite the large response of T_c to hydrostatic pressure, thermal expansion measurements show that the orthorhombic distortion does not appear to be significantly affected by superconductivity [89]. This contrasts the behaviour in $Ba(Fe_{1-x}Co_x)_2As_2$ [124], and suggests a lack of both coupling and competition between superconductivity and orthorhombicity. Superconductivity in FeSe also resides in a crossover regime between the BCS limit, in which $k_B T_c \sim \Delta \ll E_F$, and the Bose-Einstein condensate (BEC) limit in which $k_B T_c \sim E_F$. This is due to the size of the superconducting gap with respect to the small Fermi energy, and means the coherence length becomes comparable to the inter-particle distance [125].

Lastly, we discuss what can be understood from studying the superconductivity in $FeSe_{1-x}S_x$, especially as this isoelectronic substitution suppresses nematicity without inducing magnetic order. An obvious approach is to study the superconducting gap as a function of increasing sulphur doping using QPI. In doing so the band anisotropy is observed to smoothly decrease and, more strikingly, a phase transition in the gap structure occurs at the nematic quantum critical point (NQCP), subsequently shrinking discontinuously beyond this point [109]. This is supported by thermal conductivity and specific heat measurements which suggest an abrupt change in the gap structure at the NQCP [108]. Within the nematic regime ($0 \leq x \leq 0.17$) there is two-gap behaviour, one small but anisotropic and the other large and more isotropic, and for $x > 0.17$ the larger gap *also* becomes strongly anisotropic. These observations are important as they tell us that superconductivity is strongly affected by the orbital-dependent nature of the nematic fluctuations. We conclude by mentioning an ARPES study of $FeSe_{0.93}S_{0.07}$ which observes both a large anisotropy and nodal gap distribution, demonstrating clearly the effect nematicity has on superconductivity [126].

2.4.2 Nematicity

As introduced in Section 2.3, two schools of thought exist regarding the origin of nematicity in FeBCs, driven by either magnetic or orbital ordering. These can originate from both itinerant or localised pictures. An important aspect of the itinerant spin-nematic scenario to explain nematicity in the pnictides was the proximity to long-range magnetic order. This is absent in FeSe and so there is a natural tendency to suppose that orbital order is key. We cannot neglect the spin degree of freedom however, which

*One cannot discuss FeSe without also mentioning the attention garnered by the enhancement of T_c to 58 K for single layer FeSe on $SrTiO_3$ [121]. Of the less conventional studies: T_c can be enhanced by stretching it on Scotch Tape [122], or by simmering it in alcohol [123].

is still at play and known to exhibit strong fluctuations. Unsurprisingly no consensus has been reached on the origin of nematicity in FeSe either and, although the basic ideas are as presented in Section 2.3, we highlight relevant work pertaining specifically to FeSe.

Simple ferro-orbital ordering due to a population imbalance of d_{xz} and d_{yz} orbitals (giving order parameter $\phi = (n_{d_{xz}} - n_{d_{yz}})/(n_{d_{xz}} + n_{d_{yz}})$) is not likely to drive the transition as ARPES measurements show only a small average splitting between these bands [95]. Another candidate is unidirectional bond order [96], in which on-site orbital energies are not affected, but intersite hopping terms are anisotropic. This would give bands that agree well with ARPES results, however no microscopic motivation for such an ordering exists. Conversely the Knight shift measurements of Ref. [127], give values too large to be explained by the orthorhombic distortion alone, and the spin-lattice relaxation rate does not change significantly through the structural transition. Their results are explained well by ferro-orbital ordering and, as supported by Landau theory, this advocates orbital-driven nematicity. Several theory papers additionally support orbital ordering through comparison of calculated band structures with ARPES measurements [128–131]. Most notable of these is Ref. [131] in which local correlations such as from Hund's rules are accounted for, and the properties of the orbital-ordered state are shown to be severely constrained by Hund's coupling.

The previously presented spin-nematic scenario proposed for the pnictides [76], would seemingly not be applicable to FeSe. But in extending this model through utilisation of FeSe's uniquely small Fermi surface, a near degeneracy between magnetic and charge-current density wave fluctuations is found [132]. These compete for long range order, suppressing the Néel temperature and the magnetic correlation length, thus supporting spin-nematicity. Other theoretical models attempt to analyse the results via the Hubbard model to determine which fluctuations show the dominant instability [133].

2.4.3 Orbital-selective physics

As established in Section 2.3.2, Hund's coupling J can give rise to electronic correlations even in systems away from half-filling and without large U/t – i.e. not in close proximity to a Mott insulating state. Theoretically, an additional consequence of Hund's coupling can arise which experimental evidence increasingly points to being important in FeBCs. Hund's rule coupling acts as a 'band decoupler', subsequently enabling orbital decoupling of correlations, and 'orbital-selective' phenomena. Due to the multiorbital nature of iron-based compounds, Hund's driven orbital-selective correlations are

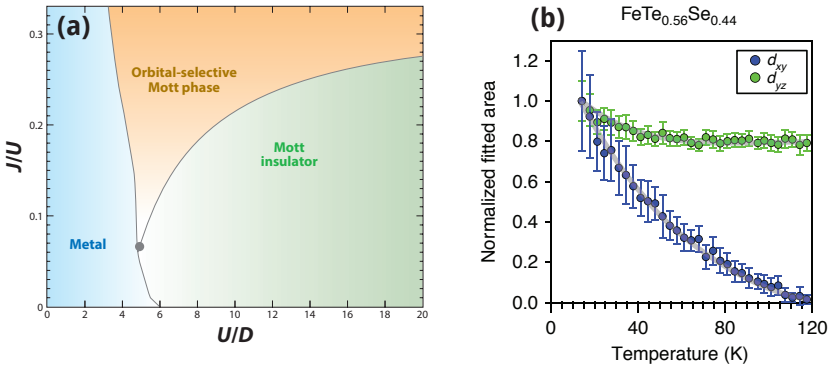

Figure 2.14 | Evidence for the orbital-selective Mott phase. **(a)** Phase diagram as a function of interaction strength U/D and Hund's coupling J/U for a three-band Hubbard model occupied by four electrons. D is the half-filled bandwidth. Republished with permission of Annual Reviews, from Ref. [63]; permission conveyed through Copyright Clearance Center, Inc. **(b)** Measure of the spectral weight (i.e. degree of coherence) in $FeTe_{0.56}Se_{0.44}$ from ARPES. Reproduced from Ref. [67]. CC BY 4.0.

expected to be important, as we now show.

Such decoupling is predicted by mean-field theory [134], and occurs due to the suppression of orbital fluctuations under strong J. In the extreme case, orbital-selective correlations on one band cause it to become completely decoherent, i.e. a localised Mott insulator, whilst the other(s) remain itinerant – this is known as an orbital-selective Mott transition (OSMT).

Conceiving different scenarios which display orbital-selective Mott physics is not difficult. The simplest approach is to take the degenerate Hubbard model, introduce differing intraorbital repulsions, and neglect interorbital hopping; one orbital becomes Mott insulating, whilst the others do not [135]. Alternatively, through crystal field splitting of two half-filled bands of equal bandwidth, one can remain half-filled, whilst under light non-integer dopings the other can become itinerant [136]. *Physical* realisations of these very specific conditions, however, would suggest that it is a rare phenomenon. In the breakthrough work of Ref. [137] an OSMT was shown to be a much more widespread feature of multiorbital systems. They considered a three-band Hubbard model (one crystal-field split and the other two degenerate) with equal bandwidths and populated by four electrons, giving the phase diagram shown in Figure 2.14(a). The underlying mechanism is orbital decoupling, occurring under sufficiently large Hund's coupling and crystal-field splittings. From the phase diagram

in panel (a) we see a nonzero J is needed for an OSMT, and increasing J decreases the critical U required for an OSMT, while increasing the critical U required for a full Mott insulating transition. This subsequently widens the range for the orbital-selective Mott phase.

Such physics offers an explanation of why FeBCs are not described fully by a localised picture due to strong correlations, nor an itinerant picture from weak correlations. Different orbitals may have different correlations, giving a coexistence of itinerant and localised charge carriers. For the pnictides, doping is an available tuning parameter which can alter the relative occupation of orbitals, allowing an even stronger test for the presence of orbital selective Mott physics [138]. The number of electrons per iron can be tuned from five to six, and orbital decoupling means the *individual* orbital population dictates its correlation strength, and a band closer to half-filling will have stronger correlations. This is supported by calculations which show the quasiparticle weight is sensitive mostly to its own filling [138]. The $d_{xz,yz}$ and d_{xy} orbitals are the least occupied and closest to half filling, and should therefore have much larger mass renormalisations than d_{z^2} or $d_{x^2-y^2}$ – the largest being for d_{xy}. ARPES measurements on single-crystalline FeSe support this, with d_{xy}, d_{yz}, and d_{xz} hole-band renormalisations of 9, 3, and 3.7, respectively [139].

FeSe is one of the most strongly correlated FeBCs, with Hubbard bands being observed in ARPES [140], but a well-defined quasiparticle peak at the Fermi level – it is a metal after all. Orbital-selective Mott physics is suspected to be at play. Although in FeSe the electron-per-iron number is fixed at around six, J still acts a band decoupler suppressing charge fluctuations between different orbitals. This was first shown theoretically by first-principles calculations in Ref. [141]. The first experimental support for its applicability to chalcogenides was provided by the ARPES measurements of Ref. [67]. They studied $FeTe_{0.56}Se_{0.44}$, and at low temperatures observed a metallic state with strong orbital-dependent renormalisation, and at high temperatures an orbital-selective Mott phase in which d_{xy} becomes completely incoherent (indicated by a complete loss of spectral weight) whilst the others remain itinerant – as shown in Figure 2.14(b). These features are 'universal' in the chalcogenides, also appearing in $K_{0.76}Fe_{1.72}Se_2$ and monolayer FeSe on $SrTiO_3$. Theoretically these observations can be understood by the proximity to an OSMT as predicted by both a slave-spin and dynamical mean-field theory for sufficiently large U and J [67].

Relating discussions back to nematicity, the orbital order we discussed in Section 2.4.2 is inherently 'orbital selective' in a simpler sense of the expression. Splitting the xz, yz degeneracy makes the occupation of one orbital energetically favourable and

this contributes to orbital-selective coherence in addition to band decoupling. Recently Ref. [142] found that by considering a model with orbital-selective spin fluctuations, several unique features of the nematicity in FeSe could be explained, most notably its suppression under pressure.

So far, our discussions involving experimental support have relied on ARPES. More recently, remarkable Bogoliubov quasiparticle interference imaging has provided another tool for direct determination of the orbital-selective nature of the electronic structure. The Davis group of Cornell University first applied this technique to measure the superconducting energy gaps of FeSe, whereby they observed superconductivity to be orbital-selective [26]. Electrons in the d_{yz} orbital form Cooper pairs preferentially over electrons in other orbitals, and this can arise from a difference in correlation strengths for electrons with different orbital character, suggesting d_{yz} to be the most coherent and d_{xy} the least. Even more recently, this technique was applied to the normal metal state of FeSe [143]. Namely they investigated the quasiparticle weight of different bands at 10 K (i.e just above T_c) to directly probe whether or not they exhibit orbital selective correlations. Their measurements found $Z_{xy} < Z_{xz} \ll Z_{yz}$ with $Z_{xy} \sim 0.1$, $Z_{xz} \sim 0.2$, $Z_{yz} \sim 0.8$; where Z is the quasiparticle weight – i.e. d_{yz} is delocalised and has good coherence, d_{xz} states are significantly less coherent, and d_{xy} have the lowest coherence. This is in agreement with the previous study in the superconducting state, and suggests that the loss of coherence in d_{xy} is more abrupt than in Figure 2.14(b). In general this work provides direct experimental evidence for the importance of Hund's coupling in giving orbital-selective coherence, firmly assigning FeSe the label of Hund's metal.

3 | Experimental Methods

In Chapter 2 we introduced the concept of generalised rigidity being a fundamental consequence of broken symmetry, using this to explain the origin of the elastic properties of solids. We also saw how the order parameter in a lowered-symmetry phase can be tuned with a corresponding conjugate parameter as an external field. This motivated our use of uniaxial strain as a tool to investigate the nematic state in FeSe. In reviewing experimental work to date, we further motivated the use of large anisotropic strains to fully polarise the population of domains, and thus investigate single-domain properties in transport below T_S. In this chapter we will establish the theory describing mechanical elasticity. This will build the foundation for understanding how to experimentally probe the nematicity in FeSe via apparatus that applies a controlled, tuneable deformation. We will give an overview of this apparatus, as well as describing a significant developmental effort to enable the strain-tuning of FeSe through attachment to a carrier, or 'platform'. Finally, we will briefly describe the system set up to measure this material across a wide temperature range, with high levels of control.

3.1 Strain-tuning

3.1.1 Introduction

A core result of thermodynamics is that as a system reaches infinite size, it may be accurately described by macroscopic thermodynamic observables such as entropy, volume, and magnetisation. These observables appear in free energy expressions alongside conjugate variables temperature, pressure, and magnetic field. Experimentally, these variables can be used as external fields whose utilisation underpins studies of the physical and chemical properties of condensed matter. The conjugate pair of pressure and volume are unique as each may be viewed as an external field. As we will see in more detail in Section 3.1.2, these variables correspond to stress and strain, the

distinction of which depends on whether displacement (volume) or force (pressure) is the controlled parameter. Application of pressure* is a well-established technique whose results are too considerable to survey completely. To give a brief overview: the most dramatic effect of pressure is to drive transitions between phases of matter. This of course applies to the more elementary liquid to solid transition, but it can also drive more complex transitions in strongly correlated systems - for instance the superconductivity in elemental metals such as for barium above 5.5 GPa [144]. The discovery of high-temperature superconductivity in $YBa_2Cu_3O_{7-\delta}$ (YBCO) emanated from the observation of an increase of T_c in La-Ba-Cu-O under hydrostatic pressure [145], suggesting the replacement of La^{3+} for a smaller ion Y^{3+} [146]. For such strongly correlated systems pressure can be used to investigate how the electronic states change in response to lattice distortion. Even for a simple metal, electrical properties are governed by states near the Fermi surface, the shape of which depends on the real-space dimensions of the unit cell, resulting in modified conductivity under pressure.

In Chapter 2 we already touched on measurements of FeSe under pressure. The majority of these studies were conducted under hydrostatic conditions, that is with equal normal stresses applied in all three directions. FeSe displays a notable response under hydrostatic stresses, with an enhancement of T_c at a rate of 5.8 K/GPa [101], and an antiferromagnetic transition at around 1.2 GPa [147]. However, for highly anisotropic layered materials such as the cuprates, ruthenates, and iron-based superconductors, uniaxial (i.e. along just one axis) pressure is a powerful tool. The changes in electronic structure induced by hydrostatic pressure are normally much smaller than that of the anisotropic modification from uniaxial pressure, and it is a much cleaner tuning parameter than chemical doping. Despite, until recently, uniaxial pressure being less commonly used in condensed matter than hydrostatic pressure, the technique has given several important results. For YBCO, uniaxial pressure was used to show that the cancellation of opposite effects within the $a-b$ plane gives the small hydrostatic pressure dependence of T_c [148]. For iron-based superconductors it was importantly utilised to demonstrate that the nematic phase is electronically driven. This was first carried out for $Ba(Fe_{1-x}Co_x)_2As_2$ [45], and then later for FeSe [94].

The physical importance of these pressure techniques is clear. In many cases they can however be primitive, and limited by poor strain homogeneity or tuneability, or both. In Section 3.2.2 we will describe an already-established, novel approach using piezoelectric actuators to achieve both compressive and tensile uniaxial pressure. With

*For now we use the term 'pressure' generally regardless of whether the controlled parameter is stress or strain.

some development, this will go on to form the basis of the apparatus we will use for experiments on FeSe. Deformation is the controlled parameter of this apparatus, and so we enter the regime of strain-tuning. To use the language of stress and strain coherently, we will first construct a more rigorous framework.

3.1.2 Linear elasticity

Hooke was the first to observe that to good approximation there seems to be a linear relation between the force on a body and its resulting deformation ($F = k\delta$). This forms the basis of linear elasticity. The constant of proportionality k refers to the material's stiffness and is a function of its elastic properties and dimensions. Separation of these two factors is possible via the introduction of stress and strain. Stress is a measure of the internal restoring forces within a material, and has units of force per unit area, whereas strain is a unitless measure of deformation. If one considers a force F normal to the area A_0, the stress is $\sigma = F/A_0$, with a resulting deformation δ in direction L_0 giving a strain of $\varepsilon = \delta/L_0$. Hooke's law thus becomes

$$\sigma = E\varepsilon. \tag{3.1}$$

We now have a parameter E, the Young's modulus, which encompasses the material's elastic response. Equation 3.1 forms a relationship between 'normal' components of stress and strain along a single direction (i.e. uniaxially), but for a complete picture we must also consider shear. For shear stress the force acts tangentially to the area, but can be defined analogously as $\tau = F/A_0$, and for small displacements the shear strain γ is simply the angular deviation from a right-angled edge. This gives the shearing counterpart to Hooke's law

$$\tau = G\gamma, \tag{3.2}$$

where G is the shear modulus. It is clear that more rigour is required here as there are two independent shear directions for a given area A_0.

Hookean behaviour is built upon the underlying assumption of 'linear' and 'elastic' behaviour. The former dictates that stress be proportional to strain (as we have already seen), and that strains are small such that changes in geometry can be neglected. This essentially corresponds to taking only the first term in the Taylor expansion of the interatomic potential, and is the reason for the 'zero' subscript used in the previous paragraphs. The elastic condition enforces deformations to be time-independent and for complete recovery of original dimensions upon load removal. With these in mind we can now formulate a general description of stress and strain.

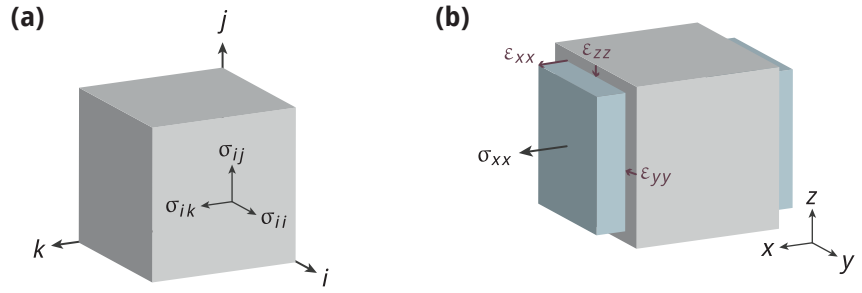

Figure 3.1 | (a) Diagrammatic representation of the components of the stress tensor. Indices that are repeated correspond to normal stress, whereas those that are not correspond to shear stress. As indicated for normal components, positive and negative values correspond to tension and compression respectively. **(b)** A positive normal strain in one direction gives rise to negative strains in the other two orthogonal directions - this is referred to as the Poisson effect.

Because stress is a physical quantity it must obey certain transformation rules which make it a tensor. The fact that it describes the relationship between two different directions makes this tensor second-rank. As such it can be labelled with two indices which encompass both normal and shear components. σ_{ij} denotes a force along i, acting on an area normal along j, where $i = j$ and $i \neq j$ represent normal and shear components respectively. In generalised three-dimensional Cartesian coordinates $i, j = \{x, y, z\}$, and the stress tensor will consist of nine components. These are summarised in Figure 3.1(a). Strain is also a second-rank tensor, ε_{kl}, but here $k = l$ indicates an extension is along k, and $k \neq l$ a rotation in the k-l plane. We can now write down a generalised Hooke's law which gives the constitutive equations that link stress and strain for linear, elastic materials. These are

$$\begin{aligned} \sigma_{ij} &= \sum_{k,l} C_{ijkl}\varepsilon_{kl}, \\ \varepsilon_{ij} &= \sum_{k,l} S_{ijkl}\sigma_{kl}. \end{aligned} \tag{3.3}$$

The quantities C_{ijkl} and S_{ijkl} in Equation 3.3 are referred to as the stiffness and compliance respectively. These are fourth-rank tensors, and are inversely related by $[S_{ijkl}] = [C_{ijkl}]^{-1}$. Both compliance and stiffness tensors have 81 components, but symmetry considerations reduce the number of these which are independent. In

the small strain limit both σ_{ij} and ε_{ij} are symmetric*, which gives a reduction to 36 independent components. Furthermore, from the symmetry of the strain energy function $W = \frac{1}{2}C_{ijkl}\varepsilon_{ij}\varepsilon_{kl}$ then $[S_{ijkl}]$ and $[C_{ijkl}]$ are symmetric, further reducing this number to 21 [150]. This is the maximum number of elastic constants that a material can have. It is further decreased by consideration of specific symmetries within a material, which can be based on crystallographic symmetries or explicit elastic anisotropies. We will now examine the different elements that make up the compliance tensor†, commencing with consideration of an isotropic material.

Isotropic case

The elastic properties of an isotropic material will be direction-independent, and it is convenient to introduce a simpler notation, as shown in Table 3.1. If we consider a cube of material aligned with the coordinate axes (as shown in Figure 3.1), we can construct the normal strains by considering a normal force along each axis. For this we must introduce the Poisson effect, as shown in Figure 3.1(b), which describes the intuitive contraction of a material along directions perpendicular to the applied tension. As such, a uniaxial stress gives rise to triaxial strain, and using Equation 3.1 and we can write

$$\varepsilon_{ii} = \frac{1}{E}\left(\sigma_{ii} - \nu\sigma_{jj} - \nu\sigma_{kk}\right). \tag{3.4}$$

Due to isotropy, only one elastic modulus E and Poisson ratio ν are needed. If we do the same for shear components using Equation 3.2 the relation is simply‡

$$\varepsilon_{ij} = \frac{1}{2G}\sigma_{ij}.$$

For full isotropy there is no shear-type Poisson effect, and there is no influence on normal stress from shear. This reduces the compliance tensor to three independent components, $1/E$, $-\nu/E$ and $1/G$. It can be shown [151] that for an isotropic material the Young's modulus, Poisson ratio and shear modulus are related by $G = E/2(1+\nu)$,

*When considering infinitesimal displacement, the strain tensor can be shown to be $\varepsilon_{ij} = \frac{1}{2}\left(\frac{\partial u_i}{\partial x_j} + \frac{\partial u_j}{\partial x_i}\right)$ which clearly obeys $\varepsilon_{ij} = \varepsilon_{ji}$ [149].

†The algebra for the compliance tensor is a little neater than that of the stiffness tensor.

‡There is a subtlety with factors of two here: the γ used in Equation 3.2 does not strictly form a tensor component as it does not obey the relevant transformation rule due to factors of two. $\varepsilon_{ij} = \frac{1}{2}\gamma_{ij}$ is the proper tensor component, and that is what we use in the text here. See Ref. [151] for further details. Furthermore, we do not add a factor of two between tensor and contracted notations, e.g. $\varepsilon_{23} = \varepsilon_4$. As such the notation used in Table 3.1 is not strictly 'Voigt'.

Tensor	11	22	33	23, 32	13, 31	21, 12
Contracted	1	2	3	4	5	6
Engineering	xx	yy	zz	yz	xz	xy

Table 3.1 | Table of compact notation for the labelling of tensor elements. Contracted indices 1-3 and 4-6, refer to normal and shear components respectively.

meaning the isotropic compliance equation can be written neatly as

$$\varepsilon_{ij} = \frac{1+\nu}{E}\sigma_{ij} - \frac{\nu}{E}\delta_{ij}\sum_k \sigma_{kk}. \tag{3.5}$$

Using the notation in Table 3.1 the compliance tensor can be represented in pseudo-matrix form

$$\begin{Bmatrix} \varepsilon_1 \\ \varepsilon_2 \\ \varepsilon_3 \\ \varepsilon_4 \\ \varepsilon_5 \\ \varepsilon_6 \end{Bmatrix} = \frac{1}{E}\begin{bmatrix} 1 & -\nu & -\nu & 0 & 0 & 0 \\ & 1 & -\nu & 0 & 0 & 0 \\ & & 1 & 0 & 0 & 0 \\ & & & 1+\nu & 0 & 0 \\ & & \text{symm.} & & 1+\nu & 0 \\ & & & & & 1+\nu \end{bmatrix}\begin{Bmatrix} \sigma_1 \\ \sigma_2 \\ \sigma_3 \\ \sigma_4 \\ \sigma_5 \\ \sigma_6 \end{Bmatrix}. \tag{3.6}$$

This can be rewritten in terms of the two independent components $C_{11} = 1/E$ and $C_{12} = -\nu$. This case will be useful for general mechanical considerations of the apparatus, for which it is sufficient to treat materials as isotropic. To treat the anisotropy of FeSe the above description must be extended.

Anisotropic case

FeSe is a layered material, meaning its elastic properties are highly anisotropic and a distinction must be made between in- and out-of-plane constants. For the more general orthotropic case (complete anisotropy in all three directions) we must distinguish between the elastic modulus, shear modulus and Poisson's ratio along x, y and z. Thus the normal components of strain in Equation 3.4 become

$$\varepsilon_{ii} = \frac{\sigma_{ii}}{E_i} - \frac{\nu_{ij}\sigma_{jj}}{E_j} - \frac{\nu_{ik}\sigma_{kk}}{E_k},$$

where E_i is the elastic modulus along axis i, and ν_{ij} is the Poisson's ratio for a distortion along j with the force along i. Similarly the shear components become

$$\varepsilon_{ij} = \frac{\sigma_{ij}}{2G_{ij}}$$

where G_{ij} is the shear modulus in j on the plane with normal along i. For FeSe, which is $4/mmm$ tetragonal, the elastic properties will be symmetric about in-plane rotations of 90°. If the a and b axes are in the xy-plane then by symmetry

$$E_x = E_y, \quad \nu_{xy} = \nu_{yx}, \quad \nu_{xz} = \nu_{yz}, \quad \nu_{zy} = \nu_{zx}, \quad G_{xz} = G_{yz}.$$

The symmetry of the compliance tensor gives the relation $\nu_{xz}/E_x = \nu_{zx}/E_z$, and bringing all of this together, we can now write the constitutive equation

$$\begin{Bmatrix} \varepsilon_1 \\ \varepsilon_2 \\ \varepsilon_3 \\ \varepsilon_4 \\ \varepsilon_5 \\ \varepsilon_6 \end{Bmatrix} = \begin{bmatrix} \frac{1}{E_\parallel} & -\frac{\nu_\parallel}{E_\parallel} & -\frac{\nu_\perp}{E_\perp} & 0 & 0 & 0 \\ & \frac{1}{E_\parallel} & -\frac{\nu_\perp}{E_\perp} & 0 & 0 & 0 \\ & & \frac{1}{E_\perp} & 0 & 0 & 0 \\ & & & \frac{1}{2G_\perp} & 0 & 0 \\ & & \text{symm.} & & \frac{1}{2G_\perp} & 0 \\ & & & & & \frac{1}{2G_\parallel} \end{bmatrix} \begin{Bmatrix} \sigma_1 \\ \sigma_2 \\ \sigma_3 \\ \sigma_4 \\ \sigma_5 \\ \sigma_6 \end{Bmatrix}, \tag{3.7}$$

where to simplify notation we have used symbols $\parallel$ and $\perp$ to refer to in- and out-of-plane quantities respectively. In total, six independent elastic constants are needed to describe this scenario, and the above approach is instructive as it allows one to write the compliance in terms of real elastic properties. More generally, the independent stiffness tensor components are C_{11}, C_{33}, C_{12}, C_{13}, C_{44} and C_{66}, with symmetry imposing $C_{22} = C_{11}$, $C_{13} = C_{23}$, and $C_{44} = C_{55}$. It is worth noting that the often-derived case for transverse isotropy simply adds the additional constraint of $G_{xy} = E_x/(1 + \nu_{xy})$, i.e. $C_{66} = C_{11} - C_{12}$, reducing the number of independent components to five. From the components of the compliance tensor in Equation 3.7 one can easily construct more general forms for the in- and out-of-plane Poisson's ratios: $\nu_\parallel = -S_{12}/S_{11}$ and $\nu_\perp = -S_{13}/S_{33}$; and Young's moduli: $E_\parallel = 1/S_{11}$ and $E_\perp = 1/S_{33}$.

3.1.3 Elastic properties of FeSe

Having developed a framework for describing the elasticity of an anisotropic system, we can now discuss the elastic properties of FeSe. As already explained in Section 2.4.1,

FeSe is $P4/nmm$ tetragonal in its high-temperature phase and at $T_S \sim 90\,\mathrm{K}$ undergoes a structural transition, subsequently becoming $Cmma$ orthorhombic. Our direction conventions are shown in Figure 2.9 – the Fe-Se bond direction is parallel to the axes of the tetragonal unit cell. We now discuss the elastic properties of FeSe in the previous framework without concern about which mechanism drives the structural transition. Although in principle a structural transition should result in a loss of symmetry in the stiffness and compliance tensors, requiring nine independent components, one can accurately describe the system by treating the broken-symmetry phase as a small distortion from tetragonal. As such only the six stiffness components C_{11}, C_{33}, C_{12}, C_{13}, C_{44} and C_{66} (which can be written in terms of $E_\parallel$, $E_\perp$, $\nu_\parallel$, $\nu_\perp$, $G_\parallel$, $G_\perp$) are needed to describe FeSe, even at low temperatures. Although the C_{66} component is independent in this case, the difference of in-plane components $C^T = C_{11} - C_{12}$ is still an important quantity for a tetragonal material - commonly referred to as the tetragonal shear*. This is understood from the components of the constitutive equation under a transformation of in-plane coordinates by 45°. As shown in full in Appendix A, the difference of normal strains $\frac{1}{2}(\varepsilon_{xx} - \varepsilon_{yy})$ corresponds to a shear strain ε'_{xy} in the rotated frame, and as such C^T corresponds to $2C'_{66}$. One can view this as demonstrating that the two tetragonal-to-orthorhombic (T-to-O) symmetry breaking fields† are $\varepsilon_{xx} - \varepsilon_{yy}$ and ε_{xy}. These strains have a symmetry corresponding to the B_{1g} and B_{2g} irreducible representations of the $4/mmm$ point group [152], and can be denoted as such. This can be shown by decomposing the general strain pseudo-matrix into components which are symmetric with respect to C_4, and C_2 rotations

$$\begin{aligned}\begin{bmatrix}\varepsilon_{xx} & \varepsilon_{xy}\\ \varepsilon_{xy} & \varepsilon_{yy}\end{bmatrix} &= \frac{1}{2}\left(\varepsilon_{xx}+\varepsilon_{yy}\right)\begin{bmatrix}1 & 0\\ 0 & 1\end{bmatrix} + \frac{1}{2}\left(\varepsilon_{xx}-\varepsilon_{yy}\right)\begin{bmatrix}1 & 0\\ 0 & -1\end{bmatrix} + \varepsilon_{xy}\begin{bmatrix}0 & 1\\ 1 & 0\end{bmatrix}\\ &= \varepsilon_{A_{1g}}\begin{bmatrix}1 & 0\\ 0 & 1\end{bmatrix} + \varepsilon_{B_{1g}}\begin{bmatrix}1 & 0\\ 0 & -1\end{bmatrix} + \varepsilon_{B_{2g}}\begin{bmatrix}0 & 1\\ 1 & 0\end{bmatrix}.\end{aligned}$$

$$\varepsilon_{A_{1g}} = \frac{1}{2}\left(\varepsilon_{xx}+\varepsilon_{yy}\right), \quad \varepsilon_{B_{1g}} = \frac{1}{2}\left(\varepsilon_{xx}-\varepsilon_{yy}\right), \quad \varepsilon_{B_{2g}} = \varepsilon_{xy}. \tag{3.8}$$

The modifications due to $\varepsilon_{A_{1g}}$ are isotropic, whilst for $\varepsilon_{B_{1g}}$ and $\varepsilon_{B_{2g}}$ changes are anisotropic. The above language will be used throughout this thesis, and further information can be found in Ref.s [153] and [56]. The equivalence of $\varepsilon_{B_{1g}}$ and $\varepsilon_{B_{2g}}$ strains under a 45°

*The symbol most commonly used in literature is C' however this causes confusion with the dash used to denote the rotated coordinate frame in Appendix A.

†For x and y aligned with the in-plane directions of the tetragonal unit cell.

rotation highlights the importance of coordinate-system clarity when discussing these strains in FeSe. In general C^T will be a recurring parameter for directional measurements on $4/mmm$ tetragonal materials conducted under a 45° in-plane rotation of the unit cell. This applies to our experiment, in which we apply strain along the $[110]_T$ direction. Similarly Kuo et al. utilise this rotation to extract the m_{66} component of elastoresistance [52]. Also noteworthy is that the requirement of a positive strain energy, the criterion for crystal stability, introduces the constraint $C^T > 0$ for a tetragonal system.

Because a material's elastic constants dictate its dynamic behaviour, their extraction is possible from the sound velocity at which elastic waves propagate. These have the same symmetry as corresponding quantised vibrational modes, i.e. phonons, whose temperature-dependent dispersion describe a crystal's elastic response with temperature. The approach to a structural phase transition is characterised by a frequency decrease of one of these modes due to the 'softening' of particular elastic constants. In principle, these elastic constants should go to zero at a second-order structural phase transition and harden below it [5]. For a T-to-O structural phase transition, the spontaneous orthorhombic strain must either be $\varepsilon_{xx} - \varepsilon_{yy}$ or ε_{xy} meaning a softening in either $C_{11} - C_{12}$ or C_{66}. The observation of an ab-plane rotation of the orthorhombic unit cell by 45° degrees with respect to the tetragonal unit cell implies that the spontaneous strain is ε_{xy}, and thus due to a C_{66} instability. This motivates the tuning of the $\varepsilon_{xy} = \varepsilon_{B_{2g}}$ strain to couple directly to the orthorhombic distortion - as we will see in Section 3.3.4.

In Ref. [154] an ultrasound technique was used to measure sound velocities and thus determine the elastic constants and their temperature dependance in FeSe. They directly measured the sound velocity ($v = \sqrt{C/\rho}$) for C_{11}, C_{33}, C_{44}, C_{66} and C^* modes, where $C^* = \frac{1}{2}(C_{11} + C_{12}) + C_{66}$. Direct acquisition of data for the C_{13} and $C_{11} - C_{12}$ modes was not possible due to sample geometry and attenuation below 100 K respectively. They conclude that both C_{11} and $C_{11} - C_{12}$ soften at the transition, and both remain soft down to low temperature. Confusingly this work is cited by others to support the claim that the transition occurs in the expected C_{66} channel [92]. Details are lacking, but it is possible that the ultrasound measurements were conducted with propagating waves along different directions, one of which being along an axis at 45° to the tetragonal unit cell. Additionally, no attempt was made to detwin the crystal. Using Equations A.18 to A.20, and assuming that the measurements in Ref. [154] are referenced to the tetragonal unit cell, the in- and out-of-plane Poisson's ratios and Young's moduli can be calculated – these are shown in Table 3.2.

T	$E_{\parallel}$ (GPa)	$E_{\perp}$ (GPa)	$\nu_{\parallel}$	$\nu_{\perp}$
150 K	57.9	30.9	0.18	0.22
90 K	21.2	30.9	0.70	0.23
5 K	17.1	30.0	0.94	0.24

Table 3.2 | In- and out-of-plane Young's moduli and Poisson's ratios for FeSe calculated from the ultrasound measurements of Ref. [154]. The in-plane Young's modulus $E_{\parallel}$ undergoes significant softening due to the structural phase transition that occurs at ~ 90 K. Interpolation was required to obtain all tensor components at these three temperatures.

Two theoretical studies have calculated the elastic constants, both using density functional theory. The first, Ref. [155], calculates zero-temperature values of $E = 73$ GPa and $\nu = 0.179$. The apparently analogous calculation in Ref. [156] yielded $E = 134$ GPa and $\nu = 0.196$ without commenting on the apparent discrepancy. These studies do not determine E and ν using the direct relations derived in Appendix A, but rather by taking the arithmetic mean of theoretical maxima and minima of the bulk and shear moduli. These are therefore 'effective' values, averaged between anisotropic directions. The disparity between these studies indicates the need for additional experimental investigation.

Böhmer et al. [92] measured the relative change of the in-plane Young's modulus (along $[110]_T$*) using a three-point bending setup in a capacitance dilatometer. They observed significant softening on approach to the structural phase transition with an $\sim 82\,\%$ reduction with respect to room temperature. This is in qualitative agreement with the ultrasound measurements [154], and the Young's modulus below T_S also remains constant. As can be seen for the form of Young's modulus in the rotated frame, Equation A.25, if C_{66} is smaller than $\frac{C_{11}}{2} + \frac{C_{12}}{2} - \frac{C_{13}^2}{C_{33}}$ it dominates $E_{[110]_T}$. Based on evidence from hole- and electron-doped $BaFe_2As_2$ [157], as well as from the ultrasound measurements, this is found to be true. As such the decrease in $E_{[110]_T}$ represents a softening in C_{66}.

*Along the Fe-Fe bond direction, i.e. at 45° to the tetragonal unit cell directions. See Figure 2.9.

3.2 Apparatus for pressure application

3.2.1 Background

In Chapter 2 we motivated the investigation of FeSe under uniaxial pressure, and in Section 3.1.1 introduced the general importance of experiments on strongly correlated materials with this technique. We will now look at established apparatus for applying uniaxial pressure from a technical standpoint, subsequently motivating the need for a novel piezo-based approach. Control is a principal design challenge for pressure apparatus. For hydrostatic pressure, one needs to apply a controlled force such that the stress tensor is as close as possible to $[\sigma_{ij}] = -p\delta_{ij}$*. This is most commonly achieved using a diamond anvil cell (DAC) which does so by pressing two opposing, flattened diamonds onto a fluid pressure medium which surrounds the sample. Usually one of these diamonds is fixed, with the other on a sliding piston driven by a spring [158]. The DAC is however an inherently uniaxial device, and can thus be used as such. For uniaxial pressure one aims for just a single normal component of the stress tensor, and the DAC accomplishes this via a controlled force applied perpendicular to the ends of a sample. Because the surface area over which the force is applied can be smaller than for the gasket of hydrostatic apparatus, the forces can in turn be smaller, meaning materials such as hardened steel are often used instead of diamond.

There are several limitations to this method however. For high strain homogeneity, sample and anvil faces must both be smooth, flat and parallel on a scale below that of the compressive displacement (typically 1 µm). Achieving these requirements is extremely challenging due to the polishing precision required, and the often less-than-ideal shape and mechanical properties of samples. Even if they can be realised, frictional locking between the sample ends and the anvils provides a further contribution to strain inhomogeneity. This constraint opposes the sample's desire to expand due to its Poisson's ratio, thus giving rise to a non-trivial strain profile [159]. Such strain inhomogeneity can become problematic for sensitive measurements due to the broadening of transitions at higher pressures [160].

Tuneabililty is another severe restriction of most anvil-based apparatus for use at low temperatures, as the force must be applied at room temperature. Not only does this mean thermal cycling between discrete pressure steps, but also possible plastic deformation, because the yield strain of materials can be much lower at room temperature than low temperature. C. Pfleiderer et al. [161] developed a compact cell

*Provided the sample is shaped such that its edges are parallel to the principle stress directions.

for tuneable uniaxial pressure application, enabling in situ control at low temperatures. This was achieved via helium filled bellows, which require a complicated pressure-regulation system. A simpler and more direct approach to address the issues above is to mount samples directly onto a piezoelectric actuator. Such actuators, or 'stacks' utilise the inverse piezoelectric effect through which an applied voltage gives rise to a mechanical strain. This technique was encountered in Chapter 2 for its use in the determination of electron-driven nematicity in iron-based compounds [45, 91, 94]. However, direct on-stack sample mounting suffers from two major limitations. Provided the stiffness of the sample is sufficiently small compared to that of the stack then $\varepsilon_{\text{sample}} = \varepsilon_{\text{stack}}$, and the maximum strain a sample can experience is limited to that of the stacks. For lead zirconium titanate (PZT) at room temperature this is up to ~0.15 %. Secondly, piezoelectric stacks *increase* in length upon cooling by 0.1 % [162], which can strain samples beyond the range achievable by voltage application at low temperature, making tuning through zero strain unachievable.

Piezoelectric actuators

Since piezoelectric actuators constitute such an important component of the apparatus used in this thesis, it is worth describing their operation in more detail. As mentioned above, the piezoelectric effect describes a relationship between the electric field (E) and strain (ε) within a material. With these two quantities being first- and second-rank tensors respectively, this effect is quantified by a third-rank tensor – the piezoelectric modulus d_{ijk}. Formulating this gives

$$\varepsilon_{jk} = d_{ijk} E_i. \tag{3.9}$$

The most commonly used piezoelectric material is PZT. This has $4mm$ tetragonal symmetry meaning its piezoelectric modulus consists of only five non-zero components, three of which are independent: $d_{31} = d_{32}$; $d_{15} = d_{24}$ and d_{33}.* In order to lengthen the material along z (the poling direction), a field $E_3 = E_z$ is required. This will give rise to a positive strain along the field direction according to d_{33}, and a negative strain, as per Poisson's effect, perpendicular to the field direction given by d_{31}. For PZT 5H at room temperature $d_{33} = 593$ pm/V [163] which with a typical maximum field of 2.5 MV/m [164] corresponds to a maximum strain of ~ 0.15 %. Treating the actuator like a parallel plate capacitor with an electrode separation of 0.1 mm, this field

*Here only the first subscripted index has been contracted, and uses the same convention as in Table 3.1. As such $d_{13} \equiv d_{113} \equiv d_{xxy}$.

corresponds to a maximum applied voltage of 250 V. To achieve larger displacements, PZT can be stacked together to increase the poling direction length. Stacking is additionally advantageous as small electrode separations can be retained, meaning smaller voltages are required to obtain larger fields. Piezoelectric moduli generally decrease with temperature [165], resulting in a suppressed strain range upon cooling for a given field. This can be balanced by larger permissible maximum electric fields at low temperatures.

Control regimes

Some clarification is required at this point regarding the nomenclature of apparatus for applying pressure. So far we have used the term 'pressure' loosely, however there is an important difference between stress (that is applied force), or strain (applied displacement) as the controlled parameter. For the 'uniaxial' anvil-based apparatus already introduced, a spring with a much lower spring constant than the sample is used to apply a controlled force (which acts as a converter between displacement and force - as per Hooke's law). As such the stress is controlled, and because the force acts in only one direction, the stress is uniaxial. For direct attachment of a sample to a piezoelectric stack, the displacement is the tuning parameter and as such the controlled variable is strain, but this strain is not strictly uniaxial. This is due to Poisson's ratio, which as in Equation 3.7 gives a triaxial strain response to a uniaxial stress. Forcing the ends of a sample to move by a controlled displacement will give a controlled strain in one direction, corresponding to an uncontrolled uniaxial stress. This in turn gives uncontrolled strain in the other two directions. This is the regime of control of the apparatus we will describe in Section 3.2.2.

The difference between these two control regimes becomes particularly important for apparatus design, as displacement control is typically made challenging by differential thermal contraction, whereas spring-based force control is not. Furthermore, apparatus control should ideally be independent of the sample's elastic properties. In practice this is never true, but in certain limits it can be effectively achieved. True strain control is achieved in the limit of the rig being much stiffer than the sample $k_{\text{sample}} \ll k_{\text{rig}}$ – as discussed in more depth in Chapter 5. From a measurement standpoint, the distinction can also be important. For a material which exhibits a structural phase transition upon cooling, one will observe different results for controlled-stress and controlled-strain experiments. This is seen from the Landau theory developed in Section 2.1.2 in which stress is the conjugate field. If the applied displacement is fixed instead, the sample may break up into structural domains at the transition.

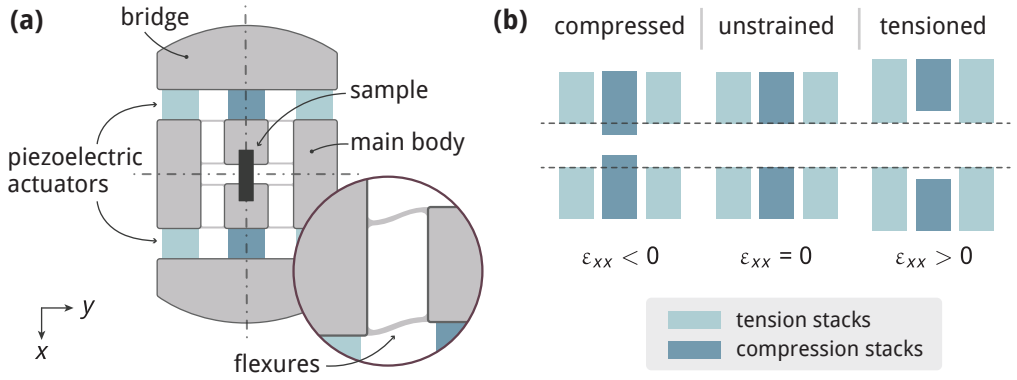

Figure 3.2 | (a) Basic design of the current generation of uniaxial-stress rig used for applying strain to FeSe. This differs from the design of Ref. [166] by symmetric placement of six piezoelectric actuators, and an un-recessed mounting area, enabling the use of platforms. Inset: flexures permit motion along x whilst restricting it in y and z. **(b)** Operation of the piezoelectric actuators to achieve compressive and tensile strains. Due to their ends being fixed by the bridge piece, a positive voltage to the centre actuators will compress the sample, and to the outer actuations will tension it.

3.2.2 Piezo-based uniaxial pressure cell

In Section 3.2.1 we introduced the simple method of direct sample-to-piezostack mounting to achieve in-situ strain tuneability at low temperatures, and discussed its limitations. In attaching just one end of the sample to the stack and keeping the other end fixed, i.e. making it freestanding, these limitations can be partially overcome. The sample strain will now be limited by a ratio of stack length to free sample length, $\varepsilon_{\text{sample}} = L_{\text{stack}}\varepsilon_{\text{stack}}/L_{\text{sample}}$, meaning large strains are attainable if $L_{\text{stack}} \gg L_{\text{sample}}$. The large contact area between sample and stack is also avoided, eliminating problematic differential thermal contraction. However, the ordinary thermal contraction of PZT is still a problem. With some ingenuity, this can also be alleviated. It is possible to use two sets of parallel stacks that work in opposition, such that upon the application of a positive voltage, one extends the sample and the other compresses it. Provided these stacks are made from the same material and are the same length, the effect of their thermal expansion will in principle cancel out.

This leads one to the design shown in Figure 3.2(a). This apparatus was developed in our group by Dr Clifford Hicks and former PhD students, and its design is described in

full in Ref. [166]. It is worth overviewing some key points regarding its construction and operation. It is comprised of three primary components, the main body, piezoelectric actuators, and bridge pieces. The main body comprises of a 'fixed' outer part and 'moving' inner parts, to which the sample is attached. Flexures between the fixed and moving parts permit motion along the longitudinal direction x while providing a high-spring-constant barrier for transverse and twisting motion – see the inset of Figure 3.2(a). In the devices we use, the flexures and rig body are machined out of the same single piece of material. As shown in panel (b), a positive voltage on the central stacks compresses the sample, whereas the same on the outer stacks tensions it. Conversely at low temperatures negative voltages can be used to reverse this operation. These can be used together, giving the relation between sample and stack strain shown in Equation 3.10:

$$\varepsilon_{xx,\ \text{sample}} = \frac{L_{\text{stack}}\left(\varepsilon_{xx,\ \text{stack 1}} - \varepsilon_{xx,\ \text{stack 2}}\right)}{L_{\text{sample}}}. \tag{3.10}$$

This equation also demonstrates that the thermal contraction of the stacks should not affect the sample strain.

The bridge rigidly fixes the outside ends of the stacks, and must be stiff to minimise loss of strain due to its deformation. The bonding strength of the stacks to the bridge is also crucial, as under strain the tension and compression stacks apply opposing forces, and bonding failure would limit the maximum applicable force. In this vein, differential thermal contraction between the stacks and the main body must be minimised. The thermal contraction of PZT transverse to the poling direction is 0.13 % between room temperature and 4 K [162], which is similar to that of titanium at 0.15 % [167] - making it the material of choice for the main body and bridge pieces. Furthermore titanium has a high elastic limit, which is useful for the flexures.

The ability to tension a free-standing sample requires each end to be rigidly attached to a plate, which constitutes an exchangeable interface between the apparatus and sample. Although use of epoxy for this means that sample faces need not be polished, severe asymmetry is introduced by having only one face fixed, in turn leading to strain inhomogeneity. This is overcome by the addition of a rigid cap foil, securing both the top and bottom surfaces of the sample. An unavoidable consequence of epoxy use for a free-standing sample is a the partial absorption of applied displacement due to epoxy deformation*, and strict strain control would require it to be infinitely rigid.

*This acts like a system of three springs in series: a stiff sample spring, and two soft epoxy springs giving $x_{\text{sample}} = x_{\text{stack}}/(1 + 2k_{\text{sample}}/k_{\text{epoxy}})$ – see Section 5.2.1.

This deformation does however allow for relief of stress concentration, and enables the deformation to be gently built up along the sample's length. Finite element analysis (FEA) for Sr_2RuO_4 samples yielded a sample strain of ~70 %–80 % of that expected from the stacks (Ref. [168] Supplementary Material). Ref. [166] reports strains of ±0.23 % on Sr_2RuO_4 samples cut using a wire saw and then polished; and with an average ratio w/L of ~ 4.4. This was later extended to compressions of −0.6 % [160]. In general, larger strains are achievable at lower temperatures due to the increase of yield strength upon cooling, however for the studies above samples broke below this limit due to stress concentration from rough edges. The sample mounting method described above will subsequently be referred to as the 'conventional' technique.

The device used in this thesis, shown in Figure 3.2, is a next-generation design which differs from that described in Ref. [166] in several ways. Firstly it is symmetric (from the sample's standpoint at least), with a set of three stacks on either side. Secondly a non-recessed surface allows for more versatile mounting options such as a platforms, whist maintaining the ability to use the conventional technique. Lastly capacitive sensing is used in place of a strain gauge for determination of the displacement. For this, two parallel plates are attached to each side of the central gap, allowing the stack displacement to be calculated from the change in capacitance via $C = \epsilon_0 A/d$. A more detailed schematic of this device is shown in Figure 3.3(b) and it will be referred to simply as the 'rig' henceforth.

3.3 Solid platforms

This was work conducted in collaboration with Dr Joonbum Park and was a significant developmental effort. The design of the final platforms, as well as establishment of anodisation oxidation technique was developed by Dr Park. My contribution focused on achieving the oxidation of titanium thermally, as well as developing a fabrication method for mounting, contacting, and measuring samples on solid titanium platforms. Later contributions were provided by Dr Alexander Steppke and Dr Hilary Noad, in particular for the direct measurement of platform strain. A manuscript explaining this work is in progress, but currently unpublished [169]. Initial development of these platforms occurred alongside a related concept utilising a sample gap to maximise achievable strains. The development of this 'gapped' platform and its associated rig will be the focus of Chapter 5.

3.3.1 Motivation

We have now introduced a method for applying a uniaxially controlled strain, but before we can apply this technique to FeSe, some challenges must be addressed. The first limitation of the conventional sample mounting method introduced in Section 3.2.2 is the requirement of millimetre-sized samples. High quality single crystal samples of novel materials are often not this large, and smaller samples can give higher quality, better homogeneity, and larger resistance signals. The challenge with FeSe, on the other hand, is not small crystal sizes but its mechanical properties (see Section 3.1.3). A low Young's modulus and elastic limit from weak van der Waals bonding between layers reduces shear stress applicable before plastic deformation. For fixed-fixed ends, the theoretical buckling limit of a column of length L, width w, thickness t and Young's modulus E is $F_{\text{buckle}} = \pi^2 E w t^3 / 3L^2$, provided $w > t$. However, the spring constant of such a bar also scales with Young's modulus

$$k = \frac{Ewt}{L}, \tag{3.11}$$

meaning the force required to achieve a given strain is $F = Ewt\varepsilon$. As such the buckling strain is independent of Young's modulus and width

$$\varepsilon_{xx,\ \text{buckle}} = \frac{\pi^2 t^2}{3L^2}. \tag{3.12}$$

In principle then the low E should not be a problem for straining a free-standing bar of FeSe. The weak layer bonding of FeSe does however give a low yield limit $G_\perp$ which makes samples very susceptible to shear strains. In practice we found it impossible to handle a free sample of FeSe without accidentally deforming it, and compressing a bent sample only causes it to bend further. The range of applicable tensions is anyway small due to fracturing of the sample. A new approach is needed.

We can tackle these challenges by supporting FeSe samples along their length. Although the direct sample-on-stack technique provides this support, as discussed in Section 3.2.2 its shortcomings were the motivation for the piezo-based uniaxial pressure cell in the first place. A simple solution is to attach the sample to an intermediate carrier, or 'platform', which can be mounted into our already developed cell. The cell then strains the platform, which in turn strains the sample. More specifically, the cell uniaxially stresses the platform by a controlled displacement, which biaxially stresses the sample, giving rise to a triaxial strain in the sample - as will be described in depth in Section 3.3.4. Not only does this enable soft materials such as FeSe to be measured, but also miniature samples shaped using a focused ion-beam.

3.3.2 Design and modelling

The first important consideration for designing a platform for use in the uniaxial pressure cell is its spring constant. As we discussed in Section 3.2.1, for strain to be a good control parameter we had the requirement that $k_{\text{sample}} \ll k_{\text{rig}}$.* With the addition of a platform, controlling strain requires that the platform follows the rig, and the sample follows the platform $k_{\text{sample}} \ll k_{\text{platform}} \ll k_{\text{rig}}$. Using Equation 3.11 the spring constant for a typical Sr_2RuO_4 sample ($L = 1\,\text{mm}$, $w = 200\,\mu\text{m}$, $t = 50\,\mu\text{m}$) is $\sim 2 \times 10^6\,\text{N/m}$. This gives an order-of-magnitude estimate for how low the platform's target spring constant should be kept. The platform must be large enough to handle and attach to the rig, therefore the easiest method for spring constant minimisation is a reduction of dimensions at the sample location. This reduction should occur smoothly in order to minimise strain concentration at abrupt corners. This leads one to the 'bow-tie' like geometry as shown in Figure 3.3(a). The low spring constant neck also creates a short region across which the majority of displacement is transmitted. This is important to achieve strains larger than $\delta_{\text{stacks}}/D_{\text{holes}}$, which is limited by the large distance between tapped holes on the rig $D_{\text{holes}} = 11\,\text{mm}$, as shown in 3.3(a).

For material choice, we must again think about differential thermal contraction. The obvious way to minimise this is to match the platform material to the rig's main body, i.e. titanium. This has a relatively low Young's modulus of $\sim 103\,\text{GPa}$ [170], thus helping reduce the platform's spring constant. The rig's main body is constructed out of commercial pure (i.e. Grade-2) titanium and, as such, is our platform material of choice. The thermal expansion coefficient of titanium is small ($\Delta L/L = 0.151\,\%$ between RT and 4 K [167]), therefore tensioning most samples upon cooling.

For consideration of the platform thickness, our constraint for a small spring constant is balanced by our need for a high buckling strain. If the neck is much softer than the two outer parts, then the spring constant of the whole platform is approximately given by that of the neck. Further approximating it to be a bar we can use Equation 3.11, and setting central platform dimensions of $w = 500\,\mu\text{m}$, $L = 2\,\text{mm}$ (sufficient for most samples) gives the limit $t \lesssim 300\,\mu\text{m}$ for $k < 1 \times 10^7\,\text{N/m}$. Because the width does not appear in Equation 3.12 for the buckling strain, it needs to just be large enough to accommodate samples.

The design of the platform is shown in Figure 3.3(a), with important dimensions highlighted. It is 200 µm thick, and at its neck 500 µm wide. The low spring constant of the neck makes the platform susceptible to undesirable torque whilst screwing it

*Here we are referring to a force and displacement in the x-axis; $k = -F_x/\Delta_x$ with the coordinates as in Figure 3.2(a).

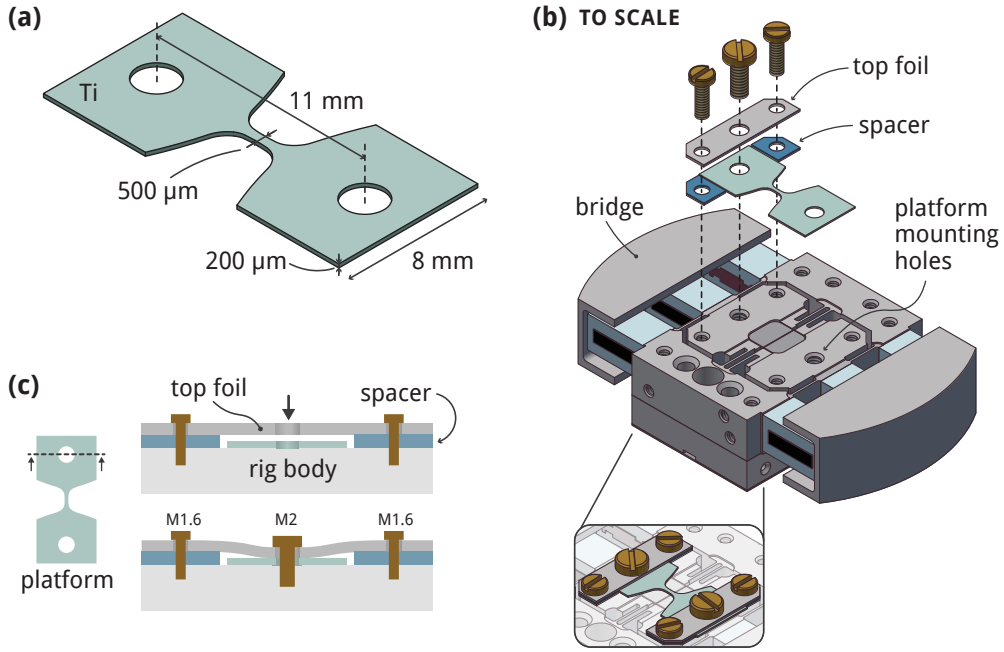

Figure 3.3 | (a) Platform design with bowtie-like geometry. A sample placed in the centre experiences a strain set by the length of the short and narrow, low-spring-constant neck. **(b)** Attachment of the platform to a new-generation uniaxial stress cell. Direct mounting is possible via the two tapped holes on the flat top surface. **(c)** Method for rigidly attaching the platform to the rig whilst minimising the amount of torque on the platform centre. A titanium top foil is first clamped either side of the platform, raised by spacers which are slightly thicker than the platform. Torque originating from the central screw is resisted and absorbed by the top foil, minimising the amount transferred to the platform and thus sample.

in place. To minimise this, a bending top foil system was conceived – see Figure 3.3(c). This transfers torque to the top foil which, being clamped at either end, is able to provide resistance and greatly reduce the torque applied to the platform. The brass screws used to secure the platform contract more than the titanium spacers and top foils, thus giving tighter clamping upon cooling. Because the platform geometry cannot be approximated by a simple bar it is necessary to conduct FEA to quantify its mechanical properties. This analysis was independently conducted, but based on that first conducted by Dr Park.

The elastic properties of pure Ti were used for simulations* with top and bottom surfaces constrained to move in the xy-plane. As shown in Figure 3.4(a), a ring constraint on the top surface was used to simulate the screw head, and a square constraint on the bottom for the contact between the platform and rig. A 0.5 N load was applied both axially to a hole on one side, and also perpendicular to the surface of the top ring. This was to simulate the force applied from the screws on the inside of the hole, and that from the clamping of the screw head, although in reality the latter will probably dominate. The results are shown in Figure 3.4(a) for both ε_{xx} and ε_{yy}. Cuts for both of these taken longitudinally and transversely from the platform centre are shown in Figure 3.4(b). The variation along cut 1 is 7 % and 11 % for ε_{xx} and ε_{yy} respectively, and 1 % and 3 % for cut 2. This is a measure of the strain inhomogeneity that a 1 mm sample will experience. On average along cut 1, the ratio $\nu_{\text{eff}} = -\varepsilon_{yy}/\varepsilon_{xx} = 0.52$, which is larger than the Poisson's ratio of 0.36 used for the material properties in the simulation. This is due to the non-trivial geometry of the platform. A crucial parameter for estimating the strain applied to the sample is the 'effective strained length'. It is defined by

$$L_{\text{eff}} = \delta x_{\text{FEA}}/\varepsilon_{xx,\text{FEA}}, \tag{3.13}$$

where δ_{xx} is the displacement between the holes, and $\varepsilon_{xx,\text{FEA}}$ the strain at the platform centre – both determined by FEA. Assuming the sample is rigidly attached to the platforms and follows its deformation, the strain in the sample will be given by $\varepsilon_{xx} = \delta_{\text{stacks}}/L_{\text{eff}}$. This corresponds to a strain reduction factor of $L_{\text{eff}}/L_{\text{sample}}$ with respect to a free standing sample.

From the FEA simulation in Figure 3.4, the effective strained length, as defined in Equation 3.13, is

$$L_{\text{eff}} = 3.46\,\text{mm}. \tag{3.14}$$

*From the Autodesk Inventor materials library: $E = 102.8\,\text{GPa}$, $G = 44.0\,\text{GPa}$ and $\nu = 0.36$.

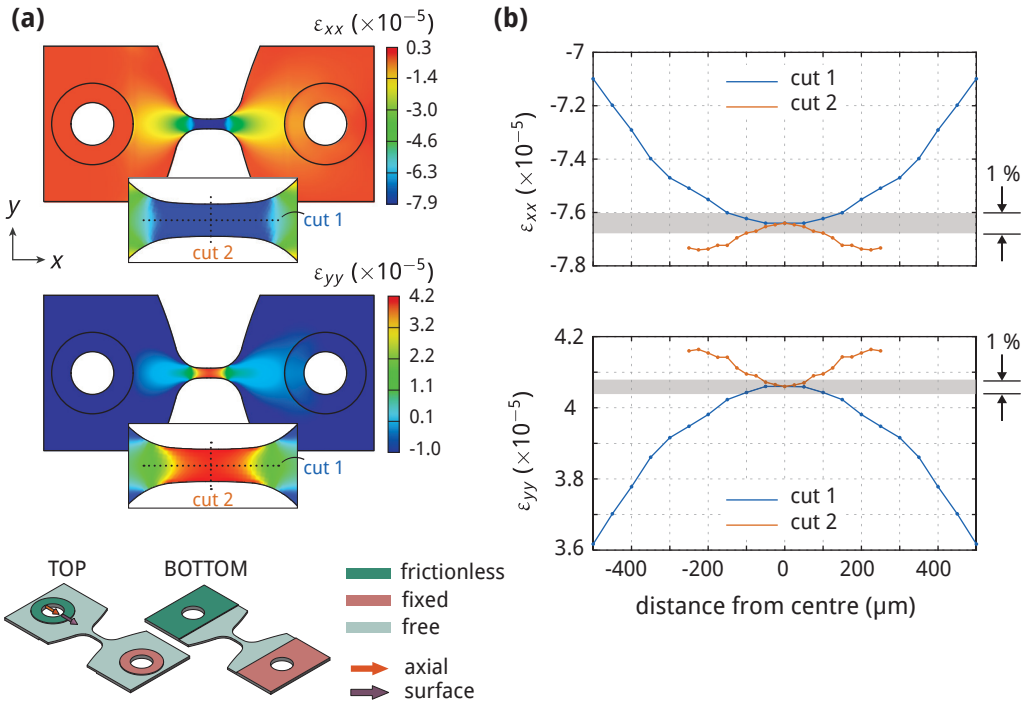

Figure 3.4 | (a) Finite element analysis result for ε_{xx} (top), and middle for ε_{yy} (middle). Bottom: overview of simulation constraints and loads. The top and bottom constraints simulate contact with the screw head and rig respectively. 0.5 N was applied both axially and as a surface force for a total load of 1 N. **(b)** Results of the simulation in panel (a) along a longitudinal and transverse cut centred on the platform middle. This gives a measure of the strain inhomogeneity at the location of a sample. A band indicating 1 % variation from the centre value is shown in grey.

Changes in simulation constraints in general did not give changes larger than 5 % in this quantity. Because the effective strained length is calculated from ε_{xx} at the platform centre, which is higher than the average across the neck, L_{eff} is an lower bound. The simulation also allows for an estimation of the spring constant of the platform. Treating the whole platform as a spring, $k_{\text{platform}} = -F_{\text{FEA}}/\delta x_{\text{FEA}} \sim 3.5 \times 10^6$ N/m, whilst considering just the central bar $k_{\text{platform}} = Ewt/L_{\text{eff}} \sim 3.0 \times 10^6$ N/m. We can compare this to the typical spring constant of an FeSe sample at room temperature ($L = 1$ mm, $w = 250$ μm, $t = 25$ μm, $E \sim 75$ GPa) which is $k_{\text{sample}} \sim 4 \times 10^5$ N/m - i.e. an order of magnitude smaller than k_{platform}. Using Equation 3.12 for the central bar defined by L_{eff}, the buckling strain is $\varepsilon_{xx,\,\text{buckle}} \sim 1.1$ %, imposing a limiting maximum sample strain of the same amount. In reality the deformation of the rig

	Temperature	Duration	Oxide thickness	Av. resistance
1	800 °C	5 hrs	~13 µm	18.0 GΩ[1]
2	700 °C	4 hrs	~1.6 µm	4.0 GΩ[2]
3	675 °C	4 hrs	~0.3 µm–1 µm	18.0 kΩ[3]

Table 3.3 | Table summarising the results from the thermal oxidation investigation. For Test 1, the oxide was thick enough that it flaked away and thickness determination was possible optically; for the others an SEM was used. Superscripts indicate the gold deposition method. (1) 5 nm of Ti was evaporated followed by 150 nm of Au; (2) 150 nm of Au directly sputtered; (3) as in method one, but with the gold sputtered rather than evaporated. The thinnest oxide layer (3) appears not to be thick enough for good insulation.

due to the presence of the platform may result in a smaller platform strain per stack displacement than expected from this analysis. This is characterised by a unitless factor a (for FEA $a = 1$, in practice $a < 1$) in the conversion from displacement to strain, $\varepsilon_{xx} = a\delta_{\text{stacks}}/L_{\text{eff}}$, which is a measure of the ideality of the setup. To determine the sample strain the factor L_{eff}/a must therefore be precisely known; its direct measurement is the topic of Section 3.3.6.

Titanium is not the only possible platform material. Dr Park conducted measurements on microstructured $CeAuSb_2$ under strain using quartz platforms [169]. Quartz has a lower Young's modulus than titanium, however is much more brittle making handling and clamping more challenging. It also benefits from being electrically insulating and optically smooth, factors advantageous for utilising a focused ion beam to structure miniature samples.

3.3.3 Fabrication

As described in Ref. [169], platforms were fabricated by means of laser cutting. Although having suitable mechanical properties and being easily machinable, a metallic platform is problematic due to its electrical properties. In order to conduct resistivity measurements, samples must be electrically isolated. It might seem that the epoxy layer needed for sample-to-platform adhesion is sufficient for this, but thin targeted bond lines and titanium's roughness make electrical shorts likely. Furthermore, microstructured samples require directly evaporated leads due to their size. We must therefore explore methods to electrically insulate the platform.

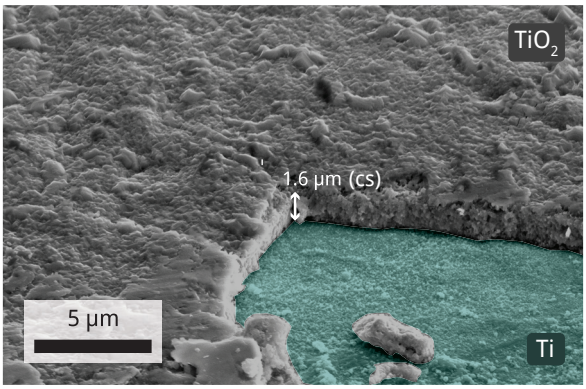

Figure 3.5 | Scanning electron microscopy image of a thermally grown oxide layer on a titanium (Ti) platform. Bare Ti is shown in green, and the oxide in grey with a thickness of $\sim 1.6\,\mu m$. Oxidation was conducted in air at 700 °C for 4 hours - i.e. Test 2 in Table 3.3. As determined from the cross-sectional (cs) scale, the roughness is on the order of hundreds of nanometres.

One approach is through oxidation - a well-established technique for minimising the effect of corrosion on titanium. Oxidation in general is just a chemical process which involves a loss of electrons, oxygen being particularly effective at this due to its electron affinity. As titanium has an available oxidation state of +4, it will readily form TiO_2. Oxygen is first adsorbed onto the titanium surface, oxidised regions will then nucleate, and grow laterally [171]. Once a complete compact oxide scale has formed, further oxidation is inhibited, making the process self-regulating. By providing additional energy to the oxygen, it is possible to overcome this self-regulation. This can be achieved either thermally or electrically, as we will now discuss.

Thermal oxidation

Thermally energised oxygen facilitates thick oxide layer growth, which can reach hundreds of microns when heated to 1000 °C for half an hour in air [172]. We investigated the electrical insulation of thermally grown oxide layers on titanium platforms. Platforms first underwent acetone and isopropyl alcohol ultrasonic bath cleaning steps. Heat was then applied in an atmospheric air environment using a tube furnace. Platforms were inserted with the furnace at the set temperature, and then removed after letting it cool naturally (this was for convenience and its effect was not investigated). For electrical measurement of the extent of insulation, gold tracks were deposited and the resistance measured between the outside of the oxide and titanium

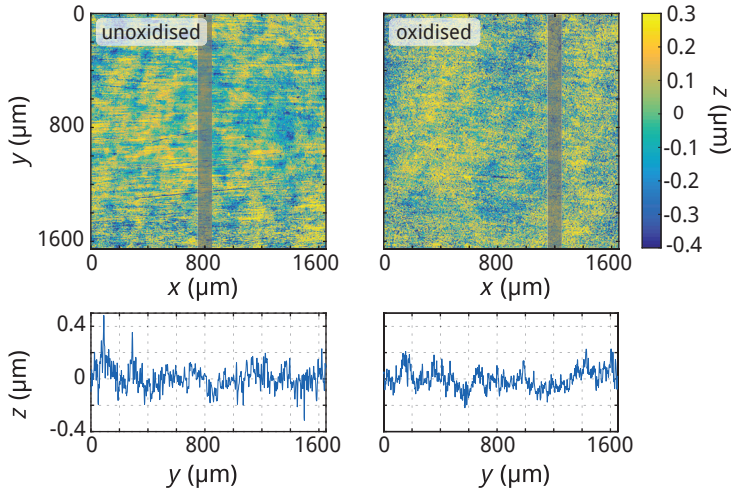

Figure 3.6 | Map of surface height across an area of 1.6 mm × 1.6 mm obtained via optical profilometry for both unoxidised and anodic oxidised titanium. Taking the root mean squared height S_q as a proxy for roughness, $S_q = 170\,\text{nm}$ and $S_q = 210\,\text{nm}$ for unoxidised and oxidised surfaces respectively. The similarity of S_q's, and slices averaged over a width of 100 μm for both cases show that oxidation has only a subtle effect on roughness as seen in the coloured surface plots.

core beneath. The results of this investigation are shown in Table 3.3. A scanning electron micrograph of oxide formation is shown in Figure 3.5 with a thickness of 1.6 μm.

Anodic oxidation

Anodic oxidation is an electrolytic passivation process through which oxygen ions are accelerated towards an anode. Using a platform as this anode, mass transport through the oxide barrier is possible, enabling growth of a thick oxide layer. To this end Dr Park constructed a small electrolytic cell, using a solution of trisodium phosphate and water (10 g/L), and by applying 210 V a ~ 1 GΩ sheet resistance oxide layer was formed after 10 minutes. Due to its time efficiency, this method was utilised for the oxidation of platforms used in the measurements of FeSe presented in this thesis. The surface roughness is an important parameter when targeting thin, uniform epoxy bond lines. We consequently quantified this roughness for unoxidised and oxidised platforms, as shown in Figure 3.6. The effect of oxidation on the surface topography is subtle, increasing its uniformity without substantially increasing the magnitude of roughness.

3.3.4 FeSe on a platform

We now examine the coupled mechanical system of a sample mounted on a platform. Let us start by considering just the platform, indicated by subscript p and with coordinates x and y which always correspond to the longitudinal and transverse directions respectively. We apply a controlled uniaxial displacement δ_{stacks} to the platform's ends. Assuming all of this goes into the platform, then as described in Section 3.3.2 strains of $\varepsilon_{xx,p} \sim L_{\text{eff}}/\delta_{\text{stacks}}$ and $\varepsilon_{yy,p} \sim -\nu_{\text{eff}}\varepsilon_{xx,p}$ are formed in the platform neck. For simplicity we neglect any spatial variation in $\varepsilon_{xx,p}$ and $\varepsilon_{yy,p}$, and because $\varepsilon_{yy,p}$ is proportional to $\varepsilon_{xx,p}$, we take $\varepsilon_{xx,p}$ as the control parameter. Here we have also assumed that $\varepsilon_{xx,p}$ and $\varepsilon_{yy,p}$ are position independent, and as such $\varepsilon_{xx,p}$ represents our single controlled parameter. Because $|\varepsilon_{xx,p}| \neq |\varepsilon_{yy,p}|$ and $\varepsilon_{xy,p}$ is in principle zero, the platform always applies symmetric and asymmetric strain components which we labelled $\varepsilon_{A_{1g}}$ and $\varepsilon_{B_{1g}}$ in Equation 3.8; these are

$$\begin{aligned} \varepsilon_{A_{1g},p} &= \frac{1}{2}(\varepsilon_{xx} + \varepsilon_{yy}) = \frac{1}{2}(1 - \nu_{\text{eff}})\varepsilon_{xx,p}, \\ \varepsilon_{B_{1g},p} &= \frac{1}{2}(\varepsilon_{xx} - \varepsilon_{yy}) = \frac{1}{2}(1 + \nu_{\text{eff}})\varepsilon_{xx,p}. \end{aligned} \tag{3.15}$$

Now let us consider a generic tetragonal sample (no subscript), with a coordinate system always aligned with the tetragonal unit cell. We assume that the platform strain is not altered by the sample's presence, and therefore that the sample is completely compliant (i.e. the epoxy and sample both have zero thickness). The latter means that the strain in the sample will simply be given by that of the platform; we will later consider the extent to which this is true in practice. We first describe '$\langle 100\rangle_T$ strain', where the tetragonal unit cell is aligned with the sample edges and coordinate system of the platform, as shown in Figure 3.7(a). If the sample follows the platform then the sample strain is $\varepsilon_{xx} = \varepsilon_{xx,p}$ and $\varepsilon_{yy} = \varepsilon_{yy,p} = -\nu_{\text{eff}}\varepsilon_{xx,p}$. The coordinate system of the tetragonal unit cell is the same as that of the platform, and so the sample experiences $\varepsilon_{A_{1g}}$and $\varepsilon_{B_{1g}}$, as defined in Equation 3.15. The applied stress will be biaxial, with non-zero components σ_{xx} and σ_{yy} that, based on Equation 3.7, take the values

$$\begin{aligned} \sigma_{xx} &= \frac{1}{S_{11}^2 - S_{12}^2}\left(S_{11} + \nu_{\text{eff}}S_{12}\right)\varepsilon_{xx,p} = \frac{E_{\parallel}}{1-\nu_{\parallel}^2}\left(1 - \nu_{\parallel}\nu_{\text{eff}}\right)\varepsilon_{xx,p}, \\ \sigma_{yy} &= \frac{1}{S_{12}^2 - S_{12}^2}\left(-S_{12} - \nu_{\text{eff}}S_{11}\right)\varepsilon_{xx,p} = \frac{E_{\parallel}}{1-\nu_{\parallel}^2}\left(\nu_{\parallel} - \nu_{\text{eff}}\right)\varepsilon_{xx,p}, \end{aligned} \tag{3.16}$$

such that the strain in the sample is constrained to be that of the platform. Important

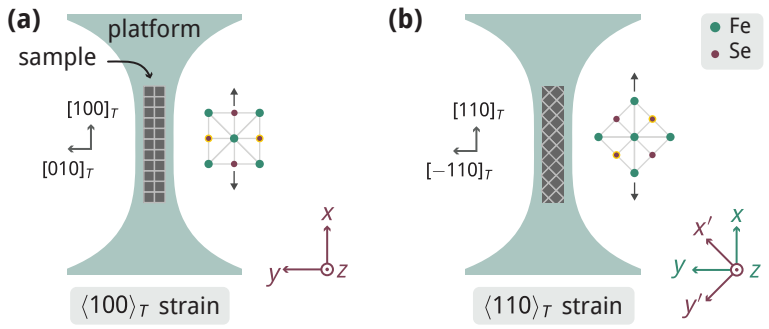

Figure 3.7 | (a) Tetragonal sample with edges aligned with the tetragonal unit cell. The platform gives rise to strain along the $\langle 100\rangle_T$ directions. The unprimed coordinates are aligned with the platform and thus tetragonal unit cell. For FeSe the strain is applied along the Fe-Se bond direction. **(b)** Tetragonal unit cell rotated in-plane by 45° with respect to the sample edges (and thus coordinate system of the platform). This corresponds to strain along the $\langle 110\rangle_T$ directions. The primed coordinates of the sample are aligned with the tetragonal unit cell. Now the strain is applied along the Fe-Fe bond direction for FeSe.

to note is that these equations contain a mixture of Poisson's ratios for the sample $\nu_{\parallel}$ (in-plane) and platform ν_{eff}. The z-axis is unconstrained, so $\sigma_{zz} = 0$ and the strain is given by

$$\varepsilon_{zz} = \frac{-\nu_{\perp}}{E_{\perp}}\left(\sigma_{xx} + \sigma_{yy}\right) = -\beta\nu_{\perp}\varepsilon_{xx,p}, \tag{3.17}$$

where

$$\beta = \frac{E_{\parallel}}{E_{\perp}}\frac{1-\nu_{\text{eff}}}{1-\nu_{\parallel}}.$$

Equation 3.17 differs from the expected form $\varepsilon_{zz} = -\nu_{\perp}\varepsilon_{xx}$ due to the fact the crystal is not freestanding, but instead constrained by the platform within the plane. A similar observation was made by Kuo et al. in Ref. [52]. Note that the renormalised Poisson's ratio $\nu^{*}_{\perp} = \beta\nu_{\perp}$ can also be larger than one.

We now consider '$\langle 110\rangle_T$ strain' where the tetragonal unit cell is rotated in-plane by 45° with respect to the coordinates of the platform and thus edges of the sample, as shown in Figure 3.7(b). We use a prime to indicate the coordinates and tetragonal

unit cell of the sample*. Using Equation A.5 to transform the coordinates of the strain tensor, the strain in the sample along the tetragonal unit cell is†

$$\varepsilon_{xx'} = \varepsilon_{yy'} = \frac{1}{2}\left(\varepsilon_{xx} + \varepsilon_{yy}\right) = \frac{1}{2}\left(1 - \nu_{\text{eff}}\right)\varepsilon_{xx,p}. \tag{3.18}$$

There is now a shear component

$$\varepsilon_{xy'} = \frac{1}{2}\left(\varepsilon_{xx} - \varepsilon_{yy}\right) = \frac{1}{2}\left(1 + \nu_{\text{eff}}\right)\varepsilon_{xx,p}. \tag{3.19}$$

Because $\nu_{\text{eff}} > 0$, $\varepsilon_{xy'}$, is larger than $\varepsilon_{xx'}$ or $\varepsilon_{yy'}$. We also observe that Equation 3.18 and 3.19 are the same as Equations 3.15; that is to say, $\varepsilon_{xx'} = \varepsilon_{yy'} = \varepsilon_{A'_{1g}} = \varepsilon_{A_{1g},p}$ and $\varepsilon_{xy'} = \varepsilon_{B'_{2g}} = \varepsilon_{B_{1g},p}$. For a nematic material this is important as $\varepsilon_{B'_{2g}}$ couples to orthorhombicity/nematicity, whereas $\varepsilon_{A'_{1g}}$ couples to the bulk [173]. Equations 3.16 for the stress in the sample due to the platform strain $\varepsilon_{xx,p}$ become

$$\begin{aligned}
\sigma_{xx'} = \sigma_{yy'} &= \frac{1}{2}\left(\sigma_{xx} + \sigma_{yy}\right) = \frac{(1 - \nu_{\text{eff}})}{2(S_{11} + S_{12})}\varepsilon_{xx,p} = \frac{E_{\parallel}(1 - \nu_{\text{eff}})}{2(1 - \nu_{\parallel})}\varepsilon_{xx,p}, \\
\sigma_{xy'} &= \frac{1}{2}\left(\sigma_{xx} - \sigma_{yy}\right) = \frac{(1 + \nu_{\text{eff}})}{4S_{66}}\varepsilon_{xx,p} = \frac{G_{\parallel}(1 + \nu_{\text{eff}})}{2}\varepsilon_{xx,p}.
\end{aligned} \tag{3.20}$$

We unsurprisingly see that σ_{xy} is proportional to $1/S_{66} = C_{66}$, i.e. the softening component whose instability gives the structural phase transition in FeSe. Because the rotation is in the xy-plane, strain along z is unaffected $\varepsilon_{zz} = \varepsilon_{zz'}$.

So far we have assumed complete compliance of the sample, as if it and the underlying epoxy both have zero thickness. In practice this clearly cannot be true, and a nonzero epoxy thickness allows some decoupling of the sample and platform strains. In the limit that the epoxy elastic moduli are much smaller than those of the sample, and neglecting strain variation across the sample thickness, we may define a load transfer length, which is the length scale over which strain in the platform is transferred to the sample. As shown in full in Ref. [166], for a sample bonded only on its bottom face, the load transfer length is

$$\lambda = \sqrt{\frac{Etd}{C_{66,e}}}, \tag{3.21}$$

*Strictly speaking we should then add primes to the stiffness and compliance tensor components. In the unrotated case the unprimed constants corresponded to coordinates aligned with the tetragonal unit cell. We will follow this convention in the rotated case.

†Here xx' refers to both subscripts being in the primed coordinates, i.e. equivalent to $(xx)'$ or $x'x'$.

where E and t are the Young's modulus and thickness of the sample, and d and $C_{66,e}$ are the thickness and shear elastic constant of the epoxy. The derivation of Equation 3.21 assumes that the sample thickness is sufficiently smaller than its width, and neglects any shears within the sample. Use of E assumes that the sample is free to deform along y and z according to its Poisson's ratios. Two regimes can be defined from λ. For the longitudinal strain, we assume in both cases that L is large with respect to λ such that the strain is completely transmitted along x and $\varepsilon_{xx} = \varepsilon_{xx,p}$. This is as per our assumption in the formalism above. For the width, if $w \ll 2\lambda$, then the transverse strain of the sample strain is decoupled from that of the platform, and we can assume that the transverse strain is given by the sample's Poisson ratio $\varepsilon_{yy} = -\nu_{\parallel}\varepsilon_{xx} = -\nu_{\parallel}\varepsilon_{xx,p}$. In this case ν_{eff} must be replaced with $\nu_{\parallel}$ in Equations 3.16 to 3.20. The difference in Poisson's ratios in Equation 3.16 vanishes, giving $\sigma_{yy} = 0$ as expected since the constraint in y has been lifted. If $w \gtrsim 4\lambda$ then the sample and platform transverse strains are strongly coupled, and $\varepsilon_{yy} = \varepsilon_{yy,p}$ as we assumed before. Ensuring the sample and epoxy dimensions give rise to one of these regimes is a necessary consideration for sample preparation. For standard unfilled epoxy Stycast 1266, at room temperature $E_e \sim 1.6\,\text{GPa}$ [174], assuming it is isotropic $C_{66,e} = E_e/2(1+\nu)$ and $\nu \sim 0.3$ then $C_{66,e} \sim 0.6\,\text{GPa}$. If FeSe has a room temperature Young's modulus of $E \sim 75\,\text{GPa}$ [155], and we take an epoxy thickness of $d \sim 10\,\mu\text{m}$ and a sample thickness of twice that $t \sim 20\,\mu\text{m}$, then the load transmission length $\lambda_{\text{RT}} \sim 160\,\mu\text{m}$. At low temperatures ($T < 80\,\text{K}$) the epoxy hardens $C_{66,e} \sim 1.7\,\text{GPa}$ and the sample softens $E_{\text{LT}} \sim 0.2E_{\text{RT}} \sim 15\,\text{GPa}$ [92] giving $\lambda_{\text{LT}} \sim 40\,\mu\text{m}$. Because we do not aim to microstructure our samples, we target the second regime where $w \sim 4\lambda$ which for low temperatures corresponds to sample widths equal to, or greater than $w \sim 160\,\mu\text{m}$. The epoxy also gives us the ability to increase the uniformity of in-plane strain throughout the sample thickness. This can be achieved via epoxy ramps which secure the sides of the sample (as shown in Figure 3.9(h)). A consequence of this is that σ_{zz} is not strictly zero near the sample edges, but because our control concerns in-plane strain, this has no detrimental effect.

Alteration of sample strain through the tuning of δ_{stacks} will normally be conducted at constant temperature, but upon cooling differential thermal contraction is an additional parasitic source of strain. Taking two materials A and B, and assuming A follows B, the strain induced by differential thermal contraction will be $\varepsilon_A(T) \approx \Gamma_B(T) - \Gamma_A(T)$ (as derived in more detail in Section 5.2.4). Here $\Gamma(T) = \Delta L(T)/L_0 = (L(T) - L_0)/L_0$, is a quantity provided in engineering tables, and the approximation comes from $\Gamma_i(T) \ll 1$. The fractional length change with temperature has been

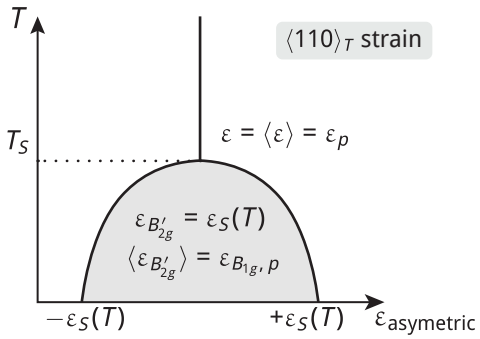

Figure 3.8 | Schematic showing the regimes of average and local control for a $\langle 110\rangle_T$ sample. For $T < T_S$ and $|\varepsilon_{xy',p}| < |\varepsilon_s|$, domain formation allows the local relaxation of $\varepsilon_{B_{2g}}$strain meaning there is a difference between the strain locally and that applied by the platform.

measured for both FeSe [89] and Ti [175], allowing the induced differential thermal strain to be calculated. FeSe contracts slightly more than titanium, resulting in a tensioning of the sample along both x and y upon cooling. For a twinned sample this saturates at its maximum value of 0.039 % below ~80 K.

So far the treatment has been applicable to any $4/mmm$ tetragonal material, but we must discuss the complication of the tetragonal-to-orthorhombic structural phase transition that occurs at ~ 90 K in FeSe. For an unstressed FeSe crystal below this temperature, a spontaneous shear strain develops, $\varepsilon_s(T)$, which we refer to as the 'structural strain'. A consequence of this shear strain is a rotation by 45° of the orthorhombic unit cell with respect to the tetragonal one - so we must take care with coordinates. In the coordinate system of the tetragonal unit cell, the spontaneous shear strain has B_{2g} symmetry, and is given by equal and opposite strains along the orthorhombic unit cell directions i.e.

$$\varepsilon_{B'_{2g}} = \varepsilon_S(T), \quad \varepsilon_{A'_{1g}} = 0. \tag{3.22}$$

Or $\quad \varepsilon_{xy'} = \varepsilon_s(T), \quad \varepsilon_{xx} = \pm\varepsilon_s(T), \quad \varepsilon_{yy} = \mp\varepsilon_s(T),$

where the coordinates are as in Figure 3.7(b) and for completeness both the symmetric/asymmetric (boxed) and x,y (unboxed) notation is used. ε_S can equally be defined via the orthorhombic distortion $\delta = (a_O - b_O)/(a_O + b_O)$. As discussed in Section 2.4.1, this transition is accompanied by the formation of micron-sized domains [176, 177], which have either a positive or negative strain as in Equation 3.22.

These domains become particularly important in our setup, and a subtlety arises when applying $\langle 110 \rangle_T$ strain, which we will now discuss. In this case the sample experiences $\varepsilon_{A'_{1g}}$ and $\varepsilon_{B'_{2g}}$ strains due to the platform. The asymmetric $\varepsilon_{B'_{2g}}$ strain is in the same symmetry channel as the spontaneous distortion and can therefore be relaxed locally due to the presence of domains and the finite epoxy thickness between the sample and platform. As such, it is necessary to make the distinction between *average* and *local* strain. $\varepsilon_{B'_{2g}}$ strain is locked to that of the platform over length scales comparable to the load transfer length: we refer to this as the average strain. However on shorter length scales we do not control $\varepsilon_{B'_{2g}}$, which is fixed by the structural instability at $\pm\varepsilon_S$; this is the local strain. The $\varepsilon_{A'_{1g}}$ component of strain acts isotropically and hence cannot be relaxed through domain repopulation, therefore the local sample strain is

$$\varepsilon_{B'_{2g}} = \varepsilon_S(T), \quad \varepsilon_{A'_{1g}} = \varepsilon_{A_{1g},p}. \tag{3.23}$$

Or $\Big|$ $\varepsilon_{xy'} = \varepsilon_s(T), \quad \varepsilon_{xx} = \varepsilon_{A_{1g}} \pm \varepsilon_s(T), \quad \varepsilon_{yy} = \varepsilon_{A_{1g}} \mp \varepsilon_s(T),$

and the *average* applied strain is

$$\langle \varepsilon_{B'_{2g}} \rangle = \langle \varepsilon_{B_{1g}} \rangle = \varepsilon_{B_{1g},p}, \quad \langle \varepsilon_{A_{1g}} \rangle = \varepsilon_{A_{1g},p}. \tag{3.24}$$

Or $\Big|$ $\langle \varepsilon_{xy'} \rangle = \varepsilon_{B_{1g},p}, \quad \langle \varepsilon_{xx} \rangle = \varepsilon_{A_{1g},p} + \varepsilon_{B_{1g},p}, \quad \langle \varepsilon_{yy} \rangle = \varepsilon_{A_{1g},p} - \varepsilon_{B_{1g},p},$

where $\varepsilon_{A_{1g},p}$ and $\varepsilon_{B_{1g},p}$ are given by the platform as defined in Equation 3.15. This is summarised schematically in Figure 3.8. The above distinction must be made for the application of strains smaller than the structural distortion, i.e. for $\langle \varepsilon_{xy'} \rangle \leq \varepsilon_{xy'}$, meaning that for applied strains beyond

$$\varepsilon_{xx,p} = \left(\frac{2}{1 + \nu_{\text{eff}}} \right) \varepsilon_S(T) \tag{3.25}$$

we are controlling locally both $\varepsilon_{A_{1g}}$and $\varepsilon_{B_{2g}}$. In general what this all means is that stress rather than strain is the proper conjugate field for tuning the nematic order parameter. However, we may nevertheless perform useful measurements with our controlled-strain setup: there is a first-order transition across ε_S due to the appearance of twins, and by tracking the location of this transition we may still precisely understand the state of the sample.

For a $\langle 100 \rangle_T$ aligned sample, the principal axes of the applied $\varepsilon_{B_{1g},p}$ platform strain are rotated by 45° from the principal axes of the orthorhombic distortion, and as such

the applied strain cannot be relaxed locally due to domain population redistribution. However, we must still make the distinction between the local and average strains due to the spontaneous structural distortion. On average we apply $\varepsilon_{A_{1g},p}$ and $\varepsilon_{B_{1g},p}$, but locally these strains are experienced in addition to the spontaneous $\varepsilon_{B_{2g}}$ component.

Having explained in detail the strains applied to, and experienced by the sample, we can simplify the notation without loss of understanding. When conducting our measurements we have a single control parameter $\varepsilon_{xx,p}$, and this is the natural variable against which to plot data. However as highlighted by Equation 3.25, for $\langle 110\rangle_T$ strain it is more practical to plot against the asymmetric component (i.e. $\varepsilon_{B_{1g},p}$ in Equation 3.15) as this has the same symmetry as the spontaneous distortion. Therefore we refer to the asymmetric strain simply as ε_a, and use this henceforth as our single strain parameter. The strains in Figure 3.8 become

$$\varepsilon_a \equiv \varepsilon_{B'_{2g}}, \quad \langle\varepsilon_a\rangle \equiv \langle\varepsilon_{B'_{2g}}\rangle, \tag{3.26}$$

and in this notation we can say that for $-\varepsilon_S \leq \langle\varepsilon_a\rangle \leq +\varepsilon_S$ we only control the average strain $\langle\varepsilon_a\rangle = \varepsilon_{B_{1g},p}$. In converting our measured strain to $\varepsilon_{B_{1g},p}$ an error is introduced through the uncertainty in the experimentally determined ν_{eff} (Table 3.4), however this is expected to be comparable to that from the determination of zero strain. For consistency, we also use this notation for $\langle 100\rangle_T$ strain, however as we cannot detwin the sample it is not particularly more instructive to do so.

3.3.5 Sample preparation

Samples were provided by Kyoto University (Matsuda group). Growth was conducted as described in Ref. [87], using chemical vapour transport with a temperature gradient of 160 °C to 430 °C in a single-zone furnace tilted by 15°. Fe and Se powder (1:1.1) with KCl/ACl_3 flux were sealed in ampoules of 30 mm inner diameter and 15 cm length.

The main steps to prepare samples for measurement were as follows

cut → cleave → deposit contacts → transfer to platform → add gold wires.

This is shown schematically in Figure 3.9 and we now describe these steps in more detail. A bulk crystal was first wire-saw cut into a long, narrow bar. As confirmed by Laue diffraction, the orientation was determined from natural grown edges and surface facets, which occur along the Fe-Se direction. For measurements with strain applied along the $[100]_T$ directions, cut edges were along the Fe-Se bond direction -

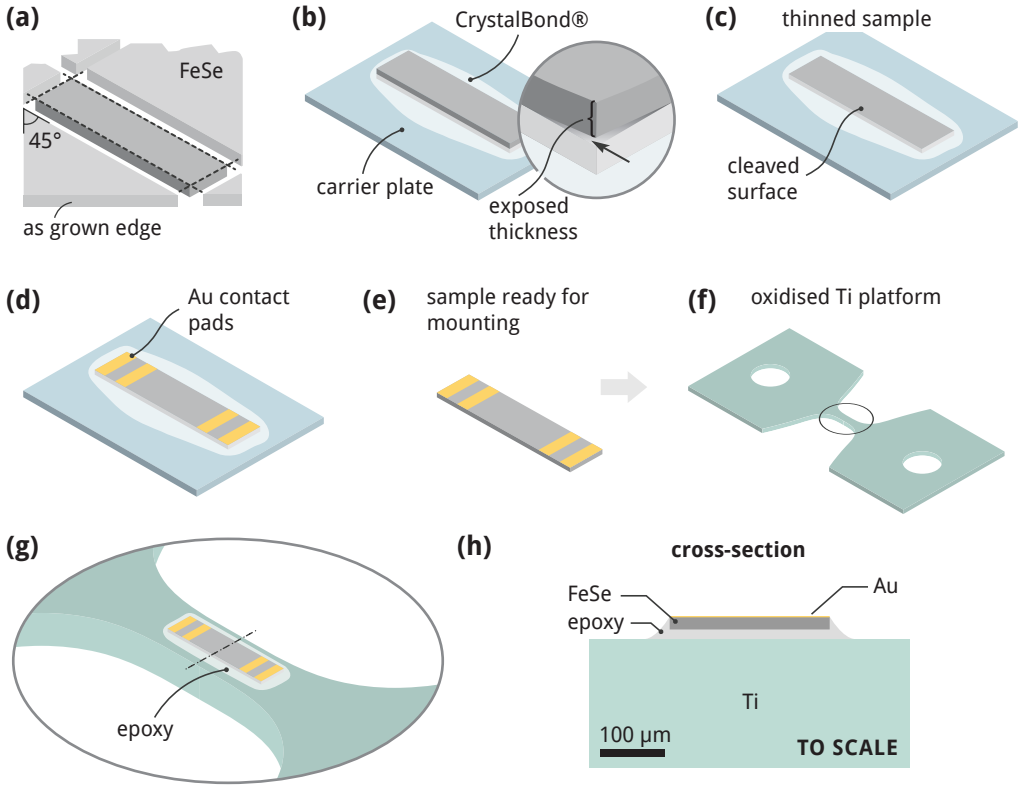

Figure 3.9 | Schematic (not to scale unless indicated) showing the steps in sample preparation. **(a)** Sample cut with the wire saw. For samples prepared in the $\langle 110 \rangle_T$ direction, cuts were made at 45° to as grown edges. **(b)** Sample mounted on a carrier plate using CrystalBond™, with exposed thickness to be cleaved. **(c)** Sample thinned using the scotch-tape method. **(d)** Evaporation of gold contact pads. These were defined either with a pre-applied GE varnish mask or, post-deposition through use of a focused ion beam. **(e)** Sample released using acetone to dissolve the CrystalBond. **(f)** The platform was prepared by cleaning and anodisation steps. **(g)** Sample adhered to the platform using a small amount of MasterBond EP29LPSP unfilled epoxy. **(h)** Cross section (to scale), of a lateral cut taken at the centre of the platform. This is based on $[110]_T$ sample 1, see Table B.1.

i.e. along as grown directions, and for $[110]_T$ measurements cut edges were along the Fe-Fe bond direction - i.e. at 45° to as grown edges. This method allows alignment to within approximately ±3°.

Samples were temporarily fixed to a glass carrier plate with Crystalbond™ in order to be cleaved. For controlled removal of material, the extent of edge coverage was loosely engineered using a heated wire to locally manipulate the bonding material and partially expose the upper part of the sample, as seen in Figure 3.9(b). Cleaving was initially conducted with regular Scotch™ tape. Although effective, it was too adhesive in situations where the cleaved piece was thick enough to be useable, and removal from the tape always resulted in severe deformation. Because FeSe layers are so weakly bonded, only a lightly adhesive material is required, and cleanroom-grade low-adhesion dicing tape was found to be ideal, enabling recovery of cleaved pieces. Targeting thin samples is necessary to minimise the strain transmission length and maximise coupling between the sample and platform. Achieving thicknesses below 20 μm is challenging as cleaves vary from several atomic layers to tens of microns thick, however tracking material removal using an optical profiler assisted in this process.

Many different approaches have been utilised to address the challenge of contacting FeSe. In Ref. [101] simply silver paste and gold wires are used, in Ref. [147] contacts are spot welded, whereas in [91] low-resistance contacts strong enough to apply strain are indium soldered (their patented technique [178]). Through the experience of S. Hosoi, we established our own reliable technique for creating low-resistance ohmic contacts. Four gold contact pads were deposited* immediately after cleaving, minimising formation of any insulating surface oxide. These were typically 100 μm wide, and whilst this width increases uncertainty in determination of resistivity, it provides sufficient space for wire addition and enhances the probability of a low resistance pathway. Contact definition was achieved by creating a mask with GE varnish, which is close-contact, and easy to remove without damaging the sample†.

Acetone was used for sample lift-off from the carrier plate, followed by an isopropyl alcohol wash. Samples were handled with polymer-tipped micro-tools from MiTeGen. These soft, flexible and intricate tools were vital for preparation of such an easily deformable material. For attachment to the oxidised platform (see Section 3.3.3) epoxy was first approximately spread to the length of the sample. MasterBond EP29LPSP was chosen for this due to its cryogenic compatibility and wicking properties. After

*The thickness was 150 nm, sputtered after a 10 minute cleaning plasma etch, without use of a intermediate adhesion layer.

†For the final sample we measured, gold was deposited over the entire sample and contacts were defined using focused a ion-beam.

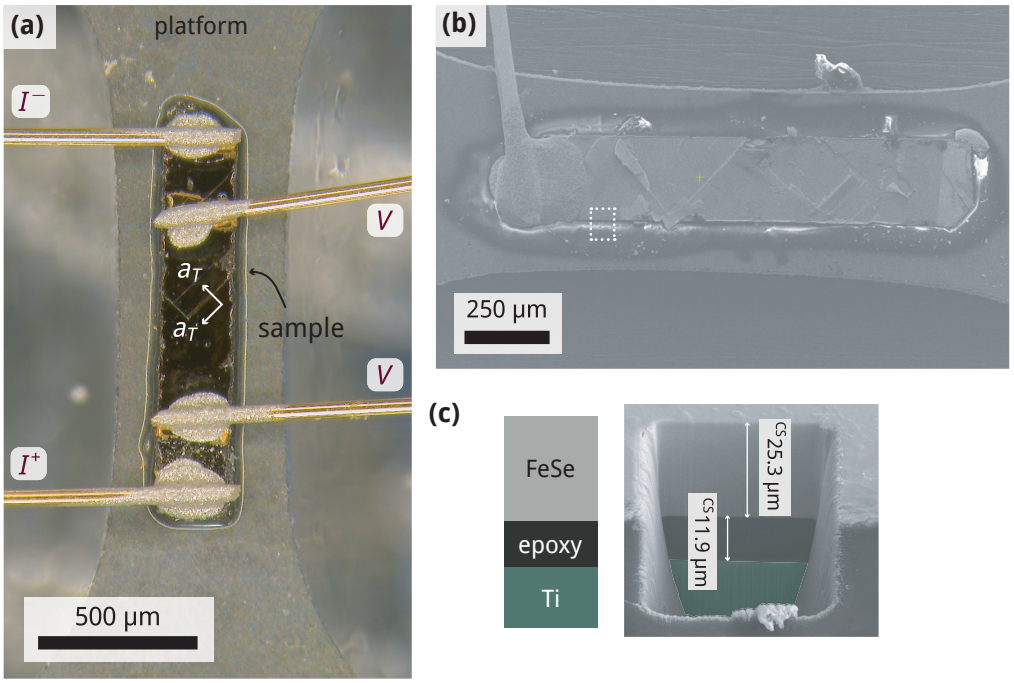

Figure 3.10 | (a) Optical micrograph showing a fabricated sample ($[110]_T$ s2 in Table B.1) in its final state. The tetragonal unit cell can be seen from surface facets. **(b)** SEM image showing the wicking of epoxy around the sample ($[110]_T$ s1). **(c)** SEM image showing a cross section through the sample in panel (b) to precisely measure the sample and epoxy thicknesses after having finished measurements. Sample, epoxy and titanium layers can be distinguished clearly, and based on this image are $\sim 25\,\mu m$ and $\sim 12\,\mu m$ thick respectively, but this will vary by a few microns locally.

placement, the sample was pressed on very gently with a micro-tool to decrease the epoxy layer thickness and increase its uniformity. The epoxy was cured at 70 °C for 10 h. The wicking of epoxy around the sample during curing created ramps holding its edges, as shown in Figure 3.9(h) and Figure 3.10. Finally, thin* gold wires were attached to the contact pads with RT-curing silver epoxy, which consistently gave ohmic contacts with resistances of a few ohms. An optical micrograph of a sample in its final state is shown in Figure 3.10(a). As shown in panel (c), this method produced epoxy thicknesses of approximately 10 µm which could be measured accurately (but destructively) after measurement using a focused ion beam to cut a cross section through the sample. Lastly, platforms were attached to the rig using the method described in Section 3.3.2.

*50 µm diameter wire was used for all but the the last sample in which 25 µm wire was used.

FeSe is known to be sensitive to oxygen [179]. Minimisation of exposure to air is therefore necessary, particularly at elevated temperatures. Our samples were stored in a nitrogen flow chamber (RT, 25 % humidity) before use, and were exposed to heat in atmospheric conditions briefly (~ 5 min) at $\sim 110\,^{\circ}$C due to the Crystalbond™, and continually for 10 h at $\sim 70\,^{\circ}$C during epoxy curing. The total duration of room temperature exposure to air was approximately 30 h.

Detailed information regarding the samples measured in this thesis can be found in Table B.1, and optical micrographs in Figure B.1.

Laue diffraction

Although as-grown crystal edges and surface facets are expected to be along the Fe-Se bond direction, we sought confirmation of this before utilising it as a reliable method for orienting samples. Utilisation of Laue diffraction for this brings certain challenges, the solutions to which may be of general importance for other materials whose size and crystal structure make orientation difficult. Simulation of the expected diffraction pattern and intensities for an x-ray beam incident normal to the xy-plane of FeSe (i.e. along the [001] direction) reveals a lack of strong peaks. This is particularly evident when comparing for example to Sr_2RuO_4, as shown in 3.11(a). Furthermore, a sample width of only $\sim 200\,\mu$m, our largest available at the time, was on the order of the X-ray beam spot size resulting in a reduction of counts. Finally, our concern was with distinguishing rotations of 45°, and the symmetry of the predicted pattern under this rotation made differentiating between the two problematic.

Image processing was necessary to optimise the visibility of all spots, and thus alleviate the issue of their scarcity. A simple contrast adjustment was not suitable due to our requirement of lower contrast in the centre to distinguish points from a dark background, and vice versa for the bright outer regions. As such, we utilised an adaptive histogram equalisation (AHE) technique for local contrast alteration. We used the 'enhance local contrast' function within ImageJ [182] which is a contrast-limited AHE, redistributing clipped counts across all histogram bins.

Initial acquisitions with the c-axis of the sample parallel to the beam lead to few visible points, inhibiting successful orientation. To address this we rotated the sample, creating a $\sim 10^{\circ}$ angle between the c-axis and beam (Figure 3.11(b)), to move the [001] spot out from the unmeasured centre region. CLIP* was used for fitting the observed pattern. Accurate measurement of the sample-to-plate distance was crucial due to the

*Cologne Laue Indexation Program [181].

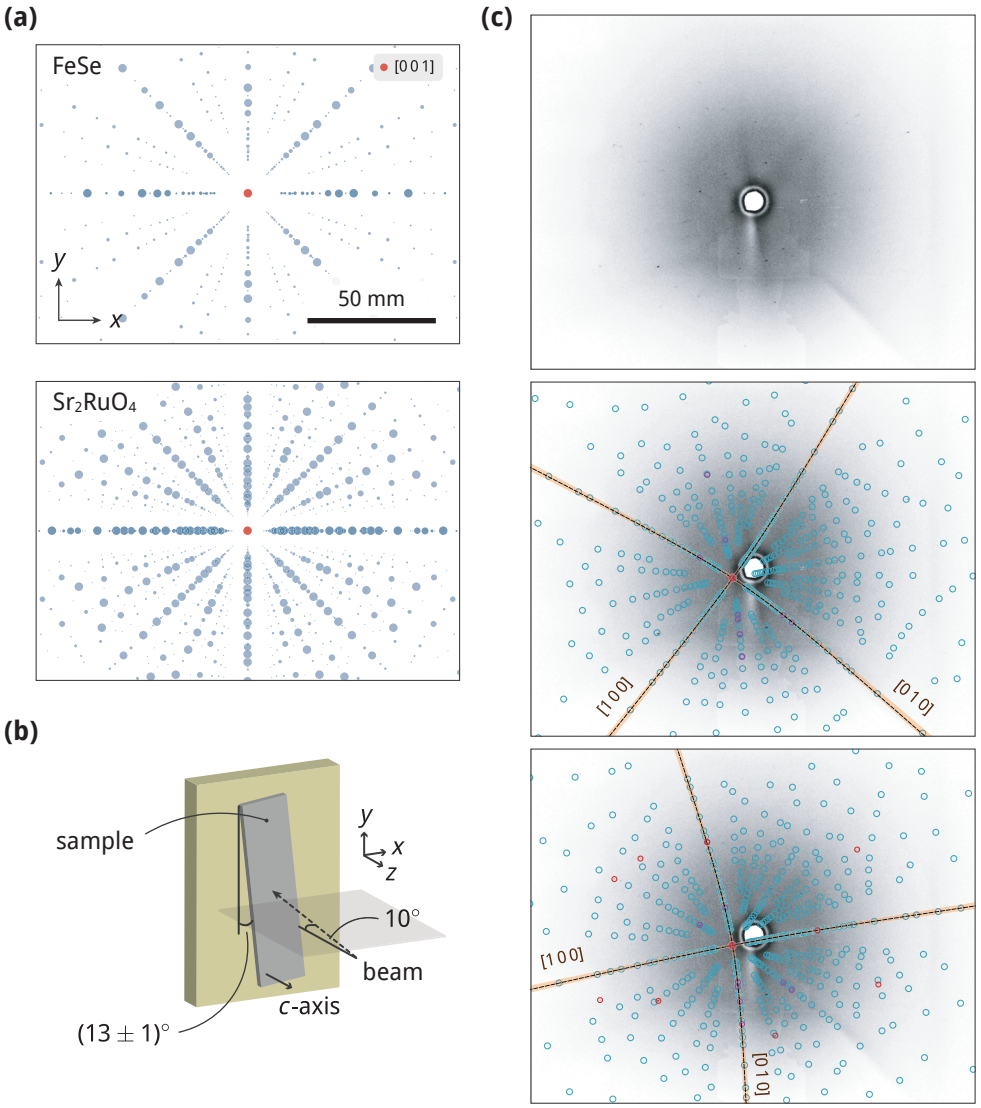

Figure 3.11 | (a) Comparison of Laue diffraction patterns of FeSe and Sr_2RuO_4 simulated using QLaue [180] with a sample-to-detector distance of 50 mm. Point scarcity and similarity under a 45° rotation is evident for FeSe. **(b)** Schematic of the measurement set up with the sample c-axis at $\sim 10^\circ$ to the beam, and a small rotation between the sample and its holder. **(c)** Top: contrast enhanced image of diffraction pattern. Middle: fitting solution of image above using CLIP [181]. When accounting for the rotation of the sample with respect to the holder, this solution has the principal axes (indicated in orange) at $\sim 45^\circ$ to the sample edges, meaning they are aligned with the Fe-Fe bond direction. Bottom: solution rotated clockwise by 45°. Points which no longer fit are circled in red, indicating incompatibility with an Fe-Se edge-aligned orientation.

sensitivity of the pattern on this parameter. The best solution had a deviation over three times smaller than the next-best, and agreed with our known [001] point - indicating successful orientation. When accounting for the $(13 \pm 1)^\circ$ rotation of the sample with respect to its holder as shown in Figure 3.11(b), the x- and y-axis corresponding to the [110] and $[\bar{1}10]$ lines respectively, showing the sample's edges to be at 45° to the tetragonal unit cell. Under rotation of the solution by 45°, the distinction we are trying to ascertain, around half the measured points no longer matched the solution (indicated in red in 3.11(c)).

3.3.6 Strain scale

As highlighted by Section 3.3.4, the parameters $\varepsilon_{xx,p}$ and $\varepsilon_{yy,p}$ are central to our understanding of the strain we apply to a sample bonded to a platform. We therefore need to know how to convert the capacitive readout, indicating stack displacement, to these strains. As discussed in Section 3.3.2, for $\varepsilon_{xx,p}$ this corresponds to knowledge of L_{eff}/a where L_{eff} is the effective strained length and a is a conversion factor ~ 1 that accounts for any discrepancy between measured and actual displacement due, e.g., to deformation of the cell under the load from the platform. For $\varepsilon_{yy,p}$ we must know the platform's effective Poisson's ratio ν_{eff}. To this end we directly measure the strain using an optical microscopy technique. This notable experimental effort was motivated and led by Dr Alexander Steppke with assistance from Dr Hilary Noad. The basis of this technique is to track well defined features under an optical microscope, using two-dimensional Gaussian fitting of pixel intensity, which can be done to a precision higher than that of the individual pixels. This is a well-established method for material characterisation within engineering fields [183] and, provided the surface stays flat, enables accurate determination of the two-dimensional strain tensor of a deformed surface. The roughness of titanium naturally provides numerous trackable features allowing robust statistical strain determination.

It is possible to determine the displacement d of a feature i with applied stack displacement δ_{stacks} (where δ_{stacks} is determined from capacitance change) in both x and y:

$$\mathbf{d}_i(\delta_{\text{stacks}}) = d_{i,x}(\delta_{\text{stacks}})\hat{x} + d_{i,y}(\delta_{\text{stacks}})\hat{y}$$

The strain can be calculated between two points i and j

$$\varepsilon_{xx,ij}(\delta_{\text{stacks}}) = \frac{d_{i,x}(\delta_{\text{stacks}}) - d_{j,x}(\delta_{\text{stacks}})}{d_{i,x}(0) - d_{j,x}(0)},$$

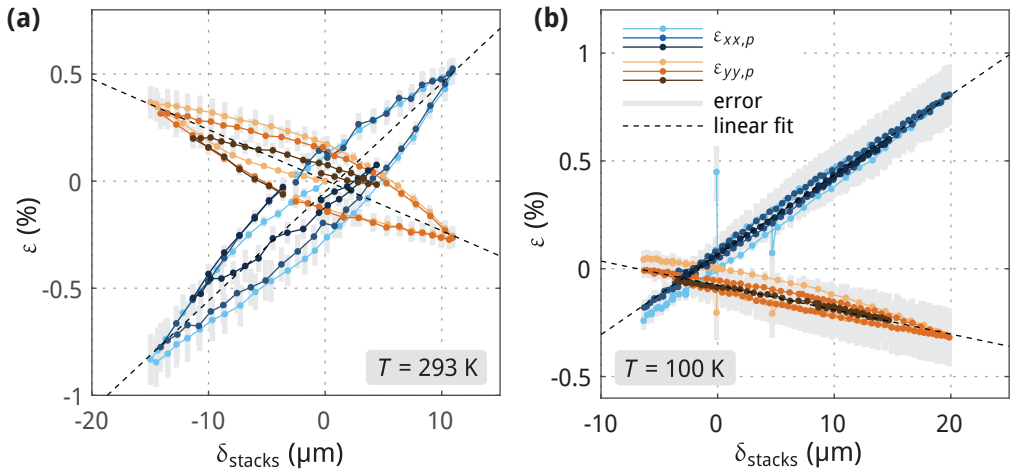

Figure 3.12 | Plots of platform strain determined by digital image correlation, as a function of stack displacement measured via the change in capacitive-sensor readout. The zero-strain point is defined through the image against which displacements are measured, and is therefore arbitrary. Although we choose this to correspond to zero volts, it may be far from zero strain due to differential thermal contraction and stack hysteresis. **(a)** Strain along x (blue) and y (orange) at room temperature $\sim 293\,\mathrm{K}$. The light-to-dark colouring corresponds chronologically to the measurement order. There is large hysteresis due to the low plastic limit of titanium at this temperature. **(b)** Measurement repeated at $100\,\mathrm{K}$, showing significantly reduced hysteresis due to an increase in yield strain. Here we can reliably conduct linear fits to extract the effective strained length and Poisson's ratio.

and similarly for $\varepsilon_{yy,ij}$. Some points are separated only in x and not in y, meaning that the numerator for ε_{yy} determination is very small, leading to large errors. As such a minimum $d_{i,y}(0) - d_{j,y}(0)$ cutoff must be used - and vice versa for points separated in y and not x. Furthermore, for local strain determination a cutoff must be used for both x and y. As such there is a trade off between strain map resolution, and precision. This processing is the basis of DICe* - an open source digital image correlation tool that was used for all subsequent extraction of platform strain.

By taking optical micrographs of the platform and using this software, we measured $\varepsilon_{xx,p}$ and $\varepsilon_{yy,p}$ locally at the platform centre with a field of view of $\sim 740\,\mu\mathrm{m} \times \sim 410\,\mu\mathrm{m}$. This was conducted as a function of δ_{stacks} at room temperature and, by using an optical flow cryostat, at $100\,\mathrm{K}$. Averaging over this strain field gives a single value

*Digital Image Correlation Engine.

T (K)	L_{eff}/a (mm)	ν_{eff}
293	2.00 ± 0.09	0.46 ± 0.06
100	2.7 ± 0.2	0.3 ± 0.1

Table 3.4 | Table showing values L_{eff}/a and ν_{eff} extracted from linear fitting to strain versus stack displacement data – Figure 3.13. Large hysteresis due to plastic deformation weakens the reliability of the values extracted at 293 K. Errors originate from gradients at which a straight line fits within the error bar extremes.

of $\varepsilon_{xx,p}$ and $\varepsilon_{yy,p}$ for each stack displacement - as shown in Figure 3.12. This method can also extract $\varepsilon_{xy,p}$ which was found to be negligible in comparison to $\varepsilon_{xx,p}$. The room temperature measurement in panel (a) is hindered by the low plastic deformation limit of pure titanium, which is evident from the large hysteresis. Depending on the preparation and treatment method, titanium is expected to have a yield strain of 0.18 %–0.45 % at room temperature [170, 184], beyond which it behaves plastically. At low temperatures the yield limit increases (Ref. [185] reports this to be by a factor of ~ 1.75 down to cryogenic temperatures – but additional support is lacking), and we observe the hysteresis to be much smaller. We therefore acknowledge that, with its increased elastic limit, grade 5 titanium (Ti6Al4V) might be more suited for solid strain platforms – a conclusion reinforced by challenges met during measurements, as presented in Section 4.2.3.

From a linear fit to $\varepsilon_{xx,p}$ plotted against δ_{stacks}, a value for L_{eff}/a can be extracted, and from the absolute ratio of the gradients along y and x, as can ν_{eff}. The results are shown in Table 3.4. Fitting to both up and down strain-sweeps means that there is a significant deviation between actual strain and that inferred from L_{eff}/a, which is worse at low strains. As such the high temperature value of L_{eff}/a does not give a good conversion from displacement to the strain experienced by the sample. This is not a problem as all our measurements are conducted below 120 K. For both high- and low-temperature measurements the first data set (lightest blue/orange) was ignored due to displaying open-loop hysteresis which would skew the fit.

The difference between the experimentally determined quantity L_{eff}/a shown in Table 3.4 and the value of L_{eff} determined from FEA (3.46 mm) gives us an ideality factor of $a \sim 1.3$. That $a > 1$ implies that in reality part of the platform-rig system acts more rigidly than expected. This may be because the clamping method holds fixed a larger proportion of the platform's end than in the FEA. Finite rig stiffness is also

expected to have an effect, as some displacement will go into deforming the rig rather than the platform. However our measure of displacement comes from the capacitive sensor which is rigidly attached directly to either side of the main rig body across which the platform is screwed in place. Furthermore any lack of stiffness would give $a < 1$. Because of the direct coupling between the sensor and platform, variations in rig construction are not expected to affect the measured platform properties; the above platform characterisation was conducted using a different rig (with an identical design and construction) from that used for measurements.

As taken from Table 3.4, we use the following values to convert from stack displacement to $\varepsilon_{xx,p}$ and $\varepsilon_{yy,p}$ throughout this thesis, and therefore emphasise them below

$$L_{\text{eff}}/a = (2.7 \pm 0.2)\,\text{mm}, \quad \nu_{\text{eff}} = 0.3 \pm 0.1, \quad \text{at } T \sim 100\,\text{K}.$$

Our platform therefore applies a ratio $\varepsilon_{B_{1g}}/\varepsilon_{A_{1g}} = (1+\nu_{\text{eff}})/(1-\nu_{\text{eff}}) \sim 1.9$. We compare this to the approximate value from piezoelectric-stack measurements of ~ 3 [52].

3.4 Measurement setup

3.4.1 Pulse tube refrigeration & VTI

We used a cryogen-free, variable-temperature-insert (VTI) system which provides continuous temperature control from 1.5 K–300 K* for the majority of our measurements (see Table B.2). In this system, cooling power is provided by a two-stage pulse tube (PT) cryocooler (made by SHI† and described in Ref. [186]) which condenses circulating ultra-pure helium gas. The flow of this gas is controlled by a needle valve, allowing the cooling power of a variable temperature insert to be tuned. The cryocooler provides a cooling capacity at the first stage of 40 W at 45.9 K and at the second stage of 0.9 W at 4.23 K.

The operational principle of pulse tube refrigeration is based on the observation that a blanked plumbing line connected to a compressor gets hot at its closed end [187]. Adding a regenerator after the compressor as a periodic heat exchanger causes the opposite end of the tube to cool as the blanked end heats. This occurs because the pulsed pressure change in the tube draws gas in at the hot end when the pressure is low, but expels it when the pressure is high at a temperature greater than when it entered. The heat exchanger then releases this heat. The opposite happens at the cold end. For

*Teslatron™ PT from Oxford Instruments.
†Sumitomo Heavy Industries.

these so called 'surface heat pumping' processes, the tube must be thermally isolated to ensure adiabatic conditions. Helium is used as the working gas due to its monotonic ideal gas behaviour and low condensation temperatures. Pulse tube refrigeration is described in more detail in Ref.s [188–190].

We operated with a small amount of helium exchange gas (a few cubic centimetres at room temperature) in the sample space to achieve a base temperature of 1.5 K. We tested this to ensure it was a sufficiently small amount of gas to enable operation of piezoelectric stacks at several hundreds of volts without electric discharge. The temperature of the system was controlled via heaters at both the lower part of the VTI and the probe. Separation of the control of these two in both time and temperature minimised the interference of PID loops. Thermal coupling between the VTI and probe gave a maximum temperature difference between them of ~ 10 K, meaning both required constant control to sweep temperature. The sample temperature was measured via a calibrated Cernox® sensor on the main body of the rig.

3.4.2 Measurement technique

Having described the pressure cell, sample preparation steps and method for cooling the sample, all that remains is to describe our actual measurement technique and procedure. With the contacts added to the sample as shown in Figure 3.10(a), we performed four-terminal AC resistivity measurements as a function of temperature and strain ($\varepsilon_{xx,p}$). We applied an AC current I through the outer two contacts and measured the voltage across the inner two. This gives a voltage signal $V = I\rho_{xx}L_c/A$, where x refers to the longitudinal platform direction, L_c is the distance between the voltage contact pads, and A is the sample's cross-sectional area. Due to the contact pad width, there is an $\sim 200\,\mu$m uncertainty in L_c which makes accurate determination of ρ difficult. For a sample orientated with its edges along the tetragonal unit cell as in Figure 3.7(a), and under zero applied strain $\langle\varepsilon\rangle = 0$, the measured resistivity is $\rho_{xx} = \rho_{[100]_T}$ for $T > T_S$; and $\rho_{xx} = \frac{1}{2}\left(\rho_{[110]_O} + \rho_{[-110]_O}\right)$ for $T < T_S$. For a sample with its edges at 45° to the tetragonal unit cell as in Figure 3.7(b) $\rho_{xx} = \rho_{[110]_T}$ for $T > T_S$; and $\rho_{xx} = \rho_{[100]_O}$ for $T < T_S$. In both cases, the sample forms twins below T_S. This does not affect the form of resistivity written above for a $\langle 100\rangle_T$ sample, but results in a average being measured for a $\langle 110\rangle_T$ sample: $\rho_{xx} = \frac{1}{2}\left(\rho_{[100]_O} + \rho_{[010]_O}\right)$. For a $\langle 110\rangle_T$ sample under $|\langle\varepsilon_a\rangle| > |\varepsilon_s|$ detwinning should occur, and it is possible to probe the resistivity of a single domain type, i.e $\rho_{xx}\left(\langle\varepsilon_a\rangle = -\varepsilon_s\right) = \rho_{b_O}$. In our experiment we measured both $V(T)$ for fixed ε_p and $V(\varepsilon_p)$ for fixed T.

We used a lock-in amplifier* for low-noise measurement of the voltage, and for our frequency range of $< 1\,\mathrm{kHz}$, this gives an input noise of $2.5\,\mathrm{nV}/\sqrt{\mathrm{Hz}}$. Current was supplied using an in-house built source with common-mode noise rejection. We typically applied currents of 1 mA (see Table B.2) which did not give measurable heating. The room-temperature in-plane resistivity of high-quality FeSe was previously measured to be $400\,\mu\Omega\mathrm{cm}$ [125]. For our typical L_c/A of $700\,\mathrm{cm/cm^2}$ this corresponds to a signal of $\sim 3\,\mathrm{mV}$ for a 1 mA current. This is large enough with respect to the noise to be measured without need for additional signal amplification. Top injected current contacts can be problematic for anisotropic layered materials. The ratio of out-of-plane to in-plane resistivity ρ_c/ρ_{ab} in $FeSe_{0.4}Te_{0.6}$ is around 44 at 290 K and 70 at 15 K [191]. The length-to-thickness ratio needed for current to spread out along the c-axis is $(\rho_c/\rho_{ab})^{1/2}$; if we take the above value as holding for FeSe, this gives ~ 8 at 15 K. The voltage-to-current contact distance as a ratio of sample thickness is shown in Table B.1, this exceeds 8 for samples $[100]_T$ s1, and $[110]_T$ s3 - the two we primarily present data from. We also attached coils for measurement of AC magnetic susceptibility, as described fully in Ref.s [192, 193]. This was used as a probe of the superconducting transition that occurs at 9 K. Our use of this technique was hampered by poor signal-to-noise levels, most likely caused by low coil windings and large sample-to-coil distances.

To control the platform strain $\varepsilon_{xx,p}$, we apply voltage to the piezoelectric stacks using an auxiliary output of the lock-in amplifier, passed through a high-voltage (HV) amplifier with a gain of 100. The specification for the auxillary outputs of the SR860 is a range of $\pm 10.5\,\mathrm{V}$ at 1 mV resolution, which with the HV amplifier is a resolution of 0.1 V. The change of stack length δ_{stacks} from this applied voltage was determined via a 3-point capacitance measurement of the parallel-plate sensor using a high-precision capacitance bridge†. We then used a feedback loop on the stack voltage to hold the capacitance constant, as described in more detail in Section 3.4.3. At higher temperatures where the length change per volt is large, the minimum δ_{stacks} set by the 0.1 V resolution can restrict high levels of control. In our case the signal change corresponding to this step size was smaller than the noise level.

3.4.3 Software developments

As described in Section 3.4.2 the platform strain was controlled via feedback of the stack voltage to target a specific capacitance and thus strain. Significant software

*Stanford Instruments SR860.

†Andeen-Hagerling AH 2550A.

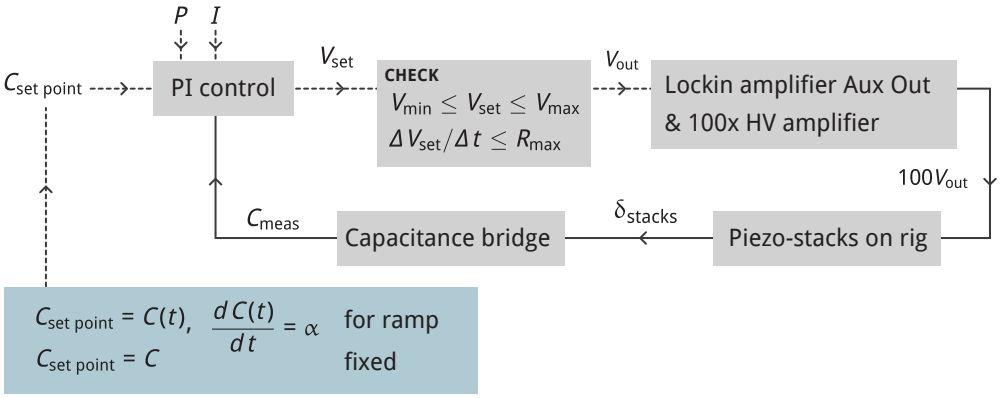

Figure 3.13 | Diagrammatic representation of the strain control software. This was implemented as a virtual instrument in our central measurement program allowing it to operate continuously even when not collecting data. Dashed lines represent virtual/digital inputs and outputs, i.e. from user input or commands sent to hardware. Solid lines represent measurable/analogue inputs and outputs. P and I values are dependent on the piezoelectric constants at a given temperature, however good control was achieved with fixed values. Checks are important to protect the sample; these include making sure the voltage is within a sensible range, as well as checking the rate of change of applied voltage is not too high.

development was required in order to implement such strain control into the already established LabView-based measurement program written by Dr Thomas Lühmann. Ideas for its operation were conceived by myself and Dr Alexander Steppke, who assisted its implementation by Dr Lühmann. The strain control module operates as a virtual instrument in the measurement program, providing unprecedented levels of continuous control which will become standard for future strain measurements. An overview of its operation is shown schematically in Figure 3.13. It utilises a feedback loop control with proportional (P) and integral (I) terms which allows us to maintain a constant capacitance to within 0.01 %. Capacitance can also be ramped linearly, either for an individual ramp in one direction, or in a quasi-oscillatory way for low-frequency 'wiggling'-type experiments. Managing the sharing of stack voltage is possible via easy switching of the primary stacks, as well as voltage compensation allowing a percentage of the primary voltage to be applied to the opposing stacks. Finally, limits on both the voltage and rate of change of voltage were implemented. These are crucial for prevention of sample damage by unwanted voltage application. All of these features can be fully automated.

4 | Strain-Tuning of FeSe

In this chapter we investigate the effect of strain, applied both longitudinally and transversely to the nematic-driven structural distortion, on the electrical transport of single-crystal FeSe across a wide temperature range, from 100 K to 5 K. We address our initial question of whether there is evidence for a crossover even under conditions where the lattice cannot deform. We also demonstrate precise characterisation of the elastoresistivity of FeSe over a wide strain range. In particular, by isolating the effect of twin boundaries, we are able to precisely characterise the elastoresistivity below T_S, something that has not been possible before.

The experimental technique, apparatus, and mounting procedures are explained in depth in Chapter 3. In total four FeSe samples were prepared and measured; full details can be found in Appendix B. One of the four was prepared for $\langle 100 \rangle_T$ strain, and the others for $\langle 110 \rangle_T$ strain. Of these three, we mostly concentrate on data from the last sample measured ($[110]_T$s3 in Table B.1). This was the thinnest, at $t \sim 10\,\mu$m, giving the smallest strain transfer length, and the most homogeneous out-of-plane strain profile. Unless indicated otherwise, data under $\langle 110 \rangle_T$ strain were obtained from this sample. In the subsequent presentation of data, 'high temperature' refers to the region near T_S at zero strain, i.e. ~ 90 K, whereas 'low temperature' the region near $T_c \sim 9$ K. Between these two is the 'intermediate-temperature' regime.

To reiterate the important notation convention from Section 3.3.4, the strain used in this Chapter, ε_a, is the asymmetric component calculated via $\varepsilon_a = \frac{1}{2}(1 + \nu_{\text{eff}})\,\varepsilon_{xx,p} \sim 0.65\,\varepsilon_{xx,p}$. Here the platform strain is given by $\varepsilon_{xx,p} = a\delta_{\text{stacks}}/L_{\text{eff}}$. We use values of a/L_{eff} and ν_{eff} at 100 K (Table 3.4), and $\delta_{\text{stacks}} = \epsilon_0 A\left(\frac{1}{C_0} - \frac{1}{C}\right)$, with C being the measured capacitance. This is expanded on in Section C.1. Although we use this strain scaling when plotting, it should be emphasised that we do not isolate the asymmetric electronic response. Continuing to clarify terminology used in this chapter: a 'temperature ramp' refers to measurement of resistivity whilst slowly varying temperature at a fixed strain (more strictly a fixed capacitance); whereas for 'strain ramps' we hold the temperature fixed and sweep the voltage applied to the piezoelectric

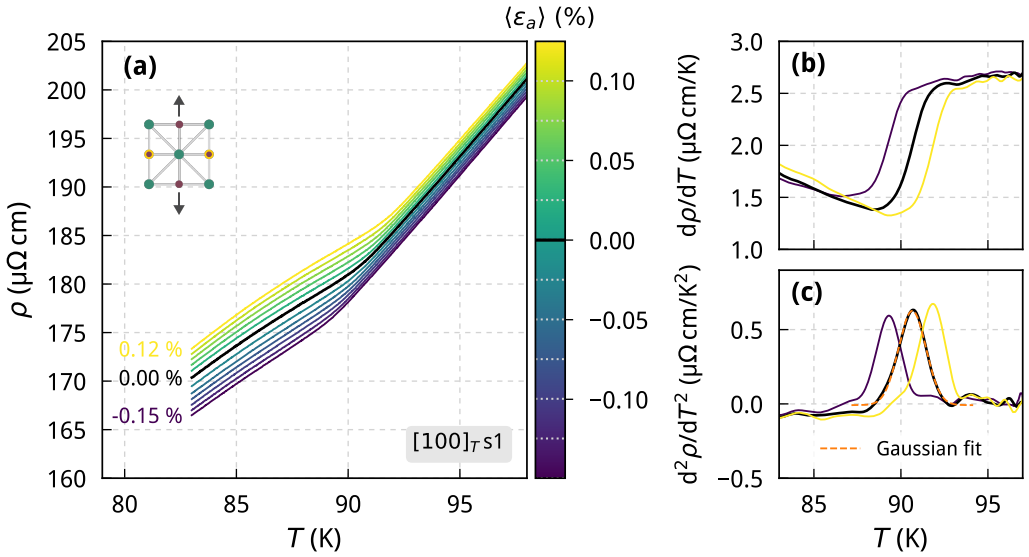

Figure 4.1 | Resistivity ρ as a function of temperature for applied $\langle 100 \rangle_T$ strain. **(a)** For $\rho(T)$, the structural phase transition is indicated by an abrupt decrease in slope upon cooling. Zero strain is highlighted in black, and strain intervals are shown in the legend. **(b)** First derivative $\mathrm{d}\rho/\mathrm{d}T$ for zero strain, as well as maximum compression (−0.15 %) and tension (0.12 %). **(c)** Peaks in the second derivative $\mathrm{d}^2\rho/\mathrm{d}T^2$ at the transition. The width and peak location are extracted by a Gaussian fit – as shown for zero strain.

actuators. The temperature at which we ramp to the next strain (and vice versa) will be specified where necessary. As we will see, this is important due to history dependence when exploring some parts of the $\rho(T, \varepsilon_a)$ phase space.

4.1 $\langle 100 \rangle_T$ strain

We start by presenting data under $\langle 100 \rangle_T$ strain – that is, strain applied along the Fe-Se bond direction. This is a transverse field to the nematic order and so the response is expected to be weak. As described in Section 3.3.4, in this configuration the sample will experience controlled $\varepsilon_{A_{1g},p}$ and $\varepsilon_{B_{1g},p}$ strains due to the displacement applied to the platform. The principal axes of $\varepsilon_{B_{1g}}$ are rotated by 45° from the principal axes of the structural distortion, so $\varepsilon_{B_{1g}}$ does not relax locally and we need not distinguish between average and local strains. The sample experiences $\varepsilon_{A_{1g}}$, $\varepsilon_{B_{1g}}$ and $\varepsilon_{B_{2g}}$ locally (the first two constrained by the platform and the last fixed by the structural distortion), and remains twinned at all applied strains – even just below T_S where the distortion is small.

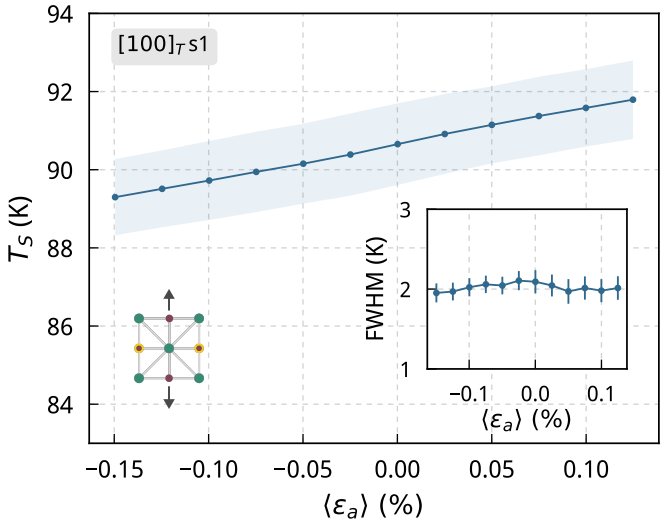

Figure 4.2 | Dependence of the structural transition temperature T_S and width (FWHM) on $\langle 100 \rangle_T$ strain. The width is shown as a shaded region in the range $T_S - \text{FWHM}/2 \leq T \leq T_S + \text{FWHM}/2$ in the main plot, and separately in the inset. T_S responds linearly to $\varepsilon_{A_{1g}}$ and $\varepsilon_{B_{1g}}$ across the measured range, whilst the width remains approximately constant.

4.1.1 High temperature

Let us begin at high temperatures. Longitudinal resistivity measured as a function of temperature, $\rho(T)$, for strain intervals between $0.12\,\%$ and $-0.15\,\%$ is shown in Figure 4.1(a). The temperature was swept at 200 mK/min, and the strain changed at 100 K. At zero strain the structural phase transition (T_S) is marked by a change in slope at around 90 K. This is seen more clearly as an abrupt drop in the first derivative upon cooling, as shown in Figure 4.1(b). We can extract the transition temperature and a phenomenological transition width by fitting a Gaussian to the peak in $\mathrm{d}^2\rho/\mathrm{d}T^2$; we take the transition width to be the full width at half maximum of the fitted Gaussian – this is shown in panel (c). This method will subsequently be used for all extractions of T_S from $\rho(T)$*.

The transition from tetragonal to orthorhombic crystallographic symmetry is second order and, as already established, the formation of twin domains is energetically favourable. Our application of $\varepsilon_{B_{1g}}$ strain will break the tetragonal symmetry, however the principal axes are rotated by 45° from those of the spontaneous distortion.

*This is not the only method for extracting T_S, and a comparison of different methods will be given in Section 4.2 for $\langle 110 \rangle_T$ strain.

Therefore, a change of rotational symmetry will still occur at T_S, and the transition will remain second-order under the strain applied from the platform. Our measured resistances average over the domain structure in the material which, because $\langle 100\rangle_T$ strain is not a conjugate field to the transition, is expected to stay essentially unchanged as strain is applied. The $\varepsilon_{A_{1g}}$and $\varepsilon_{B_{1g}}$strains transfer locally to the sample, and we observe the response to this in panels (b) and (c) of Figure 4.1. This can be seen more clearly by following the extraction procedure above to give the strain dependence of T_S and the transition width, as shown in Figure 4.2. T_S varies linearly with strain, with a positive slope of gradient $\sim 9\,\mathrm{K}/\%$. As we might expect, the width remains constant (within error) with a value of $(2.0 \pm 0.1)\,\mathrm{K}$. Later we will compare these data with the response from $\langle 110\rangle_T$ strain.

4.1.2 Low temperature

We now examine the behaviour at low temperatures. Both resistivity and magnetic susceptibility were measured as a function of temperature to determine the strain dependence of the superconducting transition T_c – as shown in Figure 4.3(a). Similar to the structural transition temperature, T_c also varies linearly in response to strain, but with a negative gradient, decreasing in temperature under tension. Magnetic susceptibility is a more reliable method for T_c determination and we observe a $\sim 10\,\%$ drop in the susceptibility signal χ_{norm} (that is, the mutual inductance of the two coils placed on top of the sample), as shown in Figure 4.3(b) for $\langle \varepsilon_a \rangle \sim 0$. T_c is then taken to be the temperature corresponding to the peak in $\mathrm{d}\chi/\mathrm{d}T$. Resistivity for the same measurement sweep is shown in panel (c). Here, T_c can be extracted via a slice at constant resistivity, and various thresholds can be chosen. A downward turn in resistivity occurs 1–2 K above the onset of the transition in susceptibility, likely as a result of percolating current paths. However, the extracted slope $\mathrm{d}T_c/\mathrm{d}\langle \varepsilon_a \rangle$ is not sensitive to the choice of threshold. As shown in Figure 4.3(a), choosing a very low threshold of $0.5\,\mu\Omega\mathrm{cm}$, gives values of T_c very similar to those from susceptibility. Linear fits to $T_c(\langle \varepsilon_a \rangle)$ from susceptibility and the low-resistivity slice give an equal gradient of $-1.9\,\mathrm{K}/\%$. Also worth noting: T_c is determined from an average of increasing- and decreasing-ramps; the temperature was swept at 100 mK/min whilst passing through the transition; and the strain was changed at 15 K rather than above T_S.

In Appendix C a supplementary plot is provided, Figure C.1, showing the resistivity and smoothed susceptibility versus temperature for various strains.

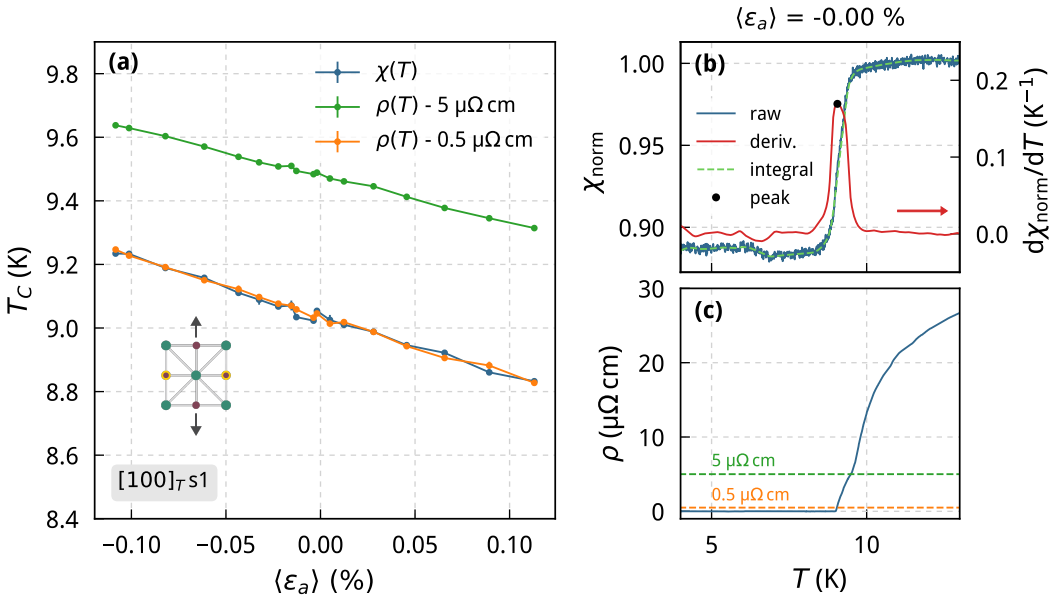

Figure 4.3 | Variation of the superconducting transition temperature T_c under $\langle 100 \rangle_T$ strain. **(a)** T_c determined from resistivity $\rho(T)$ and magnetic susceptibility $\chi(T)$. **(b)** Normalised magnetic susceptibility $\chi_{\text{norm}} = \chi(T)/\chi(T \sim 12\text{K})$, shown for zero strain. T_c is extracted from the peak in the first derivative. **(c)** Resistivity from the same measurement sweep as in (b). Slices at two different resistivity thresholds, 5 μΩcm and 0.5 μΩcm, give a very similar values of $\mathrm{d}T_c/\mathrm{d}\langle\varepsilon_a\rangle$. The lower threshold additionally matches well to T_c from susceptibility. These are both plotted in panel (a).

4.2 $\langle 110 \rangle_T$ strain

Rotation of the sample by 45° within the plane gives us a very different probe of the electronic properties of FeSe. Strain is now applied along the Fe-Fe bond direction, and denoted as $\langle 110 \rangle_T$, with an asymmetric component $\varepsilon_{B_{2g}}$ of the same principal axes as the spontaneous distortion. The response of FeSe under $\langle 110 \rangle_T$ strain is our main experimental focus.

4.2.1 Expectations

From X-ray diffraction measurements on single-crystal FeSe, we know that as $T \to 0$ the spontaneous structural distortion is large, $(a-b)/(a+b) \sim 0.27\%$ [90], indicating strong coupling between electronic and lattice degrees of freedom.

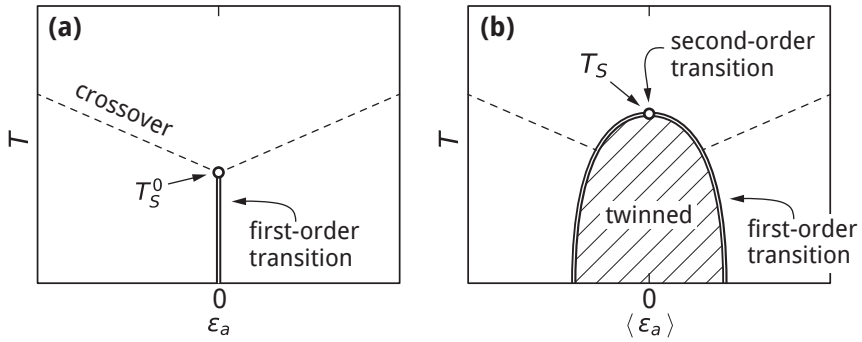

Figure 4.4 | $\langle 110 \rangle_T$ strain-temperature phase diagram for nematic order. **(a)** Scenario in which the strain is held fixed across the sample, quenching the feedback between lattice distortion and nematicity. **(b)** Realistic scenario representing our setup, in which within the twinned region the average strain $\langle \varepsilon_a \rangle$ is held fixed by bonding to the platform, but the lattice may deform locally. Reintroduction of feedback between the nematicity and lattice causes a renormalisation of the transition temperature from T_S^0 to T_S.

External distortion of the lattice is consequently a powerful tuning parameter, and as demonstrated in Section 2.1.3, $\langle 110 \rangle_T$ strain couples directly to the nematic order, whereas stress of the same symmetry couples directly only to the structural distortion and indirectly to the nematicity through strain. As we expressed in Section 3.3.4 however, strain is not the best conjugate field in our experimental setup due to domain formation. To reiterate this point more clearly, it is instructive to draw an analogy to the more familiar scenario of a ferromagnet, in which an important distinction must be made between the behaviour in a magnetic field H and magnetic induction B. Control of H is simply achieved via an external magnetic field under which the second-order para-to-ferromagnetic transition becomes a crossover. Control of B is more complicated as it includes the sample's own magnetisation M, however preparing a sample with a large demagnetisation factor causes the magnet to break up into $\pm M$ domains for $|B| < \mu_0 M$. In this case the magnetisation does not contribute at large length scales, across which B is subsequently controlled. Analogously for FeSe, stress is easily controlled and turns the second-order tetragonal-to-orthorhombic transition in FeSe into a crossover, whilst strain $\langle \varepsilon_a \rangle$ causes $\pm \varepsilon_S$ domains to form for $|\langle \varepsilon_a \rangle| < \varepsilon_S$. In our setup, this is permitted by the epoxy layer which allows the sample to deform over short length scales, and forces us to make the distinction between the average strain $\langle \varepsilon_a \rangle$, which we hold fixed by the platform, and local strain $\pm \varepsilon_S$ which is set by the distortion of a single domain.

With this understanding, and the Landau theory outlined in Section 2.1.2, we can hypothesise the strain-temperature phase diagram of the nematic transition. We first imagine a scenario in which the lattice strain is locally held fixed. This corresponds to the sample and epoxy layer having zero thickness such that atoms cannot move in response to the onset of nematic order, thus giving the extreme limit of Figure 2.2. For this scenario we obtain the familiar 2D-Ising phase diagram, as shown in Figure 4.4(a). A second-order transition occurs upon cooling at zero field, becoming a crossover at finite field due to the removal of symmetry. To first order the crossover temperature increases with strain. Subsequently an order parameter direction is favoured in the low temperature phase, the sign of which is reversed at zero field; this is a first-order transition. Because we hold the lattice fixed, strain is used as the conjugate field, and the second order transition occurs at T_S^0 – which we refer to as the 'bare' nematic transition temperature.

This scenario is not representative of our setup, however, as the sample strain is only fixed on average and not locally, enabling domains to form for $|\langle \varepsilon_a \rangle| < \varepsilon_S(T)$. Allowing the lattice to deform locally causes the transition to occur at a higher temperature, T_S, due to feedback between the nematic order parameter and structural distortion. This was encountered and explained in Section 2.1.3 as a feature of the Landau theory of bilinearly coupled order parameters. The expected phase diagram for our experiment is thus shown in Figure 4.4(b). The structural distortion's temperature dependence gives a dome-like twinned region, which is crossed via a first-order transition when cooling down at fixed strain $|\langle \varepsilon_a \rangle| < \varepsilon_S(T)$ and $\langle \varepsilon_a \rangle \neq 0$. In cooling down at a constant strain beyond this, there may still be a nematic crossover even though the sample strain is now held fixed; probing the electric properties in this regime is our initial motivation. In our setup, strain may appear to be a less-than-ideal tuning parameter – after all it is not the proper conjugate field to the nematic order parameter. However, it allows us to conduct measurements through the boundary from a twinned to detwinned crystal which, as we will see, allows the phase space of the broken symmetry state to be mapped out, and several other important observations to be made.

4.2.2 High temperature

We start again at high temperatures, initially following an analogous presentation of data to Section 4.1. Figure 4.5(a) shows the behaviour of $\rho(T)$ under $\langle 110 \rangle_T$ strain near T_S, and in comparison to $\langle 100 \rangle_T$ strain the response is striking. At zero strain we observe the same upward cusp in $\rho(T)$, and in compression the large response is twofold – the temperature at which the cusp occurs decreases rapidly, as does the resistivity

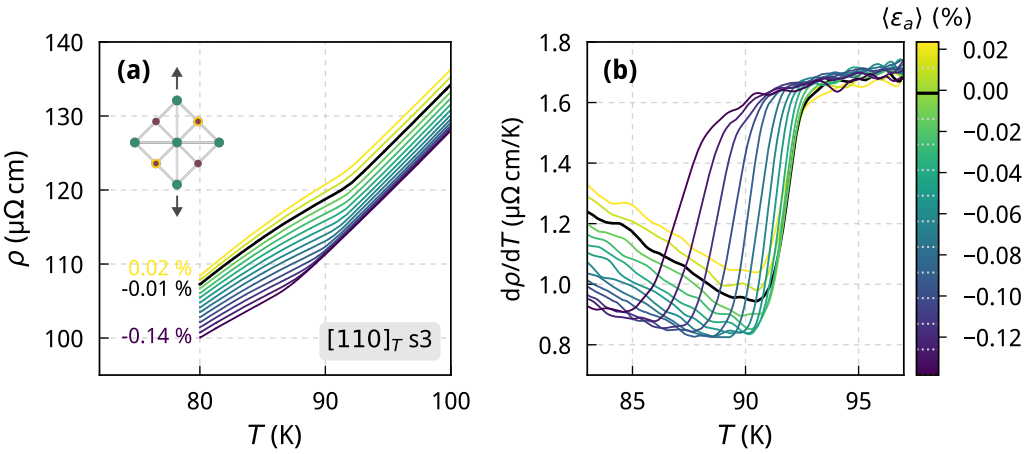

Figure 4.5 | Response of resistivity to $\langle 110\rangle_T$ strain near the structural transition. **(a)** An upward cusp signifies entry into the twinned phase, at a temperature $T_S(\langle\varepsilon_a\rangle)$ which decreases with strain. Resistivity also drops rapidly with compression, indicating a large elastoresistivity. The temperature is ramped at 100 mK/min and strain changed at 104 K. **(b)** The reduction in $T_S(\langle\varepsilon_a\rangle)$ is shown more clearly in the first derivative $\mathrm{d}\rho/\mathrm{d}T$. In these plots the sweep closest to zero strain is highlighted in black.

itself. If the cusp represents the transition into the twinned state, then its rapid shift to lower temperature matches our expectations from the previous section. We expect $T_{\text{cusp}} \to 0$ as $\langle\varepsilon_a\rangle \to \pm|\varepsilon_S(T \to 0)|$. Despite the transition now being first order at finite strain, the qualitative shape is similar to that of $\langle 100\rangle_T$ strain. In contrast, however, the elastoresistivity is greatly enhanced for $\langle 110\rangle_T$ strain with $(1/\rho)\,\mathrm{d}\rho/\mathrm{d}\langle\varepsilon_a\rangle\big|_{\langle\varepsilon_a\rangle=0} \sim 60$, compared to ~ 7 for $\langle 100\rangle_T$ strain. This is shown explicitly in Figure C.4 - a plot of $(1/\rho)\,\mathrm{d}\rho/\mathrm{d}\langle\varepsilon_a\rangle$ as a function of $\langle 100\rangle_T$ and $\langle 110\rangle_T$ strain at $T = 95$ K.

Using the same Gaussian peak fitting procedure introduced in Section 4.1, we extract the transition temperature T_S and width as a function of average $\langle 110\rangle_T$ strain from the peak in the second derivative. This is plotted for both strain directions in Figure 4.6. A dome-shaped temperature dependence of the structural distortion can now be distinguished. This can be seen more clearly in Figure C.2. The transition broadens only slightly as strain is applied, consistent with our expectation that it is stress rather than strain that is the conjugate field to the nematic order. The observed broadening is likely an artefact of the downward curvature in $T_S(\langle\varepsilon_a\rangle)$ and extrinsic strain inhomogeneity. That the transition remains narrow is also an early indication of

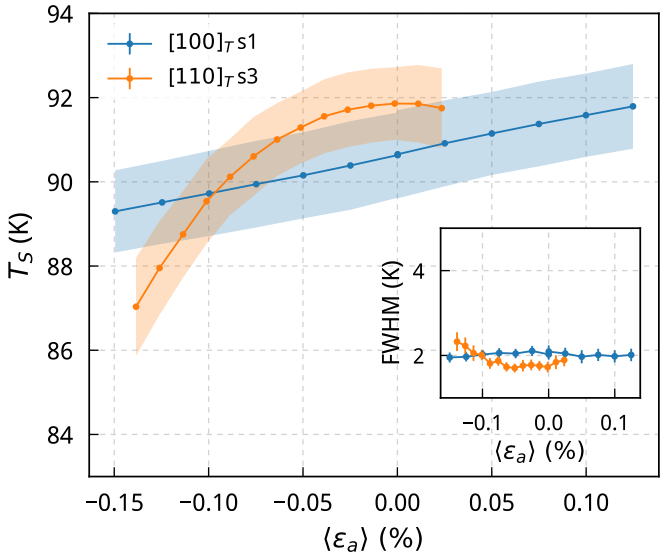

Figure 4.6 | Comparison of T_S as a function of $\langle 100\rangle_T$ and $\langle 110\rangle_T$ strain extracted from a Gaussian fit of $\mathrm{d}^2\rho/\mathrm{d}T^2$. The shaded region shows the transition width, taken from the full width at half maximum (FWHM), which is plotted separately in the inset.

low hysteresis in the formation of domains. A complete comparison of $T_S(\langle\varepsilon_a\rangle)$ for all samples measured, as well as a comparison of extraction methods, can be found in the Appendix – Section C.3. To summarise these plots: we observe the same qualitative behaviour of $T_S(\langle\varepsilon_a\rangle)$ for all three samples, and different extraction methods give the same values to within $\sim 0.3\,\%$ error at low strains.

The strong response of ρ to $\langle 110\rangle_T$ strain is a well-reported phenomenon in iron-based superconductors, albeit for a small strain range about zero [45, 93, 94]. This originates from the divergence of the nematic susceptibility as $T \to T_S^0$ from above, which can be directly measured through the induced resistivity anisotropy. Although we only measure ρ_{xx}, this divergence is still detected in our measurement as $\mathrm{d}\rho_{a,b}/\mathrm{d}\varepsilon \propto \mathrm{d}\phi/\mathrm{d}\varepsilon$, where ϕ is the nematic order parameter. This is observed more directly by measuring resistivity as a function of strain for fixed temperature, i.e. $\rho(\langle\varepsilon_a\rangle)$. This is shown in Figure 4.7 for temperatures near $T_S(\langle\varepsilon_a\rangle = 0)$. Panel (a) shows two different data sets spanning intermediate compression and tension, and we make the striking observation that $\rho(\langle\varepsilon_a\rangle)$ is non-monotonic and furthermore that the large elastoresistivity associated with the nematic polarisability only extends over a relatively small strain range of approximately $\pm 0.075\,\%$. Beyond this range the amplitude of the

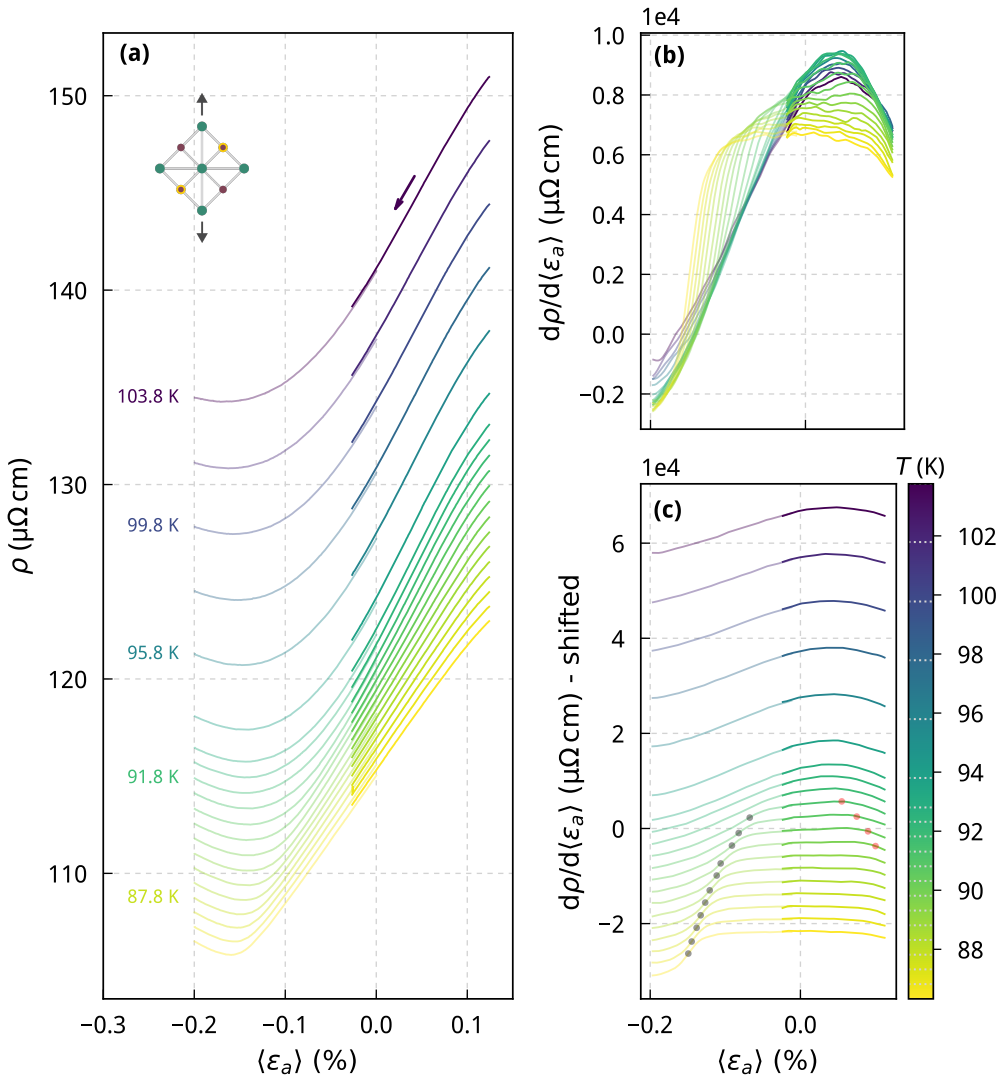

Figure 4.7 | (a) Resistivity $\rho(\langle\varepsilon_a\rangle)$ measured whilst ramping strain at constant temperature in a $\langle 110\rangle_T$ configuration. Only increasing strain-sweeps are shown, and T was changed at 0.04 % and −0.03 % for transparent and solid lines respectively. **(b)** First derivative $\mathrm{d}\rho/\mathrm{d}\langle\varepsilon_a\rangle$ of the strain ramps in panel (a). **(c)** As in panel (b), but shifted along the T-axis for clarity. Black points mark the peak in the second derivative $\mathrm{d}^2\rho/\mathrm{d}\langle\varepsilon_a\rangle^2$, and red points track the drop in the first derivative in tension – but by eye. This allows us to determine the neutral strain point.

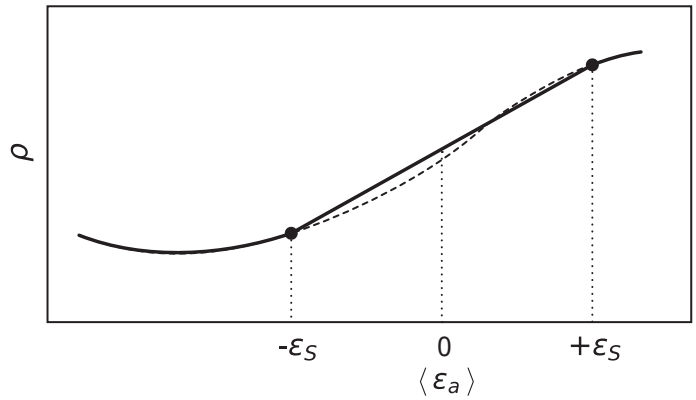

Figure 4.8 | Schematic explaining the flattening in $\mathrm{d}\rho/\mathrm{d}\langle\varepsilon_a\rangle$ around zero strain. The formation of domains for $-\varepsilon_S < \langle\varepsilon_a\rangle < +\varepsilon_S$ makes the underlying $\rho(\varepsilon_a)$ curve inaccessible. Within this range, strain tunes the volume ratio of domains giving a linear interpolation between $\rho(-\varepsilon_S)$ and $\rho(+\varepsilon_S)$.

underlying nematic order must either saturate, or start to decouple from the transport – we will discuss this further in Section 4.3. This is more readily visible in the first derivative $\mathrm{d}\rho/\mathrm{d}\langle\varepsilon_a\rangle$, shown in panel (b), which at 104 K drops to half its $\langle\varepsilon_a\rangle = 0$ value by −0.075 % strain. In this panel the diverging elastoresistivity is just visible for $T > T_S(\langle\varepsilon_a\rangle = 0)$, where $(1/\rho)\,\mathrm{d}\rho/\mathrm{d}\langle\varepsilon_a\rangle$ rises from ∼ 56 at 104 K to ∼ 74 at 92 K.

Below $T_S(\langle\varepsilon_a\rangle = 0) \sim 92\,\mathrm{K}$, a different behaviour emerges in the $\rho(\langle\varepsilon_a\rangle)$ curves; the slope becomes nearly constant over a range of applied average strain around $\langle\varepsilon_a\rangle = 0$. This is easy to explain, and follows on from the understanding that we fix the average but not local strain. The sample breaks up into domains for $-\varepsilon_S(T) < \langle\varepsilon_a\rangle < +\varepsilon_S(T)$ and within this range $\langle\varepsilon_a\rangle$ determines the relative volume ratio of the two domain types. The volume ratio should be close to its equilibrium value for a given $\langle\varepsilon_a\rangle$, under the condition that domain walls are only weakly pinned. In our data this is indicated by the small hysteresis between increasing and decreasing strain sweeps. Domains are oriented at 90° to one another, meaning $\rho_{xx} = \rho_a$ for $+\varepsilon_S$ domains, and $\rho_{xx} = \rho_b$ for $-\varepsilon_S$ domains. Therefore for $|\langle\varepsilon_a\rangle| < |\varepsilon_S(T)|$, as we redistribute domains, we may guess that $\rho(\langle\varepsilon_a\rangle)$ is a linear weighted average of ρ_a and ρ_b, giving a nearly-constant slope in $\mathrm{d}\rho/\mathrm{d}\langle\varepsilon_a\rangle$. $\rho(\langle\varepsilon_a\rangle)$ becomes linear in the limit that domain formation does not cause redistribution of the current into lower-resistivity domains. This is the case if domains are small – which we expect as the sample is thin and fixed rigidly to the platform – and if the resistivity anisotropy is not too large; we will later show it to be less than 10 %. Deviations from linearity may also occur in our setup due to the additional

application of symmetric $\varepsilon_{A_{1g}}$strain which also couples locally – however based on observations under $\langle 100\rangle_T$ strain we expect the response to this to be small. The scenario we describe is shown schematically in Figure 4.8, where the underlying $\rho(\varepsilon)$ curve is inaccessible between $-\varepsilon_S$ and $+\varepsilon_S$ and a linear interpolation of the resistivity between these points is observed instead. This neatly explains why the cusp in $\rho(T)$ at $T = T_S$ is upward for unstressed FeSe: the underlying $\rho(\varepsilon_a)$ curve is concave up at $\varepsilon_a = 0$ and so is smaller at this strain than a linear interpolation between $\pm\varepsilon_S$. $\rho(\langle\varepsilon_a\rangle)$ becomes concave down beyond $\langle\varepsilon_a\rangle \sim 0.07\,\%$ and so we expect a downward cusp in $\rho(T)$ beyond this strain.

Returning to Figure 4.7, the breaks (i.e. abrupt changes in slope) in $\mathrm{d}\rho/\mathrm{d}\langle\varepsilon_a\rangle$ can now be understood as originating from the kink in $\rho(\langle\varepsilon_a\rangle)$ at $\pm\varepsilon_S$. For a given strain ramp we can therefore extract $\varepsilon_S(T)$ from this feature, and do so via the peak in the second derivative $\mathrm{d}^2\rho\big/\mathrm{d}\langle\varepsilon_a\rangle^2$. Panel (c) shows $-\varepsilon_S(T)$ points (in black) on top of $\rho(\langle\varepsilon_a\rangle)$ offset by temperature. On average, the difference in $-\varepsilon_S(T)$ between increasing and decreasing strain ramps is $0.006\,\%$ – this highlights the small hysteresis size. As seen from the shape of $\rho(\langle\varepsilon_a\rangle)$ just above the transition, the change in slope at $-\varepsilon_S$ will be larger than at $+\varepsilon_S$, and this explains why the feature in $\mathrm{d}\rho/\mathrm{d}\langle\varepsilon_a\rangle$ is larger in compression than in tension. This, combined with the limited tension range of our measurement, means that we cannot extract $+\varepsilon_S(T)$ points using $\mathrm{d}^2\rho\big/\mathrm{d}\langle\varepsilon_a\rangle^2$. Knowledge of $+\varepsilon_S(T)$ is useful as the symmetric evolution of $\pm\varepsilon_S$ about the neutral strain point allows us to determine $\langle\varepsilon_a\rangle = 0$. In tracking $+\varepsilon_S(T)$ by eye from the initial decrease in $\mathrm{d}\rho/\mathrm{d}\langle\varepsilon_a\rangle$ (red points) we can identify zero strain to within an absolute strain error of $\pm 1 \times 10^{-4}$. The capacitance corresponding to zero strain extracted from this plot is used to calibrate the strain scale for all plots of this sample.

4.2.3 Intermediate temperatures

When conducting temperature ramps it becomes harder to identify the transition at higher strains due to intrinsic broadening from the increasing downward curvature of $\varepsilon_S(T)$, and conversely it should in principle become easier for strain ramps. However, to track $\varepsilon_S(T)$ down to low temperatures we need to extend our strain range much further in compression. This leads us to a technical issue which we must first address.

Plastic deformation

From published data [90], we expect that asymmetric strains larger than $0.27\,\%$ are needed to exceed the structural distortion at low temperatures. Achieving such

	Shorthand	Ramp parameter	Comment
1	TI	Temperature	Plastic deformation 1
2	SI	Strain	Shift by $\Delta\varepsilon_{xx,p} = -0.016\,\%$
3	TII	Temperature	Plastic deformation 2
4	SII	Strain	Shift by $\Delta\varepsilon_{xx,p} = -0.073\,\%$

Table 4.1 | Table showing the order of measurements during which plastic deformation occurred, and the shifts needed to correct strain-ramp data.

conditions in our experimental setup would require a longitudinal platform strain in excess of $\varepsilon_{xx,p} = 2\varepsilon/(1+\nu_{\text{eff}}) \sim 0.42\,\%$. This is problematic for a platform constructed from commercial pure (grade 2) titanium, which as discussed in Section 3.3.6 has a yield limit of 0.18 %–0.45 % [170, 184]. In applying large compressions to the platform, we exceeded its elastic limit, resulting in plastic deformation (PD) which affects all subsequent presentation of data.

Measurements were conducted in the order shown in Table 4.1, and alternate between temperature and strain as ramp parameters, the former coming first. The $\rho(T)$ curves near T_S shown in Figure 4.7 were obtained in the first set of temperature ramps (TI), and the subsequently-presented strain-ramp data in Figure 4.7 in SI. Based on evidence that we will now present, plastic deformation occurred twice, both times during temperature ramps in compression.

In both cases, we first increased the strain incrementally up to some maximum compression during T ramps. Subsequently conducting $\langle \varepsilon_a \rangle$ ramps not exceeding the previous maximum compression, and comparing to constant-temperature cross sections from the T-ramp data, there is a clear discrepancy at low strains. The signal then tracks this new line with little hysteresis. This is shown for the second (larger) occurrence of plastic deformation in Figure 4.9. In panel (a) we plot against the capacitive-sensor readout. In the order that measurements were taken, we show: (SI) a strain ramp to modest compression; (TII) temperature ramps under incrementally increasing compressions extending beyond that of previous strain ramp, shown as cross-sections; (SII) a strain ramp back towards zero from the highest compression reached in T ramps. Both increasing (light) and decreasing (dark) strain ramps are plotted, and the hysteresis between them is small. This is shown for several temperatures.

The low-strain behaviour of the first and second strain ramps can be matched by a single shift of SII into compression, as shown in panel (b). This is consistent with the generic stress-strain curve of a metal which begins to flatten beyond the

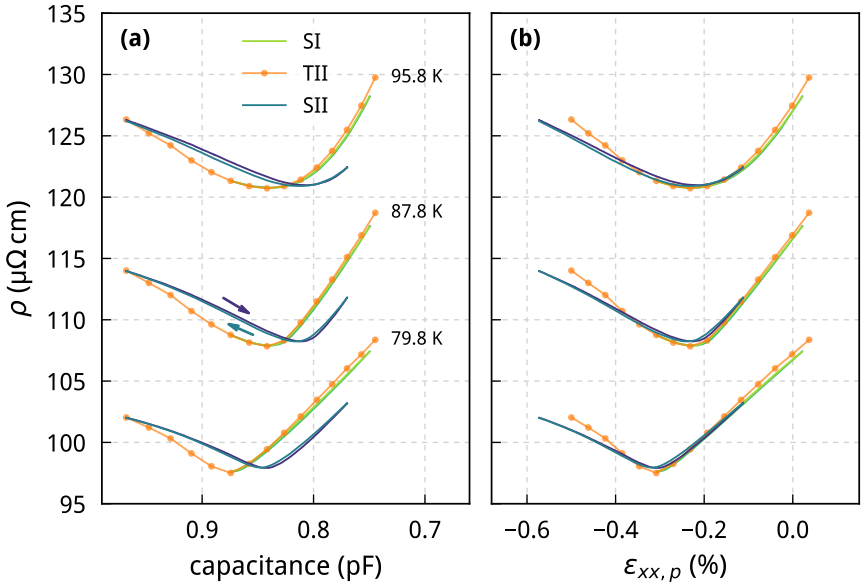

Figure 4.9 | Plastic deformation of the platform. **(a)** SI: strain ramps to intermediate strain, TII: cross sections from temperature ramps exceeding the maximum strain of SI, SII: strain ramps not exceeding the maximum strain of TII. These are plotted against the capacitive sensor readout. **(b)** As in panel (a), but shifting SII by 0.073 % into compression to match low-strain behaviour. We now plot against the longitudinal platform strain.

yield point, and is followed by a near-linear response upon returning back to zero, tracing a new line and giving a finite, locked-in 'plastic strain' at zero stress. When the platform deforms plastically under compression, ε_{xx} becomes more negative, and ε_{yy} more positive for a given stress than if it were deforming elastically. This causes opposing changes in the magnitude of symmetric and asymmetric strains, with the latter increasing. For asymmetric strain, to which the electronic response is larger, we 'lock in' an additional amount of strain. Returning to panel (b), a shift of SII by $\Delta\varepsilon_{xx,p} = -0.073\%$* is required to match low-strain data, and the small hysteresis of post-plastic-deformed data agrees with our generic expectation. The occurrence of plastic deformation beyond $\varepsilon_{xx,p} \sim -0.35\%$ in the unshifted T-sweep cross sections is now clearly apparent. The first strain ramps were conducted only at high temperatures, and so evidence that this shift works at low temperature relies on a comparison between TII and SII. Existence of domain walls, which we will later discuss, causes a qualitative

*This is equal to $\Delta\langle\varepsilon_a\rangle = -0.047\%$.

difference between T and $\langle \varepsilon_a \rangle$ ramps, and so this does not work. The first (smaller) plastic deformation is analogously corrected by a single shift of $\Delta\varepsilon_{xx,p} = -0.016\,\%$. This occurred gradually during temperature ramps beyond $\varepsilon_{xx,p} \sim -0.23\,\%$ which must correspond to the elastic limit of titanium used in our platforms. Both PD shifts are shown in Table 4.1. The T-ramp data already presented (Figure 4.5) excludes curves affected by plastic deformation, and $\langle \varepsilon_a \rangle$-ramp data already presented (Figure 4.7) are shifted by the first PD correction. All subsequent strain-sweep data are shifted by the second PD correction.

Owing to the fact that strain ramps did not exceed the maximum compression of temperature ramps, correcting $\rho(\langle \varepsilon_a \rangle)$ data is uncomplicated; a single shift parameter is needed for each PD occurrence. Correction of temperature-sweep strains is possible, but this must be conducted individually for each ramp, and thus with care. Our method for handling such corrections is shown and explained in Figure C.5, and henceforth we explicitly distinguish data points which have been individually shifted in strain. Both raw and corrected versions of strain and temperature ramps are shown in the supplementary plot Figure C.7 for the full temperature range.

Scattering theory provides a final piece of evidence to distinguish the behaviour of an elastic sample on a plastically deforming substrate, from the reverse situation in which the platform remains elastic. Plastic deformation of the sample would result in the introduction of dislocations, which would cause an irreversible increase of the resistivity. We do in fact observe a maximum increase of $\sim 0.4\,\mu\Omega$cm between the first and second strain sweeps at high temperatures, and calculate that this corresponds to an additional mean free path from defects alone of $1.2\,\mu$m*. This is a much lower defect density than that expected from plastic deformation.

Tracking $\varepsilon_S(T)$

Returning to our objective of tracking $\varepsilon_S(T)$ down to low temperatures, we conduct strain ramps at temperatures from 96 K to 15 K and at strains of $-0.09\,\%$ to $-0.39\,\%$, as shown in Figure 4.10. Panel (a) shows both increasing (solid) and decreasing (dashed) strain ramps $\rho(\langle \varepsilon_a \rangle)$, and panels (b) and (c) unshifted and shifted first derivatives $\mathrm{d}\rho/\mathrm{d}\langle \varepsilon_a \rangle$. It is important to note that for all these ramps the temperature is changed at $\langle \varepsilon_a \rangle = -0.39\,\%$ (i.e. outside the twinned phase), and the strain scale has been corrected for plastic deformation as previously discussed.

*Taking a semiclassical approach and working in the relaxation-time approximation, we first assume a parabolic 2D Fermi surface and then apply this to all the Fermi surfaces of FeSe, assuming the same mean free path for each.

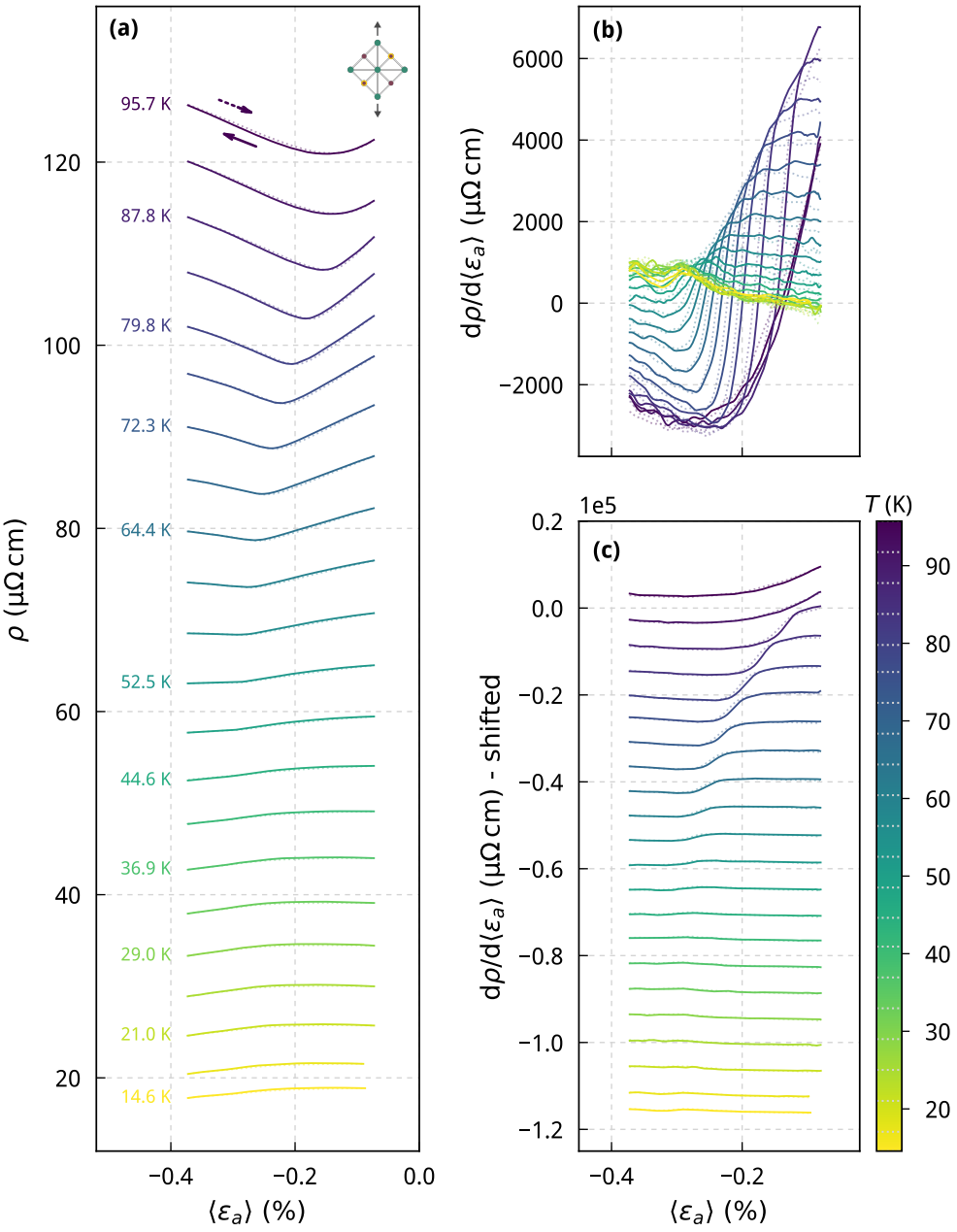

Figure 4.10 | (a) Strain ramp at constant temperature $\rho(\langle\varepsilon_a\rangle)$ along the $\langle 110\rangle_T$ direction. The temperature is changed at $-0.39\,\%$ and both decreasing (solid) and increasing (dashed) ramps are shown. **(b-c)** First derivative $\mathrm{d}\rho/\mathrm{d}\langle\varepsilon_a\rangle$ for the ramps shown in panel (a). These are shifted according to their temperature for clarity in panel (c).

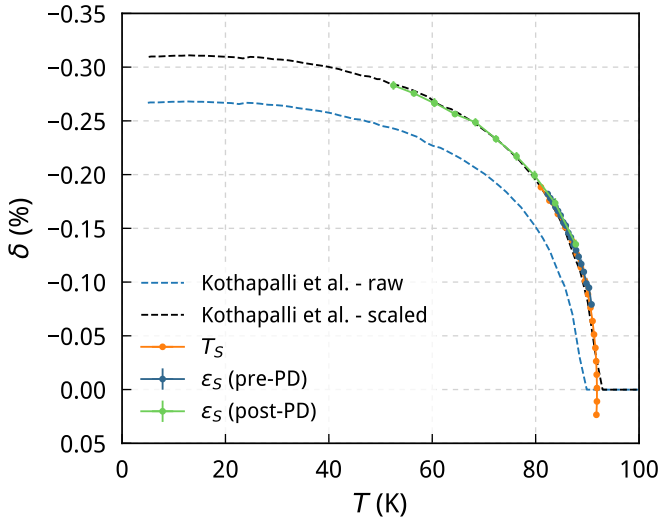

Figure 4.11 | Variation of the spontaneous structural distortion δ with temperature. Here, $\varepsilon_S(T)$ is extracted from $\rho(\langle\varepsilon_a\rangle)$ ramps, and $T_S(\langle\varepsilon_a\rangle)$ from $\rho(T)$ ramps. This is only possible down to $\sim 50\,\mathrm{K}$ due to a change in behaviour for lower temperatures. Our data are compared with the orthorhombic distortion from X-ray diffraction data, Ref. [90], which can be scaled to match ours by 1.034 along T and 1.16 along δ.

There are again clear breaks in $\mathrm{d}\rho/\mathrm{d}\langle\varepsilon_a\rangle$ – shown in panel (b), which we once more track via the peak in the second derivative $\mathrm{d}^2\rho/\mathrm{d}\langle\varepsilon_a\rangle^2$. This feature is observable below 88 K and can be tracked down to $\sim 50\,\mathrm{K}$ (shown in Figure C.6), below which a qualitative change in the behaviour of $\rho(\langle\varepsilon_a\rangle)$ complicates further extraction. The hysteresis in the location of the transition remains very small down to at least 50 K. Some hysteresis is apparent in $\rho(\langle\varepsilon_a\rangle)$ on the low-strain side of the transition. This hysteresis closes at a strain that neatly matches $-\varepsilon_S(T)$ (shown clearly in a later plot, Figure 4.18), indicating that it corresponds to hysteresis in the density of twin boundaries, and that the domains become fully polarised for $\langle\varepsilon_a\rangle < -\varepsilon_S$.

Having determined $\varepsilon_S(T)$ from two sets of strain ramps, as well as $T_S(\langle\varepsilon_a\rangle)$ from temperature ramps at low strains, we can now plot the temperature-dependence of the spontaneous structural distortion $\delta(T)$. This is shown in Figure 4.11, and we observe the expected evolution of the order parameter for a second-order phase transition. For comparison, the zero pressure data of Kothapalli et al. [90] are also plotted. They directly determined the orthorhombic distortion $(a-b)/(a+b)$ for single crystalline FeSe through measurement of in-plane lattice constants using X-ray diffraction (shown

in Figure 2.10). Although the individual error bars on our data points, originating from the difference in ramp directions, are small, other uncertainties in our strain scale should be considered to understand the discrepancy. Firstly, zero strain is only determined to within a strain of ±0.01 %. Secondly, the conversion to asymmetric strain incurs a large uncertainty from the experimental determination of ν_{eff} (Table 3.4). Here the error is $\Delta\varepsilon/\varepsilon \sim \Delta\nu_{\text{eff}}/(1+\nu_{\text{eff}}) \sim 0.08$, and this uncertainty could account for the difference between our curve and the published data.

To extrapolate the low-temperature values of $\varepsilon_S(T)$ for our sample, several approaches can be taken. One method is to scale the X-ray data to match ours, which is possible with factors of 1.034 and 1.16 for the temperature and strain axes respectively, as shown in Figure 4.11. Alternatively, if we assume the magnitude of the distortion will not become any smaller below our lowest-temperature ε_S point, then we can linearly extrapolate to zero between upper and lower bounds. This extrapolation provides a bound that does not rely on the measured values of others.

Domain-wall scattering

So far we have only compared T- and $\langle\varepsilon_a\rangle$-ramp data at high temperatures to correct for the effects of plastic deformation. Extending this comparison to low temperatures using now-corrected data, a qualitative difference is observed between these two ramp parameters. In Figure 4.12 panels (a) and (b) we plot cross sections of temperature ramp data (indicated by markers) with strain ramps $\rho(\langle\varepsilon_a\rangle)$ at the same temperature, for both 41 K and 17 K. Both start from outside the phase ($T > T(\langle\varepsilon_a\rangle = 0)$ for T ramps, and $\langle\varepsilon_a\rangle < -\varepsilon_S(T)$ for $\langle\varepsilon_a\rangle$ ramps), where the strain/temperature is also incremented. A pronounced triangle-like dependence can be seen in the temperature-ramp data, which are peaked at $\langle\varepsilon_a\rangle \sim -0.03\,\%$. This is in contrast to the flatter response in $\langle\varepsilon_a\rangle$ ramps, and we attribute this difference due to domain-wall scattering, as we now explain.

As already established, we only control the average strain for $|\langle\varepsilon_a\rangle| < \pm\varepsilon_S$, within which we tune the population of domains. Ignoring any effects of pinning, the size of these domains for a given population distribution is determined in equilibrium through minimisation of elastic and domain-wall energies. It is first necessary to understand how we influence these two energy contributions. The elastic energy, i.e. energy required to deform the sample, is large if the sample-platform bonding is strong – as it is in our case – and/or if the deformation itself is large. The energy cost for creating a static twin boundary below a second order transition is expected to be proportional to $|T - T_S|^{3/2}$ [5], and thus largest for $T \ll T_S$. If the elastic energy is large compared to the domain-wall energy, then twin-boundary creation is favoured, domains are small

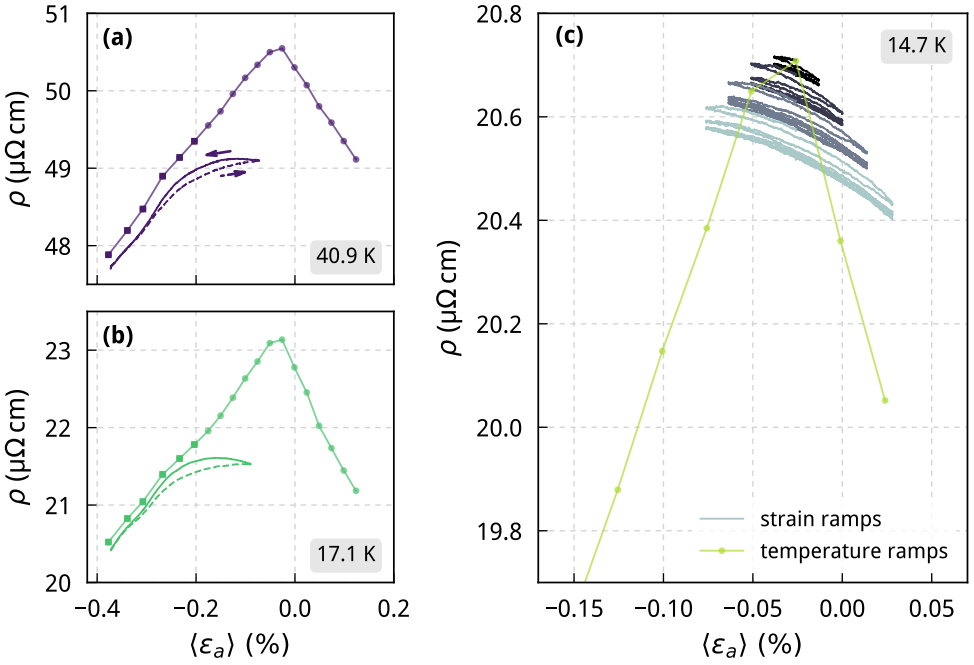

Figure 4.12 | Evidence of domain walls from comparison of $\rho(T)$ and $\rho(\langle \varepsilon_a \rangle)$ under $\langle 110 \rangle_T$ strain. **(a-b)** Comparison of T and $\langle \varepsilon_a \rangle$ ramps at $\sim 41\,\mathrm{K}$ and $\sim 17\,\mathrm{K}$. The ρ scaling is equal in both. Square markers indicate points individually shifted in strain to compensate for plastic deformation. **(c)** 'Wiggling' experiment, in which the strain is repeatedly swept back and forth between symmetrically-increasing limits at a constant temperature of $14.7\,\mathrm{K}$. This is compared to a cross-section of T-ramp data taken at the same temperature.

and the density of walls high. Scattering from these twin boundaries then contributes an extrinsic source of resistance we which can measure.

In cooling down the sample at zero strain, in equilibrium there should be an equal population of domain types, and a maximal density of domain walls as the elastic energy due to the mismatch between the average and local strain is maximum. Although the energy cost of domain-wall creation is expected to increase upon cooling, this is offset by the increasing elastic energy cost from the growing orthorhombic distortion. The additional rapid reduction in the sample's intrinsic resistivity upon cooling means that domain-wall scattering becomes observable at lower temperatures. This explains why we observe a peak near zero strain, and why this is only apparent

at low temperatures. In increasing the average strain away from zero, the average strain-local strain mismatch is reduced, reducing the equilibrium domain wall density for a given temperature and subsequently reducing the resistance. This occurs on top of an underlying change due to the resistivity anisotropy and change of domain population. The orthorhombic distortion is 90 % saturated below $\sim 50\,\mathrm{K}$ and so the peak height should be approximately temperature-independent below this temperature; our observations support this.

We now turn to strain-ramp data, which start to deviate from the temperature ramps below 70 K (Figure C.7). During these strain ramps the sample starts off completely detwinned, and entry into the twinned phase gives a small but sudden increase in $\rho(\langle\varepsilon_a\rangle)$, indicating the initial creation of domain walls. Upon sweeping strain in the reverse direction we observe hysteresis which closes abruptly for $\langle\varepsilon_a\rangle < -\varepsilon_S$, indicating complete removal of domain walls. Saturation of $\rho(\langle\varepsilon_a\rangle)$, and thus of the creation of domain walls, within the phase is explained by an insufficiency of thermal energy and this is supported by a larger difference between $\rho(T)$ and $\rho(\langle\varepsilon_a\rangle)$ at lower temperatures. We therefore describe the effect of sweeping strain as an 'annealing out' of domain walls. This can be seen more clearly by conducting a controlled test, as shown in Figure 4.12(c), in which we cool down close to zero strain from outside of the phase, and at $\sim 15\,\mathrm{K}$ repeatedly oscillate the strain between symmetric limits. Doing so causes the the resistance to irreversibly decrease, and then saturate. Increasing the oscillation amplitude again causes a further decrease which again saturates. During this measurement the temperature was stable to within $\delta T \sim 5\,\mathrm{mK}$, and $\delta T(\mathrm{d}\rho/\mathrm{d}T) \sim 5\times10^{-3}\,\mu\Omega\mathrm{cm}$ meaning this cannot originate from a temperature drift.

Resistivity anisotropy

Based on the closing of hysteresis for $\langle\varepsilon_a\rangle < -\varepsilon_S$ we can assume a complete polarisation of domains at $\langle\varepsilon_a\rangle = \pm\varepsilon_S$, and as such our measurement of $\rho(\langle\varepsilon_a\rangle)$ across $-\varepsilon_S$ allows us to extract the resistivity along the short length of the nematic domain, i.e. ρ_b, under no additional asymmetric strain. Based on our measurements under $\langle 100\rangle_T$ strain, and the fact that $\varepsilon_a/\varepsilon_s \sim 1.9$ (where ε_s is the symmetric strain) we assume negligible response in ρ from symmetric strain. Under this assumption, $\rho(-\langle\varepsilon_a\rangle)$ is equivalent to measuring an unstressed but detwinned crystal. We will later discuss the extent to which this assumption is true. Strictly speaking, proper determination of ρ_a, and thus the resistivity anisotropy, would require either large applied tensions or a sample/contact configuration allowing measurement of both longitudinal and

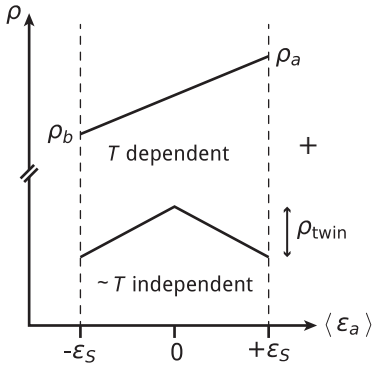

Figure 4.13 | Resistivity contributions within the twinned phase. Top: contribution from domain redistribution which linearly varies between $\rho(-\varepsilon_S)$ and $\rho(+\varepsilon_S)$. This is strongly temperature-dependent. Bottom: domain-wall scattering contribution. In equilibrium, maximal wall density occurs at zero strain and decreases symmetrically until $\langle \varepsilon_a \rangle = \pm\varepsilon_S$.

transverse resistivity. However, we can still estimate it from our data.

As shown in Figure 4.13, we know that within the twinned phase for $-\varepsilon_S \leq \langle \varepsilon_a \rangle \leq +\varepsilon_S$ there are two contributions to $\rho(\langle \varepsilon_a \rangle)$ determined from temperature ramps. The primary contribution is from domain redistribution which under the conditions explained in Section 4.2.2, and if ignoring symmetric $\varepsilon_{A_{1g}}$ strain, should be a linear interpolation between $\rho(-\varepsilon_S) = \rho_b$ and $\rho(+\varepsilon_S) = \rho_a$. At low temperatures, the contribution from twin-boundary scattering becomes discernible, and as explained in the previous section this should be symmetric about $\langle \varepsilon_a \rangle = 0$ and become approximately zero at $\langle \varepsilon_a \rangle = \pm\varepsilon_S$. Assuming this dependence of $\rho(\langle \varepsilon_a \rangle)$, the resistivity anisotropy $(\rho_a - \rho_b)/(\rho_a + \rho_b)$ is simple to extract. In conducting linear fits in the ranges $-\varepsilon_S < \langle \varepsilon_a \rangle < 0$ (denoted 'L') and $0 < \langle \varepsilon_a \rangle < \varepsilon_S$ (denoted 'R') – as shown in Figure 4.14 – and taking the gradient $\mathrm{d}\rho/\mathrm{d}\langle \varepsilon_a \rangle$, then

$$\rho_a - \rho_b = \varepsilon_S \left[\left(\frac{\mathrm{d}\rho}{\mathrm{d}\langle \varepsilon_a \rangle} \right)_{\mathrm{L}} + \left(\frac{\mathrm{d}\rho}{\mathrm{d}\langle \varepsilon_a \rangle} \right)_{\mathrm{R}} \right], \tag{4.1}$$

where $\left(\frac{\mathrm{d}\rho}{\mathrm{d}\langle \varepsilon_a \rangle} \right)_{\mathrm{R}}$ is positive above $\sim 55\,\mathrm{K}$ and negative below (see Figure C.10). The resistivity anisotropy is calculated by dividing Equation 4.1 by

$$\rho_a + \rho_b = 2\rho_t \approx 2\left[\rho(\langle \varepsilon_a \rangle = 0) - \rho_{\mathrm{wall}}\right], \tag{4.2}$$

where ρ_t is the resistivity of a fully twinned sample at zero stress, and ρ_{wall} is a temperature-independent contribution from domain walls at zero strain. From the average difference between $\rho(\langle \varepsilon_a \rangle)$ from T- and $\langle \varepsilon_a \rangle$-ramps at zero strain and temperatures below 50 K, we estimate $\rho_{\mathrm{wall}} \sim 1.3\,\mu\Omega\mathrm{cm}$. At high temperatures where the domain-wall contribution becomes negligible and $\left(\frac{\mathrm{d}\rho}{\mathrm{d}\langle \varepsilon_a \rangle} \right)_{\mathrm{L}} \simeq \left(\frac{\mathrm{d}\rho}{\mathrm{d}\langle \varepsilon_a \rangle} \right)_{\mathrm{R}}$, this is equivalent to fitting a single line across the complete $2\varepsilon_S$ range. In our case the peak in $\rho(\langle \varepsilon_a \rangle)$ does not occur precisely at $\langle \varepsilon_a \rangle = 0$, but at $\sim -0.03\,\%$ (within the error of the zero

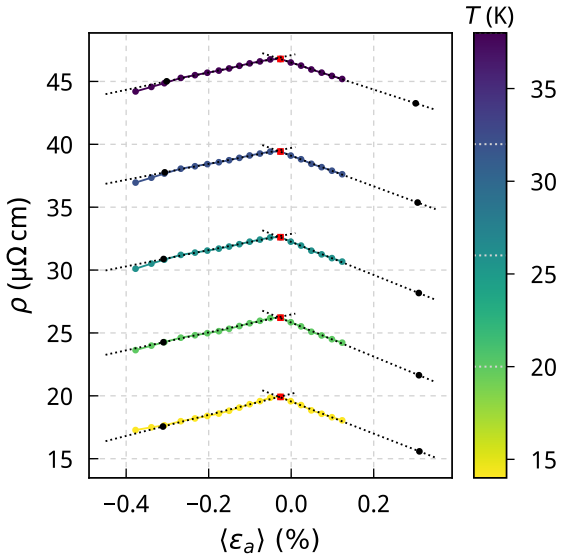

Figure 4.14 | Method for extracting the resistivity anisotropy from cross-sections of $\rho(T)$. At low temperature, the linear dependencies either side of $\langle\varepsilon_a\rangle \sim -0.03\,\%$ are fitted by straight lines. The peak around which the fit is conducted is shown by the red marker and black markers show $\pm\varepsilon_S$. In this case, scaled X-ray data have been used for low-temperature ε_S determination.

point used to define the strain axis), and so we instead fit to either side of the peak up to $\pm\varepsilon_S$. Doing so would introduce a small error if using Equation 4.1, as this equation assumes that the two lines have the same ρ-intercept. We account for this by extracting ρ_b and ρ_a directly through extrapolation of the linear fits to $\pm\varepsilon_S$.

A similar procedure is possible using strain- rather than temperature-ramp data. At high temperatures where domain walls do not contribute, this is achieved using the same method as above. We can account for the non-linearity of high-temperature strain ramps by fitting a quadratic and taking the gradient at zero strain, i.e. $\rho_a - \rho_b = 2\varepsilon_S \left.\mathrm{d}\rho/\mathrm{d}\epsilon\right|_{\langle\varepsilon_a\rangle=0}$. In this case, dividing by $\rho_a + \rho_b \approx 2\rho(\langle\varepsilon_a\rangle = 0)$ is complicated by the strain ramps not passing through zero, and this value must be extrapolated from the quadratic fit. Although using strain ramps is appealing due to the density of data points, at low temperatures we do not measure an in-equilibrium contribution from domain walls and so the resistivity deviates from that illustrated in Figure 4.13. This weakens the reliability of resistivity anisotropy values extracted using this method.

The resistivity anisotropy determined using each of these methods, via $\rho(T)$ and $\rho(\langle\varepsilon_a\rangle)$, is plotted in Figure 4.15, in which we also mark $T_S(\langle\varepsilon_a\rangle = 0)$: the temperature above which we expect the anisotropy to be zero. In both cases an average of strain ramps in each direction is taken, with error bars indicating the difference. As such, the error bars do not reflect the strain scale uncertainty or quality of the linear fit, but rather the size of hysteresis, which is much larger for strain than temperature ramps – as seen in Figure 4.15. $(\rho_a - \rho_b)/(\rho_a + \rho_b)$ rises sharply below $T_S(\langle\varepsilon_a\rangle = 0)$, peaking at 9 % at around 82 K. It then steadily decreases, becoming negative at approximately

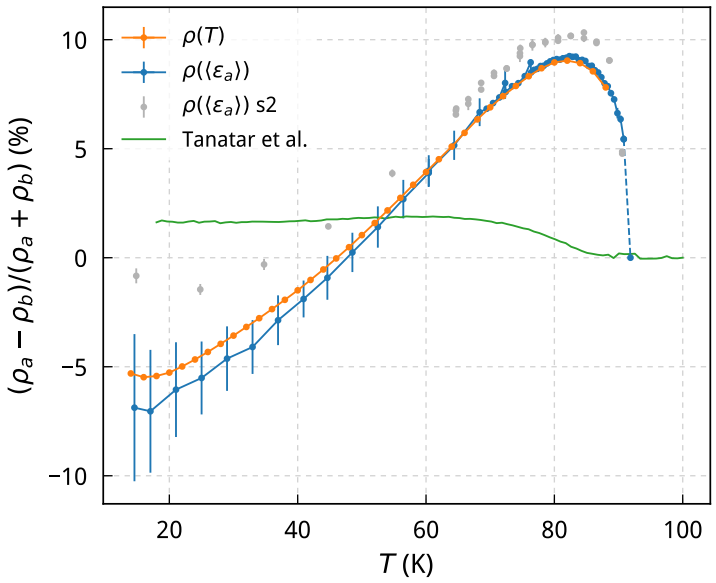

Figure 4.15 | Temperature-dependent resistivity anisotropy $(\rho_a-\rho_b)/(\rho_a+\rho_b)$ within a nematic domain. $\rho_a-\rho_b$ is extracted from linear fitting to $\rho(T)$ cross sections, and quadratic fitting to $\rho(\langle\varepsilon_a\rangle)$ curves. In both cases we take $\rho_a+\rho_b = 2\rho(\langle\varepsilon_a\rangle = 0)$, and for $\rho(T)$ subtract a temperature-independent domain-wall contribution. A marker is added at $T_S(\langle\varepsilon_a\rangle = 0)$ above which we expect the restive anisotropy to be zero. We additionally plot equivalent analysis from $\rho(\langle\varepsilon_a\rangle)$ of sample 2 and for comparison show the data of Tanatar et al. [91].

45 K. We observe a remarkable qualitative and quantitative contrast to previously published data from Ref. [91] which gradually peaks at 2 % and then remains positive and approximately constant down to low temperatures.

As expected, both extraction methods agree at high temperatures, and the less-reliable low-temperature $\rho(\langle\varepsilon_a\rangle)$ values anyway have large errors from the difference between increasing and decreasing strain directions. It is important to note that both these methods rely on low-temperature extrapolations of ε_S, as our extracted values extend only to 50 K. In this figure we use the scaled X-ray data, as shown in Figure 4.11. However, taking upper and lower bounds for the zero-temperature orthorhombic distortion based on our last extracted value does not change the qualitative features of our plot. This is demonstrated in Figure C.8, and the extraction methods are shown in Figures C.9 and C.10.

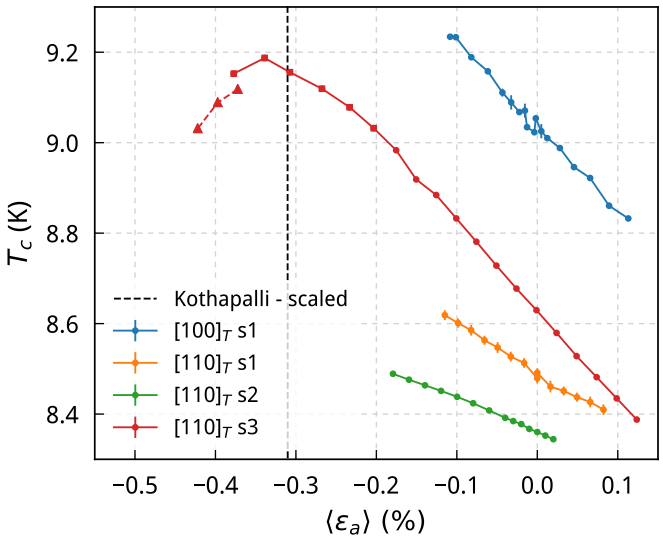

Figure 4.16 | Strain dependence of the superconducting transition temperature T_c for $\langle 100\rangle_T$ - and $\langle 110\rangle_T$ -oriented samples. $T_c(\langle\varepsilon_a\rangle)$ for the single $\langle 100\rangle_T$ sample is extracted from magnetic susceptibility, whereas for all three $\langle 110\rangle_T$ samples a slice of constant resistivity is used. For sample 3 (s3), square markers are used for points individually shifted in strain to correct for plastic deformation, whereas triangle markers are use for a high-compression dataset measured in a separate run.

Qualitative features of the resistivity anisotropy are reproduced by equivalent analysis of strain ramp data $\rho(\langle\varepsilon_a\rangle)$ from another sample (s2) – quickly peaking, then gradually decreasing and changing sign. We expect these data to be less reliable due to nonoptimal sample and epoxy dimensions, and discuss this later in combination with additional reasons that quantitative differences may occur.

4.2.4 Low temperature

We now focus on the response of the superconducting transition temperature T_c under $\langle 110\rangle_T$ strain. $T_c(\langle\varepsilon_a\rangle)$ extracted from resistivity, and averaged between increasing and decreasing temperature ramps for all three $\langle 110\rangle_T$ samples is shown in Figure 4.16. We observe an approximately linear dependence of T_c for $|\langle\varepsilon_a\rangle| < |\varepsilon_S|$ for all three samples. Resistivity ρ and magnetic susceptibility χ were simultaneously measured for samples 1 and 2, but extraction of T_c from susceptibility is made difficult by poor signal-to-noise levels and a small superconducting signature. Extracting T_c for sample 2 from the peak in $\mathrm{d}\chi/\mathrm{d}\langle\varepsilon_a\rangle$ and from a low-signal resistivity slice gives gradients of $-0.82\,\mathrm{K}/\%$ and

$-0.73\,\mathrm{K}/\%$ respectively – i.e. they agree to within 10 %. Extraction from susceptibility for sample 1 was too noisy for comparison, but a resistivity slice matching $T_c^{\chi}(\langle\varepsilon_a\rangle = 0)$ is plotted, and has a gradient of $-1.1\,\mathrm{K}/\%$. Only resistivity was measured for the main sample (sample 3), and linear fitting for $|\langle\varepsilon_a\rangle| < |\varepsilon_S|$ yields $\mathrm{d}T_c/\mathrm{d}\langle\varepsilon_a\rangle = -1.9\,\mathrm{K}/\%$; this differs notably from the previous two samples. For this sample, plastic deformation is individually corrected for at large compressions (as described in Section 4.2.3), and these points are indicated by square markers. A pronounced change in slope is observed at the highest compressions, peaking at $-0.34\,\%$. We compare the location of this peak with the value of the structural distortion from X-ray diffraction data scaled to match our data as shown by the dashed line. As already explained, these T ramps were preceded by strain ramps not exceeding the maximum compression reached when ramping temperature. Following this, we returned to measure $\rho(T)$ at even larger compressions, starting at 60 K; these points are indicated by triangle markers joined by dashed lines, and show a continuation of the positive slope. The discontinuity here is explained by a further increase of the plastic deformation during the intervening strain sweeps, and increasing the compression even further we expect additional plastic deformation of the platform to occur. Therefore, for these points the sample is experiencing a larger strain than indicated – however this does not affect the sign of the slope. For comparison, we also plot the previously presented dependence for the $\langle 100\rangle_T$ sample from susceptibility. This is linear with a slope of $-1.9\,\mathrm{K}/\%$.

In ramping $\langle 100\rangle_T$ strain, both $\varepsilon_{A_{1g}}$ and $\varepsilon_{B_{1g}}$ are varied locally, whereas for $\langle 110\rangle_T$ strain the structural instability reduces this to just the symmetric component $\varepsilon_{A_{1g}}$ in the range $|\langle\varepsilon_a\rangle| < |\varepsilon_S|$. Beyond this range, $\varepsilon_{B_{2g}}$ can also couple locally. The change in T_c for $\langle 110\rangle_T$ strains less than the structural strain reflects the response to just $\varepsilon_{A_{1g}}$, and a comparison to $\langle 100\rangle_T$ strain should highlight the $\varepsilon_{B_{1g}}$ asymmetric strain response. If making this comparison based purely on sample 3, we would draw the conclusion that $\varepsilon_{B_{1g}}$ asymmetric strain has little effect on T_c for $\langle 100\rangle_T$ strain – both are linear across the same range, with the same gradient. We do however observe significant sample-to-sample variation in the value of $\mathrm{d}T_c/\mathrm{d}\langle\varepsilon_a\rangle$ under $\langle 110\rangle_T$ strain, and therefore cannot be certain of this conclusion. It is likely that this variation is extrinsic and originates primarily from variations in sample quality, as we discuss further in the next section. A final observation: our measurements highlight the unconventional nature of superconductivity in FeSe, as the negative value of $\mathrm{d}T_c/\mathrm{d}\langle\varepsilon_a\rangle$ is against our expectation for a simple metal (with a single parabolic band) for which compression increases bandwidths and reduces the density of states at the Fermi level - thus reducing T_c.

4.3 Discussion

We first draw attention to the technical achievement of the measurements presented in this chapter. The delicate mechanical properties of FeSe pose a significant challenge for the application of large anisotropic pressures. Through development of a platform which is controllably pressurised along a single axis, and to which the sample can be fully adhered, we have successfully demonstrated the application of large strains of up to $\varepsilon_{xx} \sim -0.6\%$ longitudinally. A vital aspect of this development was precisely quantifying the transverse and longitudinal strains built up in the platform's neck, as the relevant tuning parameter is the asymmetric component arising from biaxial strain opposite in sign along x and y. Through determination of the spontaneous orthorhombic distortion of FeSe and comparison to reliable X-ray diffraction data, we demonstrate quantitative knowledge of $(\varepsilon_{xx} + \varepsilon_{yy})/2$ to within a $\sim 16\%$ error. Prior measurements conducted by others utilise anisotropic in-plane pressure only to a limited extent, most commonly to detwin the crystal [89, 97], or determine the elastoresistivity component m_{66} by applying a small symmetry-breaking strain about zero – usually in the range $\pm 0.02\,\%$ [91, 93, 94]. The study of Ref. [91] primitively applies fixed stresses to not only detwin, but also to determine the resistivity anisotropy; we will return to this. Although strain can directly couple to the nematic order parameter, through a mixture of necessity (one should not use a large strain to probe m_{66}) and lack of technical capabilities, it has not yet been utilised to its full potential. By expanding the range of applicable tuneable in-plane strain by a factor of ~ 20, we open the door to a variety of exciting experiments which can directly probe the nematic state, and thus significantly constrain theoretical models.

Experimental results will now be discussed, concentrating on measurements under $\langle 110 \rangle_T$ strain and following the order that they were previously presented. Our first new insight into nematicity is provided by ramping strain just above the zero-strain structural transition temperature $T_S(\langle \varepsilon_a \rangle = 0)$. The nematic susceptibility χ_n is defined as the gradient of the nematic order parameter ϕ for a very small strain range around zero, and this diverges as $T \to T_S^0$. Experimental determination of χ_n by others has relied on the assumption that $\rho_a - \rho_b \propto \phi^*$, thus allowing χ_n to be determined from the slope $\mathrm{d}(\rho_a - \rho_b)/\mathrm{d}\varepsilon$ (where $\varepsilon \equiv \varepsilon_{[110]_T}$). In this picture, large strains should eventually cause full polarisation of the nematic order parameter, giving a monotonic saturation of $\rho(\varepsilon)$ – as shown in Figure 4.17. Upon sweeping strain above T_S, we observe *non*-monotonic behaviour, and so this assumption must be challenged. One

*We ignore any constant offset – in reality the assumption is $\rho_a - \rho_b = a + b\phi$.

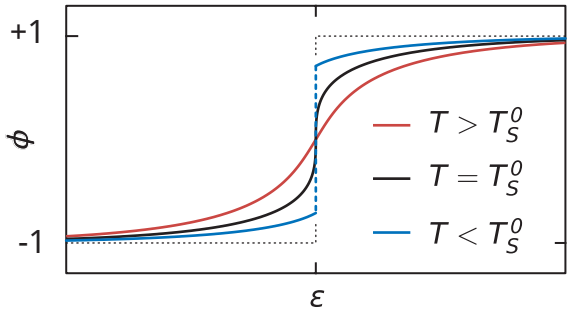

Figure 4.17 | Expected polarisation of the nematic order parameter with strain in the case that local deformation is not allowed. This is shown for temperatures above, at, and below the bare transition temperature T_S^0.

explanation is simply that $\rho_a - \rho_b \propto \phi$ ceases to be valid over a wide strain range; this might be because the nematicity simply decouples from the transport. An alternative explanation is that there may be additional terms which contribute to the relationship between ρ and ϕ, and that these become relatively more important at large strains. In this case, the fact that we observe $\rho(\langle\varepsilon_a\rangle)$ start to flatten beyond some strain would indicate that the nematicity fully polarises at a surprisingly small strain of $\pm 0.075\,\%$.

Although an apparent pitfall of our experimental setup, the lack of local strain control longitudinal to the nematic order for $|\langle\varepsilon_a\rangle| < |\varepsilon_S(T)|$ is in fact hugely advantageous, because it provides a method for determining the spontaneous structural distortion. For strains within this range, we tune only the domain population, giving a linear weighted average between $\rho(-\varepsilon_S) = \rho_b$ and $\rho(+\varepsilon_S) = \rho_a$, and the anomaly in $\rho(\langle\varepsilon_a\rangle)$ at $-\varepsilon_S$ allows the orthorhombic distortion to be tracked. Somewhat serendipitous is that in compression this linear dependence evolves near a minimum of the underlying curve, giving a large change in slope and a particularly pronounced feature at $-\varepsilon_S$. As already mentioned, this allows a vital comparison to published data to be made, demonstrating that we transmit strain effectively, and with a scale that can be determined from the capacitive readout – even at large strains. This also provides the first (so far as we know) explanation, as given in Section 4.2, of the basic observation that in unstressed samples $\rho(T)$ turns upward at T_S: the underlying $\rho(\varepsilon)$ curve is concave up around $T = T_S$ and $\langle\varepsilon_a\rangle = 0$ thus giving a signal increase due to domain formation. Furthermore, this implies that the specific anomaly we observe should not be seen whilst controlling stress for a completely detwinned sample. However, as shown in Figure 4.7, a different upturn may occur in $\rho(T)$ under controlled stress due to the negative slope in $\rho(\langle\varepsilon_a\rangle)$ for $\langle\varepsilon_a\rangle < -\varepsilon_S$.

Confirmation that the strain at which the above-mentioned feature in $\rho(\langle\varepsilon_a\rangle)$ does indeed occur at $-\varepsilon_S$, is provided by it being concurrent with the closing of hysteresis between increasing and decreasing strain ramps – as shown more clearly in Figure 4.18.

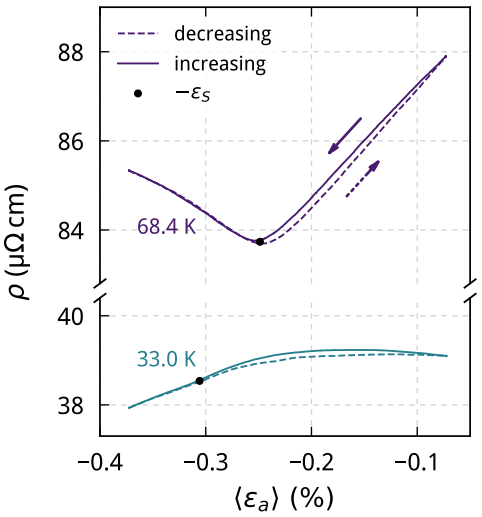

Figure 4.18 | Qualitative change of behaviour between high- and low-temperature strain ramps. Although at low-temperatures the feature representing ε_S is not trackable, the closing of hysteresis indicates $\langle\varepsilon_a\rangle < -\varepsilon_S$, and we plot ε_S from the scaled X-ray data shown in Figure 4.11.

Therefore, for $|\langle\varepsilon_a\rangle| > |\varepsilon_S(T)|$ we can assume the crystal is fully detwinned. As a general warning, we caution against the assumption that any non-zero force is able to detwin a FeSe crystal. Other work supports this: Ref. [44] claims to achieve only 86 % detwinning of $Ba(Fe_{1-x}Co_x)_2As_2$ under a moderate pressure of 5 MPa as determined by X-ray diffraction; and in FeSe, Ref. [97], only 80 % detwinning as determined by ARPES under an unknown pressure applied with a horse-shoe device. Our experiment again provides unique capabilities in that we can measure single-domain transport with confidence.

We now discuss our determination of resistivity anisotropy in some depth. The first question to address is: are the assumptions of our analysis valid? Most crucial to examine is the assumption that asymmetric strain dominates the response of $\rho(\langle\varepsilon_a\rangle)$, i.e. that $\rho(\langle\varepsilon_a\rangle = -\varepsilon_S) \equiv \rho_b(\sigma = 0)$. When introducing the analysis, we claimed this assumption to be valid on the basis that $(1/\rho)\,\mathrm{d}\rho/\mathrm{d}\langle\varepsilon_a\rangle$ was much smaller for $\langle 100\rangle_T$ than for $\langle 110\rangle_T$ strain at high temperatures. This is a weak statement and, with the appreciable implications of our resistivity anisotropy extraction, must be strengthened. The most direct and unequivocal approach is to measure ρ_{xx} and ρ_{yy} simultaneously in order to decompose the resistivity tensor into symmetric and antisymmetric components. Much work has been dedicated to this issue by the Fisher group for decomposing the elastoresistivity tensor in the pnictides [52, 57, 194]. Simultaneous measurement of transverse and longitudinal resistivities under large tuneable in-plane strain is a significant (and challenging) technical development – led by Dr Alexander Steppke – and is currently ongoing. Although not an experimental

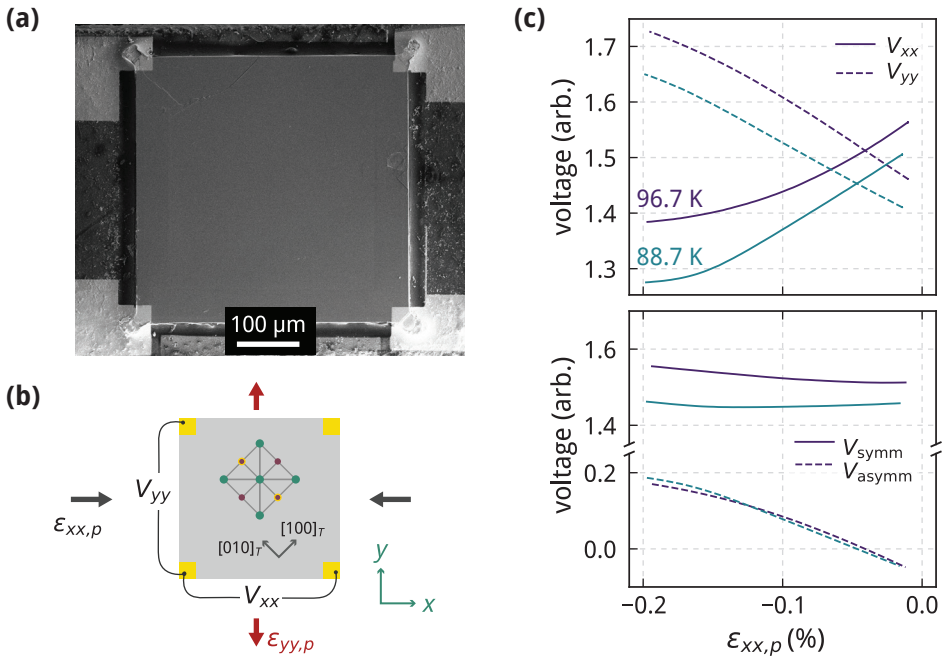

Figure 4.19 | (a) Platform-mounted FeSe sample with a Montgomery-like geometry for simultaneous measurement of longitudinal and transverse resistivity. **(b)** Direction conventions: strain is applied biaxially along x and y with the sample prepared with its edges at 45° to the tetragonal unit cell. Current is applied via the opposite two contacts for each direction. **(c)** Top: simultaneous measurement of V_{xx} and V_{yy} for temperatures above and below $T_S(\langle\varepsilon_a\rangle = 0)$. Bottom: decomposition into symmetric $\frac{1}{2}(V_{xx} + V_{yy})$, and asymmetric $\frac{1}{2}(V_{xx} - V_{yy})$ components.

effort of myself, it builds on the work in this thesis and, due to its direct implications for the data presented in this chapter, we will discuss the preliminary results that have been obtained.

The sample is prepared in a Montgomery configuration – i.e. thin and square (to within ∼ 2 %) with contacts in each corner and edges aligned with the principal axes of the resistivity tensor [195] – by precise microstructuring using a FIB. ρ_{xx} and ρ_{yy} are determined 'simultaneously' by switching between longitudinal and transverse voltage measurements whilst slowly ramping temperature or strain. The sample setup and measurement of V_{xx} and V_{yy} for high-temperature strain sweeps are shown in panels (a-b) and (c) of Figure 4.19 respectively. As seen in panel (c), the high-temperature strain

response is dominated by an asymmetric response $(V_{xx} - V_{yy})$*. At larger compressions this starts to saturate, whereas the symmetric component $(V_{xx} + V_{yy})$ turns upward. Although this might confirm the non-monotonic behaviour of $\rho(\langle\varepsilon_a\rangle)$ as originating from the asymmetric response, the large-compression behaviour could also suggest that it is caused by the upward turn of the symmetric component, especially because the asymmetric component saturates. Measurements at larger compressions are needed to draw a more definite conclusion. A weak symmetric response additionally suggests that the xy band does not strongly contribute to conduction at these temperatures; this is in support of the low coherence observed by measurements presented in Section 2.4.3. Furthermore, ramping temperature and conducting analysis equivalent to that of Section 4.2.3, for the resistivity anisotropy from $\rho(T)$†, indicates that both the peak at $\sim 80\,\mathrm{K}$ and suppression with a sign change below $\sim 45\,\mathrm{K}$ are features originating from the intrinsic resistivity anisotropy.

The resistivity anisotropy data presented in Figure 4.15 can now be discussed with confidence. First, we notice that although the resistivity anisotropy can be utilised above T_S, it is not a suitable order parameter across a wide temperature range, and does not track the structural strain as predicted by Landau theory (Figure 2.2). This is not surprising since resistivity is not a thermodynamic quantity, and several mechanisms give rise to an anisotropy in electrical transport such as anisotropic Drude weight [50, 51], or anisotropic scattering (which can be from magnetic fluctuations and thus inelastic [48], or from impurity scattering and thus elastic [47]). Anisotropic scattering is expected to dominate the high-temperature response, and an anisotropic Drude weight the low-temperature anisotropy. If as simple as a crossover between these two mechanisms, our measurements would indicate these contribute to the resistivity anisotropy with opposite signs. The previous theoretical work of Ref. [196] predicted that $\rho_a > \rho_b$ (for all temperatures investigated – down to $0.3T_S$, i.e. $\sim 28\,\mathrm{K}$), peaking at 8.6% at $\sim 0.55T_S$. In our measurements a similar peak of $\sim 9\%$ is observed, but at a temperature of $\sim 0.9T_S$. This theory is based on an orbital-ordering scenario, in which the orbital splitting increases the spin susceptibility on the yz sections of Fermi surface (with x defined to be along a which is larger than b). Inelastic scattering is therefore stronger on yz rather than xz Fermi surface sections, and because

*These are preliminary data, and so we just plot the bare measured voltages. The conversion from voltage to resistivity is relatively involved, but to first order they are proportional and this conversion should not alter our conclusions.

†We must use the scaled orthorhombic distortion $\delta(T)$ from the data of Kothapalli et al. [90] as shown in Figure 4.11. These scaling factors depend on the exact strain scale of the sample-platform-rig setup – however, for qualitative features this should not matter.

conduction is dominated by the hole pocket – see Figure 2.12(d) – the resistivity is higher along x (i.e along a). One hypothesis which is supported by recent (but currently unpublished) theoretical work by the same group, is that a sign change can occur due the low temperature anisotropy being dominated by elastic impurity scattering which, if isotropic, would give higher conduction along the flatter parts of the FS (i.e. yz), and $\rho_a < \rho_b$.

Another possibility is that changes in orbital coherence may contribute to the crossover in behaviour across $\sim 50\,\mathrm{K}$. As discussed in Section 2.4.3, recent quasiparticle interference measurements [143] for normal-state FeSe found that at low temperatures d_{xy} and d_{xz} bands have significantly smaller quasiparticle weights than d_{yz}, the latter therefore being most coherent. If at high temperatures d_{xz} and d_{yz} are equally coherent, then, as described above, scattering would be highest in d_{yz}, giving $\rho_a > \rho_b$. Upon cooling, the relative loss of coherence in d_{xz} may cause scattering to become strongest on the d_{xz} sections of Fermi surface giving, $\rho_b < \rho_a$. Although attractive, this mechanism would require d_{xz} to *lose* coherence – relative to the yz Fermi surface sections – upon decreasing temperature, which would be unexpected and contrary to the behaviour shown in Figure 2.14.

Several last points regarding our determination of resistivity anisotropy must briefly be discussed, starting with the difference between the two samples. As seen in grey in Figure 4.15, the resistivity anisotropy of the second sample becomes negative at a lower temperature, and has a smaller low-temperature magnitude. In this measurement we note that strain was not swept outside the twinned phase between each strain ramp, however based on our wiggling experiments, this cannot explain the disparity. Another possible explanation is that asymmetric strain is not transferred as well at low temperatures. Alternatively, inspection of Table B.1 shows that $\rho_{300\mathrm{K}}/\rho_{12\mathrm{K}}$ is 18 % lower for the second sample than for the first, and because there is still considerable inelastic scattering at 12 K, this difference would extrapolate to a considerably larger difference in residual resistivity. As discussed, impurity scattering contributes to the resistivity anisotropy, however based on the first sign-change hypothesis we proposed, one might expect this to enhance, rather than suppress, the low-temperature anisotropy.

Secondly, we comment on the considerable contradiction between our data and the resistivity anisotropy determined by Tanatar et al. [176], which might be explained by considering differences between their method and ours. Based on the earlier discussion, and fact that a clear anomaly is observed in $\rho(T)$ at T_S, their sample is likely still partially twinned. Looking at Figure C.10 (although in compression, rather than tension as in their experiment) if one traces two lines of constant stress inside rather than

outside the twinned phase, no change in sign will occur when extrapolating to zero strain. To observe this change in sign, one must either fully detwin the sample, or measure in both compression and tension. Another possibility is that the difference originates from differences between samples rather than methods. It is known that a lower residual resistivity ratio results in lower values of T_S and T_c [87], and our measurements are mostly consistent with this. If the differences in resistivity anisotropy between our samples in Figure 4.15 originates from small differences in purity, then it is possible that the data of Tanatar et al. will deviate even further as T_S is even lower for their sample, and thus likely of even lower quality. However, the second sample does not tend towards the data of Tanatar et al. and thus this argument is less convincing than that of differing methods. As already mentioned, the only other distinguishing feature between our two samples is their thickness, with the second being $\sim 70\,\%$ thicker than the first. This gives a larger strain transmission length, meaning the transverse strain is dictated more by the sample rather than platform's Poisson's ratio. The sample of Tanatar et al. is freestanding and therefore the transverse strain is set ***fully*** by the Poisson's ratio of the sample. The downfall in this argument in explaining the observed disparity is again that our second sample does not have reduced anisotropy at high temperatures, and therefore cannot extrapolate to being three times smaller at its maximum.

In addition to the sign change in resistivity anisotropy at $\sim 45\,\mathrm{K}$, the dichotomy between high- and low-temperature behaviours manifests itself clearly in strain-ramp data. As seen in Figure 4.18, $\rho(\langle\varepsilon_a\rangle)$ has a negative gradient for $|\langle\varepsilon_a\rangle| > |\varepsilon_S|$ at high temperatures, and changes sign below $\sim 55\,\mathrm{K}$. This sign change can be seen more directly by calculating the elastoresistivity $(1/\rho)\,\mathrm{d}\rho/\mathrm{d}\langle\varepsilon_a\rangle$, as shown in Figure 4.20 both as a function of temperature and strain, with $|\langle\varepsilon_a\rangle| > |\varepsilon_S|$ data being highlighted in the latter. Such a change in sign is also observed at similar temperatures by small-strain elastoresistivity studies, despite samples being twinned [91, 93, 94].

Lastly, we discuss the response of the superconducting transition temperature to $\langle 110\rangle_T$ strain. Most striking in our data is the sign change in $\mathrm{d}T_c/\mathrm{d}\langle\varepsilon_a\rangle$ at large compressions beyond $-\varepsilon_S$, i.e. where our applied strain increases the unit cell orthorhombicity rather than altering the domain population. We first preface this by emphasising that the shape of the points in this plot is sensitive to the resistivity-slice threshold from which T_c is extracted (see Figure C.11); however we have found good agreement between T_c from $\rho(T)$ and $\chi(T)$ for constant-resistivity slices at low-signal thresholds. For $|\langle\varepsilon_a\rangle| < |\varepsilon_S|$, only $\varepsilon_{A_{1g}}$couples locally, and so the negative slope of $\mathrm{d}T_c/\mathrm{d}\langle\varepsilon_a\rangle$ within this range reflects the response to symmetric strain. For $|\langle\varepsilon_a\rangle| > |\varepsilon_S|$,

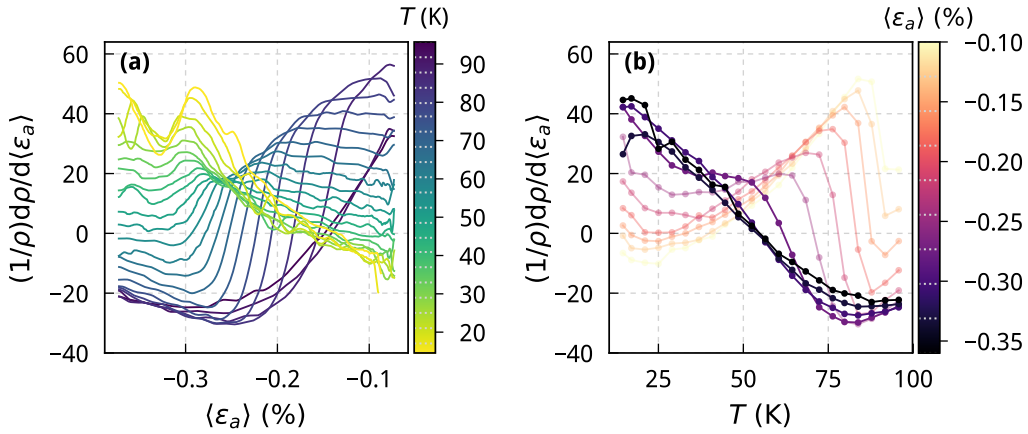

Figure 4.20 | (a) Elastoresistivity $(1/\rho)\,\mathrm{d}\rho/\mathrm{d}\langle\varepsilon_a\rangle$ determined from the strain-ramp data presented in Figure 4.10. **(b)** Constant-strain cross-sections extracted from the curves in panel (a). Cross sections for $|\langle\varepsilon_a\rangle| > -|\varepsilon_S(T \to 0)|$, i.e. in the range where the sample should be detwinned for all temperatures, are opaque.

we observe a positive slope – i.e. increasing the orthorhombicity decreases T_c – and this must originate from the response to asymmetric strain. This positive slope tentatively indicates, in a general sense, that tetragonality favours superconductivity. The Ehrenfest determination of Ref. [89] finds a negative sign of $\mathrm{d}T_c/\mathrm{d}\varepsilon$, again cautioning against incomplete detwinning. As for the difference in $\mathrm{d}T_c/\mathrm{d}\langle\varepsilon_a\rangle$ for $|\langle\varepsilon_a\rangle| < |\varepsilon_S|$ between different samples, one possibility is a variation in the amount of symmetric strain transferred, but this would contradict the expected difference in resistivity anisotropies. Most likely is that sample purity strongly dictates the slope (it is already found to significantly affect the value of T_c [87]): $\langle 100\rangle_T$ sample 1 and $\langle 110\rangle_T$ sample 3 have the largest (almost identical) slopes and also the highest (similar) quality.

Interestingly, in our measurements the sign change occurs for $\langle\varepsilon_a\rangle$ slightly beyond rather than *at* ε_S, and a similar feature is quantitatively observed in $\rho(\varepsilon)$ at low temperatures – as shown in Figure 4.18. This speculatively suggests a lack of coupling between strain and the electronic structure precisely at the transition, with the coupling becoming stronger under further compression. Further analysis and more concrete conclusions would require this feature in T_c to be reproduced in a more systematic study via measurement of high signal-to-noise ratio magnetic susceptibility for a higher density of strains through the transition, and without any plastic deformation of the

platform. Here we rely on a single data point, and at a strain affected by plastic deformation.

Coming full circle, we comment on our initial motivation of whether there is any sign of a crossover in FeSe under an applied orthorhombicity exceeding $\varepsilon_S(T \to 0)$, such that there is no spontaneous lattice deformation. Inspecting the the elastoresistivity of Figure 4.20(b), there is one other feature we observe other than the sign change at $\sim 55\,\mathrm{K}$ – a subtle crossover at $\sim 80\,\mathrm{K}$. More measurements and theory are needed to make further conclusions regarding this feature. An interesting study which might directly elucidate the existence of a nematic crossover would be to increase the sample-platform coupling through reduction in sample and epoxy thicknesses. The most extreme version of this would be to measure single-layer FeSe grown directly on a substrate, which is then strained. In this case $T_S \to T_S^0$ and the crossover should extend into finite strain from the zero-strain transition temperature.

4.4 Conclusion and future work

In this chapter, experimental results obtained on FeSe under controlled in-plane anisotropic strain have been described. Application of $\langle 100 \rangle_T$ strain – in which the sample remains twinned – displays only a weak response in electronic transport, as well as a linear dependence of T_S and T_c with opposite signs, the latter increasing with compression. In this configuration we do not apply strain with the same principal axes as the orthorhombic distortion, and we attribute the weak response to this.

Tuning $\langle 110 \rangle_T$ strain reveals exciting behaviour. Above the transition, we observe that sweeping strain gives an unexpected non-monotonic behaviour, indicating that care should be taken in simply assuming the nematic order parameter to be proportional to the resistivity anisotropy when far from the bare transition temperature T_S^0. Upon lowering temperature, we observe a novel side-effect of controlling strain for a material which undergoes a structural transition: for applied strains less than the spontaneous distortion only the symmetric strain can couple locally, with domain redistribution relaxing the anisotropic component. This enabled the orthorhombic distortion to be tracked down to $\sim 50\,\mathrm{K}$, giving the expected mean-field dependence in agreement with other literature. A linear interpolation of resistivity inside this range reveals (for the first time) why the observed feature at T_S for an twinned sample appears as it does. Through measurement of $\rho(\langle \varepsilon_a \rangle)$ and $\rho(T)$ both inside and outside the twinned phase, we were able to extract the resistivity anisotropy, making the observation of a large peak of $\sim 9\,\%$ at $82\,\mathrm{K}$, which is rapidly suppressed becoming negative below $\sim 45\,\mathrm{K}$.

Support via additional measurement of the transverse resistivity indicates this is a robust and reproducible dependence, having important implications for theoretical work studying the effect of different mechanisms on influencing and dominating the resistivity anisotropy.

A general, but important, trend highlighted by our measurements is the qualitative change between high-temperature ($\gtrsim 50\,\mathrm{K}$) and low-temperature ($\lesssim 50\,\mathrm{K}$) behaviours. Most clearly apparent in elastoresistivity in the detwinned state, the underlying mechanism – potentially from orbital-selective coherence – is likely closely tied to nematicity. We additionally revealed how domain walls can be 'annealed' by sweeping strain, and a change in sign of $\mathrm{d}T_c/\mathrm{d}\langle\varepsilon_a\rangle$ in compressing the lattice into a fully detwinned state, indicating that T_c favours tetragonality.

Possible extensions of this work are numerous. As alluded to in the previous section, simultaneous measurement of transverse and longitudinal resistivities is a vital future direction, which should enable decomposition of symmetric and asymmetric strain responses. Although challenging technically, our initial attempts and current on-going measurements provide a proof of concept, and have already informed important aspects of the work presented in this thesis. The most convincing method for determining the resistivity anisotropy is ramping strain through the structural strain and extracting the resistivity at $\pm\varepsilon_S$. With measurement of both ρ_{xx} and ρ_{yy} this represents direct determination of unstressed ρ_a and ρ_b, and any symmetric contribution can additionally be quantified.

Technique-wise, the primarily limitation highlighted by our measurements is the platform material. Plastic deformation due to a small yield strain complicates application of compressions beyond approximately $-0.2\,\%$ in the current setup – far from the amount require to detwin the sample, and far from the maximum strain applicable by the apparatus. An obvious and simple replacement is grade 5 titanium (Ti6Al4V), however a longer term development might be to utilise silicon: it has a very high yield strength, and fractures beyond this rather than deforming plastically.

Numerous interesting aspects of the influence of strain on FeSe are not touched upon by our work. One example is the interplay between superconductivity and domains, as investigated recently using ARPES [115]. Furthermore, many of the results presented in this chapter require additional theoretical support to have true impact on the understanding of FeSe and iron-based superconductors in general. A useful place to start would be determination of the evolution of the band structure and Fermi surfaces under $\varepsilon_{B_{2g}}$.

Theoretical studies investigating the nature of the nematic state in FeSe are numer-

ous and ever-increasing. The technical challenge of these studies is the many moving parts; for a full picture one must combine orbital-dependent coherence, and intertwined orbital and spin fluctuations. Without experiments to ground these models and predictions, they have limited significance. Furthermore, when working with unstressed FeSe alone, it is difficult to tightly constrain all the inputs for an unbiased theoretical model of the nematic order in FeSe. The results presented in this chapter are a first step towards providing necessary extra constraints. Theoretical models now not only have to fit to unstressed FeSe, but also a whole series of orthorhombically distorted lattices that we induce.

5 | Apparatus Development

5.1 Motivation

As demonstrated in Chapter 4, application of in-plane strain on platform-mounted samples is a powerful tool for investigating the electronic properties of FeSe. Although we extended the established piezoelectric-based method to enable measurement of soft materials such as FeSe and microstructured samples, this method does not expand the strain range accessible, and this was never the motivation for developing such platforms. Attempting to apply larger strains to samples on solid platforms is not fruitful as the sample strain is limited by the platform's effective length. Design-wise, significant reduction of the effective strained length is not possible as the the neck cannot feasibly be made shorter without sacrificing strain homogeneity and low stress concentration. Furthermore, for titanium platforms the material's yield strength becomes a limiting factor if strains of up to 1 % are to be reached. Seeking an alternative platform material with a higher yield strength would extend the limit to the the buckling point, but if we aim to push pure, single-crystal samples to their mechanical limit, then these strain increases are too marginal and a new methodology must be conceived.

We start then from a position of minimal constraints, with the simple requirement of being able to apply the largest possible uniaxially-controlled strain. Returning to a free-standing configuration allows the sample strain to again be limited by its length, and as such a reduction in sample size directly gives us an increase in strain for a given applied displacement. In micro-structuring samples using a focused ion beam (FIB) – as briefly introduced in Section 3.3.2 – an order-of-magnitude reduction in dimensions compared to solid-platform FeSe is easily achievable. Furthermore, samples can be shaped with precise geometries and smooth edges, resulting in high achievable strains and a reduced extrinsic breaking limit from stress concentration along rough edges. The benefits of such miniature samples are evident immediately; for a sample with a 100 μm free length, only a 1 μm displacement is needed to achieve

1 % strain. Conversely this also works against us, as inadvertent displacements can consequently cause large sample strains, and this issue motivates the need for new apparatus. Clamping and handling such miniature samples can again be achieved with a platform – but one that permits them to be free-standing. The apparatus must then apply a few microns of displacement to the platform, whilst minimising inadvertent strains.

Making this apparatus stress-controlled has several benefits. Firstly, stress control can be achieved using a spring to convert displacement to force, and this spring can take up differential thermal contraction which would otherwise cause problematic inadvertent displacements. Secondly, for materials which undergo a structural transition such as FeSe, the control parameter – i.e the applied force – can remain constant through the transition. We therefore pursue uniaxial-stress, stress-controlled apparatus for pressurising miniature samples to their ultimate mechanical limit.

Development of both the rig and platform which form this apparatus are the focus of this engineering-based chapter. This work was conducted collaboratively with Dr Clifford Hicks, to whom the final rig design – discussed in Section 5.6 and shown in Appendix D – is credited. I worked on the development of the components presented in Sections 5.4-5.5 of this chapter, concentrating on the platform and force-sensor design, as well as conducting material tests, calculations and finite element analysis to support the rig-design process.

It is worth taking a moment to explain the time-order of this development in relation to the apparatus described in Chapter 3. Both solid and gapped platform projects began simultaneously, and both were motivated by the sample-size limitations of the conventional strain cell. The aim with gapped platforms was always to apply extremely large strains to miniature samples, and with solid platforms to strain small and/or delicate samples using a simple method, without concern for a high upper strain limit. Due to their design and fabrication simplicity, solid platforms were developed rapidly, allowing them to be utilised for measurements before a final gapped platform design was reached. Arriving at a final design, and subsequently fabricating the gapped platforms took approximately a year, meanwhile both metallic and quartz solid platforms went through continual development from experience with sample mounting and measurement. The design, fabrication, and oxidation testing of the titanium platforms (used for FeSe measurements) occurred alongside the gapped platform development, but before the microstructure rig design was finalised. Consequently, measurements on FeSe started before the arrival of parts and construction of the rig.

The device presented in this chapter differs from that of Ref. [197] due to its ability

to accept miniature samples, therefore enabling stresses to be applied which are large enough to push samples to their mechanical limit. Furthermore, whilst the device of this chapter also has a force sensor, it operates in force-control mode, whereas the device of Ref. [197] uses displacement as a controlled parameter.

5.2 Principles of apparatus development

This section highlights important considerations that must be made when designing apparatus for applying pressure at cryogenic temperatures. These form the basis for understanding the final design of our stress-controlled rig for microstructured samples. Additionally, this section might provide an informative, and otherwise uncompiled, introductory resource for future students wishing to explore the area of stress/strain apparatus design.

5.2.1 Modelling as a system of springs

A complicated dynamic, mechanical system can be reduced into a system of ideal springs, as described by Hooke's law, either in series or parallel with each other. This allows one to estimate the displacement and force on individual springs under a given displacement or force applied to the system. This is particularly helpful when designing apparatus as one can convert force and displacement constraints into physical constrains on the dimension of a part. It can also help determine whether a rig is predominantly controlled-stress or controlled-strain. This is especially useful in cases where the system is too complicated to model using finite element analysis (FEA), or when a more rapid estimation is required.

Series

Consider two springs in series, as shown in Figure 5.1(a), aligned with the x-axis, and labelled 1 and 2. The behaviour of this combined-spring system can be trivially derived using Hooke's law in one dimension: $F_i = -k_i x_i$. In applying a force F to this system, both will experience the same force, whereas the total displacement x will be shared between them. This is formalised along with the total spring constant k (where $F = -kx$) in terms of constituent springs, in Equation 5.1.

$$F_1 = F_2 = F, \quad x_1 + x_2 = x, \quad k = \frac{k_1 k_2}{k_1 + k_2}. \tag{5.1}$$

Sharing of the displacement x is given by the ratio of spring constants $x_1/x_2 = k_2/k_1$,

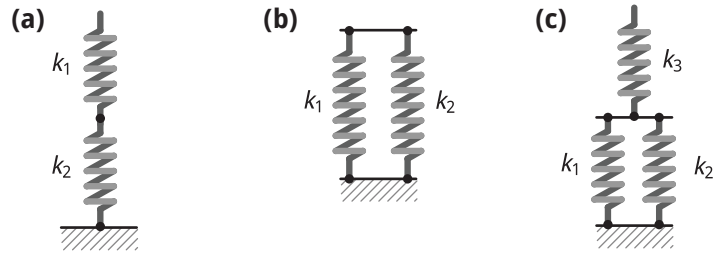

Figure 5.1 | (a) Two springs in series. The forces on both are equal to each other, and to the force applied to the system. The total spring constant is $1/k_{\text{total}} = (1/k_1) + (1/k_2)$. **(b)** Two springs in parallel. Now the displacement of both is the same and equal to that of the system. Spring constants simply add $k_{\text{total}} = k_1 + k_2$. **(c)** For more complicated combinations, alike arranged springs (i.e. springs directly in series or parallel which each other) can be contracted. Here the parallel springs k_1 and k_2 are first combined, and this effective spring is combined in series with k_3.

giving

$$x_1 = \frac{x}{1 + k_1/k_2}, \quad x_2 = \frac{x}{1 + k_2/k_1}. \tag{5.2}$$

If $k_1 \gg k_2$ then $k \approx k_2$ and $x_2 \approx x$, i.e. as expected, all the displacement goes into the softer spring. This can be generalised to N springs in series:

$$F_i = F, \quad \sum_i^N x_i = x, \quad \frac{1}{k} = \sum_i^N \frac{1}{k_i}. \tag{5.3}$$

And similarly for the sharing of displacement

$$x_i = \frac{x}{1 + k_i \sum_{j \neq i}^N \frac{1}{k_j}}. \tag{5.4}$$

Parallel

For two springs in parallel (Figure 5.1(b)), the displacement of each is now the same and equal to the total, whereas the force is shared. The total spring constant is just the sum of the constituents, and these relations are shown in Equation 5.5.

$$x_1 = x_2 = x, \quad F_1 + F_2 = F, \quad k = k_1 + k_2. \tag{5.5}$$

Analogously the force is now shared according to $F_1/F_2 = k_1/k_2$, meaning

$$F_1 = \frac{F}{1 + k_2/k_1}, \quad F_2 = \frac{F}{1 + k_1/k_2}, \tag{5.6}$$

and if $k_1 \gg k_2$, then all the force goes into the stiffer spring. Again, generalising to N springs gives

$$x_i = x, \quad \sum_i^N F_i = F, \quad k = \sum_i^N k_i. \tag{5.7}$$

$$F_i = \frac{F}{1 + \frac{1}{k_i}\sum_{j\neq i}^N k_j}. \tag{5.8}$$

Combinations

More complicated arrangements can be tackled by combining alike-arranged springs – i.e. in series or parallel with each other. Doing this until all constituents have been contracted to a single effective spring allows the force or displacement of one to be determined under a force or displacement applied to the system as a whole. Dealing with multiple springs requires notational bookkeeping, and the simplest approach is to concatenate individual indices: for example, combining two springs i and j gives $F_{ij} = -k_{ij}x_{ij}$. Let us consider a simple compound system of two springs in parallel, which are together in series with another spring – as shown in Figure 5.1(c). Parallel springs are combined first to give the combination $k_{12} = k_1 + k_2$, and this is combined in series with the third spring to give $k = k_{123} = k_{12}k_3/(k_{12} + k_3)$. Expressions 5.2 and 5.6 are then used to write the force and displacement in each spring as a function of the force and displacement applied to the system as a whole.

The distinction of individual springs need not be a real, physical one. For example the solid platform introduced in Chapter 3 can be decomposed into three springs in series, two with large k_L at either end and one with small k_S in the centre. If $k_L \gg k_S$ then $k_{\text{total}} \approx k_S$, and this matches our FEA calculation in Section 3.3.2. Alternatively individual springs can represent individual components. In general this is a simple, but surprisingly useful and versatile tool, which in Section 5.6.3 we will use to decompose the stress-controlled apparatus developed in this chapter.

5.2.2 Stress versus strain control

The previous section gives us a framework to discuss the differences between stress- and strain-controlled apparatus more precisely. We take 'strain control' to mean the sample experiences a controlled displacement, and 'stress control' a controlled force. An important, but more subtle, distinction is that an applied strain will be independent of the force that the sample generates, and conversely an applied stress will be independent of the resulting sample strain; this is true even when the stress-strain

	Series	Parallel
Stress-controlled	always	when $k_{\text{sample}}/k_{\text{rig}} \to \infty$
Strain-controlled	when $k_{\text{rig}}/k_{\text{sample}} \to \infty$	always

Table 5.1 | Stress- and strain-control regimes for springs in series and parallel.

relationship is nonlinear. In the simplest picture we represent the sample and rig as two springs acted on by an external infinitely stiff actuator. If the sample and rig are in series then the force will be the same in both, and stress is the natural control parameter. In the limit $k_{\text{rig}}/k_{\text{sample}} \to \infty$, the displacement of the sample will equal the applied displacement, and strain control is achievable. For springs in parallel, this is reversed, as shown in Table 5.1, with the displacement being the same in both, and the control of force only possible when the rig is much softer than the sample.

The piezoelectric-based uniaxial pressure cell introduced in Section 3.2.2 is designed to control strain. The external control parameter is the stack displacement and as in Table 5.1, strain control permits elements of any spring constant to be in parallel with the sample. Any part in series with the sample should have a comparatively large spring constant to ensure the the stack and sample displacements are approximately equal. Owing to the rig's simplicity, this appears to be true; the sample is only in series with large blocks of titanium which have a spring constant many times that of the sample (see Figure 3.2). However, the epoxy fixing the sample ends to the rig, which will generally be softer than the sample, also appears in series, and so the displacement is shared according to Equation 5.2.

For stress control, then, all we require is that in a spring-representation any spring (i.e. part) in parallel with the sample has a low spring constant. In reality the easiest way to apply a controlled force is through use of spring as a displacement converter, and if this spring is in series with the sample then there is no restriction on its stiffness. As we will see, however, there are benefits to making it soft.

5.2.3 Sensing

In the previous section we assumed that either a known force or known displacement could be applied, but in reality a sensor must be utilised to gain this knowledge. The conditions experienced by this sensor should be the same as the component of interest – for us usually the sample. We need a measure of the applied stress or strain field and so must sense either force or displacement. Table 5.1 tells us how to implement such

sensors: a force sensor must be in series with the sample, and a displacement sensor in parallel with it.

Capacitive sensors offer a convenient method for sensing small changes, due to the precision to which capacitance can be measured. A parallel-plate configuration is simplest, and gives an easy way to convert measured changes to force or displacement. For two parallel plates of area A and separation d, the capacitance is given by $C = \epsilon_0 A/d$ where ϵ_0 is the permittivity of free space – valid when operating the sensor in vacuo. This equation ignores any edge effects due to the finite plate size, but if $d \ll \sqrt{A}$ then this relation applies practically and we have two geometrical parameters, A and d, through which changes can be detected. Alteration of the plate separation d gives the capacitance change

$$\Delta d = d(x) - d_0 = \epsilon_0 A \left(\frac{1}{C(x)} - \frac{1}{C_0} \right). \tag{5.9}$$

If in parallel with the sample then $\Delta x_{\text{sample}} = \Delta d$ and this functions as a displacement sensor - as is the case for the piezoelectric-based rig introduced in Section 3.2.2. If in series with the sample, and the spring constant of the sensor is known, then this can operator as a force sensor, $F_{\text{sensor}} = F_{\text{sample}} = -k_{\text{sensor}} \Delta d$.

Changes in A, by alteration of the plates' overlap area, is an alternate approach to sensing displacement. For plates of area $w \times L$, with an overlap along the L dimension, then

$$\Delta L = L(x) - L_0 = \frac{d}{\epsilon_0 w} \Big(C(x) - C_0 \Big). \tag{5.10}$$

In entering reasonable numbers into Equation 5.10, one finds the sensitivity $\partial C/\partial L$ is much lower than for $\partial C/\partial d$ in Equation 5.9. In principle this overlap sensor could also be used to sense force, but implementation of this would be rather complicated. To generalise the above, in both of these examples the 'sample' can be replaced with any other component one wishes to sense the conditions of.

5.2.4 Thermal effects

Thermal effects are important for designing apparatus that operates at cryogenic temperatures as changes in dimensions upon cooling can cause inadvertent forces and displacement affecting the control of stress and strain. Length change is relative so we are concerned with *differential* thermal contraction – i.e. the difference in length change of two materials with respect to each other. We define the fractional length

change of a material i to be

$$\frac{\Delta L_i(T)}{L_{i,0}} = \frac{L_i(T) - L_{i,0}}{L_{i,0}} = \Gamma_i(T). \tag{5.11}$$

where $L_{i,0} \equiv L_i(T = T_0)$ and T_0 is some reference temperature*, and the temperature dependent length is therefore $L_i(T) = (1 + \Gamma_i(T))L_{i,0}$. Assuming we have two materials A and B with different Γ's, and that the dimensions of A follow that of B, then the difference in lengths at T is

$$\Delta_{BA}(T) = L_B(T) - L_A(T) = \Big(\Gamma_B(T) - \Gamma_A(T)\Big)L_{A,0}, \tag{5.12}$$

where $L_{A,0} = L_{B,0}$ as we are concerned only with the overlap region . This gives an expression for the strain induced in A at a temperature T to be

$$\varepsilon_A(T) = \frac{\Delta_{BA}}{L_A(T)} = \frac{\Big(\Gamma_B(T) - \Gamma_A(T)\Big)L_{A,0}}{L_A(T)} = \frac{\Gamma_B(T) - \Gamma_A(T)}{1 + \Gamma_A(T)}. \tag{5.13}$$

In general $\Gamma_i(T) \ll 1$ meaning

$$\varepsilon_A(T) \approx \Gamma_B(T) - \Gamma_A(T). \tag{5.14}$$

Since Γ is conventionally quoted as a percentage, this makes for a very quick determination of the induced strain - just take the difference of the two Γ's. A note on signs: if A contracts more than B, that is Γ_A is more negative than Γ_B, then it will be tensioned. In this case $\Gamma_B(T) - \Gamma_A(T)$ is positive, thus matching the convention that a positive strain corresponds to tension and a negative one to compression.

Another important consideration for low-temperature measurements is the amount of time for the sample temperature to equilibrate with the surroundings. Accessing the base temperature of a system relies on this, and minimising the sample-thermometer thermalisation time in particular is important for minimising thermal lag. This time should therefore be kept small with respect to the temperature ramp rate, which becomes more challenging for apparatus consisting of low-thermal-conductivity materials, or components connected by small contact areas, or both. The time for a piece of material with specific heat capacity c, thermal conductivity κ, mass m, and length L to thermalise via heat conduction in one dimension with a component it is connected to

*It is conventional to use room temperature as the reference (T_0 = 293 K). Note a sign difference between the definition of $\Gamma(T)$ in Ekin [167], who uses $\Delta L(T) = L_0 - L(T)$.

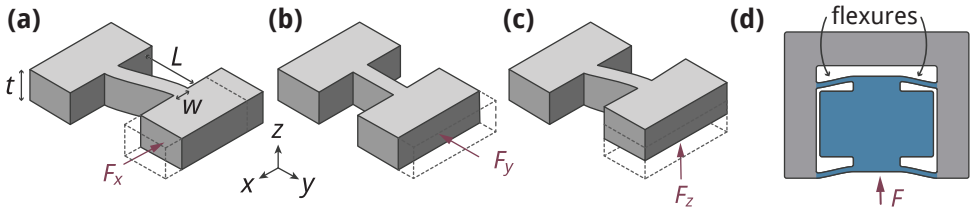

Figure 5.2 | The flexure is a deformable bar of material with $L > t > w$. We assume the material on either end is infinitely rigid. **(a)** Flexure forced along its 'easy' direction via an 's'-bending motion. **(b)** The highest spring constant is for direct compression of the flexure. **(c)** 's'-bending in z has a higher spring constant than for x, as $t > w$. **(d)** Example of moving block mechanism utilising four flexures.

with contact area A, is

$$\tau = \frac{mcL}{\kappa A}, \tag{5.15}$$

In general c decreases upon cooling and κ increases, meaning thermalisation times are shorter at low temperatures.

Calculation of thermalisation times, and specific inclusion of high thermal conductivity materials connecting various components are important considerations in the design of this apparatus (e.g. the thermalisation foils visible in Figure D.1), however the specifics of these will not be discussed in this chapter.

5.2.5 Flexures

Flexures are a vital component of uniaxial-pressure apparatus as they allow for the transmission of force and displacement primarily along a single axis. Along this axis the flexure has a low spring constant, and so motion is permitted, whereas transverse and torsional motions are resisted due to much higher spring constants. A flexure can be realised by a bar of material with one dimension much smaller than the other two. Motion along the longitudinal (x) and transverse (y, z) directions is shown in Figure 5.2, and the spring constants are given by

$$k_x = \frac{Ew^3t}{L^3}, \quad k_y = \frac{Ewt}{L}, \quad k_z = \frac{Ewt^3}{L^3}. \tag{5.16}$$

Relating the transverse spring constants to k_x gives $k_y = k_x(L/w)^2$ and $k_z = k_x(t/w)^2$, and as such if $L \gg w$ then $k_y \gg k_x$, and if $t \gg w$ then $k_z \gg k_x$ - i.e. the spring

constant is smallest along x. Carefully balancing these three dimensions for targeting spring constants in each direction can be difficult, so a general approach for increasing all constants without introducing relative changes is the addition of more flexures in parallel. In this case $k_{i,\text{total}} = Nk_i$, as per as Equation 5.5, where N is the number of flexures, and for stress control care must be taken that $Nk_x \ll k_{\text{sample}}$. The more important advantage of repeating N flexures in parallel is that k_x can be maintained by a reduction in width by $\sqrt[3]{N}$, and this allows larger ratios of k_y/k_x and k_z/k_x – i.e. increases the transversal resistance to motion. By combining four flexures in parallel, a moving block mechanism can be constructed, as shown in Figure 5.2(d). In the context of uniaxial pressure apparatus, this mechanism is important for primarily transferring uniaxial displacement, and was utilised in the piezoelectric-based pressure cell (see Figure 3.3).

An important relation for limiting flexure dimensions is the maximum strain in an 's-bending' member. This is given empirically by

$$\varepsilon_{\text{max}} = \frac{3\Delta w}{L^2}, \tag{5.17}$$

where w and L have the same definition as in Figure 5.2(a) with a displacement Δ as per $F_x = -\Delta k_x$. For the bending in panel (a) the strain maximum occurs at the interior right angle where the flexure joins the outer block. Equation 5.17 will also give the maximum strain in a suspended sample whose ends experience a mismatch causing s-bending (panels (a) and (c) in Figure 5.2). This is crucial for the miniature, free-standing samples we will consider.

5.3 Basic concept

We now establish the core concept of this apparatus. Although stress will be controlled in this apparatus, strain is a more intuitive* and practical parameter for considering mechanical targets and constraints. A consequence of this is that displacements experienced under a fixed force become sample dependent, however considering extremes of sample stiffness is sufficient for design purposes.

Let us start with the sample. We want to apply a controlled force to push a miniature sample to its mechanical limit. There are two strain types we must consider: permanent, and temporary. Strains applied only momentarily should, by and large, not exceed $\sim 0.1\,\%$ due to risk of permanent sample damage. This especially applies

*Based on experience with operating and designing *strain*-controlled rigs.

at room temperature where yield strengths and stiffnesses are lowest, and the sample is being handled. A recent uniaxial pressure cell development showed that plastic deformation occurs above $\sim 0.25\,\%$ compression in Sr_2RuO_4 [197]. Permanent strains should ideally not exceed $\sim 0.01\,\%$, a limit which originates broadly from the limit of our measurement apparatus*. Such strains often arise from height mismatches and torques originating from construction, mounting, and differential thermal contraction.

We establish our standard sample size for now as $L \sim 100\,\mu m$, $w \sim 25\,\mu m$ and $t \sim 15\,\mu m$ (along x, y and z respectively) with a moderate Young's modulus of $E \sim 100\,GPa$. Using Equation 5.17 the minimum permissible sizes of permanent y and z sample-end mismatches can be calculated for $\varepsilon_{max} < 0.02\,\%$. Along x this displacement is given directly by $\Delta_x = \varepsilon_{max} L$

$$\Delta_x < 20\,nm, \quad \Delta_y \lesssim 26\,nm, \quad \Delta_z \lesssim 44\,nm. \tag{5.18}$$

The size of these displacements highlights the primary challenge of this apparatus design. So far, the highest experimentally achieved strain using piezoelectric-based apparatus is $\sim -1\,\%$ [198], and to exceed this with a miniature sample of the dimensions above we require a force of $F = Ewt\varepsilon \gtrsim 0.4\,N$. The sample must be attached to a platform which allows it to be free-standing; this is possible with the standard moving-block design of Figure 5.2(b), where opposing sample ends are attached to the fixed and moving sections. The flexures appear in parallel with the sample, so should be as soft as possible such that the force on the platform essentially equals that on the sample. The flexures should also be as stiff as possible in y and z to suppress mismatches.

We must now apply a known force to the platform. Piezoelectric stacks are our immediate preference, and simple operation can be achieved with a stack and force sensor in series with the moving end of the platform. Direct coupling of the stacks to the platform is problematic however as their large spring constant means differential contraction would lead to large forces on the sample. This could be alleviated by adding a soft spring, again in series with the stack and platform. However if $k_{spring} \ll k_{stacks}$ then $k_{total} \approx k_{spring}$, meaning we need a large displacement to apply our small force of $\sim 0.4\,N$. The larger the displacement (i.e. the softer the spring) the better, as the control of force improves, and in particular the sample can be more reliably kept under zero force during cooling. If $k_{spring} = 1 \times 10^4\,N/m$ then we would require a displacement of $0.4\,mm$ to achieve this $0.4\,N$, necessitating piezoelectric stack lengths of $\sim 28\,cm$. This is clearly implausible.

*This is obviously material dependent, and for high-resistance samples with large elastoresistivities the signal change per $0.01\,\%$ can exceed the noise level.

A component is therefore needed which gives a large displacement and applies at least a few newtons. Stepper positioners, such as those produced by Attocube Systems, are ideal, giving several-millimetre displacements whilst applying forces of several newtons. If the spring acts ideally, and its constant is precisely known, then use of an encoded positioner means no sensor is required to determine the force on the sample. Furthermore, no restriction is imposed on the spring's stiffness for the arrangement to be stress-controlled, just the aforementioned advantages to making it soft. Zero force on the sample can be maintained during cooling by feeding back on the positioner to keep the capacitance constant.

Another way to reduce the effect of inadvertent longitudinal motion, thus ensuring $\Delta_x = 0$, is to decouple the attachment point between the spring and the platform. A certain displacement is then needed before the spring engages and force is applied. This allows for a true zero-force cool-down without the need for feedback. A force sensor must be used in this case, which allows the use of a non-encoded positioner and a spring with a known, but not precisely characterised, spring constant. However, for accurate knowledge of the force, the sensor must be fully characterised. This is the focus of Section 5.5. The complete arrangement is shown schematically in Figure 5.3, indicating approximate spring constants for the four core components: platform, spring, force sensor and positioner.

We now derive the spring constants shown in Figure 5.3, starting with the maximum force we must apply to the sample. To generate, for example, 2 % compressive or 1 % tensile strain, then a force of

$$F = Ewt\varepsilon = 2\,\% \times 200\,\mathrm{GPa} \times 50\,\mu\mathrm{m} \times 25\,\mu\mathrm{m} = 1.5\,\mathrm{N}$$

is needed in compression, and correspondingly 0.75 N in tension. Because we expect some force to be lost due to components in parallel (i.e. flexures), we specify that the device be able to generate a 1.6 N compressive and 0.8 N tensile force.

$$F_{x,\mathrm{tension}} = +0.8\,\mathrm{N}, \quad F_{x,\mathrm{compression}} = -1.6\,\mathrm{N}. \tag{5.19}$$

To determine the spring's stiffness, we must first specify the maximum displacement of the positioner. The Attocube Systems ANPx311 open-loop linear positioner [199] is well suited, giving a maximum displacement of 6 mm, and generating a maximum force of 2 N. If we want 3 mm to give say 1.8 N, then $k = 600\,\mathrm{N/m}$; this is a lower limit, therefore we say $k_{\mathrm{spring}} \sim 1 \times 10^3\,\mathrm{N\,/m}$.

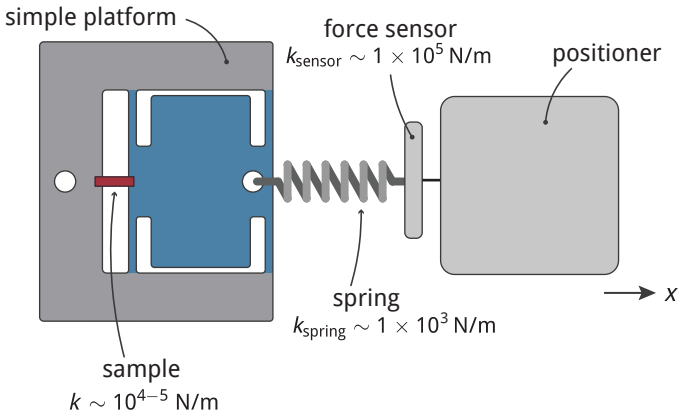

Figure 5.3 | Basic concept of stress-controlled apparatus for applying uniaxial pressure to miniature samples. The sample, approximately $100\,\mu m \times 50\,\mu m \times 20\,\mu m$ in size, is mounted onto a platform which permits longitudinal motion transferred from a positioner stepped down via a soft spring. The sample force is determined via a capacitive sensor in series with the sample. If $k_{sample} \gg k_{flexures}$ then $F_{sensor} \approx F_{sample}$.

The force sensor appears before the spring and therefore takes up some of the positioner's displacement; to minimise this it should be relatively stiff. For a capacitive sensor with a 20 µm plate separation and 20 % gap change under 1.6 N this corresponds to $k_{sensor} \sim 4 \times 10^5$ N/m. This 4 µm displacement is three orders of magnitude smaller than the positioner's displacement, and thus an insignificant loss. Section 5.5 details the force sensor's design.

Lastly, the platform's spring constant should be as low as possible along the x-direction to ensure maximal transferral of force to the sample. Similarly, along the transverse directions the stiffness should be maximised. Because these quantities are not independent (see Equation 5.16), a balance must be found to fix the dimensions. The platform design is the topic of Section 5.4.

5.4 Gapped platforms

Platform design and fabrication can be considered somewhat independently of the rest of the apparatus. As already established, the starting point is essentially a miniaturised version of the piezoelectric-rig main body, as shown in Figure 5.3 and we wish to make the flexures as soft as possible longitudinally, whilst protecting the sample transversely.

Despite being utilised primarily for its semiconducting properties, silicon (Si) is a

useful mechanical material as it has a high yield strength of 4 GPa–7 GPa [200, 201] fracturing beyond this point rather than deforming plastically, as well as exhibiting low repetition fatigue. Combining this with low cost and well-established processing techniques make silicon attractive in the field of microelectromechanical systems (MEMS), and in our case as a platform material. Additionally beneficial for us is the ease of thermal oxide formation, and its low thermal contraction of 0.022 % from RT to 4 K [167].

5.4.1 Design

Flexures are the platform's primary mechanical component. The Young's modulus of Si is $\sim 170\,\text{GPa}$ [202], so taking the lower yield stress above corresponds to a $\sim 2\,\%$ yield strain. A safe tolerance of $\varepsilon_{\max} \leq 0.1\,\%$ ensures that the flexures will not fracture. As explained in more detail in 5.4.2, using deep reactive ion etching to shape the platform limits the minimum feature size to an aspect ratio of $t/20$. Minimising k_x means minimising t and w, so choosing say $t = 200\,\mu\text{m}$ limits the flexure width to $10\,\mu\text{m}$. A sample strain of 2 % means a 2 µm flexure displacement for a 100 µm sample; we will consider protection under maximum displacement of 50 µm, which may be experienced if the sample breaks. Using Equation 5.17 a lower limit for the length can be found such that $\varepsilon_{\max} \leq 0.1\,\%$

$$L_{\max} \geq \sqrt{\frac{3\Delta w}{\varepsilon_{\max}}} \sim 1.7\,\text{mm},$$

where $\Delta = 50\,\mu\text{m}$ and $w = 20\,\mu\text{m}$. The flexure dimensions are therefore chosen to be

$$L = 1.5\,\text{mm}, \quad w = 20\,\mu\text{m}, \quad t = 200\,\mu\text{m}. \tag{5.20}$$

Using the dimensions in Equation 5.20 and calculating the spring constants in Equation 5.16 yields $k_x \sim 80\,\text{N/m}$, $k_y \sim 4.5 \times 10^5\,\text{N/m}$ and $k_z \sim 0.8 \times 10^4\,\text{N/m}$. The force loss due to four 80 N/m flexures in parallel to a 1×10^5 N/m sample (using Equation 5.6) is 0.3 %; this is extremely good. Sample protection is more crucial than force loss, so we increase all spring constants through use of twelve flexures rather than four. The above spring constants are simply multiplied by 12 for the total spring constants in each direction

$$k_x \sim 1 \times 10^3\,\text{N/m}, \quad k_y \sim 5 \times 10^6\,\text{N/m}, \quad k_z \sim 1 \times 10^5\,\text{N/m}. \tag{5.21}$$

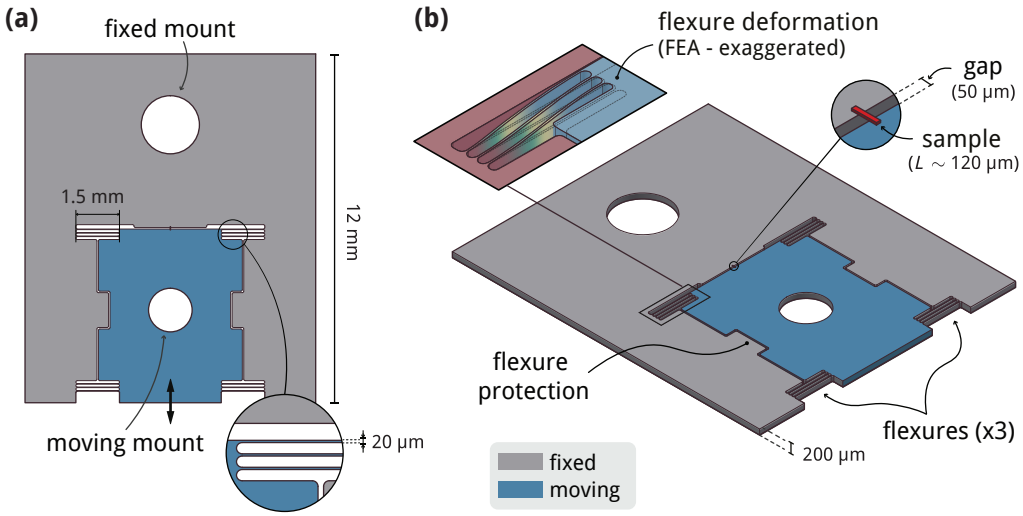

Figure 5.4 | (a) Top view of the gapped platform. Twelve 20 µm-wide flexures allow the moving part (blue) to be displaced with respect to the fixed part (grey), thus uniaxially stressing a gap-mounted sample. **(b)** Isometric view, with insets showing FEA-simulated flexure deformation (exaggerated), and a free-standing sample mounted across the gap. Both panels are to scale.

The force loss becomes 1 % which is still an acceptable error between the actual and measured force. Using Equation 5.18 for the maximum sample displacements, and Equation 5.21 the maximum y and z platform forces are

$$F_y < 130\,\text{mN}, \quad F_z < 4\,\text{mN}. \tag{5.22}$$

For the remaining platform features: the sample gap is chosen to be 50 µm and can be expanded by focused ion beam milling and the mounting holes have diameters of 2 mm and 1.5 mm on the fixed and moving sides respectively. Finally, stoppers are added for a maximum flexure displacement of 50 µm, thus protecting them if the sample breaks. The final design is shown schematically in Figure 5.4.

5.4.2 Fabrication

Deep reactive ion etching (DRIE or Bosch process) is a well-established technique for fabricating precise silicon structures with high aspect ratios ($\sim t/20$) and fast etching rates [203]. The process is shown in Figure 5.5(a): a resist mask is first patterned, then repeated etching and passivating steps are tuned to give successive material

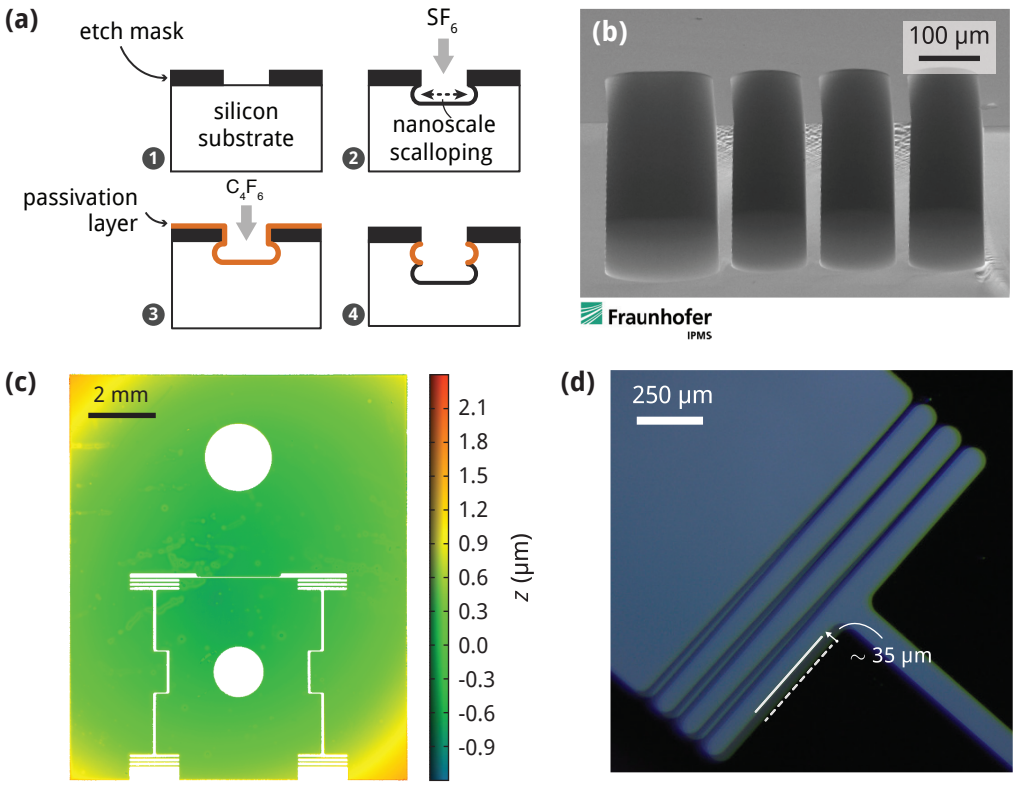

Figure 5.5 | (a) Deep reactive ion etching (DRIE) process. The passivation layer ensures etching can only occur downwards, and not outwards; this enables deep, vertical side walls. **(b)** SEM showing process development for fabrication of flexures with $w/t = 0.1$. Here three flexures and the outer sample gap can be seen. Printed with permission of Sylke Wiedemann, Fraunhofer Institute for Photonic Microsystems (IPMS). **(c)** Optical profile of final fabricated platform. **(d)** Two overlaid optical micrographs demonstrating flexure deformation under a displacement of the moving part by $\sim 35\,\mu m$.

removal with vertical sidewalls. Passivation protects against further etching allowing deep sidewalls to be formed, an artefact of which is scalloping where the scallop size determined by the etch rate (a slower rate gives smaller scallops).

The design shown in Figure 5.4 was fabricated via DRIE by the Fraunhofer Institute for Photonic Microsystems (IMPS) using 200 µm thick Si wafer. Process development was required to achieve the large thickness to width ratio of the flexures, and as a result side walls with deviations of better than 1° were achieved - see Figure 5.5(b). A thermal oxide layer $\sim 5\,\mu m$ thick was added after the DRIE to ensure electrical isolation, and the height profile is shown in Figure 5.5(c). Platforms were tested by displacing the moving part by 35 µm using a micro-manipulator, as seen in Figure 5.5(d).

5.4.3 Sample mounting

We now outline the sample mounting procedure for preparing miniature, focused-ion-beam-milled, free-standing samples on the gapped silicon platforms established above. Platform preparation is the first step. Using a FIB, the gap is increased according to the length of the sample to be mounted. Gold strip-lines (i.e. gold tracks on a flexible insulating film) are then added to the fixed side; these bridge on-platform sputtered leads to thicker wires connecting to the rig. The sample is then prepared before being mounted across the gap and there are two approaches for this. If starting with a macroscopic, bulk sample, then a thin lamella of precisely targeted dimensions can be cut using a FIB. Alternatively, if starting with a small crystal with dimensions of a correct order of magnitude, traditional wire-saw cutting and polishing can be utilised. In-plane dimensions need not be precise because the sample can be shaped after mounting, however the thickness cannot be altered after mounting. Two small epoxy drops are then deposited on either side of the gap, and the sample placed (a micro-manipulator can be used for both of these steps). Enough epoxy must be used such that smooth ramps are formed to the sample's surface, but not too much that the gap is bridged via the sample's underside. Gold is deposited over the platform, electrically connecting the sample and strip-line, and the sample shape and contacts are then defined again using the FIB. The moving side contacts must travel over the flexures to connect to the strip-line.

A gapped-platform-mounted sample is shown is shown schematically in Figure 5.6(a). For initial recipe development, a $\sim 5\,\mu m$ thick $PdCrO_2$ sample was mounted across a 100 µm gap formed between two pieces of silicon wafer – as shown in the SEM image of panel (b) and following the method outlined above.

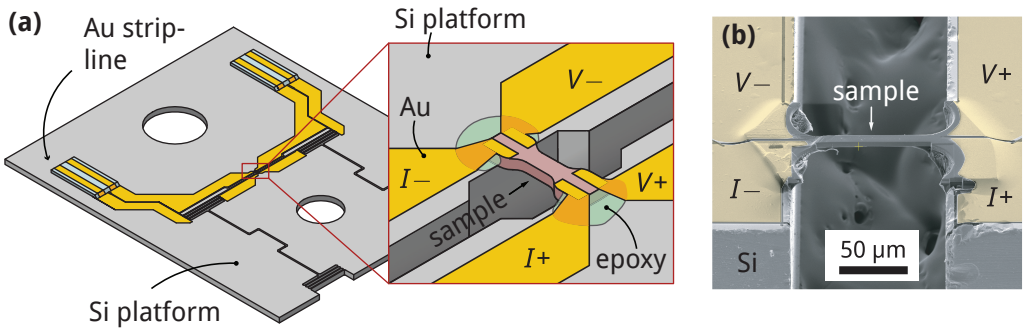

Figure 5.6 | (a) To-scale schematic showing a mounted and contacted sample. Ramped gold strip-line allows for easy contacting of wires to a fine FIB-defined leads connected to the sample. For the moving-part contact, the leads must travel along the flexures. Inset: 140 µm long sample mounted across a 100 µm gap. Here the widened gap, sample geometry and gold would all be defined using FIB lithography. **(b)** Preliminary recipe mounting development, showing a 5 µm thick sample mounted across a 100 µm gap between two pieces of silicon (Si). Gold contacts are falsely coloured.

5.5 Force sensor

5.5.1 Concept

For the force sensor in Figure 5.3, we use a bending-plate capacitive sensor, and conduct in-depth analysis to optimise its dimensions. The operation of this sensor is similar to that of a conventional parallel-plate capacitor, but with the two plates fixed at either end, thus giving a non-uniform gap profile when a force is applied. This allows for a compact sensor with high sensitivity. The basic design, and relevant parameters are shown in Figure 5.7(a). Here the two sides of the sensor are fixed, with an applied force in the $+x$-direction bending the two plates together, giving an increase in capacitance. Because of the non-uniform gap profile we must numerically calculate the force dependence of the capacitance. Furthermore, we must consider the effect of inadvertent torque which might originate from construction mismatches and differential thermal contraction. This would act to bend the top edges away from each other, and the bottom edges together, or vice versa.

In this analysis the bending of only one plate is considered with the other staying fixed, however this is identical to the case when both bend with the displacement being shared equally. The metallic region across which the capacitance is measured is smaller

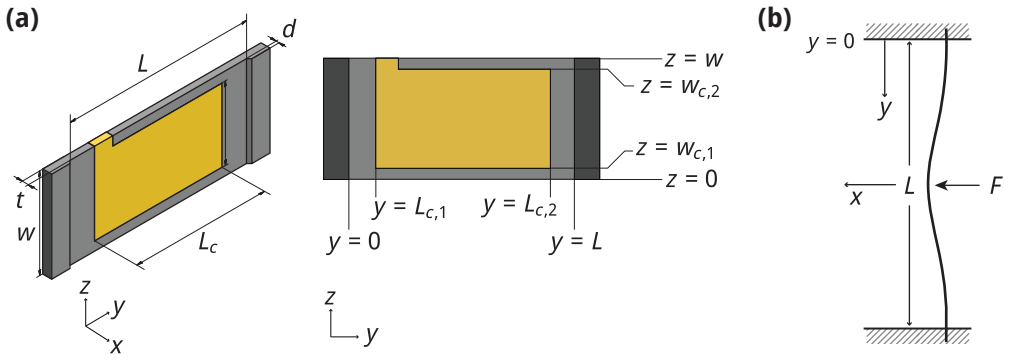

Figure 5.7 | (a) Schematic of a bending-plate capacitive sensor, where d is the plate separation at zero deformation, t the bending thickness, L and w the length and width respectively. The c subscript indicates conductive region. $L_c = L_{c,2} - L_{c,1}$ and $w_c = w_{c,2} - w_{c,1}$. **(b)** Bending of a beam with fixed ends under a force F applied in the centre. L is the undeformed length.

than the total bending area. The correction due to this offset is included, but expected to be small.

To determine the parameters of this sensor, its spring constant must first be determined. A beam fixed at both ends under a force at its centre takes on the bending profile shown in Figure 5.7(b), with the analytical form of displacement [204] of

$$x = \frac{Fy^2}{48EI}(3L - 4y), \tag{5.23}$$

for $0 < y < L/2$, where F is the load, E is the elastic modulus, and I the area moment of inertia. Maximum deflection occurs at $y = L/2$, at which $x_{\max} = FL^3/192EI$. For a rectangular cross section $I = wt^3/12$, meaning $x_{\max} = FL^3/16Ewt^3$, so the force per maximum displacement $k = F/x_{\max}$ is:

$$k = \frac{16Ewt^3}{L^3}. \tag{5.24}$$

Assigning the top plate as the one which bends, and placing the beam between $x = 0$

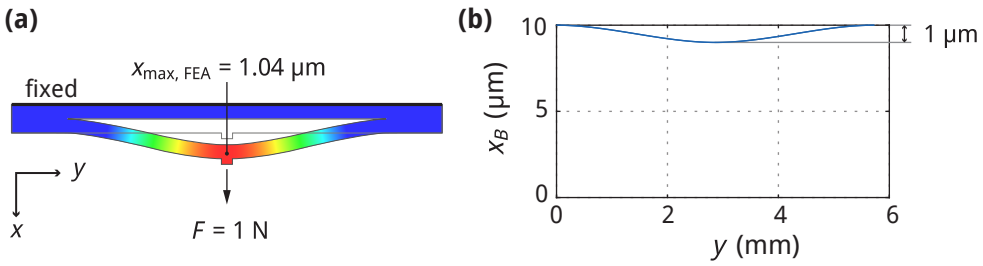

Figure 5.8 | (a) Finite element simulation of a bending-plate capacitive force sensor. This is exaggerated and shown using an outward force for clarity. **(b)** Theoretical bending given by Equation 5.25, here the displacement is 1 µm.

and $x = L$, the surface profile for the bending is

$$x_B(y,z,F) = \begin{cases} d - \dfrac{Fy^2}{4Ewt^3}(3L-4y) & \text{for} \quad 0 \le y \le L/2, \\ d - \dfrac{F(y-L)^2}{4Ewt^3}(4y-L) & \text{for} \quad L/2 < y \le L. \end{cases} \tag{5.25}$$

5.5.2 Finite element analysis

Equation 5.23 assumes that the outer ends of the bending beam are fixed infinitely rigidly, but the design of Figure 5.7 has only narrow overlap sections on either side. Before using this bending equation to inform decisions regarding dimensions we use FEA to determine the ideality of the design shown in Figure 5.7, and to do so take the test parameters

$$t = 250\,\mu\text{m}, \quad d = 10\,\mu\text{m}, \quad w = 5\,\text{mm}, \quad F = 1\,\text{N}, \quad x_{\max} = 1\,\mu\text{m}, \quad E = 150\,\text{GPa},$$

where here we have simply chosen a reasonable value for the Young's modulus without yet considering a specific material. If we want $k = 1 \times 10^6\,\text{N/m}$, then using Equation 5.24 gives $L = 5.73\,\text{mm}$. A plot of Equation 5.25 using these dimensions is shown in Figure 5.8(b). The FEA result will depend on the width of the fixed strips on either side, but taking these to be 1 mm each, as shown in Figure 5.8(a), the displacement is $x_{\text{max, FEA}} = 1.04\,\mu\text{m}$ – i.e. 4 % higher than the theoretical value. Therefore use of Equation 5.25 to model the sensor behaviour is justified.

In order to inform the analytical form of the effect of torque on the sensor, FEA must again be used. Simply taking the same parameters as before and applying a

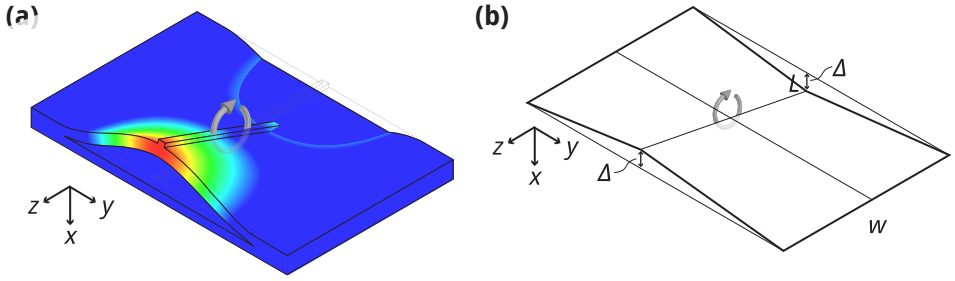

Figure 5.9 | (a) Finite element simulation of the effect of a 1 N mm torque on the centre bar running from the top to bottom edge of one plate. **(b)** First-order approximation to the bending profile shown in panel (a) to quantify the error introduced in force readout due to torque.

torque of $\tau = 1\,\text{N mm}$ yields the deformation shown in Figure 5.9(a). To first order, the deformations shown can be approximated to be linear, giving a triangle-like deformation at $z = 0$ and $z = w$, with a maximal x-displacement of Δ at $y = L/2$ – as shown in Figure 5.9(b). An analytical expression for this deformation can be formed by linearly varying between the conditions $x_T(0,z) = x_T(L,z) = 0$, $x_T(L/2,0) = -\Delta$ and $x_T(L/2,w) = \Delta$, giving

$$x_T(y,z) = \begin{cases} d - \left(\dfrac{-4\Delta}{w}z + 2\Delta\right)\dfrac{y}{L} & \text{for} \quad 0 \le y \le L/2, \\ d - \left(\dfrac{4\Delta}{w}z - 2\Delta\right)\dfrac{y-L}{L} & \text{for} \quad L/2 < y \le L, \end{cases} \tag{5.26}$$

and the value of Δ for a given torque can be determined via FEA. The capacitive sensitivity and effect of inadvertent torque can now be quantified. Most importantly the difference between the sample and sensor forces due to torque can be calculated.

5.5.3 Capacitance calculation

The total capacitance is calculated by integrating infinitesimal capacitances between $L_{c,1} \le x \le L_{c,2}$ and $w_{c,1} \le y \le w_{c,2}$

$$C_i = \int dC(y,z) = \int_{L_{c,1}}^{L_{c,2}} dy \int_{w_{c,1}}^{w_{c,2}} dz \frac{\epsilon_0}{x_i(y,z)}. \tag{5.27}$$

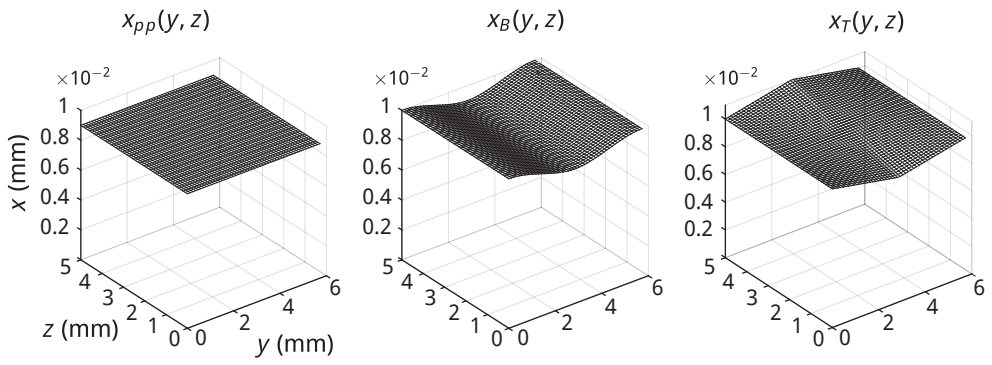

Figure 5.10 | Surface plots of the deformations considered for characterisation of bending-plate capacitor behaviour. Left: parallel plate surface $x_{pp}(y,z)$; this gives a reference capacitance for two plate separated by a uniform gap. Middle: bending profile $x_B(y,z)$ for a capacitor plate with fixed ends. Right: inadvertent bending $x_T(y,z)$ due to torque at the sensor's centre.

The subscript i labels either the case for bending $i = B$, torquing $i = T$, or $i = pp$ where

$$x_{pp}(y,z) = d - \frac{F}{k}, \tag{5.28}$$

is the profile of a simple parallel plate capacitor, for use as a reference. The effect of torque can be calculated by inserting $x_{pp} + x_T$ or $x_B + x_T$ in Equation 5.27. For $x_B(y,z)$ and $x_{pp}(y,z)$ the force is ramped linearly from 0 to F in order to determine the force dependence of the capacitance, and a constant value of torque (fixed through Δ) is used throughout the force range. The profile for these three displacements is shown in Figure 5.10. An important quantity for apparatus design is the sensitivity, i.e. the capacitance change per force change

$$S_i(F) = \frac{dC_i}{dF}, \tag{5.29}$$

for $i = pp,\ B$.

5.5.4 Results

We now have all the necessary ingredients to calculate the capacitance of a bending-plate sensor, in the absence and presence of torque. We must first choose an appropriate material. The plates should be constructed out of a material which is insulating, with a low thermal contraction and ideally smooth on the order of tens of nanometers. The

	E (GPa)	t_{min} (μm)	L (mm)	L_c (mm)	Δ (μm)
Single crystal quartz	77	350	9.3	7.8	1.3
Sapphire	350	250	10.9	9.4	1.8

Table 5.2 | Parameters for sapphire and quartz sensor used in capacitance calculations. For sapphire the Young's modulus is taken from Ref. [205], and for single-crystal quartz from Ref. [206]. t_{min} is determined by standard commercially available wafer thicknesses. L is calculated from Eq. 5.24. Dimensions of the conductive area are given by $L_c = L - 3\alpha$, $w_c = w - 2\alpha$, where $\alpha = 0.5\,\text{mm}$ is a edge offset length, and as such $w_c = 5\,\text{mm}$. FEA was used to acquire Δ by applying the torque shown in Equation 5.30.

two obvious candidates satisfying these criteria are quartz and sapphire.

After specifying the material, the order of operations for parameter assignment will be:

1. Plate thickness t determined by sensor material.
2. Plate separation d chosen based on method of separation, maximising sensitivity and minimising risk of shorts.
3. Plate width w chosen based on space available for sensor.
4. Plate displacement x_{max} (under force F_{applied}) chosen as a suitable fraction of d to give acceptable sensitivity. This sets the spring constant k.
5. Plate length L calculated from Equation 5.24 to give the required k.
6. Young's modulus E fixed by sensor material.

In general there is a risk of L becoming too large, this can help inform the decisions of points 1. and 4. - i.e. t and δ should be minimised. After determining these parameters $C_i(F)$ and $S_i(F)$ are calculated for $i = pp,\ B,\ T + B$.

We choose a plate separation of $d = 20\,\mu\text{m}$, and target a maximum displacement of $x_{\text{max}} = 2\,\mu\text{m}$ (i.e. 10 % of the gap) under the maximum force of 0.8 N *. This corresponds to a spring constant of $k = 4 \times 10^5\,\text{N/m}$. The width was chosen to be $w = 6\,\text{mm}$. The expected torque originates from a $\delta = 150\,\mu\text{m}$ alignment offset at

*We later doubled the maximum target compressive force to −1.6 N. The torque scales linearly with applied force, but the factor of ten tolerance between the expected torque and the value used in this analysis means this doubling does not alter any conclusions.

	quartz	sapphire
Anomalous force at $F = 0\,\mathrm{N}$	5 mN	10 mN
Anomalous force at $F = 0.8\,\mathrm{N}$	6 mN	11 mN
Force error at $F = 0.8\,\mathrm{N}$	0.8 %	1.4 %

Table 5.3 | Anomalous force and error of a bending-plate sensor due to a fixed torque of 1 N mm.

$F = 0.8\,\mathrm{N}$ giving $\tau = F\delta \sim 0.1\,\mathrm{N\,mm}$. Taking a factor of ten tolerance for safety means a torque of $\tau = 1\,\mathrm{N\,mm}$. Compiling the material independent parameters:

$$d = 20\,\mu\mathrm{m}, \quad x_{\max} = 2\,\mu\mathrm{m}, \quad k = 4\times10^5\,\mathrm{N/m}, \quad w = 6\,\mathrm{mm} \quad \tau = 1\,\mathrm{N\,mm}. \tag{5.30}$$

As given by the order of operations above, sample dependent parameters are shown in Table 5.2. The force-dependent capacitance was calculated using the Equation 5.27 and the parameters in Equation 5.30 and Table 5.2 for parallel-plate and bending-plate profiles, and for the latter also in the presence of a fixed torque. The sensitivity for each of these was calculated using Equation 5.29. The results for both quartz and sapphire are shown in Figure 5.11.

To first order, the deviation in capacitance at $F = 0.8\,\mathrm{N}$ caused by a torque of $\tau = 1\,\mathrm{N\,mm}$ for sensors made of both single crystal quartz and sapphire is 0.05 % and 0.09 % respectively. Although the capacitance error is extremely small, the force error depends on $\mathrm{d}C/\mathrm{d}F$. There are two important quantities: the anomalous force reading at zero force, and the error on the measured force at 0.8 N. These are shown in Table 5.3. Because sensitivity does not vary much with force, the error can be mostly calibrated out from the zero-force readout. Although the error is larger for sapphire, a 1.4 % error under an extreme torque is still satisfactory, and due to the increased sensitivity, smaller differential thermal contraction, and lack of piezoelectric effect we choose it over quartz.

We fabricated the sensor from sapphire with the dimensions shown in Table 5.2 and Equation 5.30 with the conductive region defined by 300 nm sputtered gold on top of 5 nm titanium. The two sapphire wafers were spaced using 25 µm foil, resulting in a gap of 45 µm with the addition of epoxy and a measured capacitance of 9.44 pF.

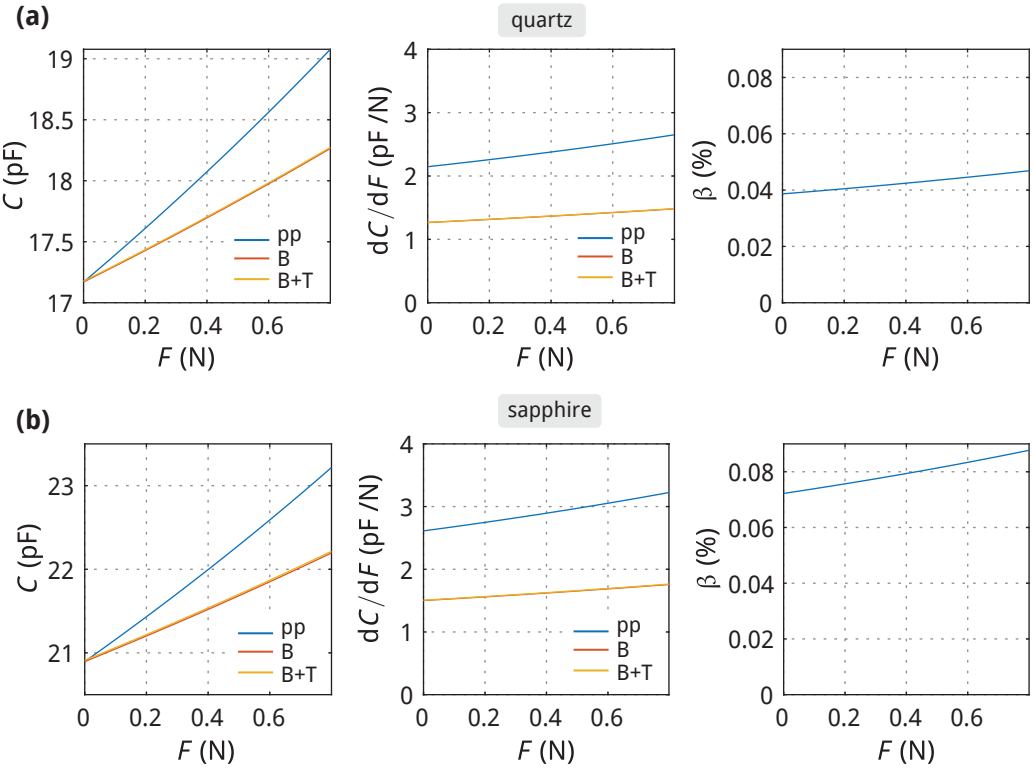

Figure 5.11 | (a) Results for quartz. Left: Simulated capacitance as a function of force for parallel-plate (pp), bending-plate (B), and bending-plate plus constant torque ($B+T$) scenarios. Middle: Sensitivity as a function of force. As expected the bending plate scenario is less sensitive. Right: capacitance error as a function of force. **(b)** Results for sapphire, as in panel (a). The capacitance (left) and subsequently sensitivity (middle) are larger than for quartz due to the larger length required to obtain the target spring constant.

5.6 Full rig

The most significant designed-based effort involves bringing together the relatively simple elements shown in Figure 5.3, i.e. the positioner, sensor, spring and platform, whilst giving consideration to the severe challenges originating from inadvertent displacements which may easily give rise to large parasitic stresses. The arrangement of these base components is shown in Figure 5.12.

Of these four components, only specification of the spring dimensions remain. A bending-foil design as shown in Figure 5.12(a), allows a given spring constant to be precisely targeted. The two bending foils are in series, $k_{\text{spring}} = k_{\text{foil}}/2$, and have

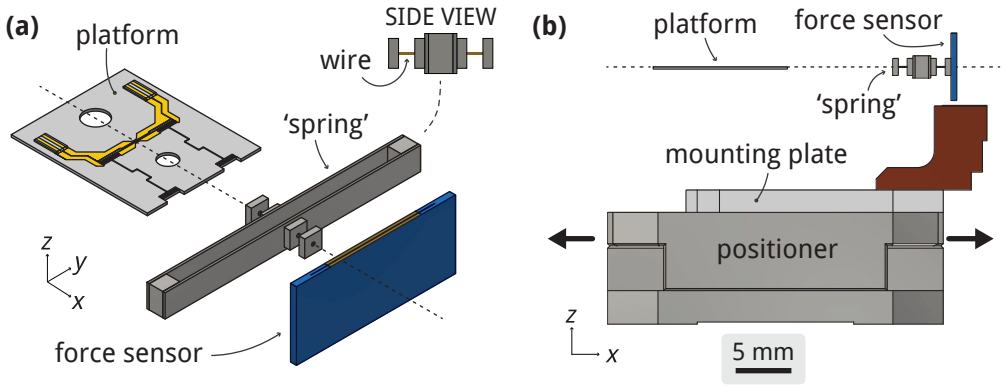

Figure 5.12 | To scale. **(a)** Linear combination of the force sensor, 'spring' and platform. **(b)** In applying a displacement x to the force sensor from the positioner, if $k_{\text{sample}} \gg k_{\text{flexures}}$ and k_{sample}, $k_{\text{sensor}} \gg k_{\text{spring}}$ then all the displacement goes into the spring i.e. $x_{\text{spring}} \sim x$, and $F_{\text{sample}} \sim k_{\text{spring}} x$.

the same analytical form of deformation as the force sensor in Section 5.5 giving $k_{\text{foil}} = 16Ewt^3/L^3$. In Section 5.3 we roughly determined a lower-bound spring constant of $k_{\text{spring}} \sim 1 \times 10^3\,\text{N/m}$, based on a 3 mm positioner displacement providing 1.8 N. We now target $k_{\text{spring}} = 2 \times 10^3\,\text{N/m}$ to keep the foil length manageable. Using $t = 200\,\mu\text{m}$ thick titanium foil ($E = 120\,\text{GPa}$), and setting $w = 2\,\text{mm}$, then $L = 19.5\,\text{mm}$ to give the target spring constant. In compression, each foil is displaced by at least $d = 1.6\,\text{N}/4 \times 10^3\,\text{N/m} = 400\,\mu\text{m}$, resulting in a maximum foil strain of $\varepsilon_{\text{max}} = 3 \cdot 400\,\mu\text{m} \cdot 200\,\mu\text{m}/9.75\,\text{mm} \sim 0.25\,\%$ – this is below the yield strain of grade 5 Ti. The total spring provides 1.6 N of compression with 0.8 mm displacement, and the positioner step size of 0.8 µm at 4 K [199] corresponds to a force interval of 1.6 mN. Using 125 µm diameter phosphor bronze wires of length 0.8 mm gives a safe buckling load of ~ 90 N.

5.6.1 Silicon assembly

Transmission of force from the spring to the platform must be carried out by a component that ensures that any construction mismatches, differential thermal contraction or other inadvertent forces or torques do not apply more than $F_y = 130\,\text{mN}$ and $F_z = 4\,\text{mN}$. This cannot be achieved by rigidly attaching the spring directly to the platform. Protection can be achieved in series through a low spring-constant component such that large inadvertent displacements give a small force, or conversely in parallel by a high-spring constant component giving small displacements under large

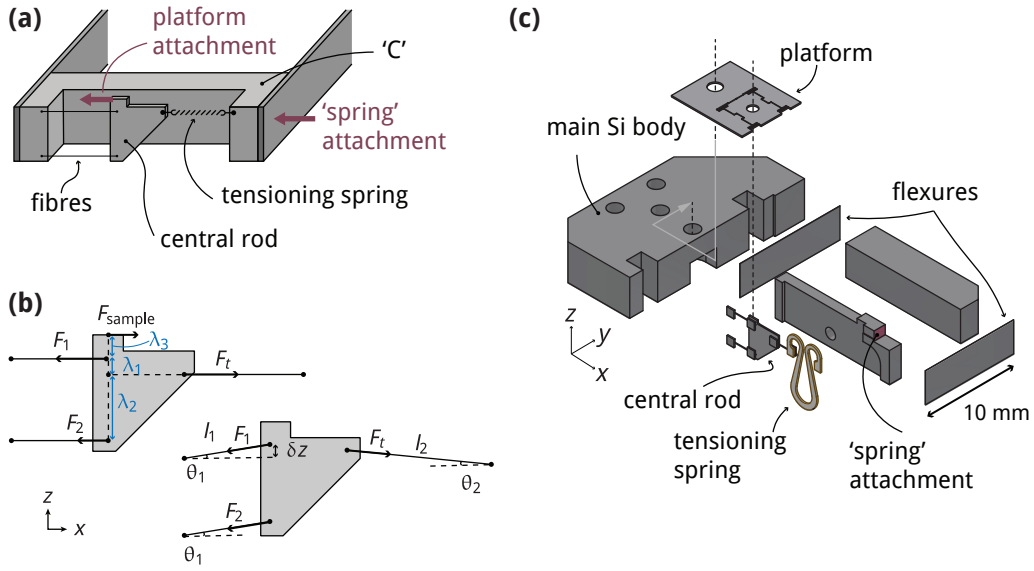

Figure 5.13 | (a) Basic concept of a component which transmits x displacement freely whilst resisting y and z motion at the spring attachment, and freely transmits x force whilst resisting dangerous y and z force at the platform attachment. **(b)** Force and torque balance diagrams. **(c)** Final design: the platform and flexures are fixed to the main silicon (Si) body.

forces. Combining these approaches we conceive of a component whose connection point to the spring transmits only *x-displacement* and minimises all others, and whose connection to the platform transmits only *x-force* and resists all others. That is to say: a low x, and large y, z spring constant to the spring attachment; and large x, small y, z spring constant to platform attachment. It it possible to achieve this with a complicated arrangement of flexures, however a simpler solution is shown in Figure 5.13(a). Here the spring-attachment criterion, $k_x \ll k_y,\ k_z$, is satisfied through use of very thin and long flexures, whereas for the platform attachment, thin fibres have a high longitudinal spring constant and extremely low transverse spring constants giving the required $k_x \gg k_y,\ k_z$. The central rod is frictionally locked to the platform only during force transmission and is otherwise decoupled, allowing for zero force to be maintained during cooling. When changing the temperature whilst applying force then the platform-attachment criterion $k_x \gg k_y,\ k_z$ allows differential thermal contraction along x to become problematic, so we soften this condition (i.e. decrease k_x) controllably with a tensioning spring; this additionally keeps the fibres taut.

The most direct way to minimise differential thermal contraction is to avoid using

different materials. There is an infinite regress here – *everything* cannot be constructed from the same material – however by maximising the number of components identical in material to the platform, i.e. silicon, inadvertent differential thermal displacements can be minimised. Most importantly we can eliminate (in principle) any slipping of the platform, by also making the component it is attached to from silicon. The assembly of components shown in Figure 5.13(a) are therefore constructed from silicon. In using pure single-crystalline silicon, thermal contraction mismatches between components of the same material are also virtually eliminated – this is not true of metallic alloys.

We must now conduct quantitative analysis to establish whether the above arrangement can satisfy $F_y < 130\,\text{mN}$ and $F_z < 4\,\text{mN}$, and start by determining the tensioning spring's properties. The forces on the central rod are shown in Figure 5.13(b). Because the system is stationary, $\sum F_x = 0$ and $\sum \tau_y = 0$ from Newton's second law, and in combination with the requirement that F_1 and F_2 be positive to keep the fibres in tension, F_t can be calculated. For 1.6 N compression, these conditions are satisfied by $F_t > 1.07\,\text{N}$, and for tension by $F_t > 1.14\,\text{N}$ where we have used $\lambda_1 = 0.9\,\text{mm}$, $\lambda_2 = 3.5\,\text{mm}$, $\lambda_3 = 0.6\,\text{mm}$. We therefore choose a tensioning force greater than both of these, $F_t = 1.4\,\text{N}$. The 'u'-shaped tensioning spring shown in Figure 5.13(c) has $k_x \sim 3 \times 10^3\,\text{N/m}$ as given by FEA when made from grade 5 titanium, and so must be pre-displaced by $\sim 500\,\mu\text{m}$ to supply 1.4 N.

The z-force condition is the most severe ($F_z < 4\,\text{mN}$) so we start with that. Inadvertent forces are permitted along z by the non-zero stiffness of the fibres/tensioning spring, and the non-infinite flexure stiffness. Considering the former first, and referring to the bottom part of Figure 5.13(b) in which the central rod is displaced by δz, the resulting restoring force is $F_{\text{vert}} = \sum_i F_{i,z} = \sum_i F_i \sin\theta_i = \sum_i F_i \delta z / l_i$, giving

$$F_{\text{vert}} = (F_1 + F_2)\frac{\delta z}{l_1} + F_t \frac{\delta z}{l_2}. \tag{5.31}$$

Force balance gives $F_1 + F_2 = F_t$ and so

$$k_{z,\text{tens}} = \frac{F_{\text{vert}}}{\delta z} = F_t\left(\frac{1}{l_1} + \frac{1}{l_2}\right) = 1.4\ \text{N} \cdot \left(\frac{1}{2.35\,\text{mm}} + \frac{1}{1.85\,\text{mm}}\right) = 1350\,\text{N/m}. \tag{5.32}$$

The above spring constant ignores the mechanical properties of the fibres, which act like beams fixed at one end, and guided under a load F at the other. In this case, the maximum deflection at the free end is $\delta x = Fl^3/12EI$, giving a spring constant (for a

circular cross-sectioned beam of radius a) of

$$k_{z,i} = \frac{12EI}{l_i^3} = \frac{3\pi E a^4}{l_i^3}, \tag{5.33}$$

where $E = 400\,\text{GPa}$, $l_1 = 2.35\,\text{mm}$, and $l_2 = 1.85\,\text{mm}$ is the distance between the rod and tensioning spring. The tensioning spring is in series with a single fibre, and these are in parallel with the other two fibres giving

$$k_{z,\text{def}} = 2k_{z,1} + \frac{k_{z,2}k_{z,t}}{k_{z,2} + k_{z,t}}, \tag{5.34}$$

where $k_{z,t} = 7.5 \times 10^3\,\text{N/m}$ (from FEA). For the fibre-tensioning spring constant to dominate over that from transverse deformation – thus not restricting the 5 µm z-compliance further – then $k_{z,\text{def}} < k_{z,\text{tens}}$. We can use this to find an upper bound on the fibre, giving

$$a < 33\,\mu\text{m}. \tag{5.35}$$

There is also a limitation on how small the fibre radius can be. Tests in which tungsten wires of radii 15 µm and 25 µm were epoxied using Epo-Tek H74 between two silicon wafers and tensioned, gave failure forces of

$$F_{\text{failure}} = 2.1\,\text{N}, \quad \text{for} \quad a = 15\,\mu\text{m},$$
$$F_{\text{failure}} = 6.8\,\text{N}, \quad \text{for} \quad a = 25\,\mu\text{m}.$$

Failure was consistently caused by a snapping of the wire rather than by a loss of adhesion to the epoxy, indicating that these forces are more measures of the ultimate tensile strength than yield strength. The largest force on a single fibre is $\sim 3\,\text{N}$ and so there is an approximate factor of two safety for a 25 µm radius wire – for further safety we choose $a = 40\,\mu\text{m}$. This gives $k_{z,\text{def}} = 2.7 \times 10^3\,\text{N/m}$ and so the total k is $\sim 4 \times 10^3\,\text{N/m}$.

If we want the force on the platform to stay below 4 mN, then the maximum z displacement of the central rod is

$$z_{\text{platform attachment}} < 1\,\mu\text{m}. \tag{5.36}$$

If the large silicon flexures have dimensions of $t = 5\,\text{mm}$, $w = 25\,\mu\text{m}$ and $L = 10\,\text{mm}$ then $k_z = 170\,\text{GPa} \cdot 25\,\mu\text{m} \cdot (5\,\text{mm})^3/(10\,\text{mm})^3 \sim 5.3 \times 10^5\,\text{N/m}$, and if all 1 µm origi-

nates from the flexures then the maximum permissible force at the spring attachment is

$$F_{z,\,\text{spring attachment}} < 0.5\,\text{N}. \tag{5.37}$$

We pause for a moment to appreciate the protection provided by the silicon assembly – our original constraint of 4 mN has been relieved to 500 mN. Under the assumption that all inadvertent effects occur at the spring attachment, the maximum z-force of 0.5 N means that our 1.6 N target x-force must be applied at an angle better than 18° – this is easily achievable. Differential thermal contraction may also occur due a thermal gradient between the rod and platform holder. If this reaches 10 K, the 1.5 mm distance between the platform attachment and tensioning-spring fibre gives $z = 35\,\text{nm}$ – this is safely less than 1 μm.

The above considerations rely on frictional locking between the pin and the platform, but this will only be true above some minimum force, below which a slip might have negative consequences. If it does not cause the sample to break, then it simply complicates the measurements slightly. If the coefficient of friction between the rod and platform is $\mu \sim 0.2$ then for a given z force $F_x > F_z/\mu$ to ensure slipping does not occur. The minimum step size of the positioner corresponds to $F_x \sim 1.6\,\text{mN}$, and so any z-force below $1.6\,\text{mN} \times 0.2 = 0.32\,\text{mN}$ should not be problematic. The above differential thermal contraction of 35 nm corresponds to a force of 0.14 mN, which is below this limit. The maximum inadvertent z force of 4 mN would require a minimum x-force of 20 mN to avoid slipping.

5.6.2 Final design

We combine the silicon assembly shown in Figure 5.13 with the base components shown in Figure 5.12, using a frame primarily constructed from copper components, connected with brass screws. The final design is shown and described in Appendix D, and is credited to Dr Clifford Hicks.

5.6.3 Spring decomposition

With the silicon assembly connecting the spring to the platform, the rig's complexity makes FEA challenging. The sample only appears in parallel with the flexures on the platform and the flexures on the silicon assembly which both have small x spring constants compared to the sample, meaning the force on the spring is approximately equal to the force on the sample. For a soft sample it is valuable to quantify the difference between sensor and sample forces. Furthermore, in decomposing the system

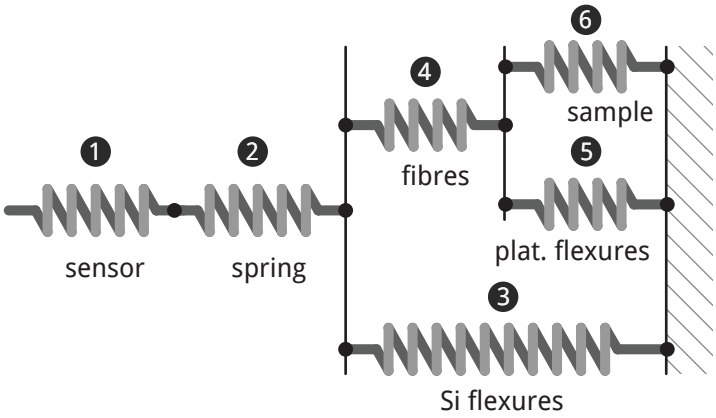

Figure 5.14 | x-axis decomposition of the components of the apparatus either in series or parallel with each other. These are numbered for indexing and, as per the convention introduced in Section 5.2.1, indices are concatenated for combined springs - e.g. the spring constant of the whole system is k_{123456}. It should be stressed that these indices are ***not*** related to the tensor notation in Table 3.1.

we can calculate the displacement of the positioner required to provide the 1.6 N compression and 0.8 N tension on the sample, as well as strain the sample will experience in these cases.

We consider two extremes of sample stiffness, and list all spring constants with an index as in Figure 5.14, these are:

1. Sensor: $k_1 = 4 \times 10^5\,\mathrm{N/m}$
2. Spring: $k_2 = 2 \times 10^3\,\mathrm{N/m}$
3. Si flexures: $k_3 = 23\,\mathrm{N/m}$
4. Fibres:
   - For sample compression, the fibres are tensioned $K_4^- = 2E\pi a^2/L = 2\pi \cdot 400\,\mathrm{GPa} \cdot (40\,\mu\mathrm{m})^2/2.35\,\mathrm{mm} = 1.7 \times 10^6\,\mathrm{N/m}$.
   - For sample tension, the tensioning spring is extended, from FEA $k_4^+ = 7.5 \times 10^3\,\mathrm{N/m}$.
5. Platform flexures: $k_5 = 0.97 \times 10^3\,\mathrm{N/m}$.
6. Sample:
   - Max: $k_6^{\max} = 200\,\mathrm{GPa} \cdot 20\,\mu\mathrm{m} \cdot 40\,\mu\mathrm{m}/50\,\mu\mathrm{m} = 3 \times 10^6\,\mathrm{N/m}$
   - Min: $k_6^{\min} = 50\,\mathrm{GPa} \cdot 10\,\mu\mathrm{m} \cdot 20\,\mu\mathrm{m}/100\,\mu\mathrm{m} = 1 \times 10^5\,\mathrm{N/m}$

Starting with the relationship between the force on the sample (F_6) and that on the

	compression	tension
stiff sample	0.03%	0.34%
soft sample	0.98%	1.29%

Table 5.4 | Difference between the force applied to the force sensor and the force experienced by the sample, i.e. $(F - F_6)/F$, expressed as a percentage, for stiff ($k_6^{\max}$) and soft ($k_6^{\min}$) samples under compressive and tensile forces. As expected, we get better stress control when the sample is stiff.

system as a whole (F), the force on the sample is shared between the platform flexures and the silicon flexures. Starting at the sample

$$F_6 = \frac{F_{56}}{1 + k_5/k_6}. \tag{5.38}$$

The force on the sample/platform combination (F_{56}) is equal to the sharing between the silicon flexures (3) and the combined fibres/sample/platform (456), therefore $F_{56} = F_{456}$ and

$$F_{456} = \frac{F_{3456}}{1 + k_3/k_{456}}, \tag{5.39}$$

where here $F_{3456} = F$. Therefore the force on the sample is

$$F_6 = F\left(\frac{1}{1 + k_3/k_{456}}\right)\left(\frac{1}{1 + k_5/k_6}\right), \tag{5.40}$$

where

$$k_{456} = \frac{k_4(k_5 + k_6)}{k_4 + k_5 + k_6}. \tag{5.41}$$

We see that if $k_3 \ll k_{456}$ and $k_5 \ll k_6$, then $F_6 \approx F$ - meaning that any force applied to the system is felt by the sample. As intended from the design, k_3 and k_5 are both flexures, with low spring constants in the longitudinal direction. However it is useful to quantify the extent to which $F_6 \approx F$ via the quantity $(F - F_6)/F$. Calculations of this quantity are shown in Table 5.4. As expected, the largest error is for a soft sample in tension, but at 1.29 % we can classify the rig as stress controlled. This is also smaller than are usual error of $\sim 10\,\%$ in strain for piezoelectric-based strain-controlled apparatus.

We follow a similar method for the sharing of displacement between the sample and

	sample compressed		sample tensioned	
	$k_6^{\max}$	$k_6^{\min}$	$k_6^{\max}$	$k_6^{\min}$
F_6 (N)	−1.6	−1.6	0.8	0.8
σ (GPa)	−2	−8	1	4
ε (%)	−1.0	−16.0	0.53	8.0
x (mm)	−0.81	−0.83	0.51	0.52

Table 5.5 | Table showing the force (F_6), stress (σ) and strain (ε) for small/soft and larger/stiffer samples under compression and tension, as well as calculation of the displacement of the positioner, x, using Equation 5.42. For a soft sample under compression the apparatus can theoretically apply large strains of up to 16 % - in reality the sample will fail before this point.

springs in series with it, giving the sample force as a function of system displacement:

$$F_6 = \left(\frac{k_6}{1 + k_{56}/k_4}\right)\left(\frac{x}{1 + k_{3456}/k_{12}}\right). \tag{5.42}$$

We use Equation 5.42 to calculate the amount of displacement x on the system for the sample to experience 1.6 N and 0.8 N, as well as the sample displacement $x_6 = F_6/k_6$, strain $\varepsilon = x_6/L$ and stress $\sigma = F_6/wt$ – this is shown in Table 5.5. To apply the target sample force, the position displacement is importantly less than the rig's stopper distance (±1 mm). The travel range of the Attocube ANPx311 is ±3 mm, which is much larger than both the positioner stopper distance and the required displacement to reach the target sample forces. For the standard sample parameters we have been considering ($L = 100\,\mu$m, $w = 25\,\mu$m, $t = 15\,\mu$m and $E = 100$ GPa), the theoretical capability of the apparatus is 2.1 % in tension and 4.3 % – large enough to push the sample to its mechanical limit.

5.7 Conclusion and outlook

Technological developments are critical to the advancement of experimental physics. In general such advances are concerned with expanding the range of externally applied control parameters – for example temperature, pressure or magnetic field. This is vital, as use of external tuning parameters to map out exotic phases of matter is at the heart of solid state research. As already established, uniaxial pressure is an effective

tool for this driving large changes in electronic structure. The apparatus presented in this chapter can apply larger tuneable uniaxial pressures than ever achieved before, and can therefore expand the phase diagram of *any* material. Its successful operation would therefore represent a significant breakthrough in experimental condensed matter physics. Unsurprisingly, pushing the limits of uniaxial pressure requires looking beyond established techniques and pushing technological boundaries which inevitably requires greater sophistication, a factor which easily succumbs to increased complexity.

The apparatus presented in this chapter is currently the most complex device yet conceived for applying tuneable uniaxial pressure at cryogenic temperatures. For this reason a whole chapter has been dedicated to the considerations required to realise its design. Also for this reason complete construction and proof of operation has not yet been achieved. The most challenging aspect of construction is the small tolerances for any mismatches, most notably for the silicon assembly, combined with the intricate combination of many small parts. An ever-present challenge of complex cryogenic devices is that they are constructed, tested and tuned for operation at room temperature. Upon reducing temperature, the exact change in behaviour due to thermal contraction cannot always be predicted. As we have done, steps can be taken in the design to ensure large overlaps of different materials are avoided, in order to minimise these inadvertent thermal effects.

At the time of writing, and due to the work of Po-Ya Yang, the bottom half of the apparatus has been constructed, and the displacement sensor shown to work, giving large step-like capacitance changes for each positioner step. He has also extended sample-preparation progress, demonstrating a complete recipe using a gapped platform whilst successfully measuring the sample's electrical properties at room temperature. The force sensor and spring have also been completed, along with successful microstructured sample-on-platform mounting. Ongoing work on the silicon assembly is challenged by the aforementioned tight construction tolerances, combined with its fragility and the pre-tensioning of the spring whilst fixing the tungsten fibres.

One would normally test and characterise a new rig empty, i.e. before installing a sample and conducting a measurement. This primarily involves ensuring operation of the sensors, and characterising their temperature dependence. For the displacement sensor, this is easily done, and has already been shown to work at room temperature. However, without a sample, the plates of the force sensor in principle have no force to measure. Due to the high sensitivity of a well-shielded three-terminal capacitance measurement, this can be used to our advantage to measure the force error, and check that it is indeed negligibly small. After installing a platform-mounted sample, the force

sensor can be properly tested, and by cooling down the rig in an optical flow cryostat, motions can be inspected and measured using a microscope. If the sample is large enough, its strain can be directly measured (as per the method outlined in Section 3.3.6, and if its elastic constants are known, this can be checked against the readout from the force sensor.

Lastly, it is worth pointing out potential challenges. The transmission of force relies on the tungsten fibres not fatiguing as they are repeatedly tensioned, and also on them remaining rigidly fixed to the silicon parts. The former can be overcome by increasing the fibre diameter, but for the latter an alternate rod attachment design must be conceived using two fibres that run the length of the central 'C' piece. This increases the force applied by inadvertent x-motion of the rod, but is simpler to construct and is less likely to fail. Implementing such a change makes it even more certain that this apparatus can operate successfully. Such certainty is additionally underpinned by the positioner being at the heart of this apparatus – it is a well-established and reliable technology designed for cryogenic use.

For the experimental results presented in Chapter 4, despite being able to use it to our advantage, we saw how in-plane controlled strain was not the most ideal tuning parameter with which to traverse the phase diagram of FeSe. The sample forms twin boundaries, and we only control average and not local strain. Controlled stress does not, in-principle, encounter such issues, as the sample becomes detwinned under any finite stress, and we can trace a line in the phase diagram which tracks along the orthorhombic distortion. Such capabilities are enabled by this apparatus, and although the soft flakey properties of FeSe were the motivation for developing solid platforms, it has been shown to FIB well, and a pristinely prepared micro-structure may alleviate the previously encountered issues and survive moderate to large tensions. This would allow the nematicity to be tuned across a greater range at intermediate to low temperatures where before we were limited by the large spontaneous distortion. If achieved, this would shed more light on the relationship between electronic transport and nematicity below T_S.

6 | Conclusion

Although historically it was possible to extract remarkably deep and revolutionary conclusions from simple experiments – just look at the work of Newton – in modern experimental physics we in general require increased sophistication to advance our understanding. For materials-based condensed matter physics, this demands apparatus which can control environmental conditions or acquire observable parameters with increasing precision. Furthermore, materials at the forefront of current research often exhibit complicated unconventional phases, for which a full understanding is still elusive. For these materials, the importance of experiment is enhanced: complicated theoretical work must be grounded in the real world, thus requiring reliable experimental data. On the other hand, however, the apparatus required to obtain such data becomes increasingly sophisticated.

In terms of control parameters, from a thermodynamic perspective we are immediately offered temperature, magnetic field, and pressure – well utilised in past and present work. Pressure and magnetic field are particularly important as they also influence the symmetry of the system. Such symmetry breaking is achieved using pressure via the application of an anisotropic distortion (i.e. strain) or force (i.e. stress). Inducing large changes in electronic band structure through anisotropic pressure is more achievable practically than by magnetic field. Application of anisotropic pressure is a well-established technique – diamond anvil cells being most common – but such devices are severely limited, normally allowing only a controlled stress to be applied, and only in discrete intervals. Although this field has seen gradual improvements, in the last few years significant technological breakthroughs have been made in our group by Hicks and coworkers, establishing the field of strain-tuning, and placing the application of anisotropic strain on a new trajectory. This has seen the realisation of *tuneable* application of anisotropic pressure in a versatile stress- or strain-controlled manner, and optimised for operation across a wide temperature range. Piezoelectric actuators are at the core of this apparatus, allowing for fine control across a large

strain range. These developments give access to a wealth of experiments previously not possible.

This thesis has described two new frontiers in strain-tuning. As motivated above, one concerns apparatus development. We have extended the capabilities of the established piezoelectric-based uniaxial pressure cell to accept samples which are mechanically unaccommodating, i.e. soft and/or flakey. This was achieved through development of a solid platform. Samples are first adhered to this platform, which is then mounted in the piezoelectric-based cell and deformed uniaxially, resulting in the transferral of biaxial stress. Such a development was vital for expanding the technique of strain-tuning to investigate iron-based superconductor FeSe. Simultaneously, this development allowed extension of the application of anisotropic strain to miniature samples, which can be precisely shaped via focused ion beam milling. Utilising optical measurements, we characterised the platform's behaviour, precisely determining the strain experienced by the sample under a given applied displacement.

Although this new technique expands material possibilities, the platform must in general be larger and stiffer than the sample, and so it decreases the available strain range. We subsequently developed a concept for novel apparatus designed to apply a large, uniaxially-controlled stress to miniature microstructured samples. This development was two-fold: concerning firstly the design and fabrication of a gapped platform to which the sample can be mounted but remain freestanding; as well as the main cell to which this platform can be attached and uniaxially deformed under a controlled force. At its core, this relatively complex apparatus utilises a linear positioner to apply large displacements converted into a small, controlled force. A complex design was required to tackle the extremely small inadvertent forces that would give rise to large parasitic stresses. We have demonstrated that such a technology can in principle be realised, and provided a detailed design based on calculations, simulations and material tests. Sample-on-platform fabrication has been experimentally demonstrated and refined, whilst rig construction is still ongoing. This apparatus is a cutting-edge technology whose ability to apply larger-than-ever uniaxial stresses, when fully operational, will reflect a significant technical breakthrough in scientific instrument development, and a new frontier in strain-tuning.

Without the motivation of different materials and physics to explore, apparatus development is futile. The other theme of this thesis has been concerned with investigating iron-based superconductor FeSe under large anisotropic in-plane strain – measurements only possible due to our unique capabilities in tuning strain. In this material the key physics we address is that of nematicity: a spontaneous breaking of

four-fold rotational symmetry driven by electronic degrees of freedom. Although in-plane anisotropies below $\sim 90\,\mathrm{K}$ associated with this nematic order are widely observed, its origin is debated and likely concerns a complicated interplay of orbital fluctuations, spin fluctuations, and orbital-selective coherence. Application of anisotropic strain with the same orthorhombic symmetry as the nematic order is a powerful tool, coupling directly to the underlying order parameter.

So far this material has evaded investigations under large anisotropic strains due to its soft and cleavable mechanical properties but the aforementioned apparatus development concerning solid platforms enabled these experiments to be conducted. We have demonstrated these platforms to be effective in transferring large tuneable anisotropic deformations, utilising this to apply strains longitudinal (i.e. $\varepsilon_{\langle 110\rangle_T}$) and at 45° (i.e. $\varepsilon_{\langle 100\rangle_T}$) to the principal axes of the nematic order, up to a maximum compression of $\varepsilon_{xx} \sim 0.6\,\%$. This alone is an important breakthrough in the field. Our initial motivation concerned investigating evidence for a nematic crossover when holding the lattice completely fixed, and in addressing this we have uncovered a collection of interesting and important observations.

Measurements under $\langle 100\rangle_T$ strain displayed an expectedly weak response in elastoresistivity $(1/\rho)\,\mathrm{d}\rho/\mathrm{d}\langle\varepsilon_a\rangle$, as well as linear changes in structural and superconducting transition temperatures, with gradients of $\mathrm{d}T_S/\mathrm{d}\langle\varepsilon_a\rangle \sim 9\,\mathrm{K}/\%$ and $\mathrm{d}T_c/\mathrm{d}\langle\varepsilon_a\rangle \sim -1.9\,\mathrm{K}/\%$.

Application of $\langle 110\rangle_T$ strain, on the other hand, exposed new and exiting behaviour. Firstly we observed a non-monotonic dependence of resistivity with strain for fixed temperatures above the renormalised nematic transition, revealing the large elastoresistivity at zero strain to extend only to $\langle\varepsilon_a\rangle \sim \pm 0.75\,\%$ – the first observation of its kind. By identifying the effect of domain walls, we precisely characterised the elastoresistivity of FeSe below T_S. This is a previously unexplored regime. Owing to local relaxation of the applied distortion below this temperature due to domain formation, we simply tune the domain population for strains smaller than the orthorhombic distortion. This uniquely allowed us to understand the origin of the resistivity anomaly at T_S for a twinned sample, as well as track the value of the orthorhombic distortion with temperature, giving an extracted low-temperature distortion of $\varepsilon_S(T \to 0) = 0.31\,\%$.

Using two different methods, and supported by supplementary measurement of the transverse resistivity, we reliably extract the single-domain resistivity anisotropy for close-to-unstressed FeSe. We reveal a surprising dependence: upon cooling $(\rho_a - \rho_b)/(\rho_a + \rho_b)$ peaks at a large value of $\sim 9\,\%$ just below structural transition temperature, being suppressed for temperatures below this, and remarkably changing

sign below 45 K. Such an observation strongly informs theoretical work concerning different contributions to the resistivity anisotropy. Furthermore, this change in sign expresses a more general dichotomy between high- and low-temperature behaviour, seen more clearly as a broad crossover in elastoresistivity for $|\langle\varepsilon_a\rangle| > |\varepsilon_S(T)|$, resulting in a change in sign of $\mathrm{d}\rho(\langle\varepsilon_a\rangle)/\mathrm{d}\langle\varepsilon_a\rangle$ at ~ 55 K. We additionally studied the strain dependence of the superconducting transition temperature, showing symmetric compression to increase T_c, and asymmetric compression (i.e. increasing orthorhombicity) to decrease T_c.

Returning to our initial motivation, i.e. whether there is any sign of crossover under large applied orthorhombicity, the most pronounced feature we observe is the change in behaviour occurring at around 50 K. There are many possible mechanisms which might cause this, however, depending on the relative influence of an anisotropic Drude weight, inelastic scattering from spin fluctuations, and elastic scattering from defects. Furthermore, orbital-selective physics is expected to be important, and we speculate as to how changes in the coherence of individual orbitals might influence our measurements. It is clear that more experiments are needed to shed further light on this issue, but this thesis paves the way for future work of this kind.

A Rotation of the Stiffness and Compliance Tensors

It is instructive to inspect the case of rotating a $4/mmm$ tetragonal system by $\pi/4$. This is useful for both the considerations when measuring a tetragonal system along the $\langle 110 \rangle_T$ -direction – e.g. in Section 4.2, or for a system that undergoes a tetragonal to orthorhombic structural phase transition with $\pi/4$ rotation, like in FeSe. We start by considering a linear isotropic piece of material in two dimensions. We want to go from a coordinate frame x, y to x', y' where the new frame is rotated by $\pi/4$. If we consider a general coordinate x_i (where in our case $x_1 = x$ and $x_2 = y$), the transformation is

$$x_i' = \sum_j \alpha_{ij} x_j, \tag{A.1}$$

where α_{ij} are the directional cosines defined by $\alpha_{ij} = \cos\left(\theta_{ij}\right)$, with θ_{ij} being the angle between the ith primed and jth unprimed axis. Together these define the rotation matrix $\mathbf{R}$ such that $\mathbf{x}' = \mathbf{R}\mathbf{x}$. In two dimensions a rotation of x and y by θ gives

$$\mathbf{R} = \begin{bmatrix} \cos\theta & \sin\theta \\ -\sin\theta & \cos\theta \end{bmatrix}. \tag{A.2}$$

For $\theta = \pi/4$ this becomes

$$\mathbf{R} = \frac{1}{\sqrt{2}} \begin{bmatrix} 1 & 1 \\ -1 & 1 \end{bmatrix}. \tag{A.3}$$

Tensors are defined by their transformation properties. For a rank-2 tensor

$$A_{ij}' = \sum_i \sum_j \alpha_{ik} \alpha_{jl} A_{kl}. \tag{A.4}$$

Using this we can transform the stress and strain tensors, where we use $i, j = 1, 2$ where $x = 1$, $y = 2$. In matrix notation this gives

$$[\varepsilon_{ij}] = \begin{bmatrix} \varepsilon_{11} & \varepsilon_{12} \\ \varepsilon_{12} & \varepsilon_{22} \end{bmatrix} \rightarrow [\varepsilon'_{ij}] = \frac{1}{2} \begin{bmatrix} (\varepsilon_{11} + \varepsilon_{22} + 2\varepsilon_{12}) & (\varepsilon_{22} - \varepsilon_{11}) \\ (\varepsilon_{22} - \varepsilon_{11}) & (\varepsilon_{11} + \varepsilon_{22} - 2\varepsilon_{12}), \end{bmatrix} \tag{A.5}$$

and similarly for $[\sigma'_{ij}]$. This immediately shows that the difference of normal strains $\varepsilon_{xx} - \varepsilon_{yy}$ represents the shear strain in the rotated frame ε_{xy}. The forth rank tensor $[C_{ijkl}]$ transforms via

$$A'_{ij} = \sum_i \sum_j \sum_k \sum_l \alpha_{im} \alpha_{jn} \alpha_{kp} \alpha_{lq} A_{mnpq}. \tag{A.6}$$

This gives 16 terms to evaluate, however some of them are zero due to symmetry. The only non zero components are $C_{1111} = C_{2222}$, $C_{1122} = C_{2211}$ and $C_{1212} = C_{1221} = C_{2112} = C_{2121}$. Using the contracted notation these correspond to C_{11}, C_{12} and C_{66}, which give the familiar psuedo-matrix constitutive equation (using the notation from Table 3.1) :

$$\begin{Bmatrix} \sigma_1 \\ \sigma_2 \\ \sigma_6 \end{Bmatrix} = \begin{bmatrix} C_{11} & C_{12} & 0 \\ C_{12} & C_{11} & 0 \\ 0 & 0 & C_{66} \end{bmatrix} \begin{Bmatrix} \varepsilon_1 \\ \varepsilon_2 \\ \varepsilon_6 \end{Bmatrix}. \tag{A.7}$$

Thus the only non-zero terms in Equation A.6 are

$$\begin{aligned} C'_{ijkl} = {} & C_{11} \left(\alpha_{i1} \alpha_{j1} \alpha_{k1} \alpha_{l1} + \alpha_{i2} \alpha_{j2} \alpha_{k2} \alpha_{l2} \right) + C_{12} \left(\alpha_{i1} \alpha_{j1} \alpha_{k2} \alpha_{l2} + \alpha_{i2} \alpha_{j2} \alpha_{k1} \alpha_{l1} \right) \\ & + C_{66} \left(\alpha_{i1} \alpha_{j2} \alpha_{k1} \alpha_{l2} + \alpha_{i1} \alpha_{j2} \alpha_{k2} \alpha_{l1} + \alpha_{i2} \alpha_{j1} \alpha_{k1} \alpha_{l2} + \alpha_{i2} \alpha_{j1} \alpha_{k2} \alpha_{l1} \right). \end{aligned} \tag{A.8}$$

Taking the α_{ij} values from Equation A.3 gives

$$C'_{11} = \frac{1}{2} (C_{11} + C_{12} + 2C_{66}), \tag{A.9}$$

$$C'_{12} = \frac{1}{2} (C_{11} + C_{12} - 2C_{66}), \tag{A.10}$$

$$C'_{66} = \frac{1}{2} (C_{11} - C_{12}). \tag{A.11}$$

And as such the transformation in psuedo-matrix form is

$$[C_{ij}] = \begin{bmatrix} C_{11} & C_{12} & 0 \\ C_{12} & C_{11} & 0 \\ 0 & 0 & C_{66} \end{bmatrix} \rightarrow$$

$$[C'_{ij}] = \frac{1}{2}\begin{bmatrix} (C_{11}+C_{12}+2C_{66}) & (C_{11}+C_{12}-2C_{66}) & 0 \\ (C_{11}+C_{12}-2C_{66}) & (C_{11}+C_{12}+2C_{66}) & 0 \\ 0 & 0 & (C_{11}-C_{12}) \end{bmatrix}. \quad \text{(A.12)}$$

We see here an important result, when rotating by $\pi/4$ the new shear component is equal to the difference between the two normal components. This appears without specific consideration of the form of these components. Now let us extend this to three dimensions with a $4/mmm$ tetragonal system. Now the non-zero components are

$$[C_{ij}] = \begin{bmatrix} C_{11} & C_{12} & C_{13} & 0 & 0 & 0 \\ C_{12} & C_{11} & C_{13} & 0 & 0 & 0 \\ C_{13} & C_{13} & C_{33} & 0 & 0 & 0 \\ 0 & 0 & 0 & C_{44} & 0 & 0 \\ 0 & 0 & 0 & 0 & C_{44} & 0 \\ 0 & 0 & 0 & 0 & 0 & C_{66} \end{bmatrix}. \quad \text{(A.13)}$$

Or more explicitly

C_{11}	C_{1111}, C_{2222}
C_{12}	C_{1122}, C_{2211}
C_{13}	$C_{1133}, C_{3311}, C_{2233}, C_{3322}$
C_{33}	$C_{3333},$
C_{44}	$C_{2323}, C_{2332}, C_{3223}, C_{3232}, C_{1313}, C_{1331}, C_{3113}, C_{3131}$
C_{66}	$C_{1212}, C_{1221}, C_{2112}, C_{2121}$

We want to rotate around the z-axis, so our rotation matrix is

$$\mathbf{R} = \frac{1}{\sqrt{2}}\begin{bmatrix} 1 & 1 & 0 \\ -1 & 1 & 0 \\ 0 & 0 & 1 \end{bmatrix}. \quad \text{(A.14)}$$

Conducting the same procedure as in the $3D$ case gives an analogous result

$$[C_{ij}] = \begin{bmatrix} C_{11} & C_{12} & C_{13} & 0 & 0 & 0 \\ C_{12} & C_{11} & C_{13} & 0 & 0 & 0 \\ C_{13} & C_{13} & C_{33} & 0 & 0 & 0 \\ 0 & 0 & 0 & C_{44} & 0 & 0 \\ 0 & 0 & 0 & 0 & C_{44} & 0 \\ 0 & 0 & 0 & 0 & 0 & C_{66} \end{bmatrix} \rightarrow$$

$$[C'_{ij}] = \frac{1}{2}\begin{bmatrix} (C_{11}+C_{12}+2C_{66}) & (C_{11}+C_{12}-2C_{66}) & C_{13} & 0 & 0 & 0 \\ (C_{11}+C_{12}-2C_{66}) & (C_{11}+C_{12}+2C_{66}) & C_{13} & 0 & 0 & 0 \\ C_{13} & C_{13} & \frac{1}{2}C_{33} & 0 & 0 & 0 \\ 0 & 0 & 0 & C_{44} & 0 & 0 \\ 0 & 0 & 0 & 0 & C_{44} & 0 \\ 0 & 0 & 0 & 0 & 0 & (C_{11}-C_{12}) \end{bmatrix}. \tag{A.15}$$

Unsurprisingly all the non-trivial combinations were captured in the $2D$ case. And again we see that the shear component $C'_{66} = (C_{11} - C_{12})/2$. Furthermore the reverse is also true, $C'_{11} - C'_{12} = 2C_{66}$. For the case of the structural phase transition in FeSe this means that depending on whether one uses the coordinate system of the high- or low-temperature phase. the instability will either be in the in-plane shear component, or the difference between the in-plane normal components. Note also that the quantity $C'_{11} + C'_{22} = C_{11} + C_{22}$ is independent of this rotation.

For completeness, we also write out the components for the compliance tensor $[S_{ij}]$ in terms of the stiffness tensor $[C_{ij}]$, and then for the compliance in the rotated frame $[S'_{ij}]$ in terms of the unrotated stiffness $[C_{ij}]$. For the former the result is given in Ref. [207], giving the relations

$$\begin{aligned} S_{11} &= \left[C_{11}C_{33} - C_{13}^2\right]/[(C_{11} - C_{12})C], \\ S_{12} &= -\left[C_{12}C_{33} - C_{13}^2\right]/[(C_{11} - C_{12})C], \\ S_{13} &= -C_{13}/C, \\ S_{33} &= (C_{11} + C_{12})/C, \\ S_{44} &= 1/C_{44}, \\ S_{66} &= 1/C_{66}, \\ \text{where} \quad C &= C_{33}(C_{11} + C_{12}) - 2C_{13}^2. \end{aligned} \tag{A.16}$$

Then for the rotated frame compliance

$$
\begin{aligned}
S'_{11} &= \left[(C_{11}+C_{12}+2C_{66})C_{33}-2C_{13}^2\right]/[16C_{66}C'], \\
S'_{12} &= -\left[(C_{11}+C_{12}-2C_{66})C_{33}-2C_{13}^2\right]/[16C_{66}C'], \\
S'_{13} &= -C_{13}/2C', \\
S'_{33} &= (C_{11}+C_{12})/C', \\
S'_{44} &= 2/C_{44}, \\
S'_{66} &= 2/(C_{11}-C_{12}), \\
\text{where} \quad C' &= \left[C_{33}(C_{11}+C_{12})-2C_{13}^2\right]/4.
\end{aligned}
\tag{A.17}
$$

Using Equation A.16, we can write out the in- and out-of-plane Poisson's ratios in terms of the stiffness tensor components (the origin of these expressions can be understood from Equation 3.7)

$$
\nu_{\parallel} = \frac{-S_{12}}{S_{11}} = \frac{C_{12}C_{33}-C_{13}^2}{C_{11}C_{33}-C_{13}^2}, \tag{A.18}
$$

$$
\nu_{\perp} = \frac{-S_{13}}{S_{33}} = \frac{C_{13}}{C_{11}+C_{12}}. \tag{A.19}
$$

And similarly for the Young's modulus

$$
E_{\parallel} = \frac{1}{S_{11}} = C_{11} + \frac{2C_{12}C_{13}^2 - C_{11}C_{13}^2 - C_{12}^2C_{33}}{C_{11}C_{33}-C_{13}^2}, \tag{A.20}
$$

$$
E_{\perp} = \frac{1}{S_{33}} = C_{33} - \frac{2C_{13}^2}{C_{11}+C_{12}}. \tag{A.21}
$$

And similarly using Equation A.17 for the Poisson's ratios in the rotated frame in terms of the unrotated stiffness components

$$
\nu'_{\parallel} = \frac{-S'_{12}}{S'_{11}} = \frac{\gamma - C_{66}}{\gamma + C_{66}}, \tag{A.22}
$$

$$
\nu'_{\perp} = \frac{-S'_{13}}{S'_{33}} = \frac{C_{13}}{2(C_{11}+C_{12})}, \tag{A.23}
$$

$$
\gamma = \frac{C_{11}}{2} + \frac{C_{12}}{2} - \frac{C_{13}^2}{C_{33}}. \tag{A.24}
$$

$$E'_{\parallel} = \frac{1}{S'_{11}} = 4\left(\frac{1}{C_{66}} + \frac{1}{\gamma}\right)^{-1}, \tag{A.25}$$

$$E'_{\perp} = \frac{1}{S'_{33}} = \frac{1}{4}\left(C_{33} - \frac{2C_{13}^2}{C_{11} + C_{12}}\right), \tag{A.26}$$

Where Equation A.25 has been rewritten as in the Supplementary material of Ref. [157]. Which shows that if $C_{66} < \gamma$ it dominates the contribution to the Young's modulus $E_{[110]_T}$.

B | Sample Details

In this appendix, all details regarding the different samples measured, and the details of such measurements are listed. Figure B.1 shows optical micrographs of all samples measured. Table B.1 overviews various sample details and B.2 measurement details.

Sample name	Shorthand	L (μm)	w (μm)	t (μm)	Epoxy t (μm)	Conducting L
$[100]_T$ sample 1	$[100]_T$ s1	2370 ± 3 *	280 ± 3 *	31 ± 3 *	–	790 to 1145 ± 5 *
$[110]_T$ sample 1	$[110]_T$ s1	1480 ± 3 *	250 ± 3 *	24 ± 1 **	14 ± 1 **	525 to 735 ± 3 *
$[110]_T$ sample 2	$[110]_T$ s2	1270 ± 30 *	250 ± 3 *	29 ± 3 *	–	538 to 817 ± 3 *
$[110]_T$ sample 3	$[110]_T$ s3	1150 ± 1 **	234 ± 1 **	10 ± 1 **	5 ± 1 **	525 to 734 ± 1 **

Sample name	$d_{I \text{ to } V}/t$	$\rho_{300\text{K}}/\rho_{12\text{K}}$	Method #	Comment
$[100]_T$ sample 1	14 ± 1	26	1	Prepared by S. Hosoi
$[110]_T$ sample 1	4.6 ± 0.5	18	1	Sample not a perfect bar
$[110]_T$ sample 2	4.5 ± 0.5	18	1	Cleaved piece from $[110]_T$ sample 1
$[110]_T$ sample 3	10.0 ± 0.3	22	2	Slight surface damage from preparation

Table B.1 | Table overviewing details of the four samples measured. $[100]_T$, and $[100]_T$, refers to a sample whose edges are aligned with, and at 45° to, the tetragonal unit cell. Method 1: mask for contact definition made pre-sputtering using GE varnish and vacuum grease. Method 2: contacts defined post-sputtering using a focused ion beam to mill away gold. *Measured with optical microscope, **measured with SEM, ***measured with an optical profiler before and cleaving.

Sample	System	Resistivity			AC susceptibility		
		I (mA)	Preamp	f (Hz)	I (mA)	Preamp	f (Hz)
$[100]_T$ sample 1	Wet He-4, 1 K	0.1	×10	113	1	×10	6676
$[110]_T$ sample 1	Dry VTI	0.1	None	473	0.2	×10	6077
$[110]_T$ sample 2	Dry VTI	1	None	719	0.2	×10	6077
$[110]_T$ sample 3	Dry VTI	1	None	719	— Not measured —		

Table B.2 | Table overviewing measurement details. For measurement 1, Stanford Instruments SR830 lock-in amplifiers were used for both resistivity and AC susceptibility measurements. For measurements 2-4, an SR860 was used for resistivity and an SR830 for AC susceptibility. The pre-amplifier used for all was an SR550.

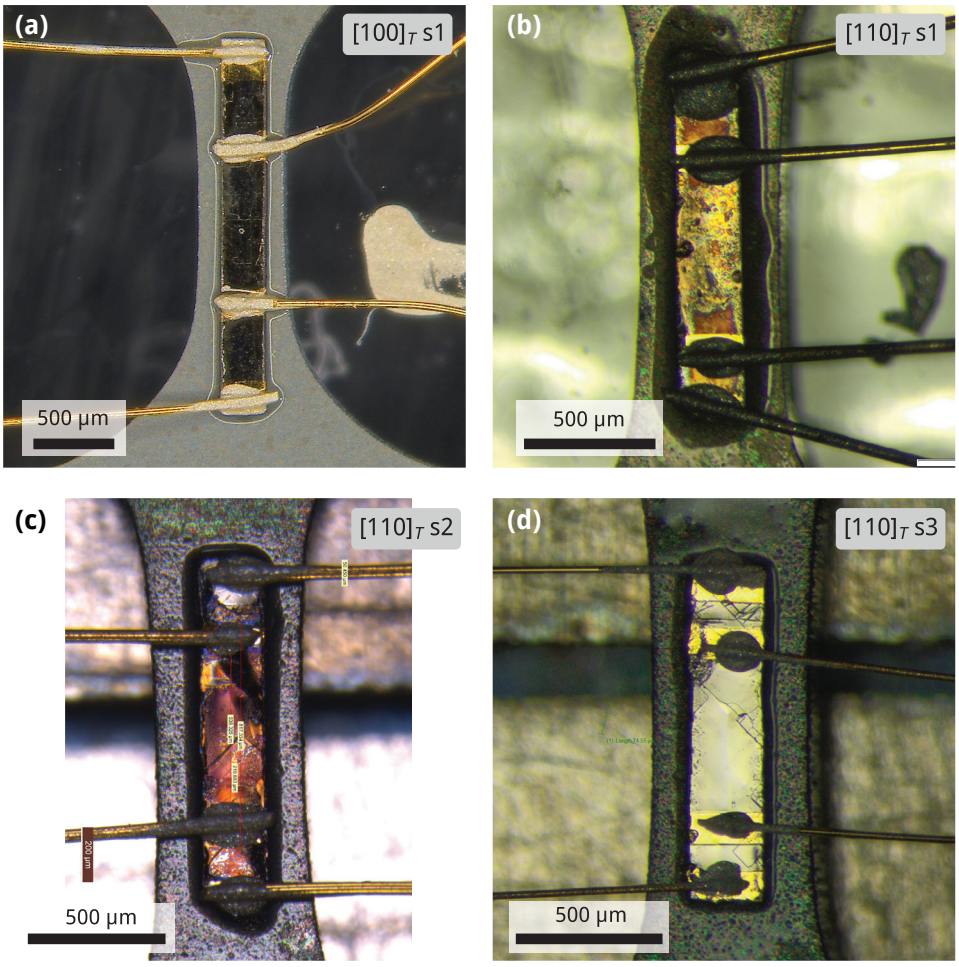

Figure B.1 | Optical micrographs of all samples measured. **(a)** $[100]_T$ sample 1. **(b-c)** $[110]_T$ samples 1-3.

C | FeSe: Supplementary Material

This appendix contains supplementary material supporting the experimental results presented in Chapter 4.

C.1 Capacitance-to-strain conversion

Care must be taken in dealing with capacitance-to-strain conversion when incorporating shifts, as this involves relative changes between inversely related quantities. Our procedure will now be clearly explained.

When conducting measurements we initially establish a capacitance we think is close to corresponding to zero strain, which we call C^*. Capacitances targeted during measurement for a given strain ε are determined by inverting Equation 5.9 to give

$$C = \frac{\alpha C^*}{\varepsilon C^* + \alpha},$$

where $\alpha = \epsilon_0 A / L_{\text{eff}}$ (ϵ_0 being the permittivity of free space). After analysis, we can better determine the zero strain point and can correct for this by shifting the strain scale. For this to work the reference capacitance for the zero shift must be the same as for the original strain determination. This is because the difference of two strains against the same reference capacitance is independent of that reference. We shift our strain scale by $\Delta\varepsilon_{\text{zero}} = \varepsilon_{0,\text{actual}} - \varepsilon_{0,\text{current}} = 0 - \varepsilon_0$. Therefore $\varepsilon' = \varepsilon + \Delta\varepsilon_{\text{zero}} = \varepsilon - \varepsilon_0$; this is equal to

$$\varepsilon - \varepsilon_0 = \alpha\left(\frac{1}{C} - \frac{1}{C^*}\right) - \alpha\left(\frac{1}{C_0} - \frac{1}{C^*}\right) = \alpha\left(\frac{1}{C} - \frac{1}{C_0}\right).$$

In other words, this is equivalent to just calculating strains with a new reference

capacitance that corresponds to the actual zero strain point.

Now we must deal with the additional shift originating from plastic deformation. Again, because we are dealing with a difference in strain, the shift is independent of reference. Furthermore because the shift does not concern the zero reference, it can be considered completely independently of C_{meas}. If we consider a reference point before and after plastic deformation (PD) and calculate the strain shift between then (provided both have the same C^*), then

$$\Delta\varepsilon_{\text{PD}} = \varepsilon_{\text{ref, after}} - \varepsilon_{\text{ref, before}}.$$

Whereas the zero shift applies to all data recorded, $\Delta\varepsilon_{\text{PD}}$ is not fixed and must be determined and applied on a measurement-to-measurement basis.

Bringing all of this together with the additional scaling to asymmetric strain (see Section 3.3.4), the complete relation for conversion of measured capacitance to strain is

$$\varepsilon_i = \gamma_{\text{asymm}}\left[\alpha\left(\frac{1}{C_{\text{meas},i}} - \frac{1}{C^*}\right) - \varepsilon_0 + \Delta\varepsilon_{\text{PD},i}\right], \tag{C.1}$$

where $\gamma_{\text{asymm}} = (1 + \nu_{\text{eff}})/2$ and ε_0 is determined with a reference capacitance of C^* from data that is not affected by any plastic deformation.

C.2 $\langle 100\rangle_T$ strain

Supplementary plots supporting results under $\langle 100\rangle_T$ strain presented in Section 4.1.

Figure	Page	Description
C.1	181	$\rho(T)$ and $\chi(T)$ measured through T_c for several $\langle 110\rangle_T$ strains.

C.3 T_S analysis

Supplementary plots concerning the T_S extraction methods relevant to Sections 4.1 and 4.2.

Figure	Page	Description
C.2	181	Comparison of T_S for all samples measured.
C.3	182	Comparison of T_S extraction methods.

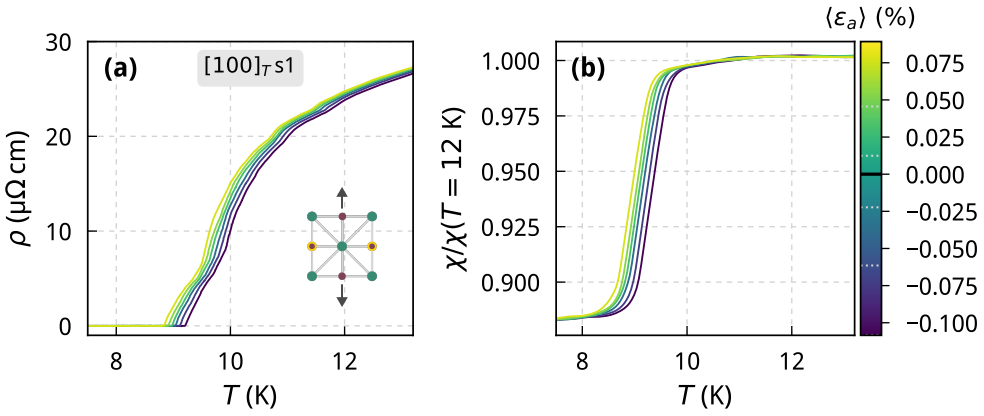

Figure C.1 | Resistivity **(a)** and magnetic susceptibility **(b)** against temperatures through T_c for several $\langle 100\rangle_T$ strains. A smoothing spline is applied to susceptibility to clarify the shift with strain.

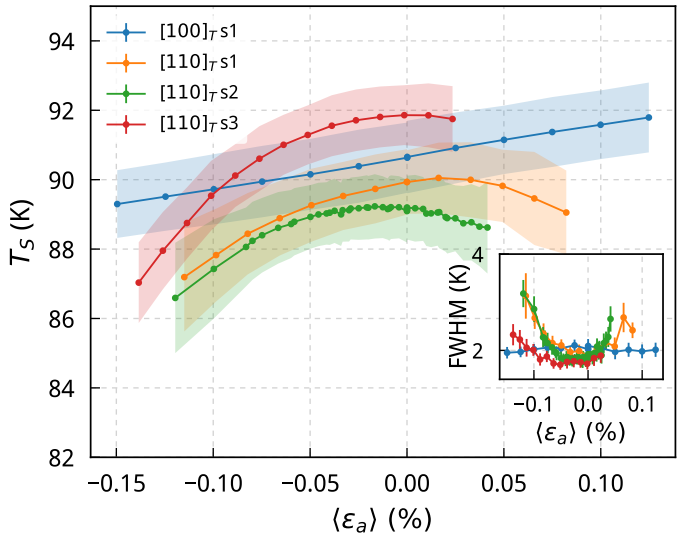

Figure C.2 | Comparison of T_S against $\langle\varepsilon_a\rangle$ for all samples, extracted via Gaussian fitting to $\mathrm{d}^2\rho/\mathrm{d}T^2$. At large strains, the transitions broaden due to the intrinsic dependence of the orthorhombic distortion, and also from extrinsic strain inhomogeneity. Fits therefore become poor, and errors larger at large compression. All $\langle 110\rangle_T$ samples show the same qualitative T_S dependence, however both sample and epoxy were thicker for s1 and s2, as well as having poorer sample quality – see Table B.1.

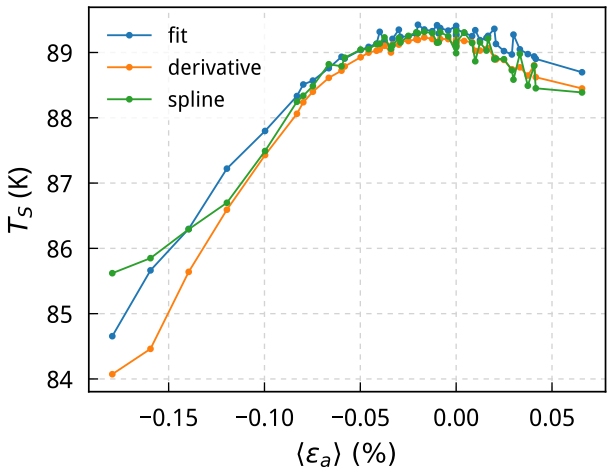

Figure C.3 | Comparison of extraction methods for the structural transition temperature T_S for $[110]_T$ sample 2. The 'derivative' method, as already described, consists of fitting a Gaussian function to $\mathrm{d}^2\rho/\mathrm{d}T^2$. For the 'fit' method, a high-order polynomial is first fitted to $\rho(T)$ and then a linear background subtracted. The resulting form has a peak which can be taken to represent T_S. Finally, the 'spline' method uses the second derivative maximum from a spline interpolation of $\rho(T)$. At low strains the error from method comparison is $\sim 0.3\,\%$. This is much larger than the individual errors from Gaussian fitting. At high strains deviations are large due to both intrinsic and extrinsic broadening. A

C.4 $\langle 110 \rangle_T$ strain

Plots supplementing the presentation of experimental results under $\langle 110 \rangle_T$ strain in Section 4.2.

Figure	Page	Description
C.4	183	Comparison of elastoresistivity under $\langle 100 \rangle_T$ and $\langle 110 \rangle_T$ strain at 95 K.
C.5	183	Individual correction of plastic deformation for temperature-ramp data.
C.6	184	Structural distortion extraction for intermediate-temperature strain ramps.
C.7	185	Comparison of temperature and strain ramps across a wide temperature range.
C.8	186	Comparison of low-temperature extrapolations of $\varepsilon_S(T)$ on the resistivity anisotropy.
C.9	186	Use of $\rho(\langle \varepsilon_a \rangle)$ to determine the resistivity anisotropy.
C.10	187	Resistivity anisotropy determination using $\rho(T)$ cross sections.
C.11	188	$\rho(T)$ measured through T_c under $\langle 110 \rangle_T$ strain.

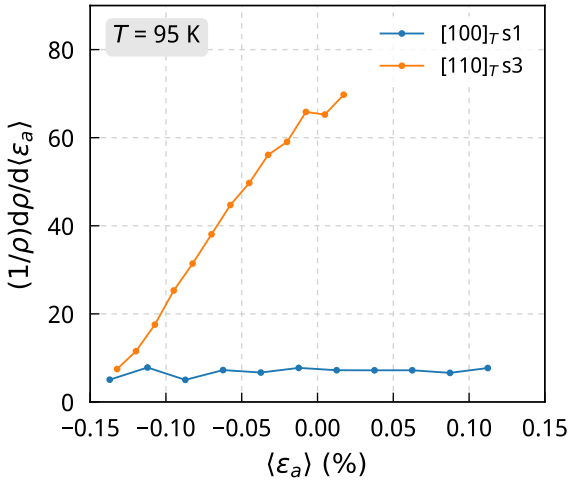

Figure C.4 | A comparison of elastoresistivity $(1/\rho)\,\mathrm{d}\rho/\mathrm{d}\langle\varepsilon_a\rangle$ under $\langle 100\rangle_T$ and $\langle 100\rangle_T$ strain, taken from temperature ramp data $\rho(T)$ at $T = 95\,\mathrm{K}$. The large difference in elastoresistivity at $\langle\varepsilon_a\rangle = 0$ can be clearly be seen, with values of ~ 7 and ~ 60 under $\langle 100\rangle_T$ and $\langle 110\rangle_T$ strain respectively.

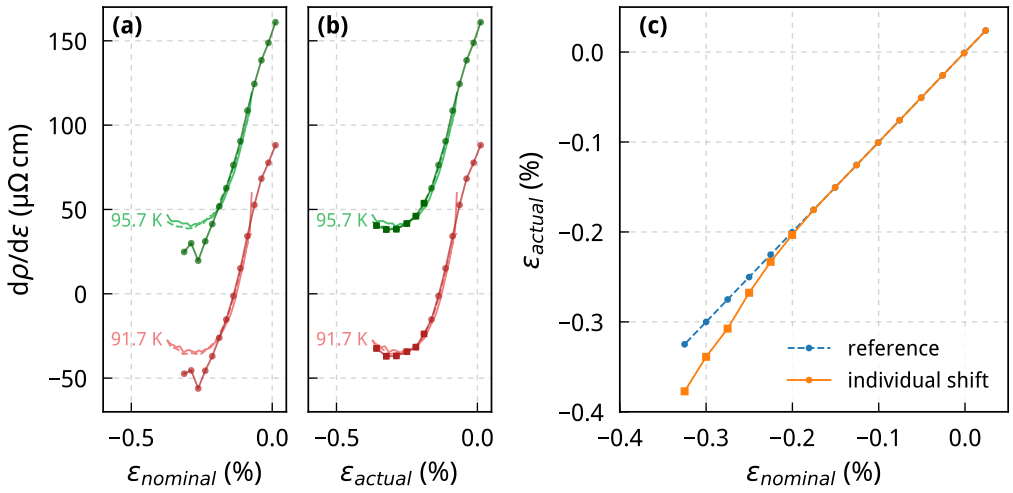

Figure C.5 | Individual correction of plastic deformation for temperature-ramp data. **(a)** Lines with markers show unshifted first derivatives of constant-strain cross-sections at high temperature, during which the platform underwent significant plastic deformation (PD) at large compressions. This is seen in the deviation from post-PD strain sweeps (no markers), already corrected by a single strain shift. **(b)** Strain-scale correction of temperature sweeps through individual shifts to match to strain sweep data. Matching first derivatives is preferable over the raw data as signal shifts are eliminated. Shifts are obtained from 95.7 K data (top) and applied to the lower-temperature curve (bottom). **(c)** Plot of the 'actual' (i.e. shifted) strain against the nominal strain read out by the capacitor. Without plastic deformation these should be equal and follow the reference line.

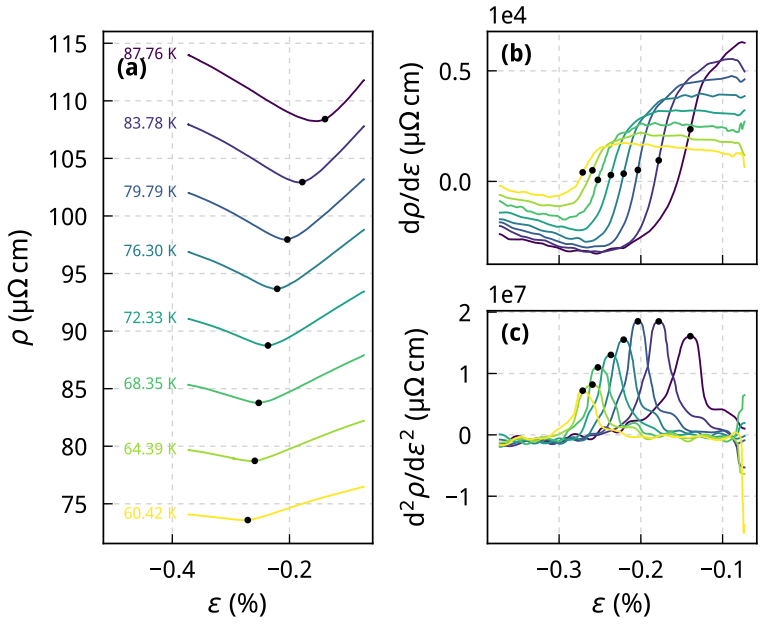

Figure C.6 | Extraction of the structural distortion from strain ramps $\rho(\langle\varepsilon_a\rangle)$ at intermediate-temperatures. **(a)** $\rho(\langle\varepsilon_a\rangle)$ curves for T near $T_S(\langle\varepsilon_a\rangle = 0)$, with marked ε_S points extracted from the peaks in the second derivative. **(b)** As in panel (a), but showing the unshifted first derivative $\mathrm{d}\rho/\mathrm{d}\langle\varepsilon_a\rangle$. **(c)** Second derivative $\mathrm{d}^2\rho/\mathrm{d}\langle\varepsilon_a\rangle^2$, showing peaks from which compression ε_S points are extracted.

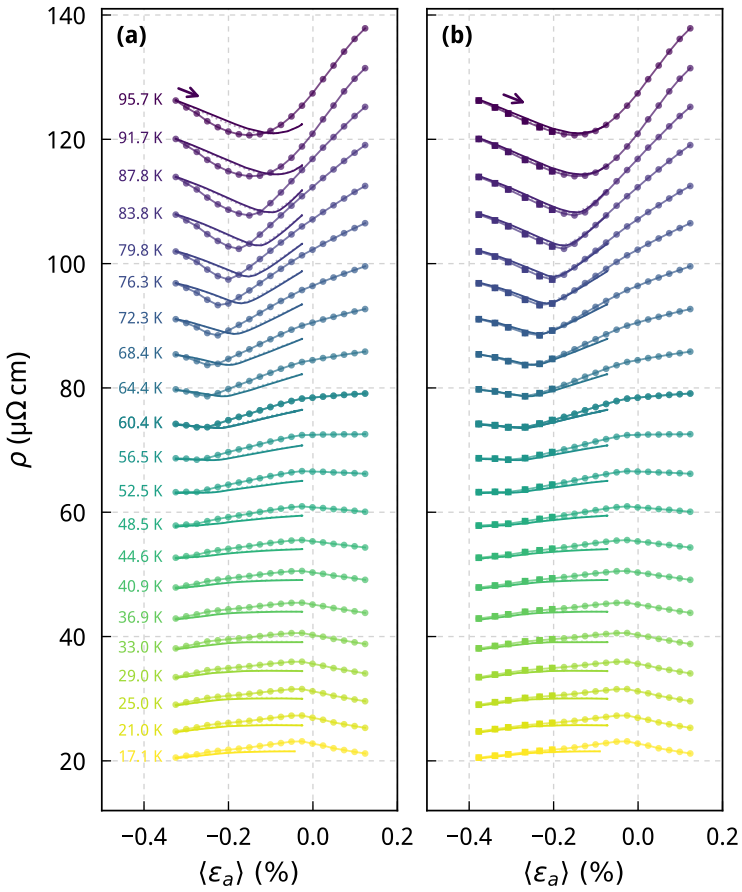

Figure C.7 | (a) Comparison of temperature-ramp cross sections at slices of constant $\langle \varepsilon_a \rangle$ with strain ramps, without any shifts compensating for plastic deformation. **(b)** Strain ramps are corrected by a single strain shift, moving them further into compression. Temperature ramp cross sections are corrected individually at large compression where the plastic deformation occurred (as shown in Figure C.5). At high temperatures, agreement between these two data sets is clear. Upon cooling the domain-wall-driven signal difference results in this being unobservable.

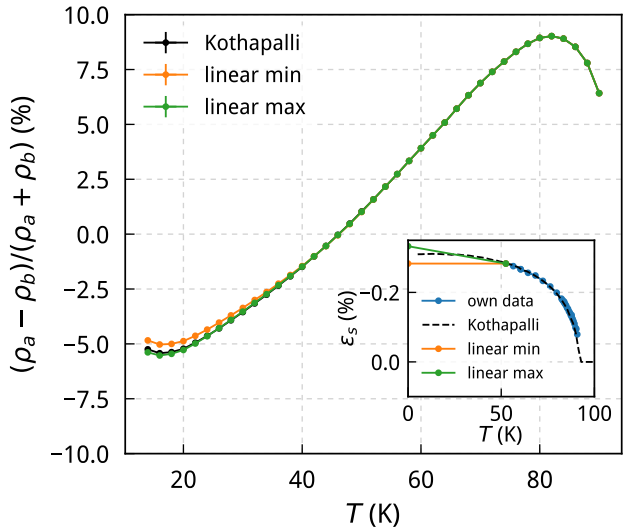

Figure C.8 | Comparison of resistivity anisotropy extracted using different low-temperature extrapolations of the structural distortion $\varepsilon_S(T)$. As shown in the inset, one option is to use $\delta(T)$ determined by X-ray diffraction [90] scaled to match our data at high temperatures. Alternatively, upper and lower limits can be placed on the maximum distortion, and linearly interpolated. A negligible effect is seen in the resistivity anisotropy.

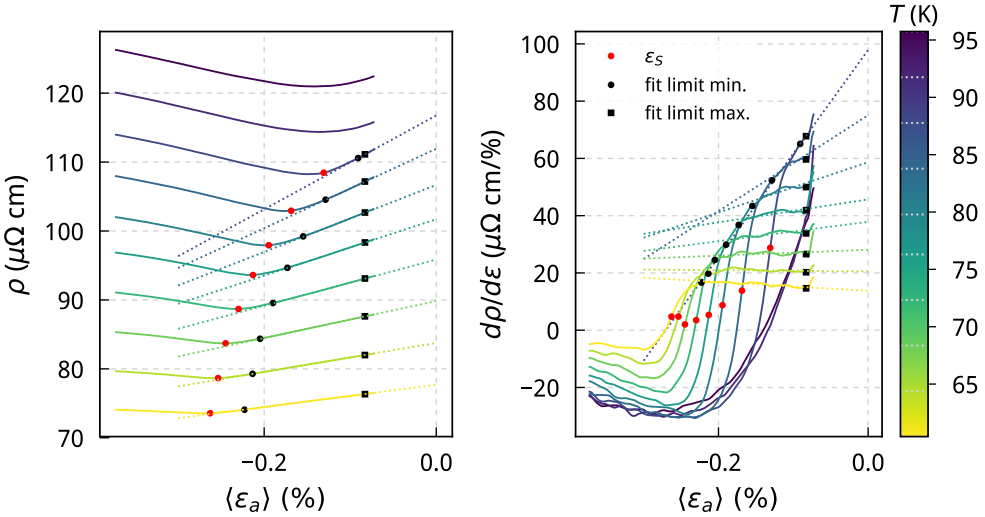

Figure C.9 | Resistivity anisotropy determined through quadratic fitting to $\rho(\langle\varepsilon_a\rangle)$ and linear fitting to $\mathrm{d}\rho/\mathrm{d}\langle\varepsilon_a\rangle$ for $|\langle\varepsilon_a\rangle| < |\varepsilon_S|$. Both the extrapolated $\rho(\langle\varepsilon_a\rangle = 0)$ value, and fitted $\mathrm{d}\rho/\mathrm{d}\langle\varepsilon_a\rangle$ extrapolated at $\langle\varepsilon_a\rangle = 0$ are used to determine $(\rho_a - \rho_b)/(\rho_a + \rho_b)$.

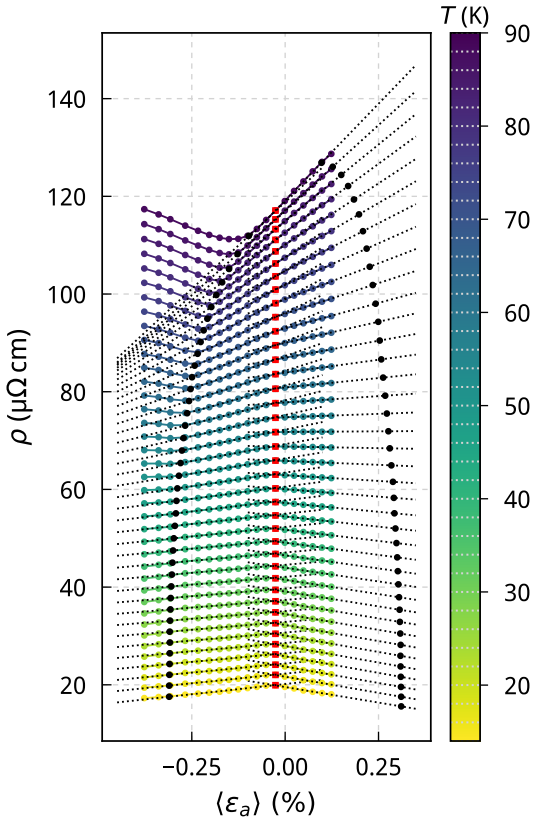

Figure C.10 | Method for determining the resistivity anisotropy through linear fitting of $\rho(T)$ cross-sections either side of the low-temperature peak, and up to $\pm\varepsilon_S$. Plastic deformation is corrected for as shown in Figure C.5. The peak should in principle occur at zero strain, but here it is at $\sim -0.03\,\%$ – as indicated by the red marker. Fitting range extremes ($\pm\varepsilon_S(T)$) are indicated by black markers which for $T > 50\,\mathrm{K}$ are derived from our own data, and below 50 K from scaled X-ray diffraction data. Linear fits are shown by dotted lines, and the fits in compression and tension have gradients of opposite sign below $\sim 55\,\mathrm{K}$.

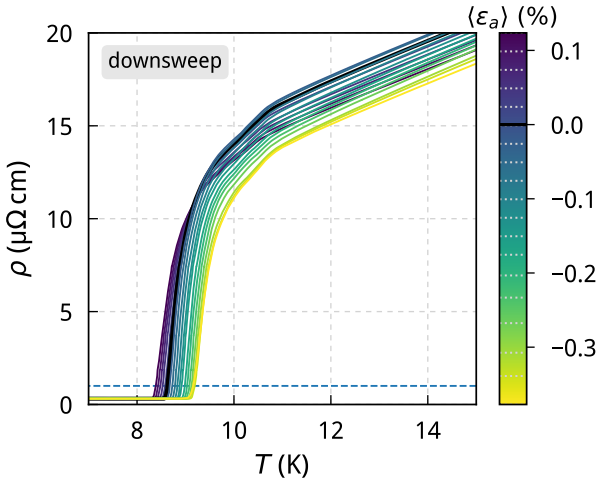

Figure C.11 | Resistivity as a function of temperature $\rho(T)$ measured through the superconducting transition temperature T_c for discrete $\langle 110 \rangle_T$ strains. The strain scale is unadjusted for any plastic deformation.

D | Microstructure Rig: Full Design

In this appendix, the final rig design for applying large strains to miniature samples is presented, bringing together the positioner, force sensor, spring and gapped platform. This is shown in Figure D.1(a), and the design of the final parts shown in this figure are credited to Dr Clifford Hicks. As an indicator of positioner motion, we add a capacitive-overlap displacement sensor (as explained in Section 5.2.3) between the top plate of the positioner and the fixed outer frame. We must shield the force sensor to enable a more precise three-terminal capacitance measurement to be made, and do so using a copper housing insulated from the rest of the rig. The silicon assembly is attached to the main copper frame using a spring which is compressed via the tightening of a penetrating screw to the outer frame. In order to minimise friction due to differential thermal contraction, the silicon assembly and copper main frame are separated using quartz-sphere set screws, as shown in panel (c). These also allow for fine adjustment of the relative placement of the two components. There are six in total, positioned along three axes, and for the upper surface (z-axis) these are indicated by blue rings in panel (a). As shown in panel (b), the platform is clamped to the main silicon body again using a compressed spring. Silicon cannot be threaded so the spring is compressed using a 'riser', and a sliding catch locking the base of the pin in place. To avoid platform damage and slipping on the platform due to differential thermal contraction, a silicon washer sits between it and the pin head. A schematic of the complete assembled rig is shown in Figure D.1(d).

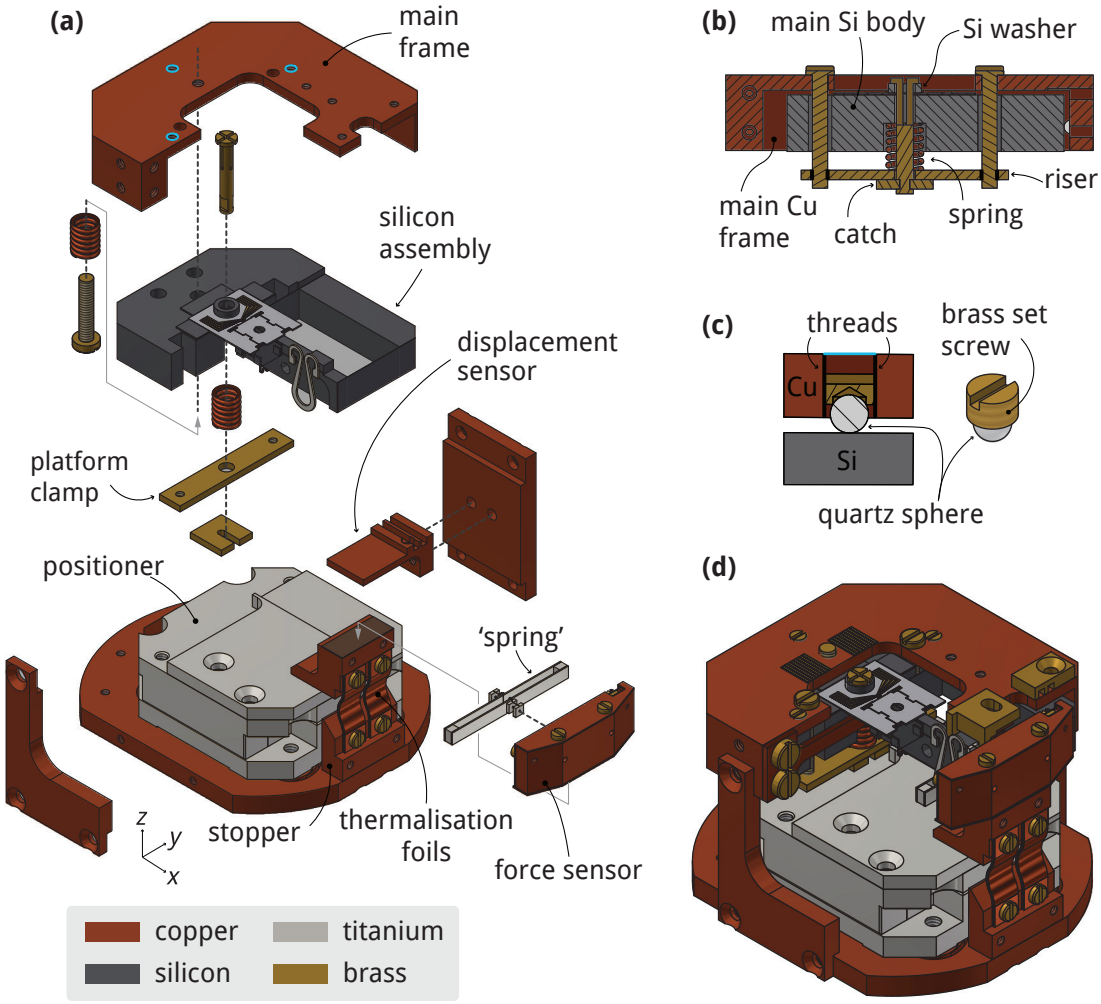

Figure D.1 | (a) Expanded view of the housing required to bring the base components together with the silicon assembly. **(b)** The platform is clamped with a spring-based mechanism compressed with two outer screws, and held in place by a sliding catch. **(c)** As shown in panel (a), the silicon assembly is pressed towards the main copper frame using a compression spring. Quartz spheres within set screws prohibit contact between these components, minimising friction due to differential thermal contraction, and permitting fine position adjustment. **(d)** Schematic of the assembled rig in its entirety.

Bibliography

[1] L. Landau, "The Theory of a Fermi Liquid." *Sov. Phys. JETP*, **3** 6, (1956), 920.

[2] L. Landau & E. Lifshitz, *Statistical Physics.* v. 5, (Elsevier Science, 2013).

[3] E. Salje & V. Devarajan, "Phase transitions in systems with strain-induced coupling between two order parameters." *Phase Transitions*, **6** 3, (1986), 235–247.

[4] V. Wadhawan, *Introduction to Ferroic Materials*, (Taylor & Francis, 2000).

[5] E. K. Salje, *Phase Transitions in Ferroelastic and Co-elastic Crystals (Cambridge Topics in Mineral Physics and Chemistry)*, (Cambridge University Press, 1991).

[6] E. Fradkin, S. A. Kivelson, M. J. Lawler, J. P. Eisenstein & A. P. Mackenzie, "Nematic Fermi Fluids in Condensed Matter Physics." *Annual Review of Condensed Matter Physics*, **1** 1, (2010), 153–178.

[7] D. D. Osheroff, R. C. Richardson & D. M. Lee, "Evidence for a New Phase of Solid He^3." *Phys. Rev. Lett.*, **28**, (1972), 885–888.

[8] F. Steglich, J. Aarts, C. D. Bredl et al., "Superconductivity in the Presence of Strong Pauli Paramagnetism: $CeCu_2Si_2$." *Phys. Rev. Lett.*, **43**, (1979), 1892–1896.

[9] J. Bednorz & K. Müller, "Possible high T_c superconductivity in the Ba-La-Cu-O system." *Z. Phys. B*, **64** 2, (1986), 189–193.

[10] Y. Kamihara, H. Hiramatsu, M. Hirano et al., "Iron-Based Layered Superconductor: LaOFeP." *Journal of the American Chemical Society*, **128** 31, (2006), 10012–10013.

[11] Y. Kamihara, T. Watanabe, M. Hirano & H. Hosono, "Iron-Based Layered Superconductor $La[O_{1-x}F_x]FeAs$ ($x = 0.05 - 0.12$) with $T_c = 26$ K." *Journal of the American Chemical Society*, **130** 11, (2008), 3296–3297.

[12] H. Takahashi, K. Igawa, K. Arii et al., "Superconductivity at 43 K in an iron-based layered compound $LaO_{1-x}F_xFeAs$." *Nature*, **453**, (2008), 376 – 378.

[13] F.-C. Hsu, J.-Y. Luo, K.-W. Yeh et al., "Superconductivity in the PbO-type structure α-FeSe." *Proceedings of the National Academy of Sciences*, **105** 38, (2008), 14262–14264.

[14] J. H. Tapp, Z. Tang, B. Lv et al., "LiFeAs: An intrinsic FeAs-based superconductor with $T_c = 18$ K." *Phys. Rev. B*, **78**, (2008), 060505.

[15] M. Rotter, M. Tegel & D. Johrendt, "Superconductivity at 38 K in the Iron Arsenide $(Ba_{1-x}K_x)Fe_2As_2$." *Phys. Rev. Lett.*, **101**, (2008), 107006.

[16] C. Wang, L. Li, S. Chi et al., "Thorium-doping–induced superconductivity up to 56 K in Gd_{1-x} Th_xFeAsO." *EPL (Europhysics Letters)*, **83** 6, (2008), 67006.

[17] P. M. Shirage, K. Kihou, C.-H. Lee et al., "Emergence of Superconductivity in "32522" Structure of $(Ca_3Al_2O_{5-y})(Fe_2Pn_2)$ (Pn = As and P)." *Journal of the American Chemical Society*, **133** 25, (2011), 9630–9633. PMID: 21627302.

[18] H.-H. Wen, X. Zhu, F. Han et al., "Physical properties of the new superconducting system $Sr_2VO_{3-\delta}FeAs$ (21311)." *Physica C: Superconductivity and its Applications*, **470**, (2010), S263 – S266. Proceedings of the 9th International Conference on Materials and Mechanisms of Superconductivity.

[19] J. Bardeen, L. N. Cooper & J. R. Schrieffer, "Theory of Superconductivity." *Phys. Rev.*, **108**, (1957), 1175–1204.

[20] J. Annett, *Superconductivity, Superfluids and Condensates.* Oxford Master Series in Physics, (OUP Oxford, 2004).

[21] I. I. Mazin, D. J. Singh, M. D. Johannes & M. H. Du, "Unconventional Superconductivity with a Sign Reversal in the Order Parameter of $LaFeAsO_{1-x}F_x$." *Phys. Rev. Lett.*, **101**, (2008), 057003.

[22] M. Gang, Z. Xi-Yu, F. Lei et al., "Nodal Gap in Fe-Based Layered Superconductor $LaO_{0.9}F_{0.1-\delta}FeAs$ Probed by Specific Heat Measurements." *Chinese Physics Letters*, **25** 6, (2008), 2221–2224.

[23] K. Kuroki, S. Onari, R. Arita et al., "Unconventional Pairing Originating from the Disconnected Fermi Surfaces of Superconducting $LaFeAsO_{1-x}F_x$." *Phys. Rev. Lett.*, **101**, (2008), 087004.

[24] S. Chi, S. Johnston, G. Levy et al., "Sign inversion in the superconducting order parameter of LiFeAs inferred from Bogoliubov quasiparticle interference." *Phys. Rev. B*, **89**, (2014), 104522.

[25] P. J. Hirschfeld, "Using gap symmetry and structure to reveal the pairing mechanism in Fe-based superconductors." *Comptes Rendus Physique*, **17** 1, (2016), 197 – 231. Iron-based superconductors / Supraconducteurs à base de fer.

[26] P. O. Sprau, A. Kostin, A. Kreisel et al., "Discovery of orbital-selective Cooper pairing in FeSe." *Science*, **357** 6346, (2017), 75–80.

[27] L. C. Rhodes, M. D. Watson, A. A. Haghighirad et al., "Scaling of the superconducting gap with orbital character in FeSe." *Phys. Rev. B*, **98**, (2018), 180503.

[28] A. Chubukov, "Pairing Mechanism in Fe-Based Superconductors." *Annual Review of Condensed Matter Physics*, **3** 1, (2012), 57–92.

[29] A. D. Christianson, E. A. Goremychkin, R. Osborn et al., "Unconventional superconductivity in Ba0.6K0.4Fe2As2 from inelastic neutron scattering." *Nature*, **456**, (2008), 930 EP –.

[30] D. S. Inosov, J. T. Park, P. Bourges et al., "Normal-state spin dynamics and temperature-dependent spin-resonance energy in optimally doped BaFe1.85Co0.15As2." *Nature Physics*, **6**, (2009), 178–181.

[31] P. J. Hirschfeld, D. Altenfeld, I. Eremin & I. I. Mazin, "Robust determination of the superconducting gap sign structure via quasiparticle interference." *Phys. Rev. B*, **92**, (2015), 184513.

[32] M. Sato, Y. Kobayashi, S. Chul Lee et al., "Studies on Effects of Impurity Doping and NMR Measurements of La 1111 and/or Nd 1111 Fe-Pnictide Superconductors." *Journal of the Physical Society of Japan*, **79** 1, (2010), 014710.

[33] S. Onari, H. Kontani & M. Sato, "Structure of neutron-scattering peaks in both s_{++}-wave and $s_{\pm}$-wave states of an iron pnictide superconductor." *Phys. Rev. B*, **81**, (2010), 060504.

[34] L. Boeri, O. V. Dolgov & A. A. Golubov, "Is $LaFeAsO_{1-x}F_x$ an Electron-Phonon Superconductor?" *Phys. Rev. Lett.*, **101**, (2008), 026403.

[35] K. Hashimoto, M. Yamashita, S. Kasahara et al., "Line nodes in the energy gap of superconducting $BaFe_2(As_{1-x}P_x)_2$ single crystals as seen via penetration depth and thermal conductivity." *Phys. Rev. B*, **81**, (2010), 220501.

[36] T. A. Maier, S. Graser, D. J. Scalapino & P. J. Hirschfeld, "Origin of gap anisotropy in spin fluctuation models of the iron pnictides." *Phys. Rev. B*, **79**, (2009), 224510.

[37] J. Paglione & R. L. Greene, "High-temperature superconductivity in iron-based materials." *Nature Physics*, **6**, (2010), 645 EP –.

[38] N. Plakida, *High-Temperature Cuprate Superconductors: Experiment, Theory, and Applications (Springer Series in Solid-State Sciences)*, (Springer, 2012).

[39] J. D. Jorgensen, M. A. Beno, D. G. Hinks et al., "Oxygen ordering and the orthorhombic-to-tetragonal phase transition in $YBa_2Cu_3O_{7-x}$." *Phys. Rev. B*, **36**, (1987), 3608–3616.

[40] C. P. Poole, H. A. Farach, R. J. Creswick & R. Prozorov, *Superconductivity (Elsevier Insights)*, (Elsevier, 2014).

[41] M. J. Lawler, K. Fujita, J. Lee et al., "Intra-unit-cell electronic nematicity of the high-Tc copper-oxide pseudogap states." *Nature*, **466** 7304, (2010), 347–351.

[42] N. Ni, M. E. Tillman, J.-Q. Yan et al., "Effects of Co substitution on thermodynamic and transport properties and anisotropic H_{c2} in $Ba(Fe_{1-x}Co_x)_2As_2$ single crystals." *Phys. Rev. B*, **78**, (2008), 214515.

[43] C. Lester, J.-H. Chu, J. G. Analytis et al., "Neutron scattering study of the interplay between structure and magnetism in $Ba(Fe_{1-x}Co_x)_2As_2$." *Phys. Rev. B*, **79**, (2009), 144523.

[44] J.-H. Chu, J. G. Analytis, K. De Greve et al., "In-Plane Resistivity Anisotropy in an Underdoped Iron Arsenide Superconductor." *Science*, **329** 5993, (2010), 824–826.

[45] J.-H. Chu, H.-H. Kuo, J. G. Analytis & I. R. Fisher, "Divergent Nematic Susceptibility in an Iron Arsenide Superconductor." *Science*, **337** 6095, (2012), 710–712.

[46] M. P. Allan, T.-M. Chuang, F. Massee et al., "Anisotropic impurity states, quasiparticle scattering and nematic transport in underdoped $Ca(Fe_{1-x}Co_x)_2As_2$." *Nature Physics*, **9**, (2013), 220 – 224.

[47] M. N. Gastiasoro, I. Paul, Y. Wang, P. J. Hirschfeld & B. M. Andersen, "Emergent Defect States as a Source of Resistivity Anisotropy in the Nematic Phase of Iron Pnictides." *Phys. Rev. Lett.*, **113**, (2014), 127001.

[48] R. M. Fernandes, E. Abrahams & J. Schmalian, "Anisotropic In-Plane Resistivity in the Nematic Phase of the Iron Pnictides." *Phys. Rev. Lett.*, **107**, (2011), 217002.

[49] M. Breitkreiz, P. M. R. Brydon & C. Timm, "resistivity anisotropy due to spin-fluctuation scattering in the nematic phase of iron pnictides." *Phys. Rev. B*, **90**, (2014), 121104.

[50] W. Lv & P. Phillips, "Orbitally and magnetically induced anisotropy in iron-based superconductors." *Phys. Rev. B*, **84**, (2011), 174512.

[51] C.-C. Chen, J. Maciejko, A. P. Sorini et al., "Orbital order and spontaneous orthorhombicity in iron pnictides." *Phys. Rev. B*, **82**, (2010), 100504.

[52] H.-H. Kuo, M. C. Shapiro, S. C. Riggs & I. R. Fisher, "Measurement of the elastoresistivity coefficients of the underdoped iron arsenide $Ba(Fe_{0.975}Co_{0.025})_2As_2$." *Phys. Rev. B*, **88**, (2013), 085113.

[53] H.-H. Kuo, J.-H. Chu, J. C. Palmstrom, S. A. Kivelson & I. R. Fisher, "Ubiquitous signatures of nematic quantum criticality in optimally doped Fe-based superconductors." *Science*, **352** 6288, (2016), 958–962.

[54] T. Shibauchi, A. Carrington & Y. Matsuda, "A Quantum Critical Point Lying Beneath the Superconducting Dome in Iron Pnictides." *Annual Review of Condensed Matter Physics*, **5** 1, (2014), 113–135.

[55] J.-H. Chu, J. G. Analytis, D. Press et al., "In-plane electronic anisotropy in underdoped $Ba(Fe_{1-x}Co_x)_2As_2$ revealed by partial detwinning in a magnetic field." *Phys. Rev. B*, **81**, (2010), 214502.

[56] M. C. Shapiro, P. Hlobil, A. T. Hristov, A. V. Maharaj & I. R. Fisher, "Symmetry constraints on the elastoresistivity tensor." *Phys. Rev. B*, **92**, (2015), 235147.

[57] M. C. Shapiro, A. T. Hristov, J. C. Palmstrom, J.-H. Chu & I. R. Fisher, "Measurement of the B_{1g} and B_{2g} components of the elastoresistivity tensor for tetragonal materials via transverse resistivity configurations." *Review of Scientific Instruments*, **87** 6, (2016), 063902.

[58] J. C. Palmstrom, A. T. Hristov, S. A. Kivelson, J.-H. Chu & I. R. Fisher, "Critical divergence of the symmetric (A_{1g}) nonlinear elastoresistance near the nematic transition in an iron-based superconductor." *Phys. Rev. B*, **96**, (2017), 205133.

[59] C. Bergemann, A. P. Mackenzie, S. R. Julian, D. Forsythe & E. Ohmichi, "Quasi-two-dimensional Fermi liquid properties of the unconventional superconductor Sr2RuO4." *Advances in Physics*, **52** 7, (2003), 639–725.

[60] F. C. Zhang & T. M. Rice, "Effective Hamiltonian for the superconducting Cu oxides." *Phys. Rev. B*, **37**, (1988), 3759–3761.

[61] O. Gunnarsson, E. Koch & R. M. Martin, "Mott transition in degenerate Hubbard models: Application to doped fullerenes." *Phys. Rev. B*, **54**, (1996), R11026–R11029.

[62] Howard University. "Chapter 2.5: Atomic Orbitals and Their Energies." Taken from `https://chem.libretexts.org/Courses/Howard_University/General_Chemistry%3A_An_Atoms_First_Approach/Unit_1%3A__Atomic_Structure/Chapter_2%3A_Atomic_Structure/Chapter_2.5%3A_Atomic_Orbitals_and_Their_Energies`.

[63] A. Georges, L. d. Medici & J. Mravlje, "Strong Correlations from Hund's Coupling." *Annual Review of Condensed Matter Physics*, **4** 1, (2013), 137–178.

[64] M. M. Qazilbash, J. J. Hamlin, R. E. Baumbach et al., "Electronic correlations in the iron pnictides." *Nature Physics*, **5**, (2009), 647–650.

[65] S.-L. Drechsler, F. Roth, M. Grobosch et al., "Insight into the physics of Fe-pnictides from optical and T=0 penetration depth data." *Physica C: Superconductivity and its Applications*, **470**, (2010), S332 – S333. Proceedings of the 9th International Conference on Materials and Mechanisms of Superconductivity.

[66] M. Yi, D. H. Lu, J. G. Analytis et al., "Electronic structure of the $BaFe_2As_2$ family of iron-pnictide superconductors." *Phys. Rev. B*, **80**, (2009), 024515.

[67] M. Yi, Z.-K. Liu, Y. Zhang et al., "Observation of universal strong orbital-dependent correlation effects in iron chalcogenides." *Nature Communications*, **6**, (2015), 7777.

[68] Q. Si & E. Abrahams, "Strong Correlations and Magnetic Frustration in the High T_c Iron Pnictides." *Phys. Rev. Lett.*, **101**, (2008), 076401.

[69] W. L. Yang, A. P. Sorini, C.-C. Chen et al., "Evidence for weak electronic correlations in iron pnictides." *Phys. Rev. B*, **80**, (2009), 014508.

[70] T. Pruschke & R. Bulla, "Hund's coupling and the metal-insulator transition in the two-band Hubbard model." *The European Physical Journal B - Condensed Matter and Complex Systems*, **44** 2, (2005), 217–224.

[71] K. Haule & G. Kotliar, "Coherence–incoherence crossover in the normal state of iron oxypnictides and importance of Hund's rule coupling." *New Journal of Physics*, **11** 2, (2009), 025021.

[72] R. Yu & Q. Si, "$U(1)$ slave-spin theory and its application to Mott transition in a multiorbital model for iron pnictides." *Phys. Rev. B*, **86**, (2012), 085104.

[73] T. Goto, R. Kurihara, K. Araki et al., "Quadrupole Effects of Layered Iron Pnictide Superconductor $Ba(Fe_{0.9}Co_{0.1})_2As_2$." *Journal of the Physical Society of Japan*, **80** 7, (2011), 073702.

[74] M. Yoshizawa, D. Kimura, T. Chiba et al., "Structural Quantum Criticality and Superconductivity in Iron-Based Superconductor $Ba(Fe_{1-x}Co_x)_2As_2$." *Journal of the Physical Society of Japan*, **81** 2, (2012), 024604.

[75] A. G. Green, G. Conduit & F. Krüger, "Quantum Order-by-Disorder in Strongly Correlated Metals." *Annual Review of Condensed Matter Physics*, **9** 1, (2018), 59–77.

[76] R. M. Fernandes, L. H. VanBebber, S. Bhattacharya et al., "Effects of Nematic Fluctuations on the Elastic Properties of Iron Arsenide Superconductors." *Phys. Rev. Lett.*, **105**, (2010), 157003.

[77] K. I. Kugel & K. D. I., "Crystal structure and magnetic properties of substances with orbital degeneracy." *Sov. Phys. - JETP*, **37** 4, (1973), 725–730.

[78] D. Khomskii, *Basic Aspects of the Quantum Theory of Solids: Order and Elementary Excitations*, (Cambridge University Press, 2010).

[79] F. Krüger, S. Kumar, J. Zaanen & J. van den Brink, "Spin-orbital frustrations and anomalous metallic state in iron-pnictide superconductors." *Phys. Rev. B*, **79**, (2009), 054504.

[80] M. Yi, D. Lu, J.-H. Chu et al., "Symmetry-breaking orbital anisotropy observed for detwinned $Ba(Fe_{1-x}Co_x)_2As_2$ above the spin density wave transition." *Proceedings of the National Academy of Sciences*, **108** 17, (2011), 6878–6883.

[81] W. Lv, J. Wu & P. Phillips, "Orbital ordering induces structural phase transition and the resistivity anomaly in iron pnictides." *Phys. Rev. B*, **80**, (2009), 224506.

[82] T. Yildirim, "Origin of the 150-K Anomaly in LaFeAsO: Competing Antiferromagnetic Interactions, Frustration, and a Structural Phase Transition." *Phys. Rev. Lett.*, **101**, (2008), 057010.

[83] Y.-Z. Zhang, I. Opahle, H. O. Jeschke & R. Valentí, "Itinerant nature of magnetism in iron pnictides: A first-principles study." *Phys. Rev. B*, **81**, (2010), 094505.

[84] J. Fink, S. Thirupathaiah, R. Ovsyannikov et al., "Electronic structure studies of $BaFe_2As_2$ by angle-resolved photoemission spectroscopy." *Phys. Rev. B*, **79**, (2009), 155118.

[85] T. M. McQueen, A. J. Williams, P. W. Stephens et al., "Tetragonal-to-Orthorhombic Structural Phase Transition at 90 K in the Superconductor $Fe_{1.01}Se$." *Phys. Rev. Lett.*, **103**, (2009), 057002.

[86] D. Chareev, E. Osadchii, T. Kuzmicheva et al., "Single crystal growth and characterization of tetragonal $FeSe_{1-x}$ superconductors." *CrystEngComm*, **15**, (2013), 1989–1993.

[87] A. E. Böhmer, V. Taufour, W. E. Straszheim, T. Wolf & P. C. Canfield, "Variation of transition temperatures and residual resistivity ratio in vapor-grown FeSe." *Phys. Rev. B*, **94**, (2016), 024526.

[88] S. Margadonna, Y. Takabayashi, M. T. McDonald et al., "Crystal structure of the new $FeSe_{1-x}$ superconductor." *Chem. Commun.*, **43**, (2008), 5607–5609.

[89] A. E. Böhmer, F. Hardy, F. Eilers et al., "Lack of coupling between superconductivity and orthorhombic distortion in stoichiometric single-crystalline FeSe." *Phys. Rev. B*, **87**, (2013), 180505.

[90] K. Kothapalli, A. E. Böhmer, W. T. Jayasekara et al., "Strong cooperative coupling of pressure-induced magnetic order and nematicity in FeSe." *Nature Communications*, **7**, (2016), 12728.

[91] M. A. Tanatar, A. E. Böhmer, E. I. Timmons et al., "Origin of the Resistivity Anisotropy in the Nematic Phase of FeSe." *Phys. Rev. Lett.*, **117** 12, (2016), 127001.

[92] A. E. Böhmer, T. Arai, F. Hardy et al., "Origin of the Tetragonal-to-Orthorhombic Phase Transition in FeSe: A Combined Thermodynamic and NMR Study of Nematicity." *Phys. Rev. Lett.*, **114**, (2015), 027001.

[93] S. Hosoi, K. Matsuura, K. Ishida et al., "Nematic quantum critical point without magnetism in $FeSe_{1-x}S_x$ superconductors." *Proceedings of the National Academy of Sciences*, **113** 29, (2016), 8139–8143.

[94] M. D. Watson, T. K. Kim, A. A. Haghighirad et al., "Emergence of the nematic electronic state in FeSe." *Phys. Rev. B*, **91**, (2015), 155106.

[95] A. I. Coldea & M. D. Watson, "The Key Ingredients of the Electronic Structure of FeSe." *Annual Review of Condensed Matter Physics*, **9** 1, (2018), 125–146.

[96] M. D. Watson, T. K. Kim, L. C. Rhodes et al., "Evidence for unidirectional nematic bond ordering in FeSe." *Phys. Rev. B*, **94**, (2016), 201107.

[97] M. D. Watson, A. A. Haghighirad, L. C. Rhodes, M. Hoesch & T. K. Kim, "Electronic anisotropies revealed by detwinned angle-resolved photo-emission spectroscopy measurements of FeSe." *New Journal of Physics*, **19** 10, (2017), 103021.

[98] Y. Suzuki, T. Shimojima, T. Sonobe et al., "Momentum-dependent sign inversion of orbital order in superconducting FeSe." *Phys. Rev. B*, **92**, (2015), 205117.

[99] T. Shimojima, Y. Suzuki, T. Sonobe et al., "Lifting of xz/yz orbital degeneracy at the structural transition in detwinned FeSe." *Phys. Rev. B*, **90**, (2014), 121111.

[100] J. P. Sun, K. Matsuura, G. Z. Ye et al., "Dome-shaped magnetic order competing with high-temperature superconductivity at high pressures in FeSe." *Nature Communications*, **7**, (2016), 12146.

[101] S. Knöner, D. Zielke, S. Köhler et al., "Resistivity and magnetoresistance of FeSe single crystals under helium-gas pressure." *Phys. Rev. B*, **91**, (2015), 174510.

[102] S. Margadonna, Y. Takabayashi, Y. Ohishi et al., "Pressure evolution of the low-temperature crystal structure and bonding of the superconductor FeSe (T_c = 37 K)." *Phys. Rev. B*, **80**, (2009), 064506.

[103] R. M. Fernandes, A. V. Chubukov & J. Schmalian, "What drives nematic order in iron-based superconductors?" *Nature Physics*, **10**, (2014), 97–104.

[104] A. E. Böhmer & A. Kreisel, "Nematicity, magnetism and superconductivity in FeSe." *Journal of Physics: Condensed Matter*, **30** 2, (2017), 023001.

[105] T. Terashima, N. Kikugawa, A. Kiswandhi et al., "Fermi surface reconstruction in FeSe under high pressure." *Phys. Rev. B*, **93**, (2016), 094505.

[106] K. Matsuura, Y. Mizukami, Y. Arai et al., "Maximizing T_c by tuning nematicity and magnetism in $FeSe_{1x}S_x$ superconductors." *Nature Communications*, **8** 1, (2017), 1143.

[107] K. Kuroki, H. Usui, S. Onari, R. Arita & H. Aoki, "Pnictogen height as a possible switch between high-T_c nodeless and low-T_c nodal pairings in the iron-based superconductors." *Phys. Rev. B*, **79**, (2009), 224511.

[108] Y. Sato, S. Kasahara, T. Taniguchi et al., "Abrupt change of the superconducting gap structure at the nematic critical point in $FeSe_{1-x}S_x$." *Proceedings of the National Academy of Sciences*, **115** 6, (2018), 1227–1231.

[109] T. Hanaguri, K. Iwaya, Y. Kohsaka et al., "Two distinct superconducting pairing states divided by the nematic end point in $FeSe_{1-x}S_x$." *Science Advances*, **4** 5, (2018), 1–7.

[110] Q. Wang, Y. Shen, B. Pan et al., "Magnetic ground state of FeSe." *Nature Communications*, **7**, (2016), 12182.

[111] Q. Wang, Y. Shen, B. Pan et al., "Strong interplay between stripe spin fluctuations, nematicity and superconductivity in FeSe." *Nature Materials*, **15**, (2015), 159–163.

[112] H. Kontani & S. Onari, "Orbital-Fluctuation-Mediated Superconductivity in Iron Pnictides: Analysis of the Five-Orbital Hubbard-Holstein Model." *Phys. Rev. Lett.*, **104**, (2010), 157001.

[113] J.-Y. Lin, Y. S. Hsieh, D. A. Chareev et al., "Coexistence of isotropic and extended s-wave order parameters in FeSe as revealed by low-temperature specific heat." *Phys. Rev. B*, **84**, (2011), 220507.

[114] F. Hardy, M. He, L. Wang et al., "Calorimetric evidence of nodal gaps in the nematic superconductor FeSe." *Phys. Rev. B*, **99**, (2019), 035157.

[115] T. Hashimoto, Y. Ota, H. Q. Yamamoto et al., "Superconducting gap anisotropy sensitive to nematic domains in FeSe." *Nature Communications*, **9** 1, (2018), 282.

[116] A. Kreisel, B. M. Andersen, P. O. Sprau et al., "Orbital selective pairing and gap structures of iron-based superconductors." *Phys. Rev. B*, **95**, (2017), 174504.

[117] L. Benfatto, B. Valenzuela & L. Fanfarillo, "Nematic pairing from orbital-selective spin fluctuations in FeSe." *npj Quantum Materials*, **3** 1, (2018), 56.

[118] J. Kang & R. M. Fernandes, "Superconductivity in FeSe Thin Films Driven by the Interplay between Nematic Fluctuations and Spin-Orbit Coupling." *Phys. Rev. Lett.*, **117**, (2016), 217003.

[119] J. Kang, R. M. Fernandes & A. Chubukov, "Superconductivity in FeSe: The Role of Nematic Order." *Phys. Rev. Lett.*, **120**, (2018), 267001.

[120] A. V. Chubukov, M. Khodas & R. M. Fernandes, "Magnetism, Superconductivity, and Spontaneous Orbital Order in Iron-Based Superconductors: Which Comes First and Why?" *Phys. Rev. X*, **6**, (2016), 041045.

[121] D.-H. Lee, "Hunting down unconventional superconductors." *Science*, **357** 6346, (2017), 32–33.

[122] W. Wang, J. Li, J. Yang et al., "Scotch tape induced strains for enhancing superconductivity of $FeSe_{0.5}Te_{0.5}$ single crystals." *Applied Physics Letters*, **105** 23, (2014), 232602.

[123] K. Deguchi, Y. Mizuguchi, Y. Kawasaki et al., "Alcoholic beverages induce superconductivity in $FeTe_{1-x}S_x$." *Superconductor Science and Technology*, **24** 5, (2011), 055008.

[124] C. Meingast, F. Hardy, R. Heid et al., "Thermal Expansion and Grüneisen Parameters of $Ba(Fe_{1-x}Co_x)_2As_2$: A Thermodynamic Quest for Quantum Criticality." *Phys. Rev. Lett.*, **108**, (2012), 177004.

[125] S. Kasahara, T. Watashige, T. Hanaguri et al., "Field-induced superconducting phase of FeSe in the BCS-BEC cross-over." *Proceedings of the National Academy of Sciences*, **111** 46, (2014), 16309–16313.

[126] H. C. Xu, X. H. Niu, D. F. Xu et al., "Highly Anisotropic and Twofold Symmetric Superconducting Gap in Nematically Ordered $FeSe_{0.93}S_{0.07}$." *Phys. Rev. Lett.*, **117**, (2016), 157003.

[127] S.-H. Baek, D. V. Efremov, J. M. Ok et al., "Orbital-driven nematicity in FeSe." *Nature Materials*, **14**, (2014), 210–214.

[128] Y. Su, H. Liao & T. Li, "The form and origin of orbital ordering in the electronic nematic phase of iron-based superconductors." *Journal of Physics: Condensed Matter*, **27** 10, (2015), 105702.

[129] S. Mukherjee, A. Kreisel, P. J. Hirschfeld & B. M. Andersen, "Model of Electronic Structure and Superconductivity in Orbitally Ordered FeSe." *Phys. Rev. Lett.*, **115**, (2015), 026402.

[130] R.-Q. Xing, L. Classen, M. Khodas & A. V. Chubukov, "Competing instabilities, orbital ordering, and splitting of band degeneracies from a parquet renormalization group analysis of a four-pocket model for iron-based superconductors: Application to FeSe." *Phys. Rev. B*, **95**, (2017), 085108.

[131] L. Fanfarillo, G. Giovannetti, M. Capone & E. Bascones, "Nematicity at the Hund's metal crossover in iron superconductors." *Phys. Rev. B*, **95**, (2017), 144511.

[132] A. V. Chubukov, R. M. Fernandes & J. Schmalian, "Origin of nematic order in FeSe." *Phys. Rev. B*, **91**, (2015), 201105.

[133] M. H. Christensen, J. Kang, B. M. Andersen & R. M. Fernandes, "Spin-driven nematic instability of the multiorbital Hubbard model: Application to iron-based superconductors." *Phys. Rev. B*, **93**, (2016), 085136.

[134] A. Georges, G. Kotliar, W. Krauth & M. J. Rozenberg, "Dynamical mean-field theory of strongly correlated fermion systems and the limit of infinite dimensions." *Rev. Mod. Phys.*, **68**, (1996), 13–125.

[135] J. Wu, P. Phillips & A. H. Castro Neto, "Theory of the Magnetic Moment in Iron Pnictides." *Phys. Rev. Lett.*, **101**, (2008), 126401.

[136] P. Werner & A. J. Millis, "High-Spin to Low-Spin and Orbital Polarization Transitions in Multiorbital Mott Systems." *Phys. Rev. Lett.*, **99**, (2007), 126405.

[137] L. de' Medici, S. R. Hassan, M. Capone & X. Dai, "Orbital-Selective Mott Transition out of Band Degeneracy Lifting." *Phys. Rev. Lett.*, **102**, (2009), 126401.

[138] L. de' Medici, G. Giovannetti & M. Capone, "Selective Mott Physics as a Key to Iron Superconductors." *Phys. Rev. Lett.*, **112**, (2014), 177001.

[139] J. Maletz, V. B. Zabolotnyy, D. V. Evtushinsky et al., "Unusual band renormalization in the simplest iron-based superconductor $FeSe_{1-x}$." *Phys. Rev. B*, **89**, (2014), 220506.

[140] M. D. Watson, S. Backes, A. A. Haghighirad et al., "Formation of Hubbard-like bands as a fingerprint of strong electron-electron interactions in FeSe." *Phys. Rev. B*, **95**, (2017), 081106.

[141] N. Lanatà, H. U. R. Strand, G. Giovannetti et al., "Orbital selectivity in Hund's metals: The iron chalcogenides." *Phys. Rev. B*, **87**, (2013), 045122.

[142] L. Fanfarillo, L. Benfatto & B. Valenzuela, "Orbital mismatch boosting nematic instability in iron-based superconductors." *Phys. Rev. B*, **97**, (2018), 121109.

[143] A. Kostin, P. O. Sprau, A. Kreisel et al., "Imaging orbital-selective quasiparticles in the Hund's metal state of FeSe." *Nature Materials*, **17** 10, (2018), 869–874.

[144] J. Wittig & B. T. Matthias, "Superconductivity of Barium Under Pressure." *Phys. Rev. Lett.*, **22**, (1969), 634–636.

[145] C. W. Chu, P. H. Hor, R. L. Meng et al., "Evidence for superconductivity above 40 K in the La-Ba-Cu-O compound system." *Phys. Rev. Lett.*, **58**, (1987), 405–407.

[146] M. K. Wu, J. R. Ashburn, C. J. Torng et al., "Superconductivity at 93 K in a new mixed-phase Y-Ba-Cu-O compound system at ambient pressure." *Phys. Rev. Lett.*, **58**, (1987), 908–910.

[147] T. Terashima, N. Kikugawa, S. Kasahara et al., "Pressure-Induced Antiferromagnetic Transition and Phase Diagram in FeSe." *Journal of the Physical Society of Japan*, **84** 6, (2015), 063701.

[148] U. Welp, M. Grimsditch, S. Fleshler et al., "Effect of uniaxial stress on the superconducting transition in $YBa_2Cu_3O_7$." *Phys. Rev. Lett.*, **69**, (1992), 2130–2133.

[149] D. Roylance, *Mechanics of Materials*, (Wiley, 1996).

[150] G. Mase, *Schaum's Outline of Continuum Mechanics.* Schaum's outline of theory and problems, (McGraw-Hill Education, 1970).

[151] J. F. Nye, *Physical Properties of Crystals: Their Representation by Tensors and Matrices*, (Oxford University Press, 1985).

[152] G. Burns, "Appendix 3 - Character Tables." In G. Burns, editor, "Introduction to Group Theory with Applications," Materials Science and Technology, pages 379 – 390, (Academic Press, 1977).

[153] M. Ikeda, T. Worasaran, J. C. Palmstrom, P. Walmsley & I. R. Fisher (2018). "Symmetric and antisymmetric strain as continuous tuning parameters for electronic nematic order." arXiv:1803.09273.

[154] G. A. Zvyagina, T. N. Gaydamak, K. R. Zhekov et al., "Acoustic characteristics of FeSe single crystals." *EPL (Europhysics Letters)*, **101** 5, (2013), 56005.

[155] S. Chandra & A. Islam, "Elastic properties of mono- and poly-crystalline PbO-type $FeSe_{1x}Te_x$ ($x = 0-1.0$): A first-principles study." *Physica C: Superconductivity*, **470** 22, (2010), 2072 – 2075.

[156] U. K. Chowdhury, M. A. Rahman, M. A. Rahman & M. Bhuiyan, "Ab-initio study on structural, elastic, electronic and optical properties of iron-based superconductor." *Cogent Physics*, **3** 1, (2016), 1265779.

[157] A. E. Böhmer, P. Burger, F. Hardy et al., "Nematic Susceptibility of Hole-Doped and Electron-Doped $BaFe_2As_2$ Iron-Based Superconductors from Shear Modulus Measurements." *Phys. Rev. Lett.*, **112**, (2014), 047001.

[158] D. J. Dunstan & I. L. Spain, "Technology of diamond anvil high-pressure cells: I. Principles, design and construction." *Journal of Physics E: Scientific Instruments*, **22** 11, (1989), 913.

[159] X. Wei & K. Chau, "Finite and transversely isotropic elastic cylinders under compression with end constraint induced by friction." *International Journal of Solids and Structures*, **46** 9, (2009), 1953 – 1965.

[160] A. Steppke, L. Zhao, M. E. Barber et al., "Strong peak in T_c of Sr_2RuO_4 under uniaxial pressure." *Science*, **355** 6321, (2017), 1–8.

[161] C. Pfleiderer, E. Bedin & B. Salce, "He activated loading device for low temperature uniaxial and anvil cell pressure experiments." *Review of Scientific Instruments*, **68** 8, (1997), 3120–3124.

[162] A. M. Simpson & W. Wolfs, "Thermal expansion and piezoelectric response of PZT Channel 5800 for use in low-temperature scanning tunnelling microscope designs." *Review of Scientific Instruments*, **58** 11, (1987), 2193–2195.

[163] A. L. Kholkin, N. A. Pertsev & A. V. Goltsev, *Piezoelectricity and Crystal Symmetry*, pages 17–38, (Springer US, Boston, MA, 2008).

[164] R. Leach & S. T. Smith, *Basics of Precision Engineering*, (CRC Press, 2018).

[165] M. W. Hooker (1998). "Properties of PZT-Based Piezoelectric Ceramics Between -150 and 250 °C." Technical Report NASA/CR-1998-208708, NASA Langley Research Center.

[166] C. W. Hicks, M. E. Barber, S. D. Edkins, D. O. Brodsky & A. P. Mackenzie, "Piezoelectric-based apparatus for strain tuning." *Review of Scientific Instruments*, **85** 6, (2014), 065003.

[167] J. Ekin, *Experimental Techniques: Cryostat Design, Material Properties and Superconductor Critical-Current Testing*, (Oxford University Press, 2006).

[168] C. W. Hicks, D. O. Brodsky, E. A. Yelland et al., "Strong Increase of T_c of Sr_2RuO_4 Under Both Tensile and Compressive Strain." *Science*, **344** 6181, (2014), 283–285.

[169] J. Park, M. König, J. Bartlett, A. P. Mackenzie & C. W. Hicks (2017). "Rigid platform for applying uniaxial pressure on micro-structured devices." Unpublished.

[170] M. Niinomi, "Mechanical properties of biomedical titanium alloys." *Materials Science and Engineering: A*, **243** 1, (1998), 231 – 236.

[171] C. Leyens, "Oxidation and Protection of Titanium Alloys and Titanium Aluminides." In C. Leyens & M. Peters, editors, "Titanium and Titanium Alloys: Fundamentals and Applications," chapter 6, pages 187–230, (Wiley-VCH, 2003).

[172] M. J. Donachie, *Titanium: A Technical Guide*, (ASM International, 2000).

[173] A. V. Maharaj, E. W. Rosenberg, A. T. Hristov et al., "Transverse fields to tune an Ising-nematic quantum phase transition." *Proceedings of the National Academy of Sciences*.

[174] T. Hashimoto & A. Ikushima, "Mechanical properties of Stycast-1266 at low temperatures." *Review of Scientific Instruments*, **51** 3, (1980), 378–379.

[175] A. F. Clark, "Chapter 3 - Thermal Expansion." In R. P. Reed & A. F. Clark, editors, "Materials at Low Temperatures," , (Metals Park, Ohio : American Society for Metals, 1983).

[176] M. A. Tanatar, A. Kreyssig, S. Nandi et al., "Direct imaging of the structural domains in the iron pnictides AFe_2As_2 (A = Ca, Sr, Ba)." *Phys. Rev. B*, **79**, (2009), 180508.

[177] I. R. Fisher, L. Degiorgi & Z. X. Shen, "In-plane electronic anisotropy of underdoped '122' Fe-arsenide superconductors revealed by measurements of detwinned single crystals." *Reports on Progress in Physics*, **74** 12, (2011), 124506.

[178] M. Tanatar, R. Prozorov, N. Ni, S. Bud'ko & P. Canfield (2010). "Low resistivity contact to iron-pnictide superconductors." US Patent US8450246B2.

[179] E. Pomjakushina, K. Conder, V. Pomjakushin, M. Bendele & R. Khasanov, "Synthesis, crystal structure, and chemical stability of the superconductor $FeSe_{1-x}$." *Phys. Rev. B*, **80**, (2009), 024517.

[180] S. B. Wilkins (2006). QLaue, Software.

[181] O. J. Schumann (2010). "Cologne Laue Indexation Program." CLIP, software.

[182] S. Saalfeld (2010). "Enhance Local Contrast (CLAHE)." Image J, Software.

[183] M. A. Sutton, J. J. Orteu & H. Schreier, *Image Correlation for Shape, Motion and Deformation Measurements: Basic Concepts,Theory and Applications*, (Springer, 2009).

[184] A. M. Howatson, P. G. Lund & J. D. Todd, *Engineering Tables and Data*, (Springer, 1972).

[185] K. Mukugi, A. Takemura & Y. Morimoto, "Low Temperature Mechanical Properties of Titanium and Weld Joints (Ti/Ti, Ti/Nb) for Helium Vessels." *The 2001 Workshop on RF Superconductivity.*

[186] M. Xu, P. Yan, T. Koyama, T. Ogura & R. Li, *Development of a 4K Two-stage Pulse Tube Cryocooler*, pages 301–307, (Springer US, Boston, MA, 2003).

[187] W. E. Gifford & R. C. Longsworth, "Pulse-Tube Refrigeration." *Journal of Engineering for Industry*, **86** 3, (1964), 264–268.

[188] R. Richardson, "Pulse tube refrigerator — an alternative cryocooler?" *Cryogenics*, **26** 6, (1986), 331 – 340.

[189] R. Radebaugh, "Development of the pulse tube refrigerator as an efficient and reliable cryocooler." *Institute of Refrigeration.*

[190] M. David, J.-C. Maréchal, Y. Simon & C. Guilpin, "Theory of ideal orifice pulse tube refrigerator." *Cryogenics*, **33** 2, (1993), 154 – 161.

[191] T. Noji, T. Suzuki, H. Abe et al., "Growth, Annealing Effects on Superconducting and Magnetic Properties, and Anisotropy of $FeSe_{1-x}Te_x$ ($0.5 \leq x \leq 1$) Single Crystals." *Journal of the Physical Society of Japan*, **79** 8, (2010), 084711.

[192] D. O. Brodsky (2015). *Investigation of correlated electron systems under uni-axial strain.* Ph.D. thesis, University of St Andrews, School of Physics and Astronomy.

[193] M. Nikolo, "Superconductivity: A guide to alternating current susceptibility measurements and alternating current susceptometer design." *American Journal of Physics*, **63** 1, (1995), 57–65.

[194] P. Walmsley & I. R. Fisher, "Determination of the resistivity anisotropy of orthorhombic materials via transverse resistivity measurements." *Review of Scientific Instruments*, **88** 4, (2017), 043901.

[195] H. C. Montgomery, "Method for Measuring Electrical Resistivity of Anisotropic Materials." *Journal of Applied Physics*, **42** 7, (1971), 2971–2975.

[196] S. Onari & H. Kontani, "In-plane anisotropy of transport coefficients in electronic nematic states: Universal origin of nematicity in Fe-based superconductors." *Phys. Rev. B*, **96**, (2017), 094527.

[197] M. E. Barber, A. Steppke, A. P. Mackenzie & C. W. Hicks, "Piezoelectric-based uniaxial pressure cell with integrated force and displacement sensors." *Review of Scientific Instruments*, **90** 2, (2019), 023904.

[198] J. Park, H. Sakai, O. Erten, A. P. Mackenzie & C. W. Hicks, "Effect of applied orthorhombic lattice distortion on the antiferromagnetic phase of $CeAuSb_2$." *Phys. Rev. B*, **97**, (2018), 024411.

[199] Attocube Systems. *ANPx311 Technical Specifications.*

[200] Y. Milman, I. Gridneva & A. Golubenko, "Construction of stess-strain curves for brittle materials by indentation in a wide temperature range." *Science of Sintering*, **39** 1, (2007), 67–75.

[201] K. E. Petersen, "Silicon as a mechanical material." *Proceedings of the IEEE*, **70** 5, (1982), 420–457.

[202] M. A. Hopcroft, W. D. Nix & T. W. Kenny, "What is the Young's Modulus of Silicon?" *Journal of Microelectromechanical Systems*, **19** 2, (2010), 229–238.

[203] F. Laermer & A. Urban, "Challenges, developments and applications of silicon deep reactive ion etching." **67-68**, (2003), 349–355.

[204] E. Oberg, F. D. Jones, H. L. Horton & H. H. Ryffel, *Machinery's handbook : a reference book for the mechanical engineer, designer, manufacturing engineer, draftsman, toolmaker, and machinist*, (Industrial Press, New York, 2008).

[205] E. R. Dobrovinskaya, L. A. Lytvynov & V. Pishchik, *Sapphire: Material, Manufacturing, Applications (Micro- and Opto-Electronic Materials, Structures, and Systems)*, (Springer, 2009).

[206] Z. Peng & S. A. T. Redfern, "Mechanical properties of quartz at the α-β phase transition: Implications for tectonic and seismic anomalies." *Geochemistry, Geophysics, Geosystems*, **14** 1, (2013), 18–28.

[207] A. Ballato, "Poisson's ratio for tetragonal, hexagonal, and cubic crystals." *IEEE Transactions on Ultrasonics, Ferroelectrics, and Frequency Control*, **43** 1, (1996), 56–62.